

**Gyroscope and Micromirror Design  
Using Vertical-Axis CMOS-MEMS Actuation and Sensing**

**by**

**Huikai Xie**

**A dissertation submitted in partial satisfaction of the requirements for the degree of**

**Doctor of Philosophy**

**in**

**Electrical and Computer Engineering**

**in the**

**Carnegie Institute of Technology**

**of the**

**Carnegie Mellon University**

**Committee:**

**Professor Gary K. Fedder, Advisor**

**Professor L. Richard Carley**

**Dr. Tamal Mukherjee**

**Mr. John A. Geen (Analog Devices, Inc.)**

**2002**

Report Documentation Page				Form Approved OMB No. 0704-0188	
Public reporting burden for the collection of information is estimated to average 1 hour per response, including the time for reviewing instructions, searching existing data sources, gathering and maintaining the data needed, and completing and reviewing the collection of information. Send comments regarding this burden estimate or any other aspect of this collection of information, including suggestions for reducing this burden, to Washington Headquarters Services, Directorate for Information Operations and Reports, 1215 Jefferson Davis Highway, Suite 1204, Arlington VA 22202-4302. Respondents should be aware that notwithstanding any other provision of law, no person shall be subject to a penalty for failing to comply with a collection of information if it does not display a currently valid OMB control number.					
1. REPORT DATE <b>2002</b>		2. REPORT TYPE		3. DATES COVERED <b>00-00-2002 to 00-00-2002</b>	
4. TITLE AND SUBTITLE <b>Gyroscope and Micromirror Design Using Vertical-Axis CMOS-MEMS Actuation and Sensing</b>				5a. CONTRACT NUMBER	
				5b. GRANT NUMBER	
				5c. PROGRAM ELEMENT NUMBER	
6. AUTHOR(S)				5d. PROJECT NUMBER	
				5e. TASK NUMBER	
				5f. WORK UNIT NUMBER	
7. PERFORMING ORGANIZATION NAME(S) AND ADDRESS(ES) <b>Carnegie Mellon University, Department of Electrical and Computer Engineering, Pittsburgh, PA, 15213-3890</b>				8. PERFORMING ORGANIZATION REPORT NUMBER	
9. SPONSORING/MONITORING AGENCY NAME(S) AND ADDRESS(ES)				10. SPONSOR/MONITOR'S ACRONYM(S)	
				11. SPONSOR/MONITOR'S REPORT NUMBER(S)	
12. DISTRIBUTION/AVAILABILITY STATEMENT <b>Approved for public release; distribution unlimited</b>					
13. SUPPLEMENTARY NOTES					
14. ABSTRACT <b>see report</b>					
15. SUBJECT TERMS					
16. SECURITY CLASSIFICATION OF:			17. LIMITATION OF ABSTRACT <b>Same as Report (SAR)</b>	18. NUMBER OF PAGES <b>246</b>	19a. NAME OF RESPONSIBLE PERSON
a. REPORT <b>unclassified</b>	b. ABSTRACT <b>unclassified</b>	c. THIS PAGE <b>unclassified</b>			

# CARNEGIE MELLON UNIVERSITY

## CARNEGIE INSTITUTE OF TECHNOLOGY

### THESIS

SUBMITTED IN PARTIAL FULFILLMENT OF THE REQUIREMENTS  
FOR THE DEGREE OF DOCTOR OF PHILOSOPHY

TITLE Gyroscope and Micromirror Design  
Using Vertical-Axis CMOS-MEMS Actuation and Sensing

PRESENTED BY Huikai Xie

ACCEPTED BY THE DEPARTMENT OF Electrical and Computer Engineering

Professor Gary K. Fedder  
MAJOR PROFESSOR DATE

Professor Pradeep K. Khosla  
DEPARTMENT HEAD DATE

APPROVED BY THE COLLEGE COUNCIL

Professor John L. Anderson  
DEAN DATE

Gyroscope and Micromirror Design  
Using Vertical-Axis CMOS-MEMS Actuation and Sensing

© 2002

by

Huikai Xie



## **Abstract**

### **Gyroscope and Micromirror Design Using Vertical-Axis CMOS-MEMS Sensing and Actuation**

by

Huikai Xie

CMOS-MEMS processes leverage mainstream CMOS technologies to achieve on-chip interface and signal processing circuitry, scalability, multi-vendor accessibility, short design cycles, more on-chip functions and low cost. However, most CMOS-MEMS processes are based on thin-film microstructures which often require wet etching for release. The Carnegie Mellon thin-film CMOS-MEMS process requires only dry-etch steps and is maskless, but has drawbacks of curling due to residual stress and temperature coefficient of expansion of the multi-layer structures. This thesis introduces a deep reactive-ion-etch (DRIE) CMOS-MEMS process which incorporates bulk Si into microstructures using backside etch. The resultant microstructures are flat and have no release holes. Electrically isolated silicon is obtained using a silicon undercut. This process is suitable for applications that require large mass and flat surfaces such as inertial sensors and micromirrors.

A technique for vertical-axis sensing and actuation using comb-finger sidewall capacitance is developed. For vertical-axis sensing, this technique has small parasitic capacitance compared to the counterparts that have an electrode on the substrate. For vertical actuation, this technique has a very large gap to substrate set by the process, so that the actuation range is not limited. A unique curled comb drive design demonstrates a maximum 62  $\mu\text{m}$  out-of-plane displacement for a micromirror scanning.

Several thin-film and DRIE devices are fabricated and characterized. A 0.5 mm by 0.5 mm microstage moves 0.3  $\mu\text{m}$  vertically at 14 V d.c. Thin-film and DRIE z-axis accelerometers (both are about 0.5 mm by 0.6 mm) have noise floors of 6  $\text{mG/Hz}^{1/2}$  and 0.5  $\text{mG/Hz}^{1/2}$ , respectively. The noise floor of a lateral-axis gyroscope is improved from

0.8 °/s/Hz<sup>1/2</sup> for the thin-film CMOS-MEMS process to 0.02 °/s/Hz<sup>1/2</sup> for the DRIE CMOS-MEMS process.

Solutions for improving the gyroscopes' performance and yield are proposed, including a new process flow for independently controlling silicon undercut and a vertical-axis electrostatic force cancellation technique for compensating the off-axis motion.

The electrostatic micromirror rotates 5° at 18 V d.c. The thermally actuated micromirror rotates 17° at 12 mA current and has been installed into an endoscopic optical coherence tomography imaging system for *in vivo* imaging of biological tissue. Transverse and axial resolutions of roughly 20 µm and 10 µm, respectively, are achieved. Cross-sectional images of 500 × 1000 pixels covering an area of 2.9 × 2.8 mm<sup>2</sup> are acquired at 5 frames/s.

To my parents,  
to my wife Yuxiao Tong,  
and to my sons Yutong and Yucheng.

# Acknowledgements

I would like to gratefully acknowledge all those people who have helped me to complete this thesis. First of all, I thank my advisor, Professor Gary K. Fedder, for his excellent guidance, support and encouragement throughout my four years' research and for helping me find a great job. His friendship will never be forgotten. I also thank my thesis committee members, Professor L. Richard Carley, Dr. Tamal Mukherjee and Mr. John A. Geen for reviewing the manuscript. Especially I would like to thank Mr. Geen for giving me very good feedback and comments during my research. Many thanks to Professor Ken Gabriel and Professor Qiao Lin for valuable discussions and Mr. Suresh Santhanam for discussions about processing issues and training me how to use SEM and RIE systems.

I thank Dr. Wilhelm Frey of Bosch for his interest and financial support to my research, for providing me a summer internship, and for his friendship and generous help in my career. Thanks to Dr. Zhiyu Pan of Bosch, one of my best friends, for supporting me not just in research but also in my personal life.

I am truly grateful to Professor Yingtian Pan of University of Pittsburgh for the fruitful collaboration, his friendship and lots of his valuable personal advice. Also thanks to Dr. Tuqiang Xie for discussions and experimental work.

I am very thankful to all my fellow colleagues, a great team with various expertise. Many thanks to Dr. Lars Erdmann of Carl Zeiss for DRIE processing and optical measurement, Xu Zhu for device fabrication processing, Michael Lu for mechanics discussions, Hao Luo and Jiangfeng Wu for analog circuit design, Hasnain Lakdawala and Bikram Baiyda for FEM simulation, Qi Jing and Sitaraman Iyer for NODAS simulation, Michael Stout and Kevin Frederick for Labview programming, Kai He for software consulting, and my other office mates: Dr. John Newmann, George Lopez, Dan Gaugel, Matthew Zeleznik, Brett Diamond, Janet Stillmann and Altug Oz.

I thank Chris Bowman and Carsen Kline of Nanofabrication Facility for keeping the equipment running. Special thanks to Mary Moore and Drew Denielson for all the administrative assistance. Thanks to Lou Anschuetz and Mathew Henson for computer maintenance, and to the ECE administrative staff: Lynn Philibin, Elaine Lawrence, Nancy Burgy, Lynne Smith, Ed Pikula and Elaine Zurcher.

Finally, I would like to express my deep gratitude to my wife Yuxiao and my two children (Yutong and Yucheng). I would never have been able to finish this thesis without their full support and understanding.

The projects were funded by the DARPA-MEMS program and U.S. AFRL, under cooperative agreement F30602-97-2-0323. Robert Bosch Corporation provided partial financial support to the gyroscope project. The biomedical imaging project was in part supported by NIH contract NIH-1-R01-DK059265-01 and the Whitaker Foundation contract 00-0149.

---

# Contents

<b>Abstract .....</b>	<b>iv</b>
<b>Acknowledgements .....</b>	<b>vii</b>
<b>Contents .....</b>	<b>ix</b>
<b>List of figures .....</b>	<b>xiii</b>
<b>List of Table .....</b>	<b>xxi</b>
<b>1 Introduction .....</b>	<b>1</b>
1.1 Scope .....	1
1.2 CMOS-MEMS Technology .....	1
1.3 Comb-finger Vertical Sensing and Actuation .....	4
1.4 Micromirrors .....	6
1.5 MEMS Vibratory-Rate Gyroscope .....	9
<b>2 CMOS-MEMS Processes .....</b>	<b>11</b>
2.1 Thin-film CMOS-MEMS Process .....	11
2.2 DRIE CMOS-MEMS Process .....	16
2.2.1 Process flow .....	18
2.2.2 Design considerations .....	21
2.2.3 Fabrication .....	23
2.3 CHARACTERIZATION .....	27
2.3.1 Cantilever beams .....	27
2.3.2 Comb-drive resonator .....	28
<b>3 Vertical Comb-Finger Sensing and Actuation .....</b>	<b>31</b>
3.1 Introduction .....	31
3.2 Thin-Film Out-of-Plane Comb-Finger Actuation and Sensing .....	32

---

3.2.1 Z-axis Actuation .....	33
3.2.2 Z-axis Displacement Sensing .....	35
3.2.2.1 Vertical Sidewall Capacitance Offset Cancellation .....	36
3.2.3 Z-axis Thin-Film Comb-Finger Accelerometer .....	38
3.2.4 X-Y-Z Microstage .....	46
3.3 DRIE CMOS-MEMS Out-of-plane Comb-Finger Sensing and Actuation ...	48
3.3.1 Three-Dimensional Electrostatic Actuation .....	48
3.3.2 Three-dimensional position sensing .....	51
3.3.3 DRIE z-axis accelerometer .....	53
<b>4 CMOS-MEMS Micromirrors: Design, Fabrication and Application .....</b>	<b>59</b>
4.1 INTRODUCTION .....	59
4.2 Electrostatic SCS CMOS Micromirror .....	59
4.2.1 Curled comb drive .....	60
4.2.2 Torsional Spring Design .....	61
4.2.3 SCS Electrostatic Micromirror Design .....	62
4.2.4 Fabricated Electrostatic Micromirror .....	62
4.2.4.1 Characterization .....	64
4.2.4.2 Summary and future work of the electrostatic micromirror ...	66
4.3 Electrothermal Micromirror .....	67
4.3.1 Mirror Design .....	67
4.3.1.1 Characterization .....	69
4.3.2 Optical Coherence Tomography Application .....	72
4.3.2.1 Introduction .....	72
4.3.2.2 MEMS Mirror-based OCT Endoscope .....	73
4.3.3 Experimental Results .....	77
4.4 Other Fabricated Micro-optical Components .....	79
4.5 A New Electrostatic Micromirror Design .....	80
4.5.1 The Concept .....	80
4.5.2 Fabrication and Discussion .....	82
4.6 Summary .....	84
<b>5 Gyroscope Theory, Modeling, Design and Simulation .....</b>	<b>85</b>

---

---

5.1	Previous MEMS Gyroscope Work .....	85
5.1.1	Modeling and Simulation of MEMS Gyroscopes .....	87
5.2	Design Issues For Vibratory Gyroscopes .....	88
5.2.1	Operational Principle Of Vibratory Gyroscopes .....	88
5.2.2	Design Issues for Vibratory Gyroscopes .....	93
5.3	Designs of CMOS-MEMS Gyroscopes .....	96
5.3.1	Basic Structures of Gimbaled Gyroscopes .....	96
5.3.2	Design Considerations .....	98
5.3.2.1	Spring Designs .....	99
5.3.2.2	Phase Issue .....	101
5.3.2.3	Noise Considerations .....	104
5.3.3	Comb Drive 3D Motion Analysis .....	106
5.3.4	Proposed CMOS-MEMS gyroscope designs .....	111
5.4	Gyroscope Simulation .....	117
5.4.1	Matlab simulation .....	118
5.4.2	NODAS Simulation .....	120
5.4.2.1	Beam and plate NODAS models for DRIE beams .....	120
5.4.2.2	NODAS Representation of a Gyroscope .....	125
5.4.3	Process Variation Simulation .....	128
5.4.3.1	OCEAN .....	130
5.4.3.2	Simulation block diagram .....	130
5.4.3.3	Simulation Settings .....	132
5.4.3.4	Inter-die Variation .....	133
5.4.3.5	Intra-die Variations .....	139
5.4.3.6	Summary .....	144
<b>6</b>	<b>CMOS-MEMS Gyroscope Design, Fabrication &amp; Characterization .....</b>	<b>147</b>
6.1	Thin-Film CMOS-MEMS Gyroscope .....	147
6.1.1	Structural Design .....	147
6.1.2	Fabrication and Characterization .....	149
6.2	DRIE CMOS-MEMS Gyroscope .....	153
6.2.1	Structural design .....	153
6.2.1.1	Vertical Actuation versus Vertical Sensing .....	154
6.2.1.2	The Gyroscope Topology .....	158



---

6.2.2	Device Design .....	160
6.2.3	Compensation Scheme .....	162
6.2.4	Simulation of the DRIE gyroscope .....	163
6.2.4.1	NODAS simulation .....	164
6.2.4.2	FEM analysis .....	166
6.2.5	DRIE Gyroscope Fabrication .....	169
6.2.5.1	Process Issues .....	170
6.2.6	Characterization .....	172
6.2.6.1	Z-accelerometer test .....	172
6.2.6.2	Optical Measurement of Vibration .....	173
6.2.6.3	Measurement Setup for Rotation Test .....	176
6.2.6.4	Zero-Rate Output (ZRO) Drift .....	177
6.2.6.5	Output Waveforms .....	179
6.2.6.6	Noise Floor .....	180
6.2.6.7	Phase Relationship .....	182
6.2.6.8	Off-axis Motion Compensation .....	183
6.2.6.9	Rotation Sweeping .....	183
6.2.6.10	Thermal Stability .....	184
6.2.6.11	Acceleration Rejection .....	187
6.2.7	Summary .....	193
6.2.8	Vertical-Axis Electrostatic Force Cancellation .....	195
6.2.9	A DRIE CMOS-MEMS Process With Controllable Si Undercut ....	196
6.2.9.1	Introduction .....	196
6.2.9.2	The concept .....	197
6.2.9.3	Process sequence .....	198
6.2.9.4	Process derivatives .....	200
<b>7</b>	<b>Conclusions and Future Work .....</b>	<b>201</b>
<b>Appendix A: DRIE CMOS-MEMS Process Flows Using Polysilicon as an Additional Etching Mask .....</b>		<b>205</b>
A.1	SCS Comb Fingers and Springs .....	205
A.2	Process Sequence for Electrical Isolation of SCS Areas .....	206
<b>Appendix B: OCEAN Script for Gyroscope Process Variation Simulation</b>		<b>208</b>
<b>Bibliography .....</b>		<b>211</b>

---

# List of figures

2.1	Cross-sectional view of the thin-film CMOS-MEMS micromachining. (a) After standard CMOS processing. (b) Anisotropic dielectric etch. (c) Deep Si etch. (d) Isotropic silicon etch for release. ....	12
2.2	A cantilever beam. ....	13
2.3	Lateral curling elimination. (a) Normal beam. (b) Normal beam with misalignment. (c) Tapered beam. (d) Tapered beam with misalignment. (e) Side view of MEMCAD simulation result (the beams are 100 $\mu\text{m}$ long; both vertical and lateral curling are visible). (f) Top view showing lateral curling with 3X exaggeration of displacement. (g) SEM of a released normal beam. (h) SEM of a released tapered beam. (i) A tapered y-spring demonstrating near perfect lateral alignment. ....	14
2.4	Capacitance estimation of a CMOS-MEMS comb drive. ....	16
2.5	The process-flow for DRIE CMOS micromachining. (a) CMOS-chip with backside etch. (b) Anisotropic dielectric etch. (c) Anisotropic silicon etch for release. (d) An optional, short isotropic silicon etch for undercut control. ....	19
2.6	Scanning electron micrograph (SEM) of a beam end: The optional isotropic etch (Fig. 5(d)) was used to attain the large undercut. ....	20
2.7	SEM of a comb-drive resonator fabricated in the DRIE CMOS-MEMS process. The thickness of the Si layer is about 50 $\mu\text{m}$ . ....	20
2.8	Schematic of a comb drive. (a) Side view of a pair of comb fingers. (b) Top view of the comb-finger array. ....	21
2.9	SEM of an electrically isolated SCS block. ....	22
2.10	Electrical isolation of silicon: (a) a metal/oxide beam after the dielectric micromachining process step with a n-well underneath; (b) deep Si etch with a small undercut; (c) isotropic Si etch with left-over silicon; (d) isotropic Si etch with complete undercut. ....	23
2.11	SEMs of the backside of the comb-drive actuator. (a) After the ASE, prior to oxygen plasma cleaning. (b) After oxygen plasma cleaning. ....	26
2.12	SEM of DRIE cantilever beam resonators. ....	27
2.13	Close-up of one corner of the comb-drive actuator. ....	28

---

2.14	The topography of the released comb-drive actuator (see Fig. 1-4) (only one quarter is shown) obtained by using phase shifting interferometry. (a) Conventional release. (b) Backside release. ....	30
3.1	Principle of vertical actuation and capacitive-sensing through comb-fingers. (a) X-axis actuator. (b) Z-axis actuator. (c) Equivalent capacitive-bridge. ....	32
3.2	Cross-sectional dimensions of the comb finger set for the Maxwell 2D field simulation. ....	33
3.3	Principle of vertical actuation and capacitive-sensing through comb-fingers. (a) Capacitance vs. z-displacement. (b) Capacitance gradient vs. z-displacement. (c) Z-displacement vs. applied voltage where fifty-two 30 $\mu\text{m}$ -long comb fingers are assumed. (d) Calculated differential capacitance vs. z-displacement. ....	34
3.4	Principle of vertical sidewall capacitance offset cancellation. (a) Two groups of comb fingers with swapped rotors and stators. (b) Equivalent circuit. ....	37
3.5	Comb finger arrangement for vertical sidewall capacitance offset cancellation. (a) Layout. (b) Equivalent circuit. ....	38
3.6	Topology design and wiring configuration of the z-axis accelerometer. (a) Schematic of the top view of the layout with a common-centroid configuration. (b) Equivalent full-bridge differential capacitive interface. ....	39
3.7	Cross-sections at different locations of a structure. (a) Spring; (b) Proof mass and frame. ....	39
3.8	Thermomechanical simulation of the z-axis accelerometer. ....	40
3.9	Top view of a released z-axis accelerometer. ....	41
3.10	Response of the accelerometer measured using a shaker table. ....	42
3.11	Spectrum of the output signal when a 0.5 G external acceleration is applied. ....	42
3.12	Frequency response of the accelerometer. ....	43
3.13	Optical measurement setup using a Michaelson interferometer. ....	44
3.14	Interference pattern around the upper anchor (each fringe occurs at 310 nm vertical displacement). ....	45
3.15	SEM of xyz microstage. ....	46
3.16	Z-displacement vs. applied voltage. ....	47
3.17	Cross-sectional views and wiring configurations of comb fingers for 3D actuation. (a) Lateral actuation (longitudinal); (b) Lateral actuation (transverse); and (c) Vertical	

---

**List of figures**

---

actuation. ....	48
3.18 Z-axis electrostatic actuation. (a) Dimensions of a DRIE comb finger set. (b) $C(z)$ and its gradient. (c) Displacement versus applied voltage. ....	49
3.19 Combined x-axis/z-axis actuation principle. ....	50
3.20 Cross-sections and wiring configurations of comb fingers for 3D vibration detection. ....	51
3.21 Wiring configuration of the z-axis vibration sensor. (a) Comb finger arrangement and wiring. (b) Equivalent circuit. ....	52
3.22 SEM of a DRIE z-axis accelerometer. (a) Full view. (b) Close-up. ....	53
3.23 Frequency response of the DRIE z-axis accelerometer. (a) Frequency response measured at the output of the on-chip circuit. The vibration is excited by using the integrated self-test actuators. (b) Frequency response of the z-displacement, measured by using an optical microvision system ....	54
3.24 Simulation of the sidewall capacitance of the z-axis comb-drive actuator. (a) Cross-section of comb fingers. (b) Capacitance versus z-displacement (c) Capacitance gradient versus z-displacement. Number of drive comb-fingers = 16; length of drive comb fingers = 0.12 mm. ....	55
3.25 Vertical electrostatic spring “hardening” effect. ....	56
3.26 Spectrum of the output signal of the DRIE z-axis accelerometer with a 100 Hz 0.5 G input. ....	57
3.27 Response of the DRIE z-axis accelerometer to 100 Hz sinusoidal excitation. Error bars indicate the measurement uncertainty. ....	58
4.1 Schematic of a curled-up comb drive. ....	60
4.2 Schematic of a folded torsional spring design. ....	61
4.3 Electrostatic micromirror topology. ....	62
4.4 Top view of the released electrostatic micromirror. ....	63
4.5 SEMs of a curled up comb drive. ....	63
4.6 Contour plot of the electrostatic mirror profile. ....	64
4.7 The mirror rotation angle versus applied voltage. ....	65
4.8 Frequency response measured by using an optical microvision system. ....	65
4.9 Electrostatic spring “softening” effect. ....	66

---

4.10	The thermal micromirror conceptual design. (a). Cross-sectional view; and (b) top view. ....	67
4.11	SEMs of a released thermal micromirror: (a) side view; (b) cross-section of A-A'; and (c) close-up of one corner. ....	69
4.12	Optical scanning angle versus applied current. (a) Mirror with jump angle scanning. (b) Mirror with smooth scanning. ....	70
4.13	Profile of the bimorph actuation mesh before and after the jump. (a) Before jump; (b) after jump; and (c) wider view after jump. ....	71
4.14	A schematic of the endoscopic OCT system. Insets A, B are a schematic of the optical arrangement and a photograph in the distal OCT scope. BBS: broadband source, PD: photodiode, CM: fiber-optic collimator, E-O: electro-optical phase modulator, FPC: fiber optic polarization controller, G: galvanometric mirror. ....	74
4.15	2-D OCT of 2 stacked microscope glass slides with thickness of 225 $\mu\text{m}$ and 1 mm, respectively. Image size: 500x1000 pixels. ....	77
4.16	<i>In vivo</i> 2-D endoscopic OCT of porcine bladder through cystotomy. U: urothelium, SM: submucosa, MS: muscularis layer. Image size: 500 x 1000 pixels covering an area of 2.9 x 2.8 $\text{mm}^2$ . ....	78
4.17	Micromirror array. Mirror size: 60 $\mu\text{m}$ x 60 $\mu\text{m}$ . ....	79
4.18	A micro-grating made of metal-1 and metal-2 layers. ....	80
4.19	Topology of a new electrostatic micromirror with a large rotation range. ....	81
4.20	SEMs of the new electrostatic mirror. (a) Top view. (b) Side view. (c) close-up of a comb drive. ....	82
4.21	SEMs of the curled comb fingers. ....	83
5.1	Gimbaled vibratory gyro. ....	89
5.2	Single-gimbal structures: (a) translational drive; (b) torsional drive. ....	97
5.3	Two-fold gimbaled structure (z is orthogonal to x-y plane). ....	97
5.4	Dual-gimbaled structures: (a) translational drive; (b) torsional drive. ....	98
5.5	Spring designs. ....	100
5.6	Phase relation of various signals in a gyroscope. ....	102
5.7	Comb finger model for 3D electrostatic force analysis. ....	106
5.8	Matlab/Simulink model for a 3D comb drive. (a) Top cell. (b) Subcell for the drive	

---

---

**List of figures**

---

mode. ....	108
5.9 Simulink simulation results. (a) $V_{ac} = 5\text{ V}$ , $V_{dc} = 18\text{ V}$ . (b) $V_{ac} = 0.5\text{ V}$ , $V_{dc} = 2\text{ V}$ . (c) $x_0$ is assumed to be $60\text{ }\mu\text{m}$ , instead $6\text{ }\mu\text{m}$ in the other conditions. ....	109
5.10 Single-axis gyroscopes with lateral drive: (a) z-axis gyro; and (b) x-axis gyro. ...	112
5.11 X/z dual-axis gyroscope with lateral drive. ....	113
5.12 Y/z dual-axis dual-gimbaled gyroscope with lateral drive. ....	114
5.13 Y-axis gyroscope design with vertical drive. ....	114
5.14 X/y dual-axis gyroscope design with vertical drive. ....	115
5.15 Single-gimbaled gyroscopes with torsional drive. ....	116
5.16 Dual-gimbaled gyro with torsional drive. ....	116
5.17 Matlab simulation. (a) Block diagram; and (b) Simulink model. ....	118
5.18 Matlab simulation result. Constant rotation in (a) and (b), and sinusoidal rotation in (c). ....	119
5.19 Calculation of moment of inertia for a "T" shape beam. (a) Beam cross-section; (b) Calculate $I_y$ (Y-axis is used as a reference axis to compute the centroid $C(Y_c, z_c)$ ; and (c) Calculate $I_z$ . ....	121
5.20 NODAS test model and frequency response simulation result. ....	124
5.21 Topology of a z-axis gyroscope. ....	125
5.22 NODAS model of the z-axis gyroscope. ....	126
5.23 Frequency response of the z-axis gyroscope. ....	126
5.24 Transient response of the z-axis gyroscope. ....	127
5.25 Block diagram for process variation simulation using OCEAN. ....	131
5.26 Settings for the gyroscope simulation. ....	133
5.27 Dependence on angular rate. (a) Resonant frequencies of drive and sense modes. (b) Vibration amplitude of drive mode. (c) Coriolis sense amplitude. ....	134
5.28 Inter-die variation: $S_i$ thickness dependence. (a) Resonant frequencies of drive and sense modes. (b) Frequency change rate with respect to $S_i$ thickness. ....	135
5.29 Inter-die variation: $S_i$ thickness dependence. (a) Excitation amplitude. (b) Sense am- plitude. (c) Sense to drive amplitude ratio. ....	137

---

---

5.30	Inter-die variation: Undercut dependence.(a) Excitation amplitude. (b) Resonant frequencies of drive and sense modes. (c) Coriolis sense amplitude. (d) Sense to drive amplitude ratio. ....	138
5.31	Parameter definition for distributed variation simulation. ....	140
5.32	Intra-die variation: Si thickness dependence. (a) Resonant frequencies of drive and sense modes. (b) Vibration amplitude of drive mode. (c) Coriolis sense amplitude. (d) Off-axis motion on the drive frame. ....	143
5.33	Intra-die variation: Undercut dependence. (a) Resonant frequencies of drive and sense modes. (b) Vibration amplitude of drive mode. (c) Coriolis sense amplitude. (d) Off-axis motion on the drive frame. ....	145
6.1	Topology of the lateral-axis gyroscope .....	148
6.2	SEM of a released gyroscope. ....	149
6.3	Lateral curling elimination. (e) a tapered y-spring demonstrating near perfect lateral alignment; (b) the cross-section of the tapered spring beam. ....	150
6.4	Resonant frequency matching and mode coupling suppression through heating. (a) SEM of a z-spring beam with an embedded polysilicon heater. (b) Frequency responses of the drive and sense modes with and without injecting current. ....	150
6.5	(a) Thermomechanical curling compensation as a function of applied current. (b) Resonant frequency tuning as a function of the z displacement at the cantilevered end of the spring. ....	151
6.6	Spectrum of the y-accelerometer at a 500 Hz, 0.05 G external acceleration, showing a resolution of $100 \mu\text{G}/\text{Hz}^{1/2}$ . ....	152
6.7	Constant rotational rate measurement. A large DC offset was present because of the coupled motion from the drive mode. ....	153
6.8	Comparison of vertical sensing and vertical actuation. ....	155
6.9	Topology of the lateral-axis DRIE gyroscope. ....	158
6.10	NODAS schematic of the DRIE gyroscope. ....	164
6.11	The simulated drive and sense modes for nominal case. ....	165
6.12	Transient analysis of the DRIE gyroscope .....	165
6.13	Layout of the DRIE x-axis gyroscope. ....	166
6.14	3D solid model of the gyroscope structure. ....	167
6.15	Compensation scheme for torsional vibration. (a) Top view. (b) Cross-sectional view.	

---

**List of figures**

---

.....	168
6.16 The first four modes in the gyroscope structure: (a) x-drive mode. (b) z-sense mode. (c) torsional y-sense mode. (d) y-sense and y-drive in-phase coupled mode. ....	168
6.17 SEM of the x-axis DRIE gyroscope. The asterisk marks the spot for optical motion measurement. ....	169
6.18 SEMs showing the electrical isolation of silicon. (a) Good electrical isolation. (b) Poor electrical isolation. ....	171
6.19 Frequency response of z-axis accelerometer. ....	172
6.20 Spectrum of on-chip output signal when a 0.5 G 200 Hz external acceleration was applied. ....	173
6.21 Frequency response of the DRIE gyroscope measured by using an optical microvision system when voltage applied to the x-drive comb fingers. ....	174
6.22 Frequency response of the DRIE gyroscope when voltage applied to the x/z-comb drives at the outer frame. ....	174
6.23 Frequency response of the DRIE gyroscope when voltage applied to the self-test z-actuators of the z-accelerometer. ....	175
6.24 Test setup for characterizing the DRIE gyroscope. ....	176
6.25 Zero-rate output of the DRIE gyroscope. (a) with floating electrodes in a noisy lab. (b) with floating electrodes in a Faraday cage. and (c) grounding floating electrodes in a Faraday cage. ....	178
6.26 Output waveforms of the DRIE gyroscope. (a) Hand-shaking. (b) Labview-controlled turntable. (c) DC-motor drive. ....	179
6.27 Measurement setup (partial) with a DC motor to generate sinusoidal rotation rate. ...	180
6.28 Spectrum of the output signal. (a) At 5 Hz 33°/s rotation. (b) At zero rotation. ...	181
6.29 Phase sweeping. (a) zero rotation rate; (b) rotation rate: 200°/s and (c) difference between (a) and (b), i.e., sensitivity. ....	182
6.30 Rotation sweep. (a) taken in 12.5 minutes; and (b) taken in 25 minutes. ....	184
6.31 Thermal drift of the DRIE gyroscope. ....	185
6.32 Acceleration sensitivity test. (a) The acceleration signal from the initial sense preamp output. Note the harmonics. (b) The output signal after demodulation. ....	187
6.33 Frequency components of the output signal of the first demodulator. ....	189



---

---

6.34	Frequency components of the output signal of the second demodulator. ....	190
6.35	SEM of the drive comb fingers. ....	192
6.36	The curling of the springs and comb fingers. (a) X-drive spring and comb fingers; and (b) z-sense spring and comb fingers. ....	192
6.37	Comb finger designs with reduced parasitic capacitance. (a) Regular sense comb fin- ger. (b) Differential sense comb finger. (c) Regular sense comb finger with an initial Si undercut. (d) Differential sense comb finger with an initial Si undercut. ....	194
6.38	SEM of a released 6-DOF IMU. ....	194
6.39	Lateral comb drive with vertical force. ....	195
6.40	Vertical force cancellation for lateral comb drive. ....	196
6.41	The cross-sectional view of the proposed CMOS-MEMS process flow. ....	199
A.1	Process flow for single-crystal silicon beams. ....	205
A.2	Process flow for electrical isolation of SCS areas. ....	206

# List of Table

Table 1-1: CMOS-MEMS comparison .....	2
Table 3-1: Parameters of the accelerometer .....	45
Table 5-1: Device parameters .....	108
Table 5-2: Comparison of NODAS simulation with ANSYS simulation .....	124
Table 5-3: Design data sheet of the gyroscope for NODAS simulation .....	127
Table 5-4: Assignment of parameter values for distributed variation simulation ....	140
Table 6-1: Geometric parameters of comb drives of the gyroscope .....	159
Table 6-2: Design data sheet of DRIE gyroscope .....	162
Table 6-3: First ten modes of the DRIE gyroscope .....	167
Table 6-4: Y-axis coupled motion reduction by compensation (All voltages at 5 V a.c. plus 15 V d.c.) .....	183
Table 6-5: Amplitude/phase list of frequency components in the output of the first demodulator .....	189
Table 6-6: Amplitude/phase of frequency components in the output of the second demodulator .....	190



# **Chapter 1**

## **Introduction**

### **1.1 Scope**

Microelectromechanical systems (MEMS) technology has grown rapidly in the last ten years and its applications range broadly from consumer electronics, automobiles and medicine to health care. Compatibility of MEMS fabrication with mainstream CMOS technologies, *i.e.*, CMOS micromachining or CMOS-MEMS, provides not only high sensitivity for microsensors, on-chip “smart” conditioning circuitry and low cost, but also has such advantages as scalability, multi-vendor accessibility and short design cycles. This thesis reports two primary contributions: extending CMOS-MEMS design to enable vertical sensing and actuation and expanding CMOS-MEMS capability by including bulk Si with thin-film microstructures. This thesis primarily discusses two types of MEMS devices, gyroscopes and micromirrors, to illustrate advances and issues with design, simulation, fabrication and application. Deep reactive-ion-etch (DRIE) CMOS-MEMS processing and three-dimensional comb finger sensing and actuation are also addressed.

### **1.2 CMOS-MEMS Technology**

Even though MEMS technology leverages integrated circuit (IC) technology, many MEMS processes are not compatible with standard IC processes. The need for special micromachining systems, complex fabrication sequences, or multi-chip packaging leads

to high cost, low yield and performance degradation. Thus, searching for IC-compatible microfabrication processes to reduce cost, improve yield and functionality has been a major research effort to enable “smart” microsystems by integrating on-chip signal processing and communications circuitry.

Complementary metal-oxide semiconductor (CMOS) processing has been the mainstream technology in the IC world for more than a decade. Design compatibility with conventional CMOS processes provides high availability and potential low cost due to the batch fabrication. There are three possibilities of CMOS-compatible MEMS technology: pre-CMOS, post-CMOS and intermediate-CMOS [1]. Table 1-1-1 lists the comparison of

**Table 1-1: CMOS-MEMS comparison**

	Planarity	Contamination concerns	Vendor accessibility	Temperature budget	
Pre-CMOS	Best	Yes	Limited	No	SNL[2]
Inter-CMOS	Good	Yes	Very limited	Yes	ADI[3]
Post-CMOS	Varies	No	Good	Varies	Berkeley[4][6] ETH[1] CMU[13][20]

these three types of process approaches. Pre-CMOS processes use wafers with pre-defined microstructures and often require a post-CMOS release process or even an in-house CMOS production line. One example is the Sandia Micromechanics Microsensors and CMOS technology (MM/CMOS) [2]. Intermediate-CMOS micromachining processes add steps between CMOS process steps, and thus have potential contamination problems. They often require a dedicated production line. Analog Devices, Inc. (ADI)’s iMEMS technology [3] embeds the deposition and high-temperature annealing of structural poly-

silicon in their BiCMOS process, in which the diffused n+ layer is used for the electrical connection to the structural polysilicon layer. Post-CMOS processes are better in the sense of the possibility to make the micromachining steps truly independent of CMOS processes. A UC-Berkeley group developed a Modular Integration of CMOS microStructures (MICS) process [4][5], but it needs high-temperature refractory metal such as tungsten as interconnect,  $\text{TiSi}_2$  as contact barrier and  $\text{Si}_3\text{Ni}_4$  for wet etch or vapor etch protection. The residual stress of the structural polysilicon layer is another process and design issue. Recently, the same group proposed thin-film polycrystalline SiGe microstructures with low deposition temperature to avoid the use of refractory interconnect metals [6].

The CMOS micromachining processes described above require extra lithography step(s) other than standard CMOS lithography steps and/or deposition of structural and sacrificial materials. Deposition temperature, possible contamination for pre- and inter-CMOS, sticking problems and protection of CMOS circuits are all serious concerns.

Baltes' group at ETH Zurich has been using a different approach for about ten years [1]. They have developed a variety of CMOS microstructures and microsensors [7]-[12]. Instead of depositing structural materials, they use the materials from CMOS processes to form MEMS structures. Structural layers consist of the aluminum and oxide layers normally used for CMOS interconnect. The silicon substrate is used as the sacrificial layer. Release of microstructures is performed through bulk micromachining and/or surface micromachining. Both frontside and backside releases have been exploited [8][9]. In some cases, complex suspended n-well structures are obtained by using an electrochemical etch-stop technique [9]. However, their bulk-micromachining release relies on the anisotropic

properties of single crystal silicon, which requires wet etching. The effort for wet etching protection is not trivial.

Carnegie Mellon's approach is similar to that of ETH in using the CMOS interconnect layers for the microstructures [13]. However, wet etching is completely eliminated from Carnegie Mellon process flows and no masks are needed. The interconnect metal layers are used as etching masks to define microstructures which consist of thin-film, composite aluminum and oxide layers. Both the dielectric etch and silicon substrate undercut are performed through dry etching. Various thin-film CMOS-MEMS devices such as accelerometers [14][15][16], gyroscopes [17][18], infrared imagers [19], and microstages [20] have been demonstrated.

The main issues of the thin-film CMOS-MEMS process include size limitation due to curling, strong temperature dependence of multi-layer structures and lack of bottom electrodes for vertical actuation and sensing.

In order to overcome these drawbacks, a deep reactive-ion-etch (DRIE) CMOS-MEMS process has been developed [22]. The new process incorporates single-crystal silicon into mechanical structures by introducing a backside silicon etch into the process sequence. The resultant microstructures are flat and have better mechanical and temperature performance. Chapter 2 describes the process flow and some example structures.

### **1.3 Comb-finger Vertical Sensing and Actuation**

Interdigitated comb drives have been widely used for electrostatic actuation, capacitive position sensing and frequency tuning. They have become an integral part of many

MEMS devices such as accelerometers [23], gyroscopes [24][25][26], and microscanners [27]. However, most of these devices utilize the lateral capacitance change between comb fingers. The use of the vertical capacitance change between comb fingers for capacitive sensing is limited by parasitic capacitance to the substrate in polysilicon processes and electrical isolation difficulties in bulk micromachining processes. For vertical actuation, the levitation effect of comb fingers was applied to phase shifting interferometric applications [28], but its small actuation range limits its further applications.

In this thesis, the development of vertical sensing and actuation was originally inspired for design requirements of a single-chip six-degree-of-freedom integrated inertial measurement unit ( $I^2MU$ ). Out-of-plane actuation also has extensive applications in micro-optics, such as scanning micromirrors for optical imaging and switching and phase-only micromirrors for aberration correction and for interferometric systems.

For vertical comb-finger sensing, a z-axis comb-finger accelerometer with a torsional suspension and an unbalanced proof mass was demonstrated by using a dissolved-wafer process [29]. Its glass substrate guarantees low parasitic capacitance but the interface circuitry has to be off-chip. For vertical comb-finger actuation, an out-of-plane comb drive for a scanning micromirror has been fabricated in a high-aspect-ratio Si process [30]. Unlike conventional interdigitated, engaged comb fingers, this z-axis comb drive has movable fingers (rotors) totally above stationary fingers (stators). High speed and large deflection were achieved, but Si wafer-to-wafer bonding and accurate two-side alignment are needed.



In contrast to the homogeneous microstructures, CMOS-MEMS structures have multiple conducting layers embedded. This feature can be used to realize vertical-axis comb-finger sensing and actuation, as detailed in Chapter 3. By using the sidewall capacitance gradient existing in CMOS-MEMS comb fingers in the  $z$ -direction, this new method not only solves the vertical sensing and actuation difficulty because of no substrate electrode, but also avoids the large parasitic capacitance for vertical sensing and the actuation range limitation associated with the substrate electrode. A three-axis microstage [20], a thin-film  $z$ -axis accelerometer [15] and a DRIE  $z$ -axis accelerometer [31] have been demonstrated and will be discussed in Chapter 3.

## **1.4 Micromirrors**

One application of vertical actuation is in scanning micromirrors. Micromirrors have obtained extensive attention in the past few years because of their applications in optical displays and all-optical switching. They are also used in a wide range of other applications, such as interferometric systems, optical spectroscopy, aberration correction and medical imaging. The requirements of micromirrors vary with different applications. Flatness, roughness and reflectivity are the common requirements across most applications. For optical displays, fill factor and pixel size are the most important parameters. For optical switches, speed and power consumption are primary requirements. Micromirrors for these two applications can be made by using thin-film technology. However, the residual stress existing in thin-film structures posts a trade-off between the size and flatness of a thin-film micromirror.

One of the emerging application areas of micromirrors is biomedical imaging, especially for optical coherence tomography (OCT) imaging. OCT is a newly developed optical imaging technique that permits high-resolution cross-sectional imaging of highly scattering media [32]-[37]. Endoscopic OCT devices for *in vivo* imaging of internal organs have been reported [33][35][37]. Conventional transverse scanning is performed either by a rotary fiber-optic joint connected to a 90° deflecting micro prism (in a circumferential pattern) [33][37] or by a small galvanometric plate swinging the distal fiber tip (in a line-scan pattern) [35], which largely increases the cost and limits applications. It is well known that micromirrors are good at light beam steering. If the transverse scanning can be conducted by a micromirror, endoscopic OCT systems will be more compact, more flexible and less expensive. However, there are special requirements to the micromirrors for OCT applications. The mirrors must be large and flat to maintain high-image quality. The maximum scanning angle must be large to have sufficient efficiency.

Micromirrors have been demonstrated by using different micromachining processes. A successful example of a surface-micromachined micromirror is Texas Instruments' digital mirror device (DMD) [43]. The aluminum thin-film technology with vertical parallel-plate actuation has difficulty in achieving large mirrors with large tilt range. Polysilicon surface micromachining processes have similar limitations. The thin-film deposition processes employed generate residual stress and stress gradients which cause curling. This curling limits the useful size of micromirrors and the small gap formed by the sacrificial layer present in surface-micromachined mirrors restricts their tilt range.

A bulk-micromachining process has been used to make sidewall mirrors [44], but the sidewall angle, smoothness and area efficiency are concerns. Another choice is to combine surface- and bulk- micromachining processes. A research group at UC-Berkeley reported a single-crystal silicon (SCS) based micromirror by using silicon-on-insulator (SOI) wafers and two-side alignment [30]. A UCLA group assembled an SCS mirror on top of polysilicon actuators [45]. It is similar to the flip-chip thin-film micromirror array fabricated at University of Colorado-Boulder [46]. However, the effort to make a thin SCS mirror and transfer it on top of a surface-micromachined polysilicon actuator is substantial. The UCLA group also reported an angular comb drive in which photoresist re-flow was used to tilt comb fingers [47]. However, the uniformity and yield are concerns.

Two micromirror designs are reported in Chapter 4. A curled comb drive with large out-of-plane actuation based on the DRIE CMOS-MEMS process is demonstrated by an electrostatic micromirror. The second design is a large, flat, thermally actuated micromirror also based on the DRIE CMOS-MEMS process. Heat-induced buckling in the thermo-mechanical actuator is analyzed. The thermally actuated micromirror has been installed into the first ever micromirror-based endoscopic optical coherence tomography (OCT) imaging system for *in vivo* imaging of biological tissue. Preliminary experiments show very promising resolution and scanning speed. This work opens the possibility to make compact, high-performance and low-cost OCT catheters and endoscopes for future clinical applications by using MEMS technology.

## **1.5 MEMS Vibratory-Rate Gyroscope**

A second application for vertical sensing and actuation is in a lateral-axis vibratory-rate gyroscope for a future single-chip IMU. Traditional gyroscopes employed in the present aerospace and military industries are bulky and exceedingly expensive, even though they have inertial-grade performance. Optical gyroscopes such as fiber optical gyros (FOG) or ring laser gyros (RLG) are relatively small and can reach to tactical- or even inertial- grade performance [48][49], but the cost is still too high for the automotive and consumer electronics applications.

Inspired by the successful commercialization of MEMS accelerometers made by Analog Devices, Inc., MEMS gyroscopes are widely believed to be a solution for medium performance requirements and have drawn extensive attention in the MEMS community in the past ten years. Various mechanisms, such as vibrating beams or rings [50][51], tuning forks [52], spinning disks [53], and surface acoustic wave [54], have been investigated. Among them, the vibratory type including tuning forks and vibrating beams or rings is dominant because it is more suitable for batch fabrication in current micromachining processes.

A number of MEMS vibratory gyroscope designs have been reported to address the automotive demand, but very few of them have been commercialized. We identify three major reasons here. (1) System complexity due to the secondary motion detection, mode coupling and imperfection compensation makes design and evaluation difficult. (2) Mechanical designs are not optimized, resulting from either the lack of thorough understanding of special issues existing in micromachined gyroscopes or the lack of appropriate

simulation tools. (3) The performance is limited by dimensional constraints of thin film technology, and there are difficulties of circuit integration and requirement for wafer-to-wafer bonding or expensive SOI wafers in bulk Si technology. Therefore, both new fabrication processes and new design tools (or modifying a existing design tool to fit a new fabrication process) are needed.

Models for DRIE CMOS-MEMS structures are developed in Chapter 5 and used to perform gyroscope simulation and study the influence of process variations to the gyroscope performance. Modelling is incorporated into the NODAS (NOdal Design of Actuators and Sensors) design methodology [55], allowing structured composition of the gyroscope model from beam, plate, comb, and anchor elements.

Chapter 6 introduces a lateral-axis vibratory gyroscope with vertical-axis comb-finger actuation fabricated the thin-film CMOS-MEMS process. A thermomechanically tuning resonance method for this gyroscope is demonstrated. A similar lateral-axis vibratory gyroscope with vertical-axis comb-finger sensing is demonstrated by using the DRIE CMOS-MEMS process. Direct motion coupling in addition to quadrature is observed and simulated. A few feasible methods to improve the gyroscope performance are proposed.

Conclusions and future work are discussed in Chapter 7.

## Chapter 2

# CMOS-MEMS Processes

There are two CMOS-MEMS processes developed at Carnegie Mellon: a thin-film version and a DRIE version. Thin-film CMOS-MEMS is a maskless post-CMOS process. Mechanical and thermal properties of thin-film CMOS-MEMS microstructures have been studied and characterized [56][57]. DRIE CMOS-MEMS is similar except a backside deep silicon etch step is added. The backside etch is used to incorporate bulk Si into microstructures to utilize the excellent mechanical properties of single-crystal silicon (SCS) and obtain large (if desired), flat MEMS structures. In this chapter, both processes are discussed in detail. A technique to reduce lateral curling for the thin-film CMOS-MEMS process is addressed. Characterization of a few example devices fabricated by using the DRIE CMOS-MEMS process are also presented. Zhu [58] provides further information about the CMOS-MEMS process developed at Carnegie Mellon.

### 2.1 Thin-film CMOS-MEMS Process

The thin-film CMOS-MEMS micromachining process is completely compatible with standard CMOS processes [13]. In the process, metal layers from previous CMOS processes are used as the etching mask for defining the microstructural sidewalls. As a result, the interface circuitry must be protected by the top metal layer. All of the metal layers (between 3 and 6 in most modern CMOS processes) can be included within a single

microstructure. Microstructures consist of the metal and dielectric layers normally used for electrical interconnect.

The cross-sectional view of the process flow is shown in Fig. 2-1. It includes only two dry etch steps. When the chips come back from a CMOS vendor, the CMOS circuits are covered by the top metal and oxide, and the microstructures are pre-designed by using the interconnect metal layers as shown in Fig. 2-1(a). First, the microstructure sidewalls are defined with an anisotropic reactive-ion-etch (RIE) of the dielectric stack using a  $\text{CHF}_3/\text{O}_2$  plasma in a Plasma Therm 790 reactor, as shown in Fig. 2-1(b). Second, a deep silicon etch (see Fig. 2-1(c)) is performed by using the Bosch Advanced Silicon Etch (ASE) process [59] in a STS system, followed by an isotropic  $\text{SF}_6$ -plasma silicon undercut to release the microstructures, as shown in Fig. 2-1(d). The isotropic etch is achieved by

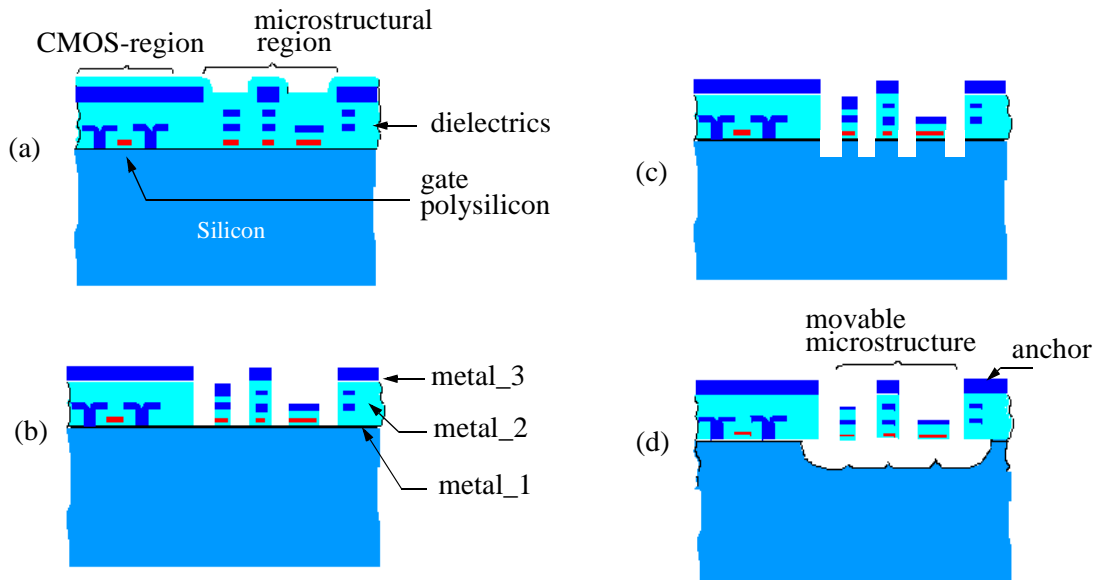


*Figure 2-1: Cross-sectional view of the thin-film CMOS-MEMS micromachining. (a) After standard CMOS processing. (b) Anisotropic dielectric etch. (c) Deep Si etch. (d) Isotropic silicon etch for release.*

greatly reducing the platen power. This process creates microstructures with high aspect-ratio and a high flexibility of wiring. The dry etch for release eliminates any sticking problems. The deep Si etch step provides independent control of the vertical gap to the substrate [58]. The gap is chosen to be relatively large, which provides small squeeze-film damping of the out-of-plane modes and minimizes electrostatic coupling to the substrate. Curling from residual stress gradients in the composite films can be compensated to the first order via a curl matching frame [14].

The CMOS-MEMS process provides beams with different thicknesses by choosing different interconnect metal layers as etching mask. Typically, beams with metal-1, metal-2, metal-3 on the top are 1.8  $\mu\text{m}$ , 3.5  $\mu\text{m}$ , 5.0  $\mu\text{m}$  thick, respectively. Therefore, various flexible suspension beams (*i.e.*, springs) can be designed (Fig. 2-1(d)). We know the stiffness of a cantilever beam (Fig. 2-2) is given by  $k_y \propto \frac{w^3 h}{l^3}$ ,  $k_z \propto \frac{wh^3}{l^3}$ . Therefore, a vertically compliant spring (z-axis spring) can be realized by using wide beams with metal-1 on the top, while a lateral-compliant spring can be realized by using narrow beams with metal-3 on the top. For example, assuming a z-axis spring has a beam width of 10  $\mu\text{m}$ , and thickness of 1.8  $\mu\text{m}$ , the z-axis stiffness will be about 30 times smaller than the x-axis stiffness.



Figure 2-2: A cantilever beam.



Another design issue with springs is the in-plane curling of spring beams, which results in lateral position offset [14]. This lateral curling is caused by the asymmetric cross-section of the spring beams that results from the process variations, especially from photolithography misalignment. For example, in Fig. 2-3(a), the three metal layers in the beam have identical width and are designed to be aligned. However, due to the finite pre-

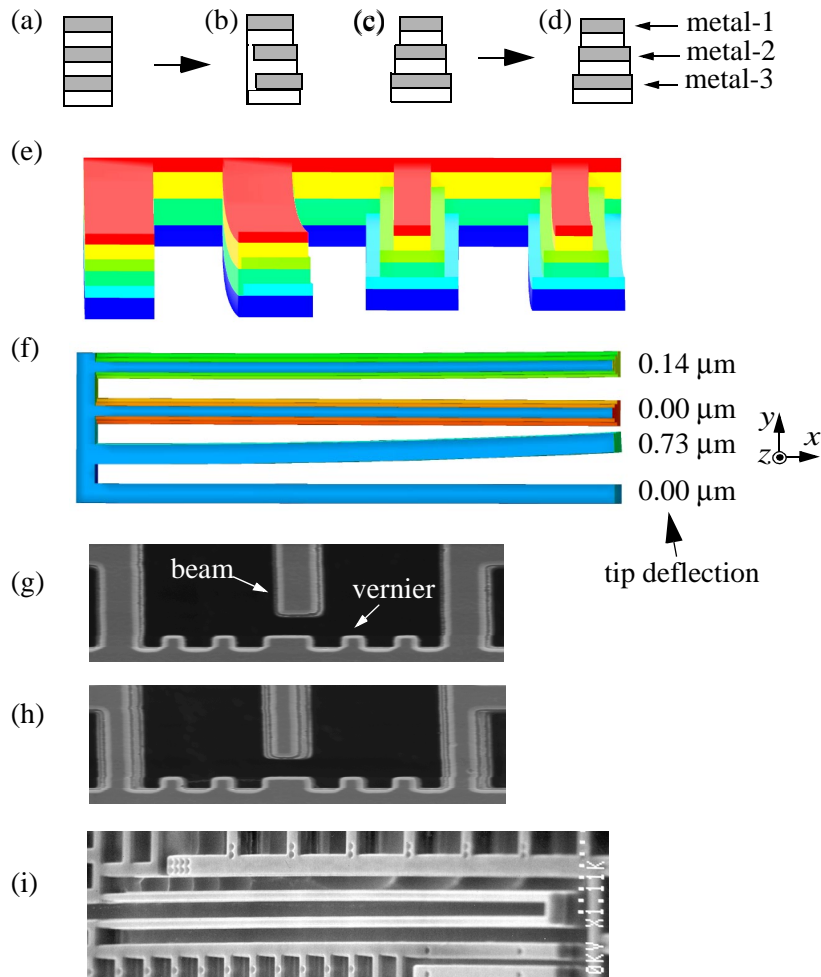


Figure 2-3: Lateral curling elimination. (a) Normal beam. (b) Normal beam with misalignment. (c) Tapered beam. (d) Tapered beam with misalignment. (e) Side view of MEMCAD simulation result (the beams are 100  $\mu\text{m}$  long; both vertical and lateral curling are visible). (f) Top view showing lateral curling with 3X exaggeration of displacement. (g) SEM of a released normal beam. (h) SEM of a released tapered beam. (i) A tapered y-spring demonstrating near perfect lateral alignment.

cision of the photolithography, the metal layers will have certain misalignment. Since all metal layers can function as the structural etching mask, oxide will fill the vacancy left by any metal layer shift, as shown in Fig. 2-3(b). Lateral curling becomes worse as beam thickness decreases.

In order to reduce this lateral curling, a special beam with tapered cross-section has been developed. As shown in Fig. 2-3(c), lower-level metal layers are made wider. As long as the width difference is larger than the photolithography error, there will be no oxide remaining beside any metal layer. Fig. 2-3(e) and (f) show the finite-element [60] simulation result in which the tapered beam has less than one-fifth of lateral curling as that of the normal beam even though the two beams are designed to have the same z-axis bending moment of inertia. The beams are  $2.4\text{ }\mu\text{m}$  wide and  $100\text{ }\mu\text{m}$  long. A misalignment of  $0.1\text{ }\mu\text{m}$  between adjacent metal layers is considered. Fig. 2-3(g) and (h) are SEMs of two released  $150\text{ }\mu\text{m}$ -long beams with a regular design and a tapered design, respectively. The tapered beam has less than  $0.1\text{ }\mu\text{m}$  lateral curl, while the normal beam curls about  $0.4\text{ }\mu\text{m}$  laterally.

The released microstructures are set by the processing to between  $15\text{ }\mu\text{m}$  to  $100\text{ }\mu\text{m}$  above the substrate, which provides low parasitic capacitance to interface electronics. For example, a 50-finger comb drive with  $30\text{ }\mu\text{m}$  overlap has 89 fF of sensing capacitance, assuming a CMOS microstructure with  $5\text{ }\mu\text{m}$ -high comb fingers and a  $1.5\text{ }\mu\text{m}$  gap, as shown in Fig. 2-4. The comb parasitic capacitance is only 1.2 fF, assuming a  $30\text{ }\mu\text{m}$ -deep cavity underneath the fingers. On the other hand, a 50-finger comb drive with  $30\text{ }\mu\text{m}$  over-

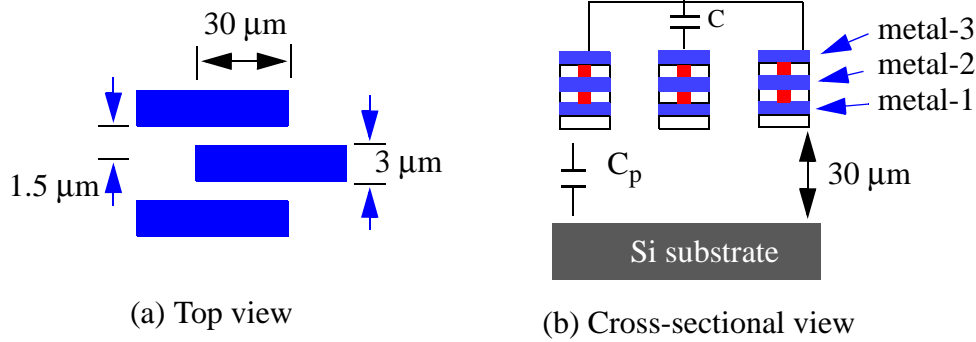


Figure 2-4: Capacitance estimation of a CMOS-MEMS comb drive.

lap in the MUMPs polysilicon process [61] has 27 fF of sensing capacitance. The parasitic capacitance is 13 fF from the fingers over the substrate, 14 aF/μm from interconnect and 1.1 pF for a standard 78 μm by 78 μm square bond pad [61]. Bond-wire or solder-bump connection to external electronics contributes additional parasitic capacitance.

Moreover, the multiple conductor layers existing in the microstructures provide high flexibility for wiring so that z-axis (out-of-plane) electrostatic actuation and z-axis capacitive sensing can be easily realized. Both lateral and vertical CMOS accelerometers, a tri-axial microstage and a lateral-axis vibratory gyroscope have been fabricated by using this process [14][15][20][17]. These devices will be discussed in Chapter 3.

## 2.2 DRIE CMOS-MEMS Process

The thin-film CMOS-MEMS process described above has the capability to realize three-dimensional actuation and motion sensing, the possibility to integrate high-performance on-chip signal conditioning circuits with digital readouts, expected multi-vendor accessibility and short design cycle times. However, the multi-layer thin-film structures

usually have large residual stress gradients which cause curling. This limits the maximum layout size of microstructures, which is critical for providing large proof mass in inertial sensors. Moreover, release holes and unwanted curvature of microstructures degrade their application in the optical domain.

Deep RIE (DRIE) technologies have advanced significantly in recent years. By alternating passivation and etching cycles, the Bosch advanced silicon etch (ASE) process [59] can typically achieve high aspect ratios between 20:1 to 30:1. For example, a bulk silicon comb-drive actuator with 100  $\mu\text{m}$ -deep comb fingers and 15  $\mu\text{m}$  gap spacing has been fabricated by using the SCREAM process [62]. Microstructures have also been released by through-wafer etching [63], made feasible by the high silicon etch rate of the ASE process ( $\sim 3 \mu\text{m}/\text{min}$ ). However, given a typical wafer thickness ( $\sim 500 \mu\text{m}$  for 4" wafers), a minimum gap spacing of 20  $\mu\text{m}$  would be needed to conform to the etch aspect ratio. Such a spacing requires large silicon area for either sensing or actuation.

Our solution is to combine the above thin-film CMOS-MEMS process, ASE and backside etch. The backside etch is used to control the thickness of the final, released, microstructures, which allows optimization of the process for a particular design. The new process sequence (Fig. 2-5) provides high-aspect-ratio and very flat microstructures. It incorporates all the advantages of CMOS composite microstructures with the excellent mechanical properties of single-crystal silicon (SCS), including fine-gap lateral electrodes micromachined from the CMOS interconnect stack. A timed lateral silicon undercut etch at the end of the process allows a combination of the CMOS thin-film structures along

with DRIE SCS structures designed within the same device. In the following section, the DRIE post-CMOS micromachining process is described and the characterization results of a few example devices fabricated in this DRIE CMOS-MEMS process are reported.

### **2.2.1 Process flow**

In order to overcome some of the drawbacks of thin-film microstructures without losing the advantages of the multi-conductor structures, we propose a new process sequence building on the previous post-CMOS micromachining process. The basic idea is to introduce a single-crystal silicon (SCS) layer underneath the CMOS multi-layer structures in such a way that the mechanical properties are dominated by the SCS layer and electrical connections are provided by the CMOS microstructure layer [64].

A diagram of the process flow is shown in Fig. 2-5. We start with a deep anisotropic backside etch leaving a 10  $\mu\text{m}$  to 100  $\mu\text{m}$ -thick SCS membrane (Fig. 2-5(a)). This backside etch step is used to control the thickness of microstructures. The cavity formed by the backside etch allows the completed die to be bonded directly to a package without interference from the released microstructures. Next, an anisotropic dielectric etch is performed from the front side (Fig. 2-5(b)). Then, in contrast to the prior work on post-CMOS processing, an anisotropic instead of an isotropic silicon etch is used for release (Fig. 2-5(c)). A thick, stiff, SCS layer remains underneath the CMOS layer, resulting in a relatively flat released microstructure, especially when compared with multi-layer thin-film CMOS-MEMS structures. As a final step, an optional timed isotropic Si etch may be

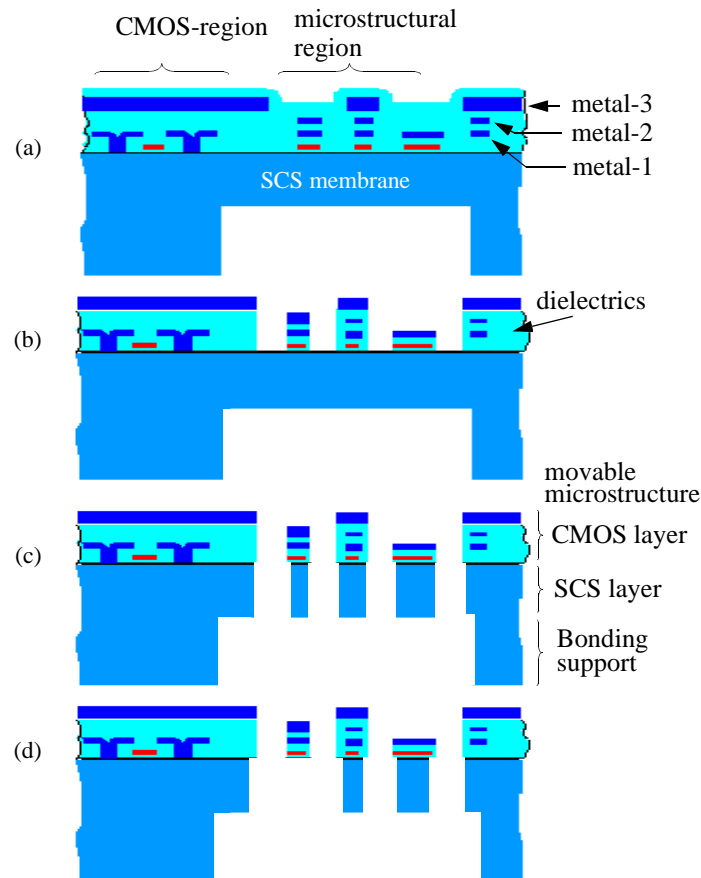
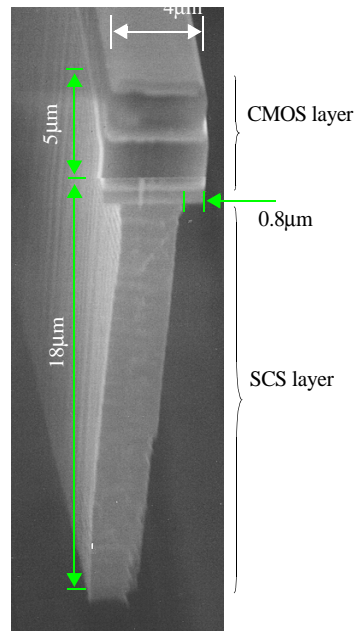


*Figure 2-5: The process-flow for DRIE CMOS micromachining. (a) CMOS-chip with backside etch. (b) Anisotropic dielectric etch. (c) Anisotropic silicon etch for release. (d) An optional, short isotropic silicon etch for undercut control.*

performed (Fig. 2-5(d)). This step provides a specific undercut of bulk Si to create compliant structures to achieve electrical isolation of single-crystal silicon.

A side view of a beam fabricated by this process is shown in Fig. 2-6. The silicon beam end is tapered, appearing tilted as an artifact of the viewing angle in the SEM. The  $0.8\ \mu\text{m}$  undercut resulted from the final optional isotropic silicon etch step. No curling compensation in lateral and vertical directions is needed and a microstructure can be designed to an arbitrary shape and orientation in the x-y plane. Furthermore, the proof

*Figure 2-6: Scanning electron micrograph (SEM) of a beam end. The optional isotropic etch (Fig. 5(d)) was used to attain the large undercut.*



mass and comb-finger capacitance for CMOS-MEMS based inertial sensors is significantly increased. The SEM of a comb-drive resonator fabricated by using the new process is shown in Fig. 2-7. In a later section, we will discuss the optical and electrical characterization of this device in detail.

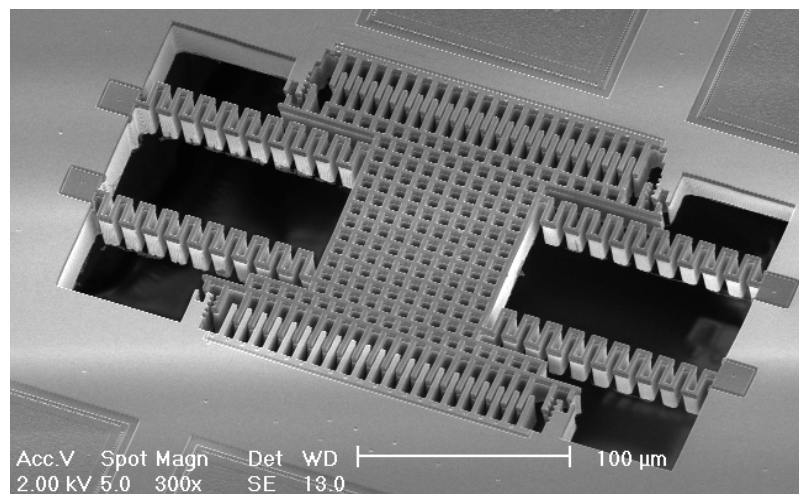


*Figure 2-7: SEM of a comb-drive resonator fabricated in the DRIE CMOS-MEMS process. The thickness of the Si layer is about 50 μm.*

### 2.2.2 Design considerations

Since there are no fixed electrodes underneath the microstructures, this technology is mainly suitable for sidewall capacitive sensing and actuation. Suppose there are two side-by-side beams, *e.g.*, a pair of comb fingers, as shown in Fig. 2-8(a). A comb drive can be constructed from an array of these comb fingers, as shown in Fig. 2-8(b). The sidewall capacitance change versus displacement in the longitudinal, transverse and vertical directions have the following relationships,

$$\frac{\partial C}{\partial x} \propto \frac{h}{g} \cdot \frac{L-w}{g+w} \quad \frac{\partial C}{\partial y} \propto \frac{h}{g} \cdot \frac{l}{g} \cdot \frac{L-w}{g+w} \quad \frac{\partial C}{\partial z} \propto \frac{l}{g} \cdot \frac{L-w}{g+w} \quad (2-1)$$

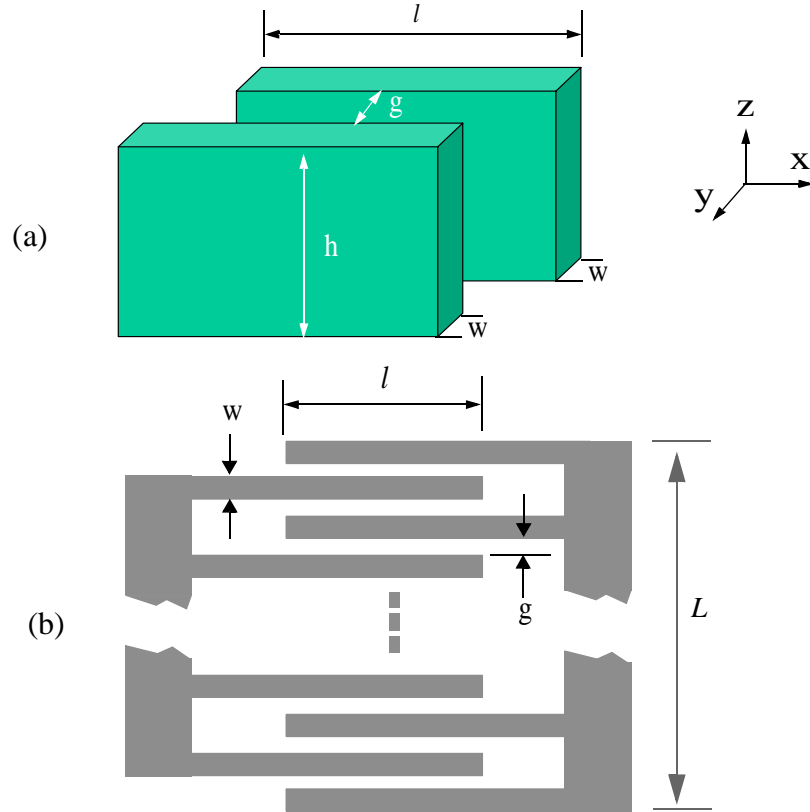
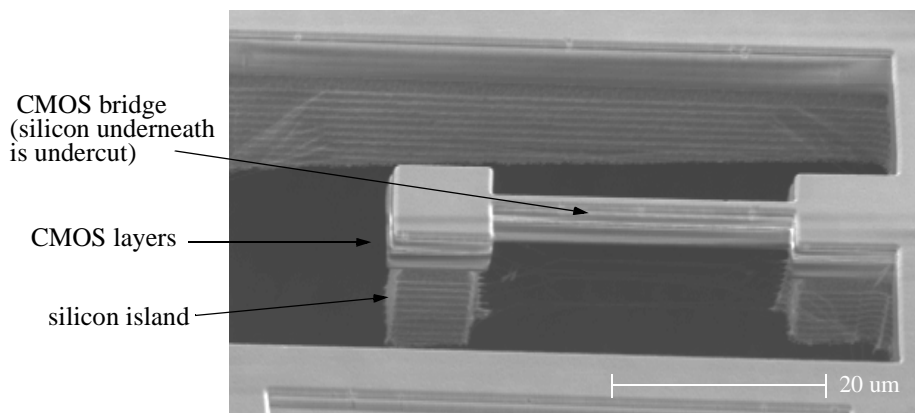


Figure 2-8: Schematic of a comb drive. (a) Side view of a pair of comb fingers. (b) Top view of the comb-finger array.



where  $l$ ,  $g$ ,  $h$  and  $w$  are the engaged length, gap, height and width of the comb fingers, respectively, and  $L$  is the total width of the comb-finger array. The total number of gaps between stator and rotor comb fingers is  $\frac{L-w}{g+w}$ . The gap aspect-ratio is  $h/g$ , which is fixed for the ASE process. If a fixed area is assumed, *i.e.*,  $L$  is fixed, then the smaller the gap, the larger the capacitance change in all three directions. The height of the comb fingers is then best set by the minimum possible gap. Thicker comb fingers would require a larger gap and result in a reduction in capacitive sensitivity. However, there is a minimum SCS layer thickness that eliminates the stress-induced curling below values of surface roughness. Note that this minimum thickness value depends on the size of the designed microstructure as well as the thickness control accuracy of the deep Si RIE process. For inertial sensors, mass is a critical parameter that dictates resolution. The SCS layer should be as thick as possible and there is a trade-off between the gap spacing and the structural thickness.

An electrically isolated SCS block is shown in Fig. 2-9, where the beam width is  $1.5\text{ }\mu\text{m}$  and the CMOS bridge provides mechanical support as well as electrical wiring.



*Figure 2-9: SEM of an electrically isolated SCS block.*

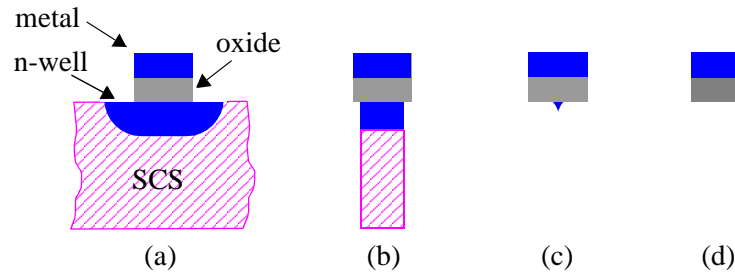


*Figure 2-10: Electrical isolation of silicon: (a) a metal/oxide beam after the dielectric micromachining process step with a n-well underneath; (b) deep Si etch with a small undercut; (c) isotropic Si etch with left-over silicon; (d) isotropic Si etch with complete undercut.*

The SCS layer underneath beams smaller than two times the deep Si RIE undercut of  $0.4\ \mu\text{m}$  are undercut. However, an additional isotropic silicon etch must be performed to undercut wider beams, as illustrated in Fig. 2-5(d). Through complete undercut of the silicon on supporting thin-film beams, released areas of bulk silicon can be electrically isolated. In addition, soft springs can be obtained by using the same principle. To further guarantee the electrical isolation, the to-be-undercut silicon region is implanted as n-well (for p-silicon substrate) to form a p-n-p junction in case there is still a remaining thin layer of silicon underneath the beam, as shown in Fig. 2-10. The n-well is left floating. The breakdown voltage of the n-well/p-substrate junction is greater than 38 V for the Agilent  $0.5\ \mu\text{m}$  CMOS process. This voltage is sufficient for many applications.

### 2.2.3 Fabrication

Single-chip processing was used to demonstrate the DRIE release sequence. The square CMOS chips (2 mm by 2 mm) are made in the Hewlett-Packard (now Agilent)

0.5  $\mu\text{m}$  three-metal n-well process available through MOSIS [65].

The chips come with an unpolished backside. Prior to the deep etching process, the backside was patterned in a photolithography step with a backside release mask using a 10  $\mu\text{m}$  layer of a high viscosity photoresist (Shipley AZ 4620). The exposure was performed with a Karl-Suss MA 56 mask aligner. The backside-frontside alignment accuracy needs to only be about 50  $\mu\text{m}$  to allow for the full wafer thickness of silicon under the bond pads on the periphery of the chip. The patterning guaranteed that a sufficient silicon frame for mechanical support of the silicon membrane remains after the deep etch. A 250  $\mu\text{m}$ -wide silicon frame is adequate for a 2 mm by 2 mm die. Larger die often have more space for the frame. The chips were mounted on a 4'' silicon wafer covered with photoresist. The backside ASE etch for defining the silicon membrane was performed in a Surface Technology Systems (STS) ICP (inductively coupled plasma) etcher. The etching-process employed was a typical ASE process [59] with an etching rate of 2.9  $\mu\text{m}/\text{min}$  for a small silicon load. The main plasma parameters for the etching part of the cycle were 600 W coil power, 12 W platen power, 130 sccm  $\text{SF}_6$  flow, and 23 mT chamber pressure. The fluorocarbon polymer passivation cycle was performed at 600 W coil power, 12 mT chamber pressure, 85 sccm flow of  $\text{C}_4\text{F}_8$  and no platen power. The duration was 12 s in the etching cycle and 8 s in the passivation cycle. After removal of the chips from the carrier wafer and an oxygen plasma clean of the chip frontside, the oxide RIE etch of the CMOS-micromachining process (Fig. 2-5(b)) was performed in a Plasma-Therm 790 reactor.

The major demands for the Si etching process are good stability of the etching rate, low surface roughness and a sufficiently uniform structural thickness. A polishing of the chip backside prior to the backside deep etch improves the smoothness of the resulting silicon membrane surface but is not necessary. The backside etch step defines the thickness of the remaining silicon membrane and high accuracy measurements of the thickness of the chips and the etch depth are necessary. The typical backside etch step of around 450  $\mu\text{m}$  is beyond the measurable range of the available stylus profilometer. A white-light profilometer (Veeco/Wyko NT2000) with a resolution of a nanometer was employed.

For performing the anisotropic silicon release step (Fig. 2-5(c)) in the STS ICP etcher, the chips were mounted on a 4'' photoresist-covered silicon wafer. The top metal of the CMOS layers served as the mask. No degradation of the top metal layer was observed, even for etching durations of several hours. No performance decrease of the ICP etcher due to use of the Al mask was detected for individual die [66]. Die-sized samples limited the amount of aluminum exposed in the chamber, thereby alleviating concerns of micro-masking from resputtering aluminum. The final optional silicon etch step (Fig. 2-5(d)) is also performed in the STS etch chamber. The isotropic etch is achieved by turning off the platen RF power and leaving on only the coil power.

Due to well known micro-loading effects of the ASE process [67], the trenches with a larger width are etched faster. Therefore, the large open areas are etched through to the backside first, before the narrow gaps. The exposure to plasma through the openings results in polymer deposition on the remaining silicon backside during the passivation

steps of the ASE.

A close-up of the backside of a comb-drive actuator after performing the anisotropic etch step is shown in Fig. 2-11(a). The polymer deposited on the backside of the SCS layer due to the relatively early etch-through of the wider gaps forms a residual structural layer that cannot be etched by continuing the ASE process. The polymer layer is removed by using a 15 minute, zero-bias oxygen plasma clean at the end of the process flow after the narrow gaps are etched through to the polymer film. The SEM in Fig. 2-11(b) shows the backside of a clean device after an oxygen plasma step is used at the end of the release procedure. The 1.2  $\mu\text{m}$  gaps are released. The bottom surface is rough due to the 450  $\mu\text{m}$ -deep Si etch that is performed on the unpolished backside of the die. The ASE undercut is smaller in corners of structures, therefore the square release holes appear as round holes on the backside.

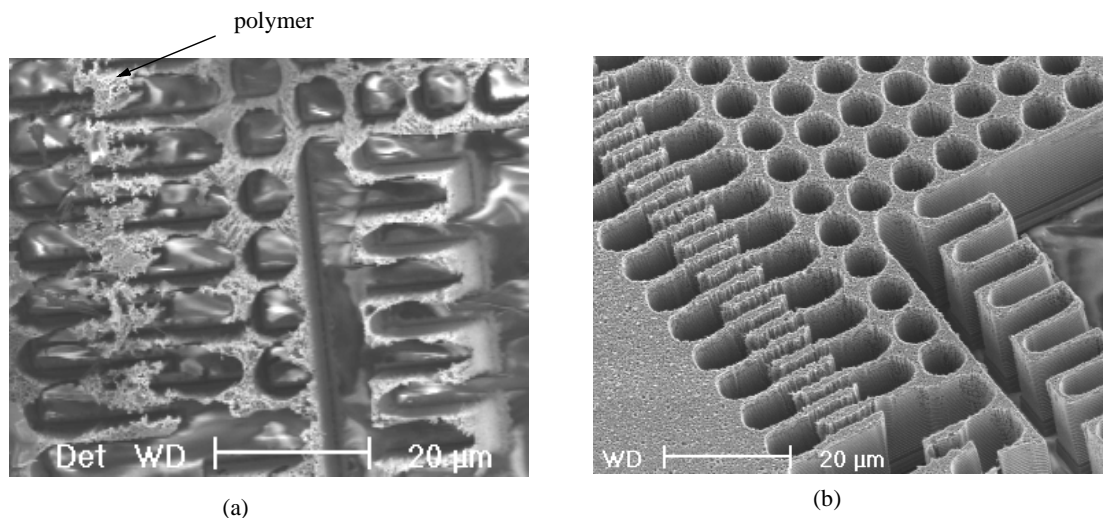


*Figure 2-11: SEMs of the backside of the comb-drive actuator. (a) After the ASE, prior to oxygen plasma cleaning. (b) After oxygen plasma cleaning.*

## 2.3 CHARACTERIZATION

### 2.3.1 Cantilever beams

In order to investigate the mechanical properties of the composite microstructures with stacked CMOS and SCS layers, an array of 110  $\mu\text{m}$ -long and 3  $\mu\text{m}$ -wide cantilever beams was designed. Fig. 2-12 shows two of the released beams. The minimum gap is 2.1  $\mu\text{m}$ , which limits beam thickness to a maximum of 55  $\mu\text{m}$  for an aspect-ratio of 25. The fabricated beam thickness is 45  $\mu\text{m}$ . The undercut of a beam or any other structure strongly depends on its separation to the surrounding structures. Larger gaps will generate larger undercut. In the figure, the typical scallops of the ASE process are present along with an undercut of about 0.4  $\mu\text{m}$  at the edges adjacent to large etch pits. The measured resonant frequency is 254 kHz, which is in good agreement with the finite element simulation of 249 kHz. For the FEM analysis, the Young's modulus of the SCS layer in the lat-

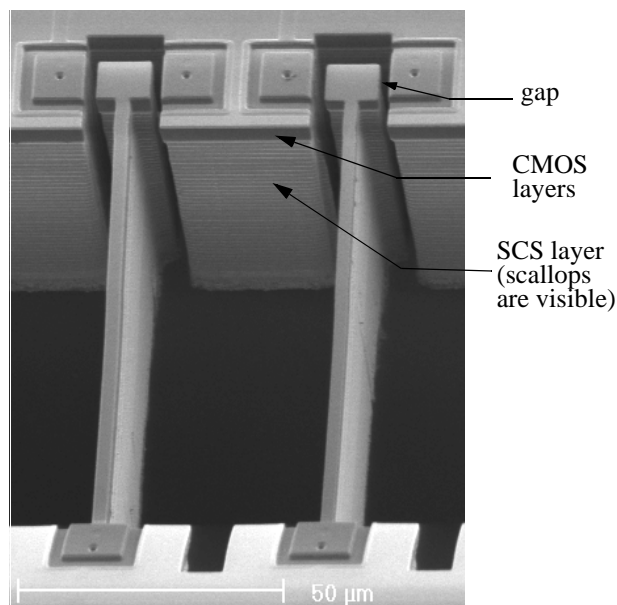


Figure 2-12: SEM of DRIE cantilever beam resonators.

eral direction aligned to the Si wafer flat (*i.e.*,  $\langle 110 \rangle$ ) is 168 GPa [68] and the CMOS layer's effective Young's modulus is 63 GPa [56].

### 2.3.2 Comb-drive resonator

Fig. 2-13 is a close-up of one corner of the comb-drive resonator shown in Fig. 2-7. The gap of the comb fingers is  $1.2\ \mu\text{m}$  and thus the underlying SCS layer has been thinned down to a  $30\ \mu\text{m}$  thickness for an aspect-ratio of 25. The underlying SCS beam width is  $0.8\ \mu\text{m}$  narrower than the CMOS layers due to the  $0.4\ \mu\text{m}$  Si undercut. The underlying SCS is not electrically isolated from the silicon substrate in this comb-drive actuator. For comparison, another comb-drive resonator having the same layout was released by using the thin-film micromachining process. Experimental measurement of displacement ampli-

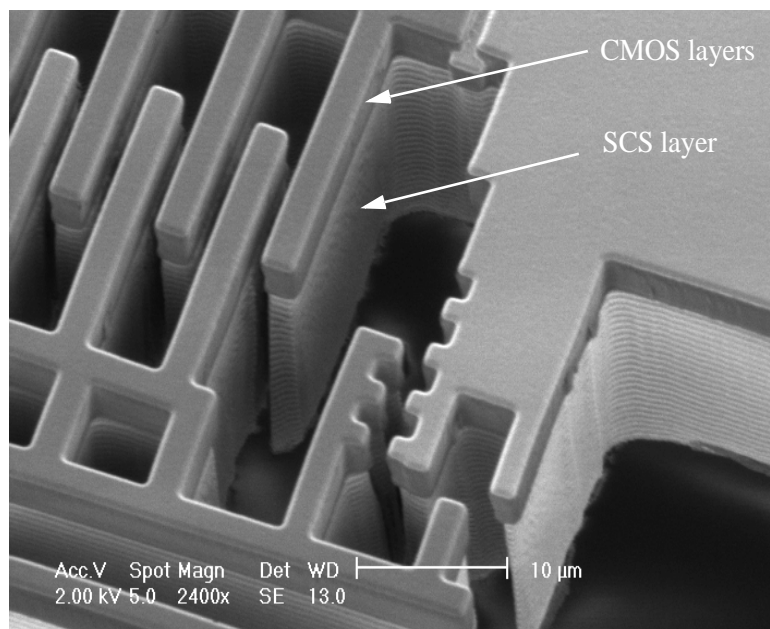


Figure 2-13: Close-up of one corner of the comb-drive actuator (see Fig. 2-7).

tude at resonance shows that the stiffness of the serpentine-spring suspension is increased by a factor of four ( $\pm 12\%$ ) by including the underlying thick SCS layer.

To evaluate the topography of the released structures, we employed a Linnik-type Michelson interferometer with LED illumination ( $\lambda=610$  nm). The topography is calculated from a series of fringe patterns using a phase unwrapping technique [69]. We achieved a measurement accuracy of better than 40 nm for the z-curling. The measured topography of a comb-drive actuator with no underlying SCS layer is shown in Fig. 2-14(a). The peak-to-valley curling measured across the 120  $\mu\text{m}$ -wide device is 1.2  $\mu\text{m}$ . For a device with underlying 20  $\mu\text{m}$ -thick SCS, the curling is 0.15  $\mu\text{m}$ , nearly an order of magnitude reduction, as shown in Fig. 2-14(b). The corresponding radius of curvature for the SCS CMOS-MEMS structure is 12 mm.



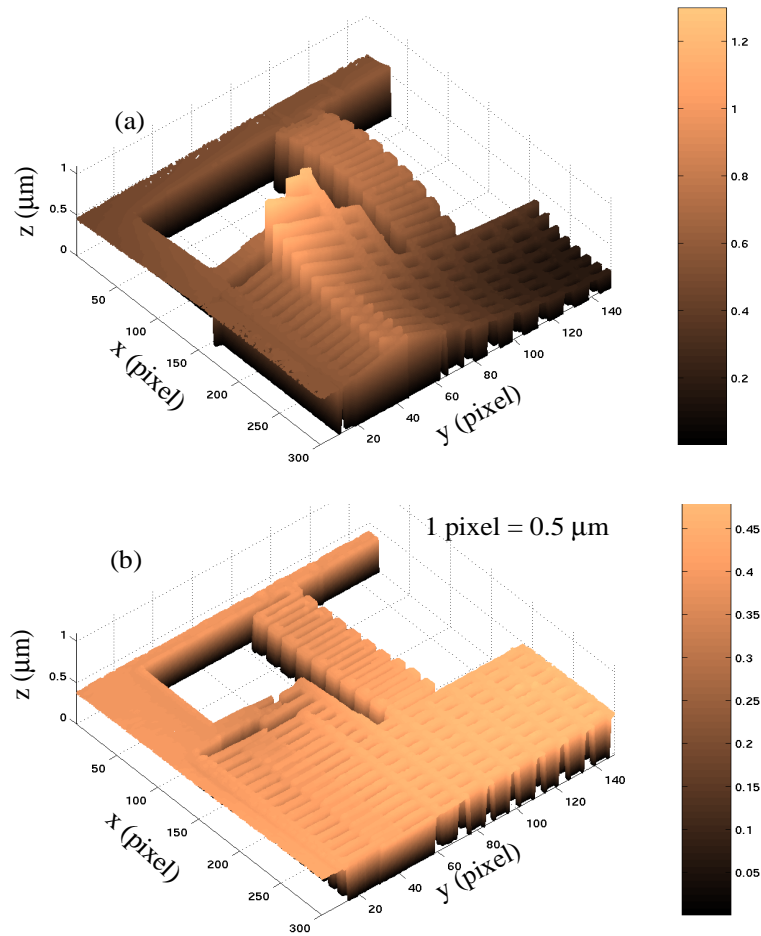


Figure 2-14: The topography of the released comb-drive actuator (see Fig. 2-4) (only one quarter is shown) obtained by using phase shifting interferometry. (a) Conventional release. (b) Backside release.

## **Chapter 3**

# **Vertical Comb-Finger Sensing and Actuation**

### **3.1 Introduction**

A unique z-axis comb-finger actuation and sensing method has been developed based on both thin-film and DRIE CMOS-MEMS processes described in Chapter 2 [21]. Combined with the comb drives' conventional lateral-axis sensing and actuation capability, three-axis comb-finger sensing and actuation can be integrated on a single chip using a single mechanical layer. Both lateral-axis and z-axis CMOS-MEMS accelerometers and gyroscopes have been demonstrated [14]-[18]. Micro-optical devices with vertical actuation also have been made by using the DRIE CMOS-MEMS process [70]-[72].

In this chapter, first the principle of the z-axis comb-finger actuation and displacement-sensing is introduced, followed by its applications in a thin-film z-axis accelerometer, a thin-film x-y-z microstage and a DRIE z-axis accelerometer. Design issues and experimental results of all three devices are presented. Micro-optical devices will be discussed in Chapter 4 and vibratory gyroscopes will be addressed in Chapters 5 and 6.

### 3.2 Thin-Film Out-of-Plane Comb-Finger Actuation and Sensing

As shown in Fig. 3-1, microstructures can have several embedded metal layers, which is a major difference from homogeneous polysilicon counterparts. These multi-conductor layer structures make it possible to construct multiple capacitors between comb fingers. There are 25 different electrode-pair configurations for combs with three metal layers that provide vertical electrostatic actuation and capacitive displacement sensing.

To determine which configuration is used, vertical curling and curl matching must be considered. Metal-3 beams should be used to minimize vertical curling [56]. The same design on both stator and rotor fingers gives the best curl matching. Meanwhile using all three metal layers maximizes the capacitance. Therefore, the comb-finger configurations shown in Fig. 3-1 are chosen.

The comb-finger configurations have two or three metal layers and are located about  $30\text{ }\mu\text{m}$  above the substrate, which leaves ample room for vertical motion. This large gap is also an advantage for capacitive comb-finger sensing because the parasitic capacitance to

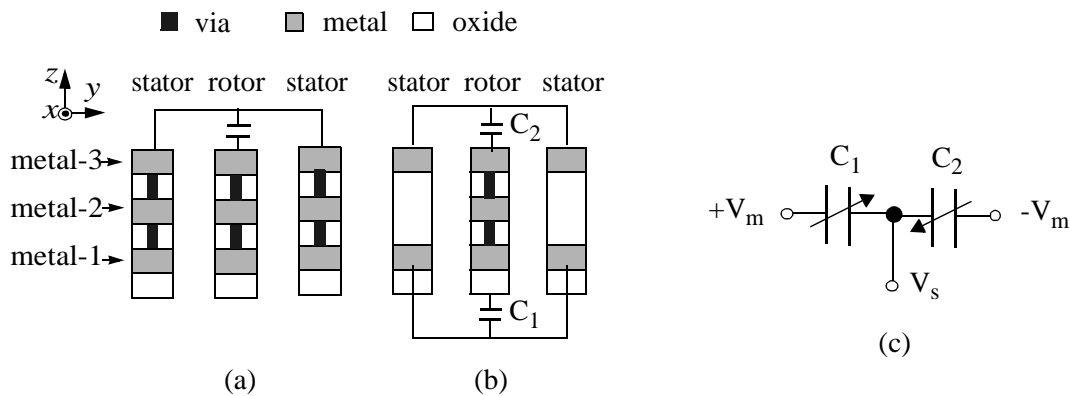


Figure 3-1: Principle of vertical actuation and capacitive-sensing through comb-fingers. (a) X-axis actuator. (b) Z-axis actuator. (c) Equivalent capacitive-bridge.

the substrate is greatly reduced. As shown in Fig. 3-1(a), if the three metal layers on the stators are electrically connected, as are the corresponding metal layers in the rotor, the CMOS comb drive has an equivalent function to a lateral-axis polysilicon comb drive.

If all three metal layers in the rotor are electrically connected while the metal-1 and metal-3 in the stator are separately connected, two sidewall capacitors,  $C_1$  and  $C_2$ , are formed, as shown in Fig. 3-1(b). When a voltage is applied across  $C_1$  or  $C_2$ , the rotor will actuate in the z-direction. If the rotor finger moves up or down by an external force (such as acceleration),  $C_1$  and  $C_2$  will change value in opposite directions and therefore the device can function as a z-axis motion detector.

### 3.2.1 Z-axis Actuation

In order to evaluate the capacitance and expected displacement, a commercial finite-element analysis tool, the Maxwell 2D field simulator [73], is employed. The cross-sectional dimensions for the simulation are given in Fig. 3-2 and are the nominal dimensions for the Agilent 0.5  $\mu\text{m}$  process. The calculated  $C_1$  and  $C_2$  in Fig. 3-1(b) and their gradients versus static z-displacements are shown in Fig. 3-3(a) and (b), respectively. Note that the

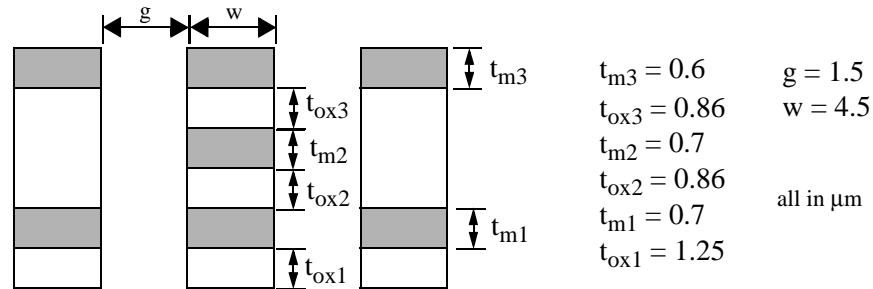


*Figure 3-2: Cross-sectional dimensions of the comb finger set for the Maxwell 2D field simulation.*

maximum displacement range is defined by the intersections of the two gradient curves with the zero-gradient line, which occur at  $-2.6 \mu\text{m}$  and  $2.2 \mu\text{m}$ , respectively (Fig. 3-3(b)).

The electrostatic force  $F_e$  is equal to

$$F_e = \frac{1}{2}NL\frac{dC}{dz}V^2 \quad (3-1)$$

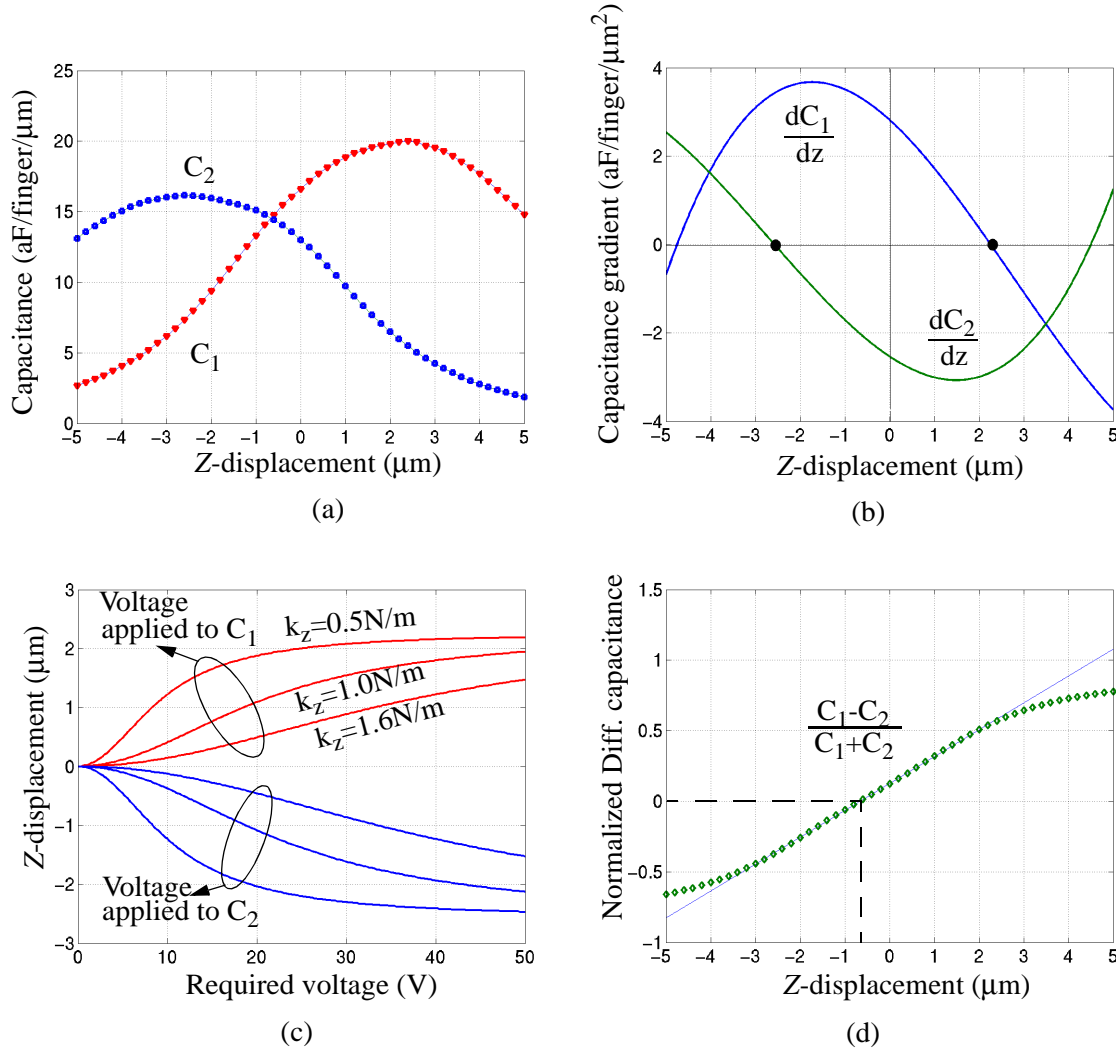


Figure 3-3: Principle of vertical actuation and capacitive-sensing through comb-fingers. (a) Capacitance vs. z-displacement. (b) Capacitance gradient vs. z-displacement. (c) Z-displacement vs. applied voltage where fifty-two  $30 \mu\text{m}$ -long comb fingers are assumed. (d) Calculated differential capacitance vs. z-displacement.

where  $N$  is the number of comb fingers,  $L$  the engaged length of comb fingers,  $C$  the unit length capacitance of a single finger, and  $V$  the applied voltage. The relationship between displacement and voltage can be obtained by numerically solving the force balance equation, *i.e.*,  $F_e = F_{spring} = k z$ , where  $k$  is the spring constant and  $z$  is the vertical displacement. The result is plotted in Fig. 3-3(c) for a series of spring constants. Displacement tends to saturate at  $-2.6 \mu\text{m}$  and  $2.2 \mu\text{m}$  when the voltage increases, which is exactly as predicted in Fig. 3-3(b).

### 3.2.2 Z-axis Displacement Sensing

Capacitance change is often used as a measure of displacement in microaccelerometers. The sensitivity in one direction depends on both the capacitance gradient and the mechanical stiffness in that direction. As an electrical circuit,  $C_1$  and  $C_2$  form a differential capacitive half-bridge, as shown in Fig. 3-1(c). If balanced modulation voltages  $\pm V_m$  are applied, the output signal  $V_s$  is expressed as

$$V_s = \frac{C_1 - C_2}{C_1 + C_2 + C_p} V_m \quad (3-2)$$

where  $C_p$  is the parasitic capacitance. Fig. 3-3(d) shows the simulation results of  $C_1$ ,  $C_2$  and their differential change with  $z$ -displacement. Parasitic capacitance in the CMOS microstructures is very small and in this theoretical analysis is assumed to be zero. Although  $C_1$  and  $C_2$  are not linear with  $z$ -displacement, the normalized differential capacitance changes linearly from  $-3.0 \mu\text{m}$  to  $+2.3 \mu\text{m}$  (Fig. 3-3(d)). If the rotor fingers are attached to a proof mass and a spring, the output voltage is

$$V_s = \frac{ma}{k} V_m(G(z)) \quad (3-3)$$

where  $G(z) = (C_I - C_2)/(C_I + C_2 + C_p)$ ,  $m$  is the mass of the proof mass,  $k$  is the stiffness of the spring in the  $z$ -axis, and  $a$  is the external acceleration in the vertical direction. The sensitivity  $V_s/V_m$  depends on the spring, proof mass and capacitive bridge, but is constant as long as the system is operating in its linear range.

Note that the wide linear displacement range ( $-3.0 \mu\text{m}$  to  $+2.3 \mu\text{m}$ ) is remarkable, since large dynamic range can be achieved without compromising sensitivity or bandwidth. Low cross-sensitivity is expected in this configuration because  $C_I$  and  $C_2$  are the summation of the capacitances formed in both sides of the stator and the stiffness of the lateral axes is designed to be much bigger than that of the  $z$ -axis.

The differential capacitance curve in Fig. 3-3(d) is not symmetric, *i.e.*,  $G(z) \neq 0$  at  $z = 0$ . Instead, a d.c. offset of  $-0.6 \mu\text{m}$  exists. This is because metal/oxide stacks are not symmetric in the  $z$ -direction. Metal-3 is thinner than metal-1 due to ion milling of top metal-3 during oxide RIE etching. Therefore  $C_I$  is greater than  $C_2$ . The oxide underneath metal-1 further boosts  $C_I$ . The d.c. offset can be compensated by a prescribed displacement of  $0.6 \mu\text{m}$  realized by properly designing the curl matching frame or by integrating a polysilicon heater and thermomechanically setting the displacement [57]. In the following section, we introduce a more convenient method to compensate the d.c. offset.

### **3.2.2.1 Vertical Sidewall Capacitance Offset Cancellation**

As discussed above, the two sidewall capacitors formed in a comb finger set are not symmetric in the  $z$ -direction. There will be a large d.c. offset if the configuration is used

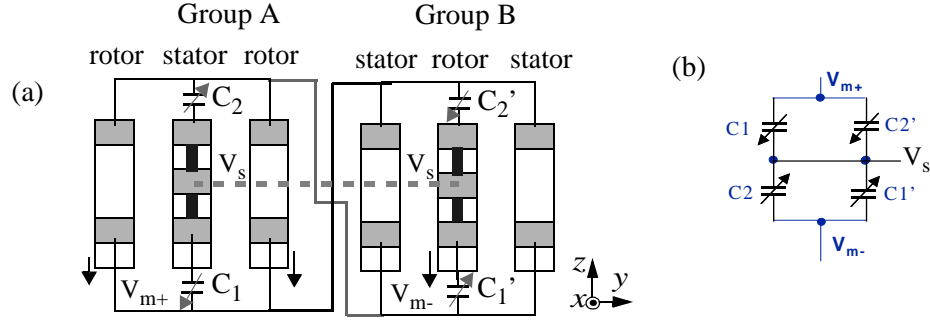


Figure 3-4: Principle of vertical sidewall capacitance offset cancellation. (a) Two groups of comb fingers with swapped rotors and stators. (b) Equivalent circuit.

for displacement sensing. This d.c. offset actually can be cancelled out by using the wiring flexibility provided by the CMOS-MEMS processes. As shown in Fig. 3-4(a), two groups of comb fingers have the same cross-section, but their rotors and stators are swapped. If the rotors move down, the top capacitor  $C_2$  of Group A and bottom capacitor  $C_1'$  of Group B increase while the bottom capacitor  $C_1$  of Group A and top capacitor  $C_2'$  of Group B decrease. If the top and bottom electrodes of Group A are respectively connected to the bottom and top electrodes of Group B, then increasing  $C_2$  and  $C_1'$ , and decreasing  $C_1$  and  $C_2'$  are grouped together, respectively, to form a capacitive bridge as shown in Fig. 3-4(b). Since each branch of the bridge has a top capacitor and a bottom capacitor, the sum of the capacitances of each branch is equal at the rest position, i.e.,  $C_1 + C_2' = C_2 + C_1'$  at  $z = 0$ .

A simplified accelerometer design is used to illustrate how to use this offset cancellation method. As shown in Fig. 3-5(a), the accelerometer has eight groups of comb fingers. Four of them are configured as Group A, and the other four as Group B in Fig. 3-4(a). Both vertical force and torque have to be cancelled out. For instance, A1 and B1 cancel each other's vertical force, but a torque may be produced. Their mirror image, A2 and B2,



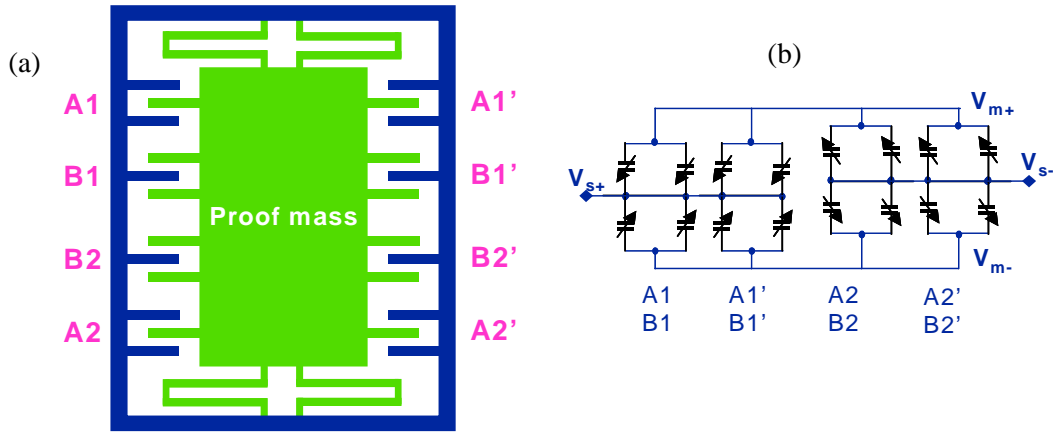


Figure 3-5: Comb finger arrangement for vertical sidewall capacitance offset cancellation. (a) Layout. (b) Equivalent circuit.

are used to balance the torque. The equivalent circuit is shown in Fig. 3-5(b), which is a fully differential capacitive bridge.

### 3.2.3 Z-axis Thin-Film Comb-Finger Accelerometer

Fig. 3-6(a) shows the topology of a z-axis accelerometer consisting of a central proof mass, two symmetric z-spring beams and two sets of comb fingers. The comb fingers are divided into four groups as shown in Fig. 3-6(a). All comb finger sets have exactly the same cross-section as shown in Fig. 3-1(b). In groups A and B, the top metal layer is connected to  $V_{m+}$ , and the bottom metal layer to  $V_{m-}$ . In groups C and D, the wiring is reversed to obtain a full-bridge differential capacitive interface as shown in Fig. 3-6(b). Moreover, the four groups constitute a common-centroid configuration which reduces the lateral-axis sensitivity and the influence of process variations.

As mentioned in Chapter 2, the CMOS micromachining process can make structures of different thicknesses at different locations by simply choosing different metal layers as

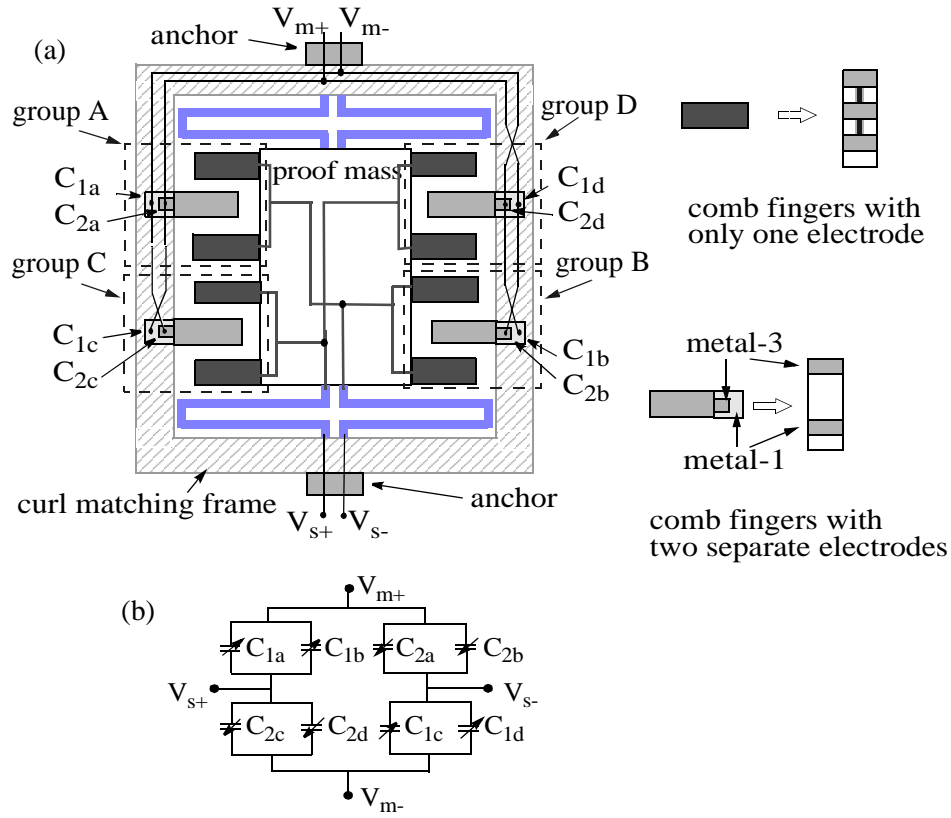


Figure 3-6: Topology design and wiring configuration of the z-axis accelerometer. (a) Schematic of the top view of the layout with a common-centroid configuration. (b) Equivalent full-bridge differential capacitive interface.

the etching mask. In order to further reduce the cross-sensitivity, the spring is covered only by metal-1 as shown in Fig. 3-7. After release, the thickness of the spring will be much thinner than the rest of the structure, making the spring soft in the z direction. Since the structure is made of multiple material layers, the residual stress gradient makes struc-

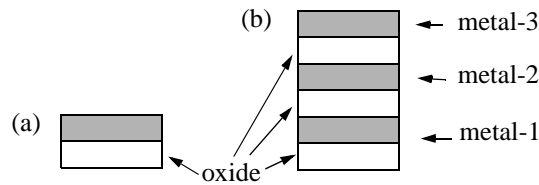


Figure 3-7: Cross-sections at different locations of a structure. (a) Spring; (b) Proof mass and frame.

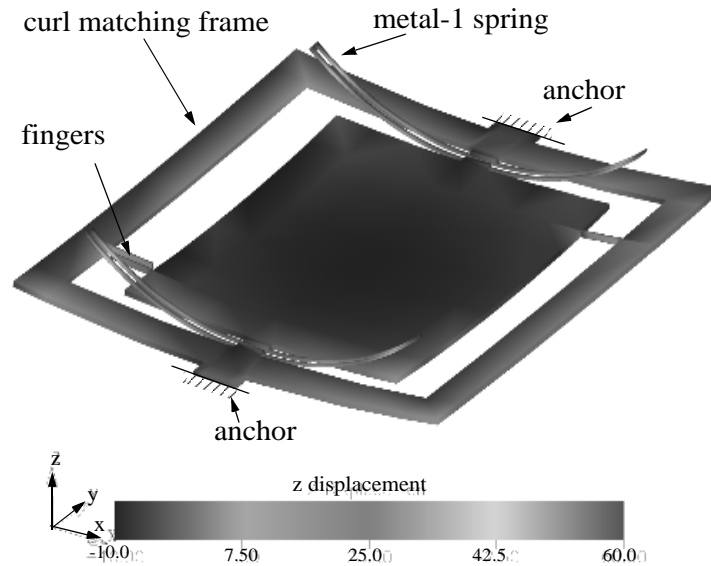


Figure 3-8: Thermomechanical simulation of the  $z$ -axis accelerometer.

tures curl up, especially for thin beams with only metal-1 on the top [14]. In order to obtain a better understanding, thermomechanical simulation is performed in MEMCAD 4.5 [60]. Two simplifications are made to reduce the number of elements in the analysis: 1) the holes on the structure for etch release are eliminated; 2) only two pairs of comb fingers are used to model the curl matching behavior. The result is shown in Fig. 3-8 which indicates that the spring curls much more than the rest of the structure. The rotor fingers match the stator fingers well through the curl matching frame.

A released accelerometer is shown in Fig. 3-9. The size of the device including the on-chip buffers and preamplifier is about 0.5 mm by 0.7 mm. The two sets of fingers outlined with a white solid line are electrically connected, as are the other two sets outlined with a white dashed line. Schematic cross-sections are shown at the top of the SEM. The spring beams curl up about  $55\text{ }\mu\text{m}$  at their ends due to the residual stress gradients arising from

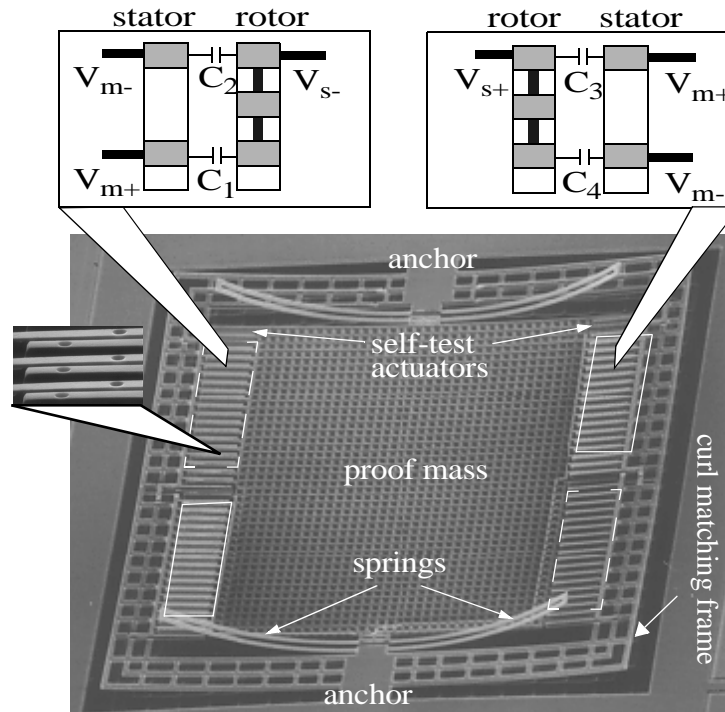


Figure 3-9: Top view of a released z-axis accelerometer.

the embedded layers inside the beams. However, the stator and rotor fingers align very well ( $< 0.5 \mu\text{m}$  vertically) as predicted by the finite-element analysis. The lateral offset of the comb fingers is less than  $0.1 \mu\text{m}$ . There is one extra pair of comb fingers at each corner of the proof mass. These comb fingers are electrically isolated from the sense comb fingers and are used as electrostatic actuators for self-test and offset adjustment.

The packaged accelerometer is mounted on a Brüel & Kjær vibration exciter (Type 4808) whose motion is monitored by a high accuracy reference accelerometer, and an HP4395A spectrum analyzer is used to measure the output signal. The response of the accelerometer is shown in Fig. 3-10, measured under a 200 Hz sinusoidal shaker excitation and an 800 mV 400 kHz sinusoidal modulation across the capacitive bridge. The out-

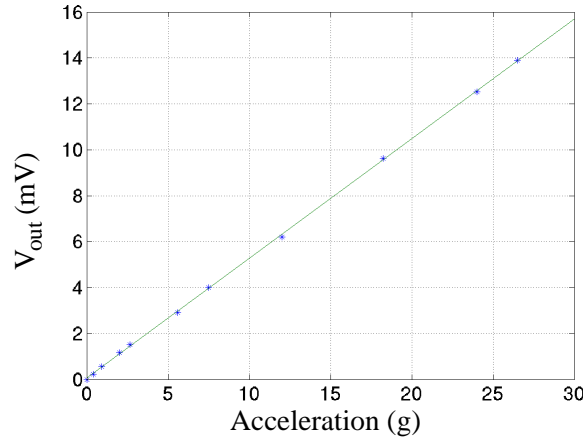


Figure 3-10: Response of the accelerometer measured using a shaker table.

put sensitivity is 0.5 mV/g. The response remains linear ( $< 1\%$  non-linearity) when the amplitude of the external acceleration increases to 27 g, which is the maximum limit of the shaker table. The theoretical linear range is  $\pm 600$  G because of the wide linear range of the differential capacitance change with z-displacement. A typical spectrum of the output signal is shown in Fig. 3-11 where a 0.5 G 80 Hz excitation acceleration is applied. The measured noise floor is  $6 \text{ mG/Hz}^{1/2}$ , which is one order of magnitude higher than the cal-

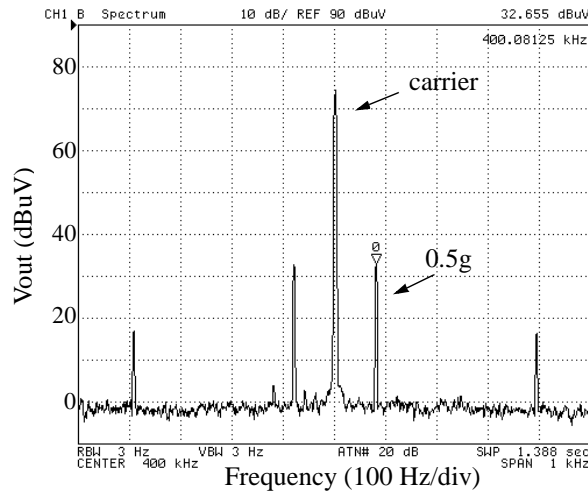
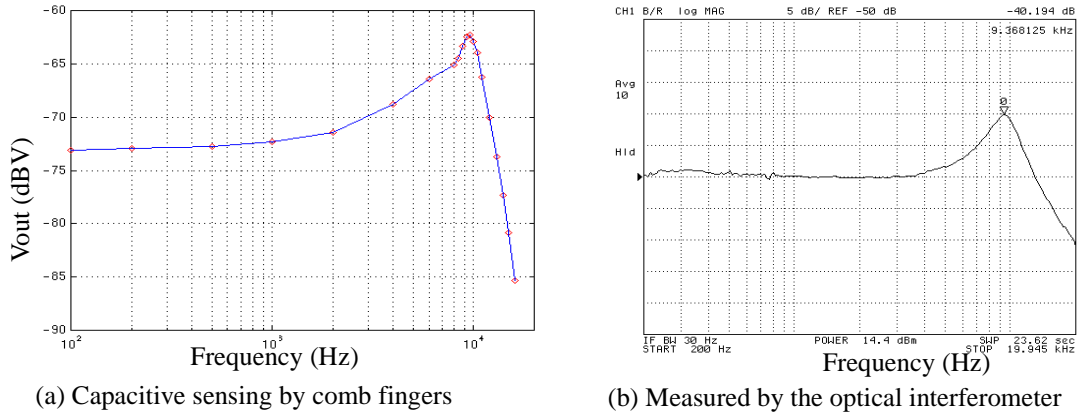


Figure 3-11: Spectrum of the output signal when a 0.5 G external acceleration is applied.



*Figure 3-12: Frequency response of the accelerometer.*

culated Brownian noise. The increased noise level is believed to be due to the test circuits and to vibration existing in the test environment.

The frequency response of the accelerometer is characterized both electrically and optically as shown in Fig. 3-12. For electrical characterization, the accelerometer is excited by applying a sinusoidal voltage to the self-test actuators. In order to reduce the effect of the feedthrough of the excitation signal, a sinusoidal signal with zero d.c. bias is used to generate force at double the input electrical frequency. The frequency response detected through the sensing comb fingers is shown in Fig. 3-12(a).

In order to explore the actual motion, a Michaelson optical interferometer system is employed. The schematic of the optical set-up is shown in Fig. 3-13. Two microscope objectives are used to image the microstructure and a flat reference mirror simultaneously onto a CCD camera or a photodiode. These two interfering optical fields result in a fringe pattern that allows the evaluation of the topography and real-time displacement measure-

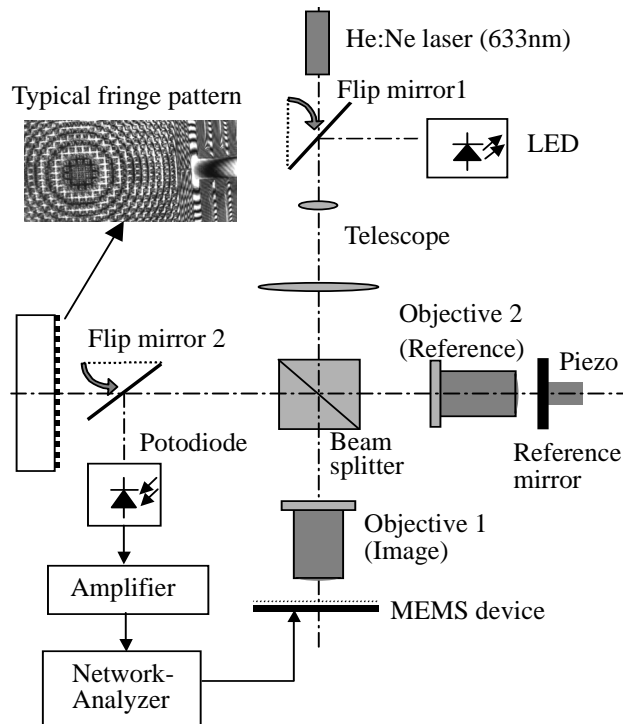
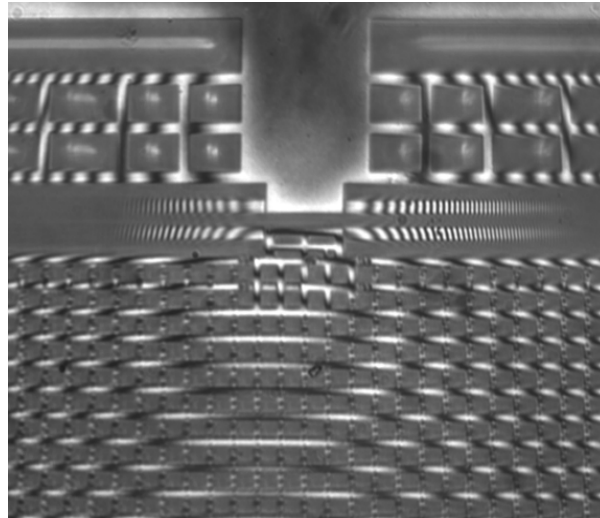


Figure 3-13: Optical measurement setup using a Michelson interferometer.

ment. A He:Ne laser ( $\lambda = 633 \text{ nm}$ ) produces high intensity fringe patterns in the dynamic measurements, while a red LED ( $\lambda = 610 \pm 10 \text{ nm}$ ) is employed to avoid speckled images in the static measurements. LEDs also have the advantage of rapid pulsing capability. A typical interference image is shown in Fig. 3-14. A photodetector combined with a network analyzer is used to conduct frequency sweeping and obtain transfer function directly. The output motion is measured using a photodetector that senses the fringe intensity at a spot on the proof mass. The measured frequency response is shown in Fig. 3-13(b). The two different measurements give close resonant frequencies of 9.2 kHz for capacitive and 9.4 kHz for optical detection. The resonant frequency predicted by MEMCAD simulation



*Figure 3-14: Interference pattern around the upper anchor (each fringe occurs at 310 nm vertical displacement).*

is 10.1 kHz. The 10% error is attributed to fabrication process variations and the simplification of the model, e.g., modeling the perforated proof mass as a solid plate. The measurement results are summarized in Table 3-1. The Q factor is only about 3, which results from the squeeze-damping of the proof mass.

**Table 3-1: Parameters of the accelerometer**

	Designed	Measured
Dimension	500x700 $\mu\text{m}^2$	-
Resonant frequency	10.1kHz	9.4kHz
Quality factor in air	-	3
Sensor sensitivity	0.75mV/G/V	0.5mV/G/V
Cross-sensitivity	-55dB	<-40 dB
Linear range	+/-600G	+/-27G
Noise floor	0.6 mG/Hz <sup>1/2</sup> (Brownian; Q=3)	6 mG/Hz <sup>1/2</sup>



### 3.2.4 X-Y-Z Microstage

Three-axis microstages have wide applications in micro-optics for precise adjustment of multi-axis scanning [74], optical switches and interferometer systems. The out-of-plane actuation is most challenging to implement within the CMOS-MEMS process.

The top view of the fabricated three-axis microstage is shown in Fig. 3-15. Separate sets of comb fingers for each direction drive the central proof mass. The y-axis and z-axis comb drives are suspended by a common set of springs that are flexible in both y and z directions. The device curls out of plane about  $8\text{ }\mu\text{m}$  at the edges due to the residual stress gradient in the multi-layer structures. However, as shown with the accelerometer, the stator and rotor fingers align well locally through use of a curl match frame.

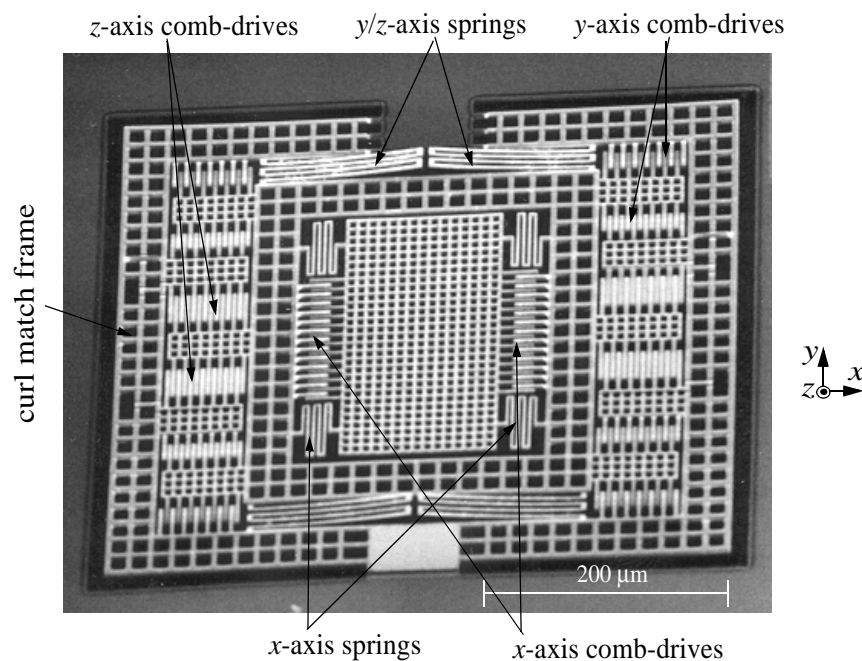


*Figure 3-15: SEM of xyz microstage.*

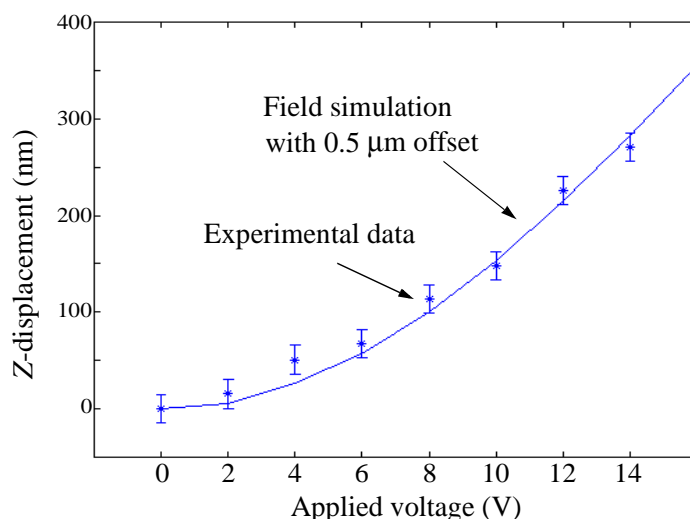


Figure 3-16: Z-displacement vs. applied voltage.

The three-axis stage was operated in the z-axis to verify the vertical actuator model. The frequency response and small z-displacement of the z-axis actuator were measured using a Linnik type Michelson-interferometer system as shown in Fig. 3-13. Note that the fringe pattern can be alternatively projected onto a photodiode with a small active area by switching flip mirror 2. The telescope guarantees the uniform illumination of the chosen field of view. The z-axis spring constant is 1.6 N/m. The experimental data does not fit exactly to the simulation in Fig. 3-3(c), because the released comb fingers have about 0.5  $\mu\text{m}$  vertical mismatch and about 0.1  $\mu\text{m}$  sidewall overetch of metal-3. Fig. 3-16 shows the measured data and the finite-element simulation with the consideration of the mismatch and the metal-3 shrinkage. The experimental data fit the theoretical prediction well. Since the microstructure is not perfectly flat, the motions in x- and y-directions can also be detected through the interferometer measurements. The measured resonant frequencies in the x, y, and z directions are 23.8 kHz, 5.08 kHz, and 6.17 kHz, respectively.

### 3.3 DRIE CMOS-MEMS Out-of-plane Comb-Finger Sensing and Actuation

As discussed above, out-of-plane actuation and sensing can be achieved as long as a vertical capacitance gradient exists. Similar to the thin-film CMOS-MEMS process, the DRIE counterpart also can be used to obtain three-dimensional electrostatic actuation and capacitive sensing. In this section, the principle is first described and then a DRIE accelerometer with integrated self-test z-axis actuators is introduced as an example.

#### 3.3.1 Three-Dimensional Electrostatic Actuation

Three-dimensional actuation can be easily realized in the DRIE CMOS-MEMS process, as shown in Fig. 3-17. In comparison to the thin-film CMOS-MEMS process, the major difference comes from the SCS layer. In the DRIE case, the three metal layers in each beam are electrically connected together as one electrode. As discussed in Chapter 2, each SCS column is electrically isolated from and can be electrically wired to any of other SCS columns. If the CMOS layer and SCS layer in each comb finger are electrically connected, the resultant comb drive functions just like a commonly used polysilicon comb drive. The lateral motion can be either longitudinal or transverse, as shown in Fig. 3-17(a)

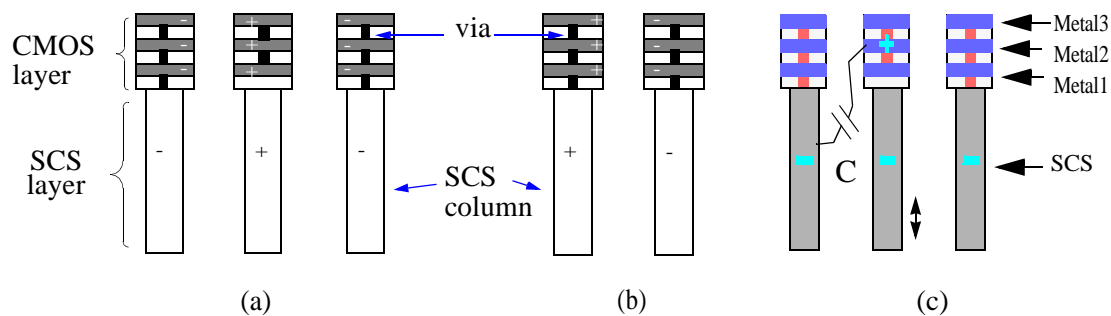


*Figure 3-17: Cross-sectional views and wiring configurations of comb fingers for 3D actuation. (a) Lateral actuation (longitudinal); (b) Lateral actuation (transverse); and (c) Vertical actuation.*

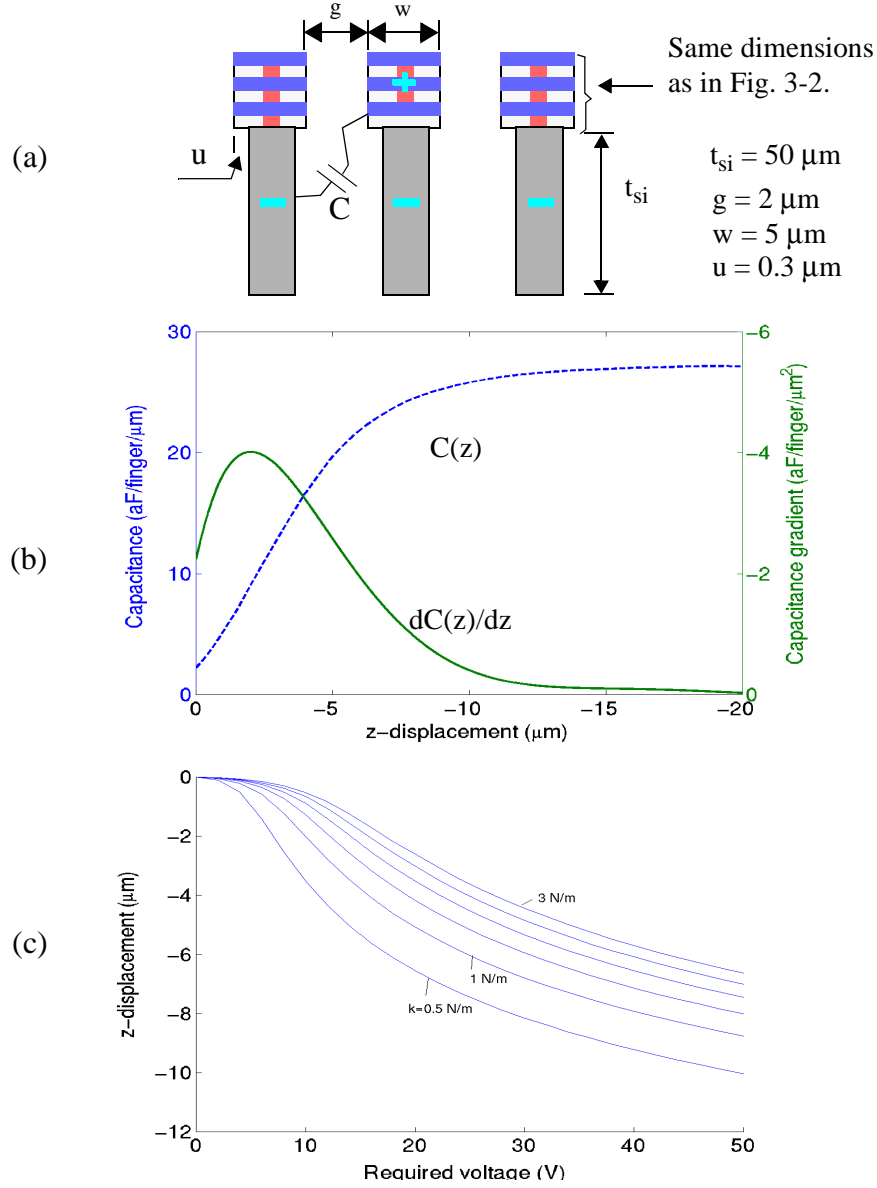
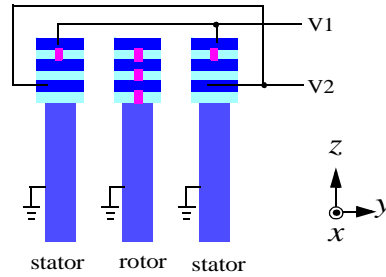


Figure 3-18: Z-axis electrostatic actuation. (a) Dimensions of a DRIE comb finger set. (b)  $C(z)$  and its gradient. (c) Displacement versus applied voltage.

and (b), respectively. On the other hand, if the CMOS layer in the rotor finger is electrically separated from the SCS layer that is electrically connected to the stator fingers as shown in Fig. 3-17(c), vertical actuation can be obtained. The sidewall capacitor  $C(z)$  is calculated by using the Maxwell 2D field simulator and the result is shown in Fig. 3-18(b).

*Figure 3-19: Combined x-axis/z-axis actuation principle.*



The dimensions of the DRIE comb finger set for the simulation is shown in Fig. 3-18(a). The gradient  $dC(z)/dz$  is always negative, so the rotor will move down ( $-z$ ) if a voltage is applied. By solving the force balance equation, *i.e.*, *elastic force = electrostatic force*, the static displacement vs the applied voltage is obtained as shown in Fig. 3-18(c) where one hundred 50- $\mu\text{m}$ -long comb fingers, a gap of 1.5  $\mu\text{m}$  and a undercut of 0.3  $\mu\text{m}$  are assumed. With this configuration, 5  $\mu\text{m}$  z-axis displacement can be achieved at 20 V driving voltage and 1 N/m spring constant.

It is also possible to construct a comb drive which can be used as either a lateral-axis actuator or vertical-axis actuator. The combined x-axis/z-axis actuator is shown in Fig. 3-19, where the stator fingers have two electrodes and the rotor fingers have one electrode. A z-axis force is generated when a voltage is applied to one stator electrode, with the other electrode grounded. A x-axis force is also generated on each finger. When the same voltage is applied to both electrodes in the stator fingers, the net electrostatic force only exists in the x-direction. However, there are two groups of comb fingers which are symmetric along the y-axis, so the x-axis forces can be cancelled out. By switching the voltage from one group of comb fingers to the other, a bi-directional motion control can be obtained in the x-direction.

### 3.3.2 Three-dimensional position sensing

Fig. 3-20 shows the cross-sectional views and wiring configurations of both lateral and vertical position sensing. For the lateral position sensing (Fig. 3-20(a)), the SCS layer and CMOS layer in each comb finger are electrically connected while the neighboring comb fingers are electrically separated. Thus, two capacitors  $C1$  and  $C2$  are formed. When the rotor finger moves horizontally,  $C1$  and  $C2$  change values oppositely. This results in a capacitive differential output as shown in Fig. 3-20(b). The advantage about this wiring configuration is that the normalized capacitance difference  $(C1-C2)/(C1+C2)$  does not change when the rotor finger moves in the  $z$ -direction (assuming the amplitude of the  $z$ -motion is much smaller than the gap, which is a typical case). Therefore, the cross-sensitivity is very low.

For the vertical position sensing, the SCS layer and the CMOS layer are electrically connected in the rotor finger but separated in the stator fingers, as shown in Fig. 3-20(c).

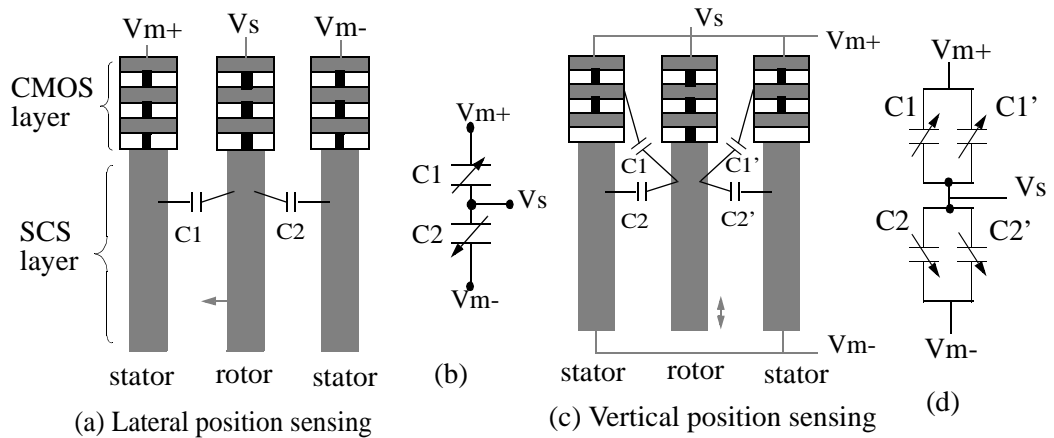
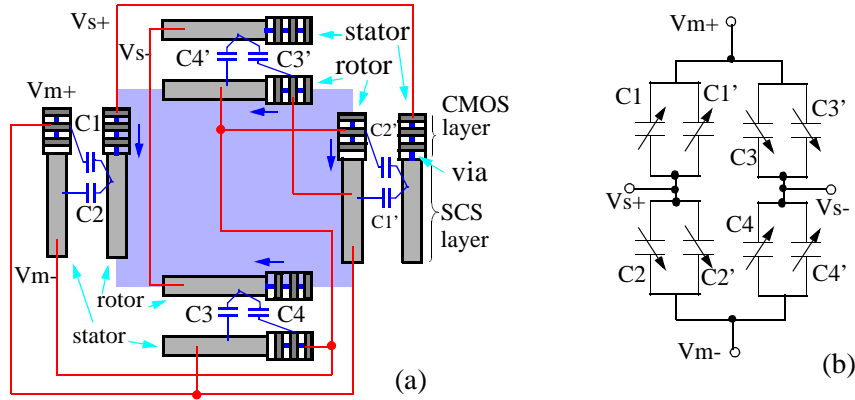


Figure 3-20: Cross-sections and wiring configurations of comb fingers for 3D vibration detection.



*Figure 3-21: Wiring configuration of the z-axis vibration sensor. (a) Comb finger arrangement and wiring. (b) Equivalent circuit.*

Four capacitors, i.e.,  $C_1$ ,  $C_1'$ ,  $C_2$ , and  $C_2'$ , are formed. The equivalent circuit is shown in Fig. 3-20(d). Again, a differential capacitive interface is constructed. Moreover,  $C_1 + C_1'$  and  $C_2 + C_2'$  are insensitive to the lateral motion (assuming the amplitude of this lateral motion is much smaller than the gap). But notice that  $C_1 + C_1'$  is not equal to  $C_2 + C_2'$  at the rest position. The main reason for this inequality is because the SCS layer is much thicker than the CMOS layer. The “T” shape cross-section due to the undercut also contributes to inequality of the capacitance. In order to make the two differential capacitors have the same value, the modulation signals are connected to the rotor fingers in two groups of comb fingers and to the stator fingers in the other two groups, as shown in Fig. 3-21(a). It is exactly the same vertical capacitance offset cancellation method introduced in Section 3.2.2.1. A fully differential capacitive bridge interface is then obtained as shown in Fig. 3-21(b) where  $C_1 + C_1' = C_2 + C_2' = C_3 + C_3' = C_4 + C_4'$  at the rest position.

### 3.3.3 DRIE z-axis accelerometer

The SEM shown in Fig. 3-22 is a released z-axis accelerometer consisting of z-compliant springs, a proof mass, comb fingers for z-axis motion sensing, and z-axis self-test comb-drive actuators. The principle of the z-axis motion sensing and actuation is described above. The z-compliant springs constitute only the CMOS interconnect layers where the underlying silicon is removed away by the undercut of the DRIE etching.

A Brüel & Kjær shaker table (Type 4808) and an HP4395A spectrum analyzer were used to characterize the micromechanical frequency response. The motional response measured at the output of the on-chip preamplifier is shown in Fig. 3-23(a). Vibration was excited by applying a 1 V peak-to-peak a.c. voltage to the integrated self-test z-axis actuators. The z-axis out-of-plane vibration mode, which is the primary mode, has a resonant frequency of 4.1 kHz and a mechanical quality-factor of 21. The quality factor is close to

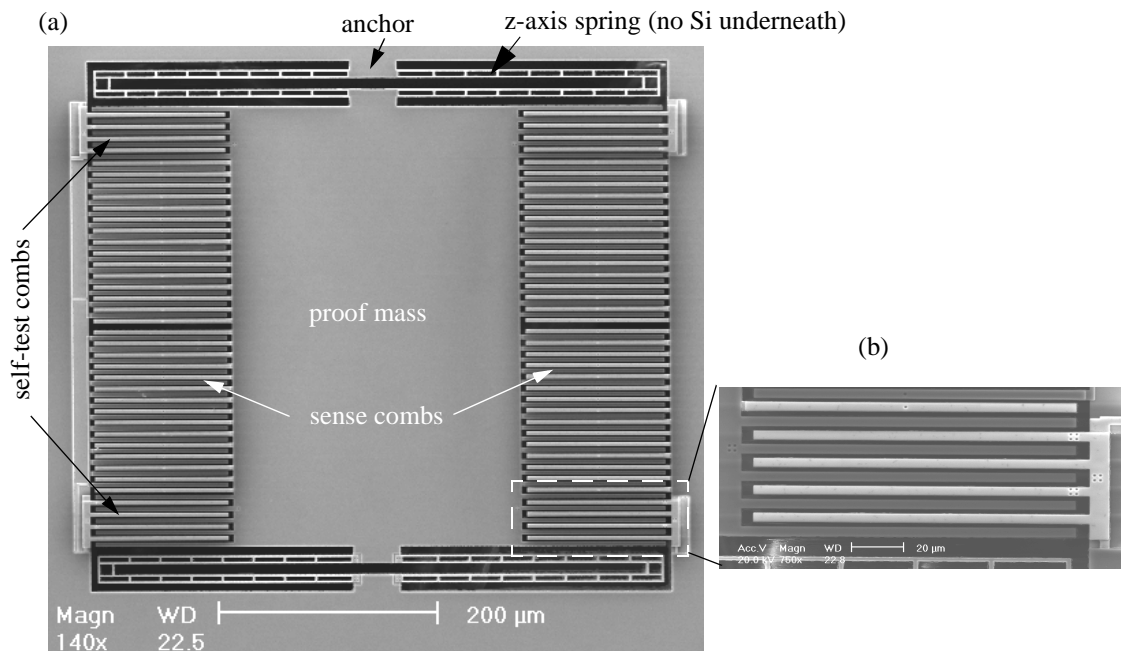
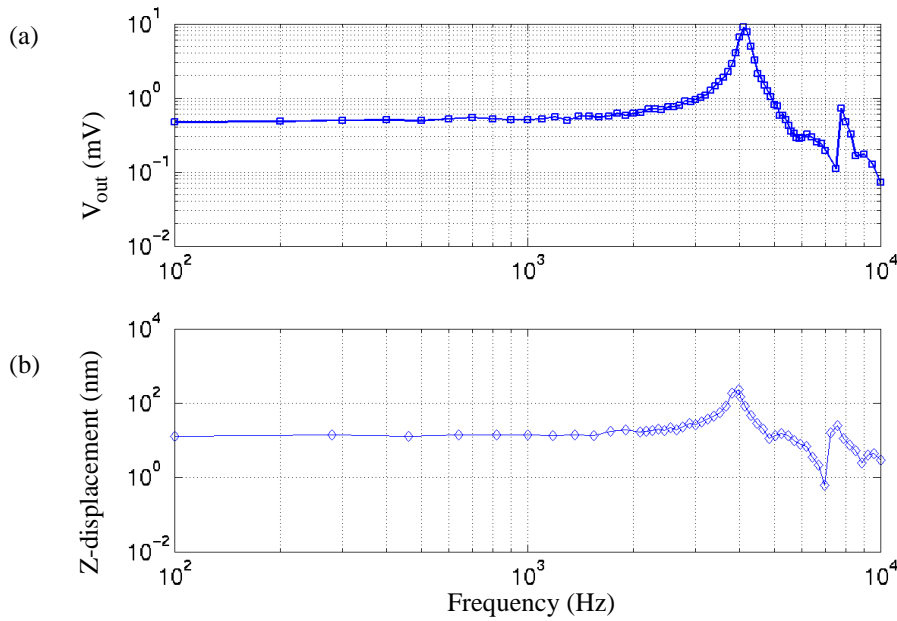


Figure 3-22: SEM of a DRIE z-axis accelerometer. (a) Full view. (b) Close-up.





*Figure 3-23: Frequency response of the DRIE z-axis accelerometer. (a) Frequency response measured at the output of the on-chip circuit. The vibration is excited by using the integrated self-test actuators. (b) Frequency response of the z-displacement, measured by using an MIT microvision system*

one order of magnitude higher than that observed from the thin-film z-axis accelerometers [15]. This is because the DRIE z-axis accelerometer has a larger mass, and has no substrate under the microstructure and therefore has no appreciable squeeze-film air damping. The out-of-plane torsional mode has a resonance frequency of 7.8 kHz. In order to verify the electrical measurement, the z-displacement of the proof mass was also measured optically by using an MIT microvision system [75]. The result is shown in Fig. 3-23(b) where a 1 V peak-to-peak a.c. voltage was applied. The z-axis and torsional modes have optically measured resonance frequencies of 3.9 kHz and 7.4 kHz, respectively. The design of the z-compliant spring sets the resonance frequency of the y-mode at three times the z-mode (12.3 kHz). In-plane modes were not observed when using the z-axis self-test actuator for excitation frequencies up to 10 kHz.

Both z-axis and torsional modes in the optical measurement have slightly lower resonance frequencies than those in the electrical measurement. This is caused by the electrical stiffness “hardening” effect of the z-axis comb drive. The cross-section of the z-axis comb finger set is shown in Fig. 3-24(a) and its dimensions are the same as given in Fig. 3-18(a).

If a voltage  $V$  is applied, a vertical force equal to  $\frac{1}{2} \frac{dC}{dz} V^2$  will be generated. Values of  $C$  and  $\frac{dC}{dz}$  as a function of  $z$  are extracted from finite-element analysis [73] and are given in Fig. 3-24(b) and (c). Near  $z = 0$ ,

$$\frac{dC}{dz} = 7.48 \times 10^{-9} - 4.05 \times 10^{-3} z \quad (3-4)$$

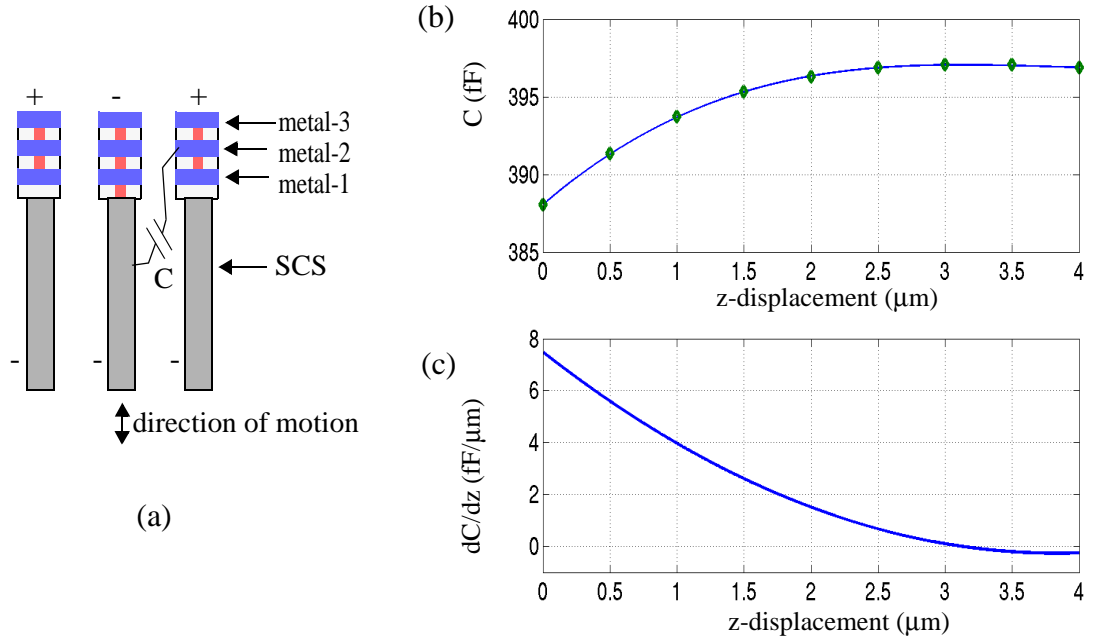


Figure 3-24: Simulation of the sidewall capacitance of the z-axis comb-drive actuator. (a) Cross-section of comb fingers. (b) Capacitance versus  $z$ -displacement (c) Capacitance gradient versus  $z$ -displacement. Number of drive comb-fingers = 16; length of drive comb fingers = 0.12 mm.

This value was calculated for 18 drive comb fingers, which is half of the total on the accelerometer. The spring stiffening force is included in the mechanical system response, *i.e.*,

$$m\ddot{z} + b\dot{z} + (k + 4.05 \times 10^{-3} V^2)z = 7.48 \times 10^{-9} V^2 \quad (3-5)$$

where  $m$  is the mass,  $b$  is the damping, and  $k$  is the mechanical spring constant of the system. Therefore, the resonant frequency of the system is equal to

$$\omega_r = \sqrt{\frac{k_{eff}}{m}} \equiv \sqrt{\frac{k}{m} \left( 1 + \frac{2.03 \times 10^{-3}}{k} V^2 \right)} = \omega_{r0} \left( 1 + \frac{2.03 \times 10^{-3}}{k} V^2 \right) \quad (3-6)$$

where  $\omega_{r0}$  is the purely mechanical resonant frequency of the system. The calculated and measured relationships between the resonant frequency and the d.c. bias voltage squared are shown in Fig. 3-25. The resonant frequency changes linearly with  $V^2$ , as predicted.

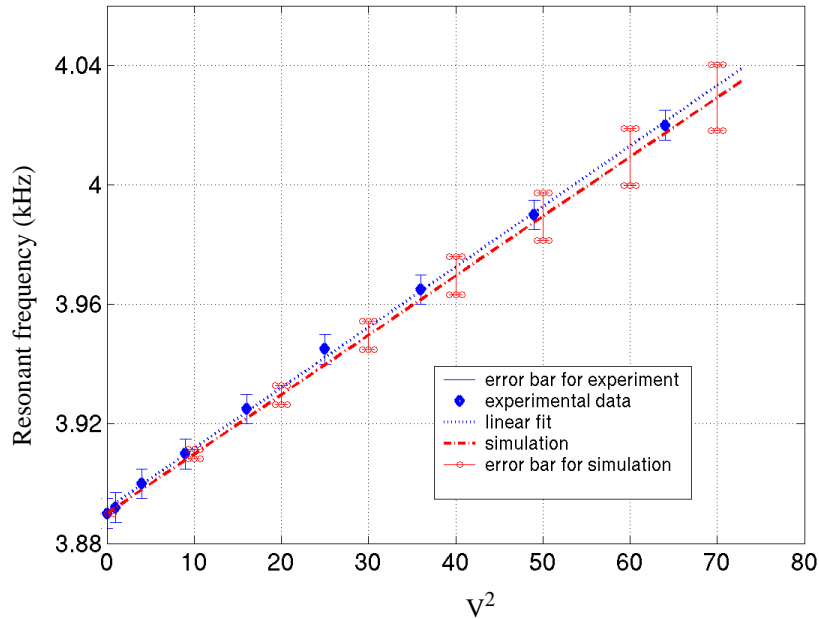


Figure 3-25: Vertical electrostatic spring “hardening” effect.

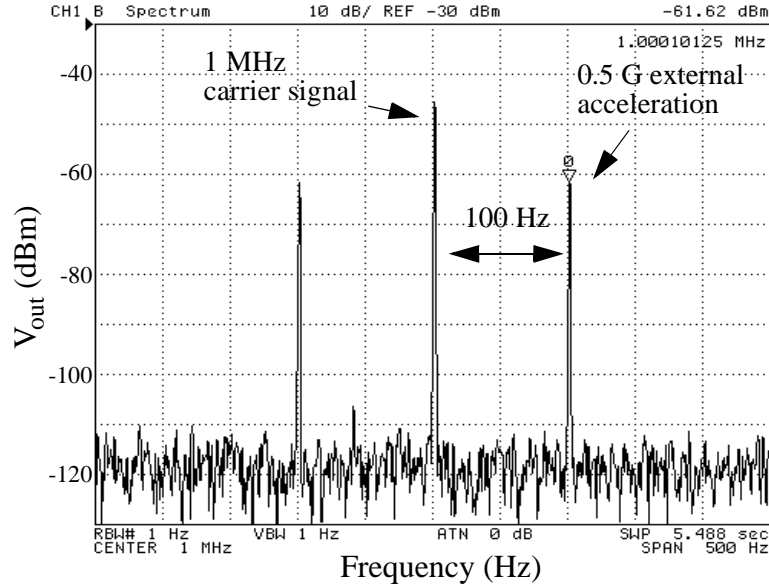


Figure 3-26: Spectrum of the output signal of the DRIE z-axis accelerometer with a 100 Hz 0.5 G input.

The spring constant in Eq. (3-6) is calculated as  $k = m\omega_{r0}^2$ . The slight difference between the calculated and measured curves is attributed to measurement uncertainty in the volume of the silicon proof mass.

The spectrum of the output signal is shown in Fig. 3-26 with a 0.5 G, 100 Hz external acceleration. The noise floor is  $1 \text{ mG/Hz}^{1/2}$ . Even though this noise floor is about five times lower than that measured in the thin-film z-axis accelerometers [15], it is still one-order of magnitude higher than the limit of the thermomechanical noise. The noise floor of the accelerometer will be greatly reduced after proper on-chip circuit design is achieved. No deterioration of the on-chip circuitry after the ASE etch was observed. Previous measurements of transistor threshold voltages in the related thin-film CMOS micromachining

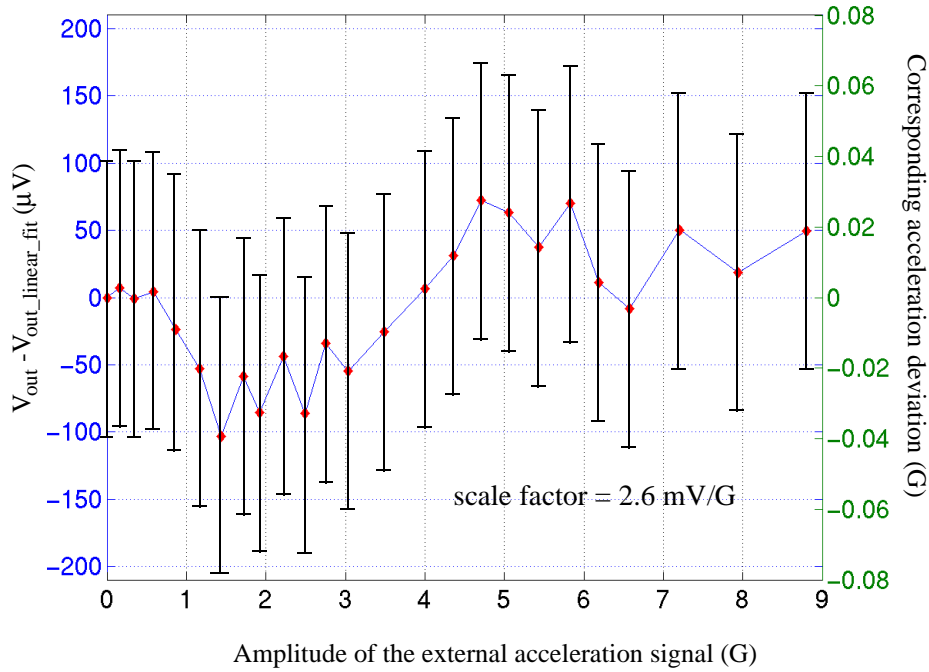


Figure 3-27: Response of the DRIE  $z$ -axis accelerometer to 100 Hz sinusoidal excitation. Error bars indicate the measurement uncertainty.

process showed no shift from the post-CMOS process steps [118]. Fig. 3-27 shows the nonlinear deviation of the dynamic response curve, measured with an 100 Hz sinusoidal acceleration signal excited by a shaker table. The device has a sensitivity of 2.6 mV/G and a linear response range of at least  $\pm 8.8$  G. Its linearity is within 0.5% of measured full scale (8.8 G).

## **Chapter 4**

# **CMOS-MEMS Micromirrors: Design, Fabrication and Application**

### **4.1 INTRODUCTION**

Based on the DRIE CMOS-MEMS process, two types of bulk Si micromirrors have been demonstrated: one is electrothermally actuated and the other one is electrostatically actuated. The electrothermal micromirror uses an Al/SiO<sub>2</sub> bimorph mesh with embedded polysilicon heater as the actuator. The electrostatic micromirror employs a novel curled comb drive. Unlike the commonly-used lateral comb drives, the stator and rotor comb fingers of the curled comb drive do not lie in the same plane, and therefore large electrically actuated displacement is achieved. The electrothermal micromirror has been installed in an endoscopic optical coherence tomography (OCT) imaging system [71].

In this chapter, first the principle, design, fabrication and characterization of the two micromirror designs are described. Then the micromirror-based endoscopic OCT imaging system is briefly introduced, followed by OCT imaging experiments of biological tissue.

### **4.2 Electrostatic SCS CMOS Micromirror**

The electrostatic micromirror employs a torsionally compliant flexure and an out-of-plane actuator for laser-beam scanning. Large out-of-plane actuation is achieved with a

curled comb drive. Torsional compliance is obtained by using a folded beam flexure instead of a torsional beam, which would increase the device size.

#### **4.2.1 Curled comb drive**

The metal-1 beam shown in Fig. 2-5(d) has only thin layers of interconnect aluminum and dielectrics. The beam curls up after it is released because of the residual stress and different coefficients of thermal expansion of the embedded materials [56]. Thus, a comb drive with the stationary and movable fingers at different levels, *i.e.*, a curled comb drive, can be created. The concept of the curled-up comb drive is illustrated in Fig. 4-1. The comb drive has two parts: a set of tilted comb-fingers and a set of flat comb-fingers. The tilted comb-fingers are composed of a curled metal-1 mesh and an array of tilted comb fingers with a thick SCS layer. The silicon substrate underneath the metal-1 mesh is completely undercut during the deep Si etch because the metal-1 mesh consists of only narrow beams. Therefore, the SCS chunks under the tilted comb fingers are electrically isolated from the silicon substrate. The SCS chunks then can be wired to any place on the chip,

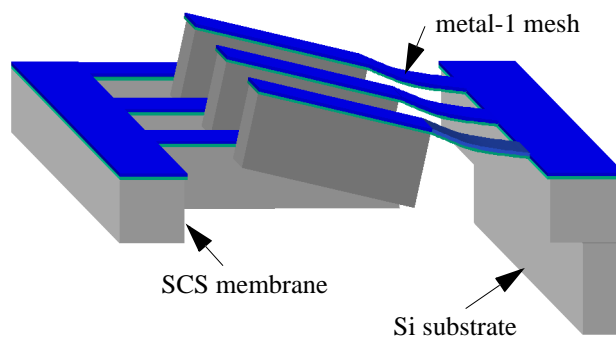


*Figure 4-1: Schematic of a curled-up comb drive.*

*e.g.*, a bonding pad. When a voltage is applied to the comb drive, the tilted comb-fingers will tend to align with the flat comb-fingers or vice versa and thus a rotation is generated. The tilt angle of the curled comb-fingers depends on the length of the metal-1 mesh and can be  $45^\circ$  or even larger. So large rotation angle can be expected.

#### **4.2.2 Torsional Spring Design**

A torsional beam is simple and robust, but the utilization efficiency of chip area is low. If a folded beam flexure is used, the z-axis compliance as well as the out-of-plane compliance is obtained. However, it has been found that a curled, folded beam flexure significantly lowers the resonant frequency ratio of the primary rotational mode over the z-axis mode [21]. Using the same technique for generating vertical curling as the curled comb drive discussed above, a curled, folded torsional spring design is shown in Fig. 4-2. The curled flexure is thin (about  $1.8\ \mu\text{m}$  thick), the curling increase the stiffness in the z-direction but decreases the torsional stiffness along the y-direction. More detail about this curled flexure is discussed in Section 6.1.2.

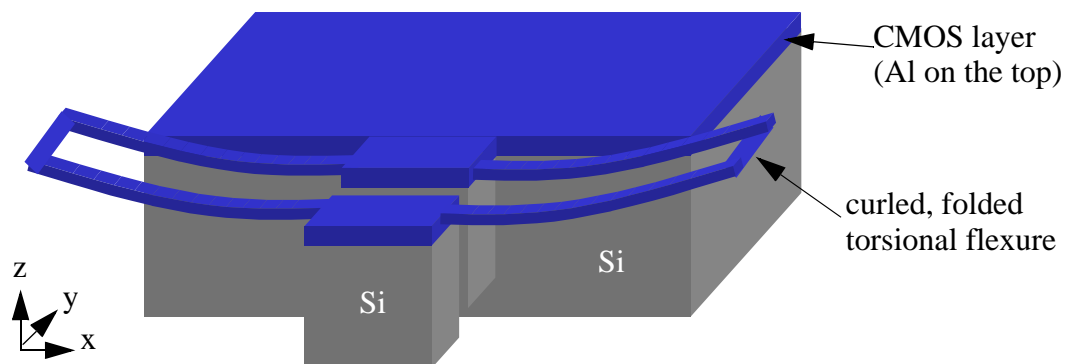


*Figure 4-2: Schematic of a folded torsional spring design.*



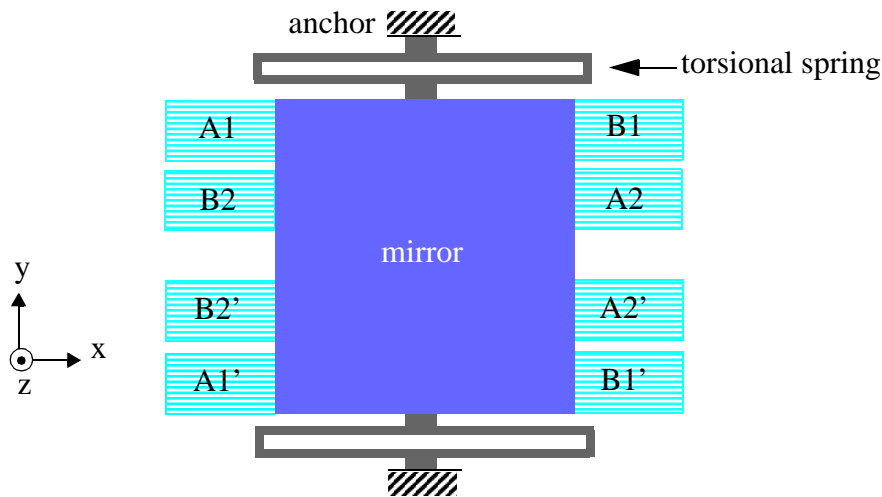


Figure 4-3: Electrostatic micromirror topology.

#### 4.2.3 SCS Electrostatic Micromirror Design

The top view of the micromirror design is illustrated in Fig. 4-3. Fig. 4-1 shows a curled comb drive with the curled comb fingers anchored on the substrate. The flat comb fingers can also be anchored. The comb drives with anchor on the curled side and flat side are denoted in Fig. 4-3 as “**A**” and “**B**”, respectively. The **A** comb drives pull the mirror up, and the **B** comb drives pull the mirror down. The comb drives are distributed on both sides of the mirror to obtain bi-directional rotation. The two sets of each comb drive double the y-axis torque and zero the net z-axis force. The comb drives **A1/B1** rotate the mirror clockwise, and **A2/B2** rotate the mirror counterclockwise.

#### 4.2.4 Fabricated Electrostatic Micromirror

The device is fabricated in the Agilent 3-metal 0.5  $\mu\text{m}$  CMOS process followed by the DRIE CMOS-MEMS micromachining process. The top view of a released device is

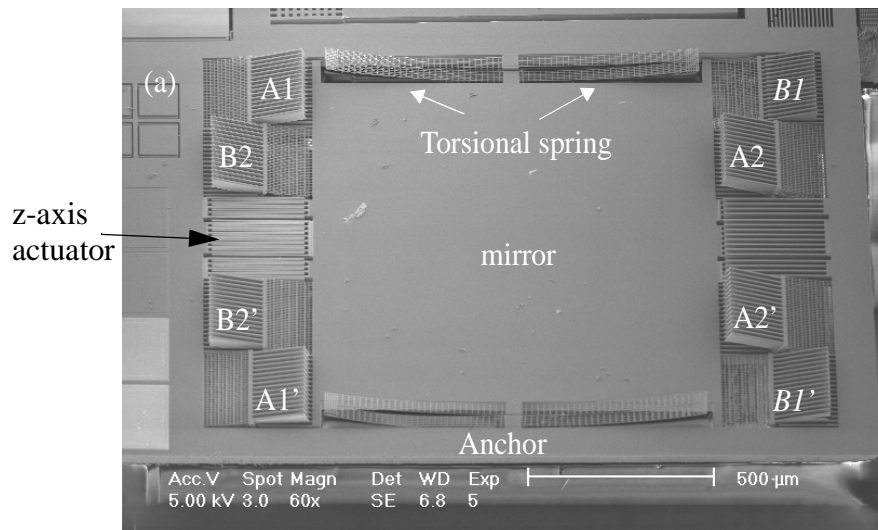


Figure 4-4: Top view of the released electrostatic micromirror.

shown in Fig. 4-4. The mirror is 1mm by 1mm in size. A z-axis actuator is also included to cancel residual z-axis force, if needed.

A view of a curled comb is shown in Fig. 4-5. The lengths of the metal-1 mesh and the SCS fingers are 120  $\mu\text{m}$  and 150  $\mu\text{m}$ , respectively. The thickness of the SCS chunks is

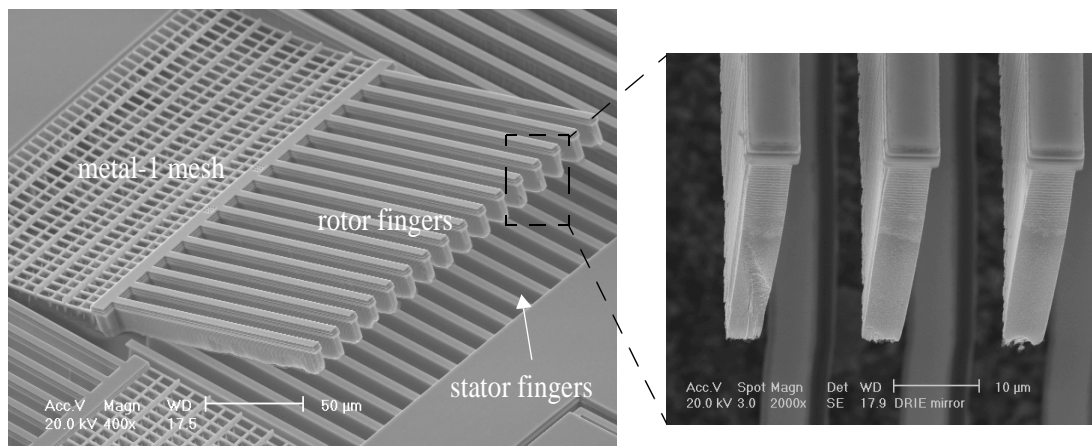
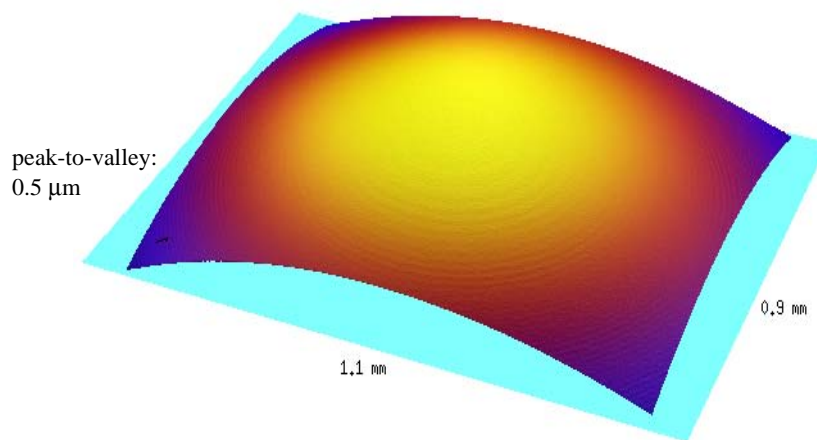


Figure 4-5: SEMs of a curled up comb drive.

about 40  $\mu\text{m}$ . A close-up of the comb finger ends is also shown in Fig. 4-5. A small initial undercut is used to assure the complete undercut of silicon underneath the metal-1 meshes and z-compliant springs. To further guarantee the electrical isolation of the silicon chunks, an n-doped well (with p-substrate) is placed underneath the metal-1 meshes and z-compliant springs as discussed in Section 2.2.2. The electrical isolation was achieved on all 10 tested devices.

#### 4.2.4.1 Characterization

The profile of the mirror surface was characterized by using a Wyko NT2000 3D Optical Profiler [76]. The measured peak-to-valley curling across the entire mirror is 0.5  $\mu\text{m}$  (Fig. 4-6), which converts to a radius of curvature of 50 mm. This curling can be reduced simply by increasing the thickness of the SCS layer. Stripping off field oxide should also reduce the combined residual stress in the top metal/oxide layer.



*Figure 4-6: Contour plot of the electrostatic mirror profile.*

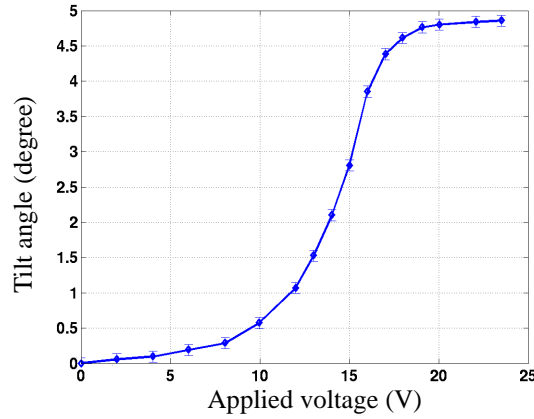


Figure 4-7: The mirror rotation angle versus applied voltage.

Both static and dynamic responses of the device have been tested. Fig. 4-7 shows the rotation angle versus the applied voltage. By applying 18 V, a tilt of  $4.7^\circ$  can be obtained. Since the width of the entire device is 1.5 mm, the z-displacement at the comb-finger tips is  $62\text{ }\mu\text{m}$ . The center plate can rotate to both sides and therefore a total rotation angle of  $9.4^\circ$  can be achieved. The rotation angle saturates above 20 V. The frequency response, measured by using an optical microvision system [75], is plotted in Fig. 4-8. The resonant

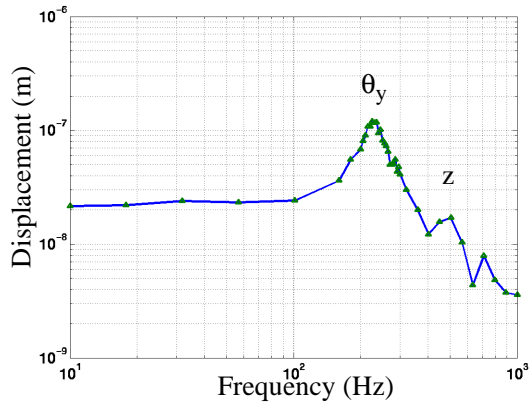


Figure 4-8: Frequency response measured by using an optical microvision system.

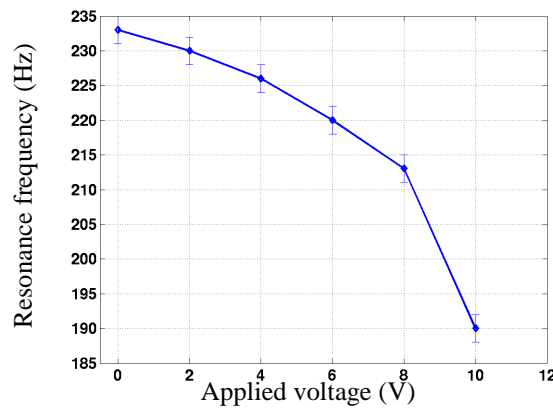


Figure 4-9: Electrostatic spring “softening” effect.

frequency is 233 Hz. The z-axis resonant mode is 500 Hz, which is twice as much as the torsional mode. An electrostatic spring “softening” effect is also observed in this vertical comb drive, as shown in Fig. 4-9.

#### 4.2.4.2 Summary and future work of the electrostatic micromirror

A large, flat micromirror with large out-of-plane actuation has been experimentally demonstrated. A maximum  $9.4^\circ$  rotation angle of a 1 mm by 1 mm mirror with a resonant frequency of 233 Hz was achieved from an initial design. The mirror topology can be optimized for larger rotation angle or larger size. For example, by simply moving the curled comb drives from the two sides to the two ends and closer to the central axis (see Fig. 4-20), even larger rotation angle can be achieved. This type of micromirror has potential applications in optical switches, optical scanners, interferometric systems and medical imaging.

### 4.3 Electrothermal Micromirror

Multilayer metal/silicon oxide beams with an embedded polysilicon heater have been used to tune the resonant frequency of a gyroscope's drive mode (see Section 6.1.2). Similar to the thermally actuated micromirror reported in [77], the beams bend down when a current is applied to the polysilicon heater. Using the same concept and combining the DRIE CMOS-MEMS process introduced in Section 2.2, a bulk-Si micromirror can be actuated electro-thermally to a large rotation angle. In this section, the operational principle and mirror design are introduced first, followed by the characterization results of the micromirror flatness and laser scanning static response.

#### 4.3.1 Mirror Design

The schematic of the mirror design is shown in Fig. 4-10. The mirror is attached to a bi-layer aluminum/silicon dioxide mesh with polysilicon encapsulated within the silicon dioxide to form a bimorph thermal actuator. The mesh curls up after being released due to

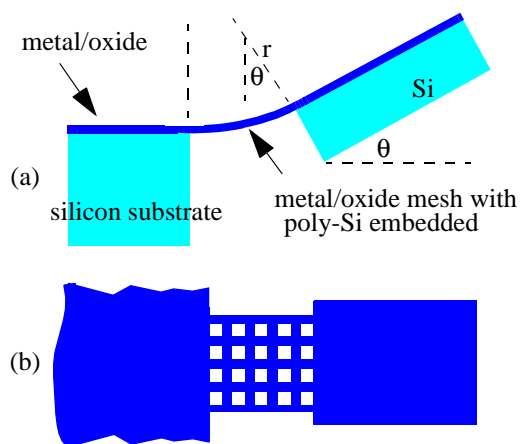


Figure 4-10: The thermal micromirror conceptual design.  
(a). Cross-sectional view; and (b) top view.

the tensile stress in the aluminum layer and compressive residual stress in the bottom silicon dioxide layer. Therefore, the radius of curvature of a bimorph beam is determined by both the initial curling and the temperature change from the polysilicon heating, and is given by  $\frac{1}{r} = \frac{1}{R_0} - \frac{1}{r_T}$ , where  $r$  is the actual radius of curvature,  $R_0$  is the initial radius of curvature and  $r_T$  is the radius of curvature due to the temperature change. By ignoring the thin polysilicon layer,  $r_T$  is readily derived as [119]

$$r_T = \frac{2}{3} \cdot \frac{t_1^2 + t_2^2 + \frac{3}{2}t_1t_2 + \frac{1}{4}\left(\frac{E_1t_1^3}{E_2t_2} + \frac{E_2t_2^3}{E_1t_1}\right)}{\Delta T(\alpha_1 - \alpha_2)(t_1 - t_2)} \quad (1)$$

where  $t_i$ ,  $E_i$  and  $\alpha_i$  are the thickness, Young's modulus and thermal expansion coefficients of the metal layer ( $i=1$ ) and the oxide layer ( $i=2$ ), and  $\Delta T$  is the temperature change on the beam.  $R_0$  is a fixed value for a given process. For instance, the radius of curvature of micromechanical beams made of metal/oxide layers in the Agilent 0.5  $\mu\text{m}$  3-metal CMOS process was measured to be 290  $\mu\text{m}$  [56].

A bulk silicon mirror coated with metal and dielectrics is attached at the end of the mesh. The tilt of the mirror follows the curvature of the mesh, and is given by  $\theta = \frac{L}{r}$ , where  $L$  is the length of the mesh. The choice of  $L$  depends on the requirements for speed and power consumption, and rigidity of the mirror assembly.

Fig. 4-11(a) shows a scanning electron micrograph (SEM) of a fabricated micromirror. The mirror tilts  $17^\circ$  at room temperature. Fig. 4-11(b) is the cross-sectional view at the

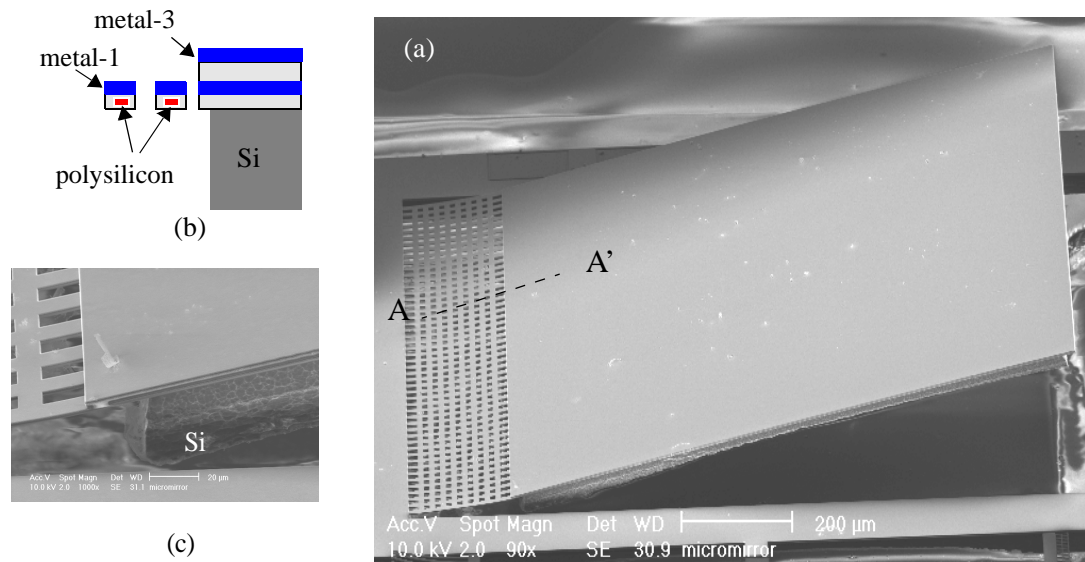


Figure 4-11: SEMs of a released thermal micromirror: (a) side view; (b) cross-section of A-A'; and (c) close-up of one corner.

joint of the bimorph mesh to the movable mirror, in which the polysilicon heater is clearly shown. Fig. 4-11(c) is a close-up of one corner of the mirror showing the supporting 40 μm-thick bulk silicon underneath the mirror Al surface.

#### 4.3.1.1 Characterization

The structural SCS layer backing the mirror provides very good flatness across the 1 mm surface. The mirror has the same surface profile as shown in Fig. 4-6. The mirror can be even flatter if the SCS membrane is made thicker during the backside etch step (Fig. 2-5(d)).

Fig. 4-12 shows the measured rotation angle changes with different heater currents of two different micromirrors. When the applied current increases, the mirror rotates downward. The resistance of the heater is 2.4 kΩ. The maximum current the polysilicon heater



can carry before thermal damage occurs is 18 mA. The two curves in each plot correspond to the increasing and decreasing currents, respectively. Note that the backward curve shifts slightly to the left of the forward curve. This hysteresis is due to thermal relaxation.

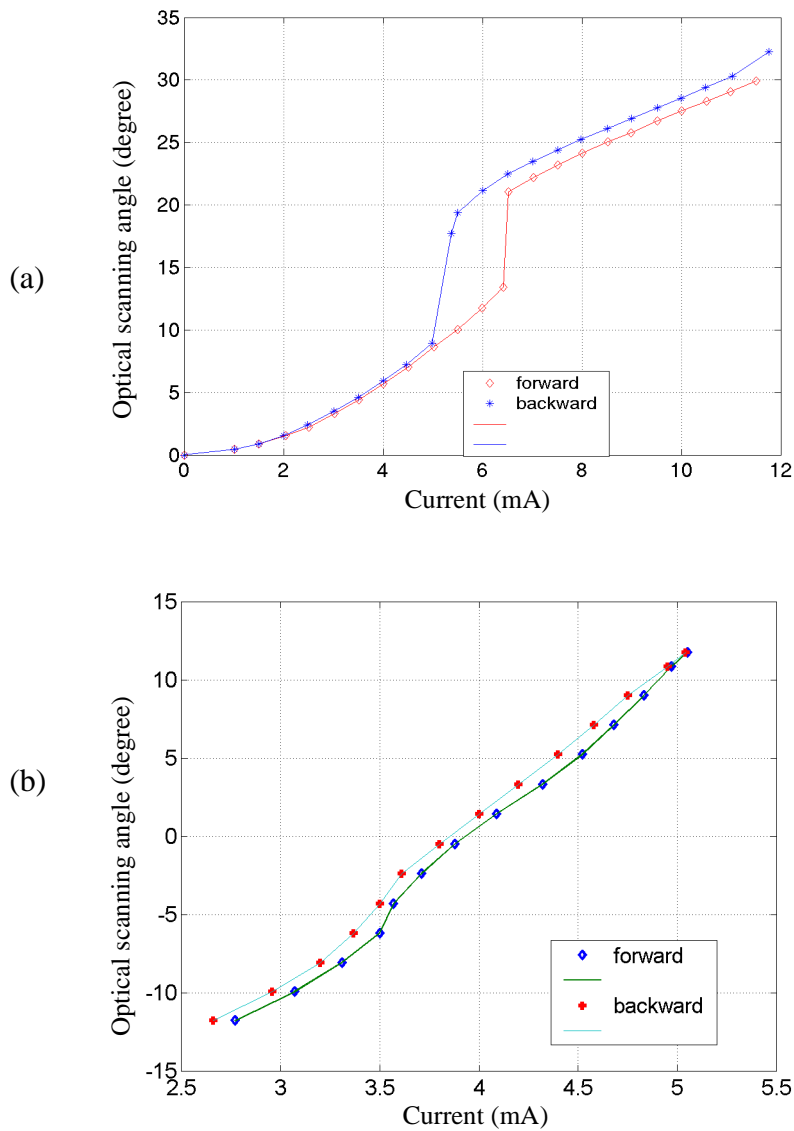


*Figure 4-12: Optical scanning angle versus applied current. (a) Mirror with jump angle scanning. (b) Mirror with smooth scanning.*

Also note that both of the curves in Fig. 4-12(a) have a discontinuity, i.e., the mirror jumps at certain applied current. In order to understand why this jump occurs, a white-light profilometer (Wyko NT2000) was employed to measure the surface profile of the bimorph actuation mesh before and after the jump. The measured results are shown in Fig. 4-13. The mesh curls uniformly before the jump (Fig. 4-13(a)), but the mesh becomes

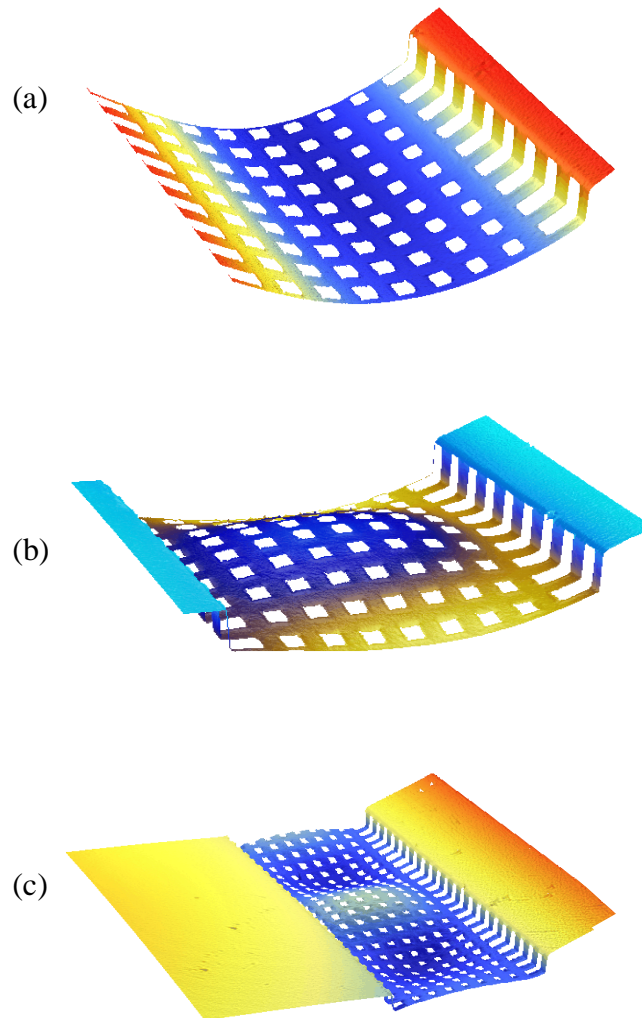


*Figure 4-13: Profile of the bimorph actuation mesh before and after the jump. (a) Before jump; (b) after jump; and (c) wider view after jump.*

buckled instantly when the jump happens (Fig. 4-13(b)). A wider view of the mesh right after the jump is shown in Fig. 4-13(c).

On the other hand, scanning without jump was also observed as shown in Fig. 4-12(b). This smooth scanning is believed to be due to the stress release caused by nano-scale crack development in the bimorph mesh or relatively high temperature annealing. Research is still ongoing to find out how to fabricate smooth scanning micromirrors with high yield.

A comprehensive reliability test of the micromirror has not been undertaken. However, one micromirror has been continuously working at a 2 Hz scan rate for more than 12 months, or 55 million cycles. No significant degradation or aging is observed. The resonant frequency of the mirror is 165 Hz, which exceeds the scanning speed requirement of 100 Hz for most endoscopic applications.

## **4.3.2 Optical Coherence Tomography Application**

### **4.3.2.1 Introduction**

Optical coherence tomography (OCT) is a newly developed optical imaging technique that permits high-resolution cross-sectional imaging of highly scattering media [32][33]. OCT is based on optical coherence-domain reflectometry, which utilizes broadband light and interferometry to detect the path length distribution of echoes of light from reflective interfaces. Two- and three-dimensional images can be obtained by combination of OCDR measurements (i.e., longitudinal scans) with sequential transverse scans. Since its first introduction to imaging the transparent and low-scattering tissue of eyes [32], OCT has

become attractive for noninvasive medical imaging because it has been demonstrated [33][34] that the internal morphological and cellular structures in the biological tissue are displayed by the spatially resolved map of the reflected light in an OCT image with high spatial resolution (e.g., 10 $\mu$ m) and sensitivity (e.g., >100dB). OCT imaging of a wide variety of biological tissue has been reported [33]-[37], including eye, skin, tooth, gastrointestinal tracts, respiratory tracts, genitourinary tracts, and their malformations. Recent technological advances include near real-time or real-time OCT[33][37], ultra-high-resolution subcellular OCT [38], dual-wavelength and spectral OCT [36][39], polarization OCT and Doppler OCT to provide enhanced image contrast and diagnostic specificity [40][41]. Endoscopic OCT devices for *in vivo* imaging of internal organs have been reported, in which transverse scanning was performed either by a rotary fiber-optic joint connected to a 90° deflecting micro prism (in a circumferential pattern) [33][37] or by a small galvanometric plate swinging the distal fiber tip (in a line-scan pattern) [35]. Nevertheless, development of high-performance, reliable and low-cost OCT catheters and endoscopes suitable for future clinical applications still remains desirable.

#### **4.3.2.2 MEMS Mirror-based OCT Endoscope**

The electrothermal micromirror shown in Fig. 4-11 has been installed in a new endoscopic OCT system to achieve high-speed transverse light scanning imaging in a slender endoscopic tube (5 mm inner diameter) and maintain high light coupling efficiency and spatial resolution. The OCT system work was performed in collaboration with Yingtian Pan of the University of Pittsburgh who performed the endoscope system construction and

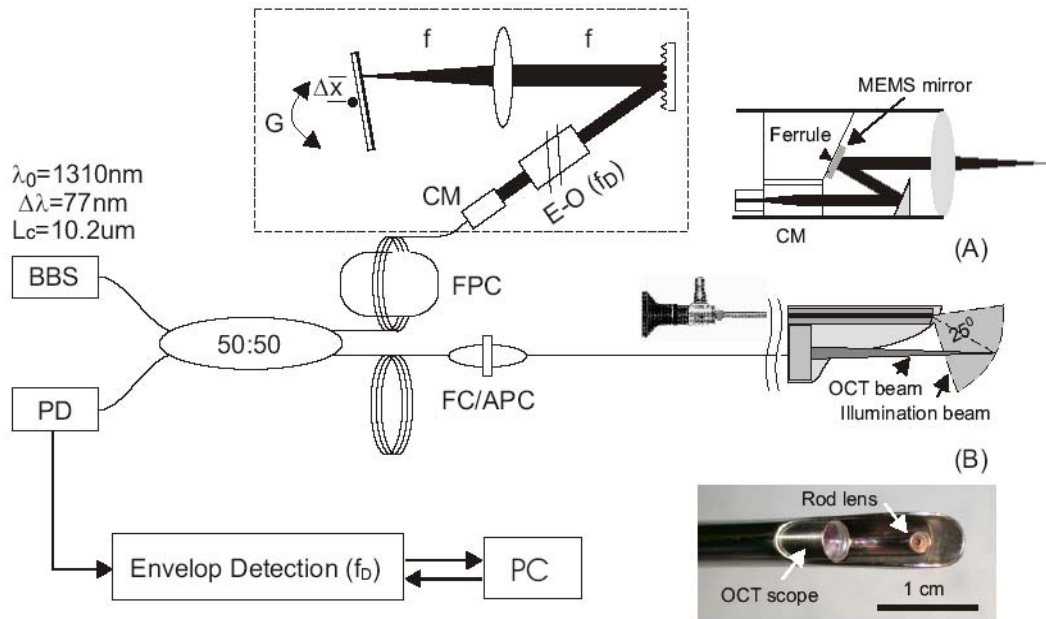


Figure 4-14: A schematic of the endoscopic OCT system. Insets A, B are a schematic of the optical arrangement and a photograph in the distal OCT scope. BBS: broadband source, PD: photodiode, CM: fiber-optic collimator, E-O: electro-optical phase modulator, FPC: fiber optic polarization controller, G: galvanometric mirror.

testing. A MEMS mirror is used to facilitate endoscopic beam steering because of its small size, potentially low cost and excellent micro beam manipulating capacity. A schematic of the endoscopic OCT system is depicted in Fig. 4-14. A high-brightness, broadband light source (AFC Technologies, Inc.) is coupled into a fiber optic Michelson interferometer. The pigtailed output power  $P$  of the light source is 12 mW, the central wavelength  $\lambda_0$  is 1320 nm and FWHM (Full Width - Half Maximum) spectral bandwidth  $\Delta\lambda$  is 77 nm. The input light beam is equally divided into two arms of the Michelson interferometer (50%:50%). In the reference arm of the fiber optic interferometer, a fiber polarization controller (FPC) is used to ensure that the polarization of light exiting the non-PM (Polariza-

tion Maintaining) fiber (SMF-28) is almost linearly polarized. The light from the fiber endface is coupled into a  $\phi 2$  mm collimated beam by an angle-polished GRIN lens as the collimator (CM) and then guided to the high-speed depth scanning unit containing an electro-optical phase modulator (E-O) and a rapid-scanning grating-lens-based optical delay line to implement OCT imaging in real time.

The principle of a grating-lens-based optical delay line has been previously outlined [33][42]. The temporal profile of a broadband light is linearly distributed at the Fourier focal plane of a grating-lens pair, thus placing a mirror at the focal plane and titling it rapidly with a galvanometer allows fast group delay. Furthermore, this method permits phase and group delays to be independently managed. In the previously reported arrangements, the phase shift was controlled by adjusting the offset  $x_0$  of the tilting mirror which resulted in increased mirror size and in turn restricted the speed of the depth scanning. To overcome this technical limitation, the galvo mirror ( $x_0 = 0$ ) is centered and an electro-optic phase modulator is inserted to generate a higher and more stable Doppler frequency shift for heterodyne detection. By carefully choosing the parameters of each component (e.g.,  $f = 80$  mm/ $\phi 35$  mm for the scan lens,  $g = 450$  lines/mm for the diffraction grating, 4 mm VM500 galvanometric mirror tilted at  $4.2^\circ$  and with 1.2 kHz repetition rate, and 2.4 MHz resonant E-O phase modulation), the high-speed depth scanner allows the acquisition of 2.4 K axial scans per second with an optical delay window of 2.8 mm (higher path length delay is possible by increasing the tilting angle). The high and stable Doppler frequency shift results in increased signal to noise performance of the signal processing electronics. Moreover, the dispersion induced by unbalanced fiber lengths and

optical components between two arms of the Michelson interferometer can be minimized by slightly moving the grating along the optical axis, which can greatly enhance the axial resolution as has been observed during the alignment.

The fiber end in the sample arm of the interferometer is connected to a pigtailed OCT scope through a modified FC/APC connector, which can be inserted into the  $\phi 4$  mm instrument channel of a 22 Fr endoscope. The inset A is a schematic of the optical arrangement in the distal OCT scope, and inset B is the photograph of an OCT scope. The light from the fiber is coupled by a 0.25-pitch solfege lens to a  $\phi 0.8$  mm collimated beam, deflected by a pair of mirrors and then focused by a laser doublet (f10 mm/ $\phi 5$  mm) to a roughly  $\phi 20$   $\mu$ m spot size on the image plane. The transverse light scanning in the OCT scope is facilitated by the thermal mirror shown in Fig. 4-11.

Since the thermal mirror has a  $17^\circ$  initial bending angle, the ferrule housing the mirror has to be tilted to roughly  $17^\circ/2$  to maintain the reflected beam to the center of the optical axis. The results on a test stage show that the mechanical scan angle is on the order of  $\pm 8^\circ$ , yielding a  $\pm 15^\circ$  optical scan angle for beam steering. However, due to improper angular setting of the ferrule endface in our initial packaging, the deflected beam deviates from the optical axis and the tested maximal scan range is 2.9 mm when a  $f = 10$  mm scan lens is used. The detected interferometric signal is pre-amplified by a low-noise, broadband transimpedance amplifier (Femto HCA-10M-100K), bandpass filtered and demodulated prior to being digitized by a 5 MHz, 12 bit A/D converter. Both depth scan and lateral MEMS scan are synchronized with the image data acquisition via two 16-bit D/A channels.

### 4.3.3 Experimental Results

To demonstrate the ability of MEMS mirrors for endoscopic light scanning imaging, a glass slide was imaged to verify the field flatness and biological tissues *in vivo* to show the image fidelity. Fig. 4-15 is an OCT image of the border of a 225  $\mu\text{m}$  thick cover slide stacked on a 1 mm thick glass plate. The 500 $\times$ 1000 pixel cross-section covering an area of 2.9 $\times$ 2.8 mm<sup>2</sup> was acquired at ~5 frames/s. The shift of the glass2 in the image is caused by the refractive index difference between air and the glass. The results demonstrate the field flatness of the endoscopic OCT system using a MEMS mirror for light steering in the lateral direction.

Fig. 4-16 is an OCT image of a porcine urinary bladder *in vivo*. Although the image fidelity (e.g., signal to noise ratio and imaging depth) is slightly lower than that obtained

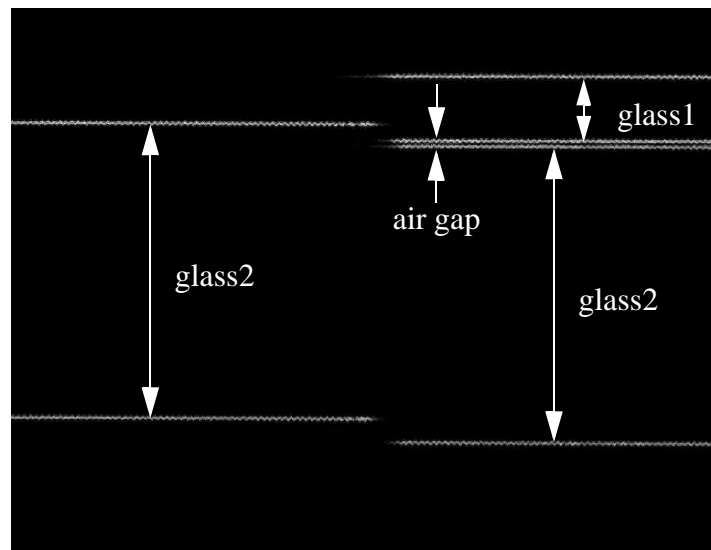
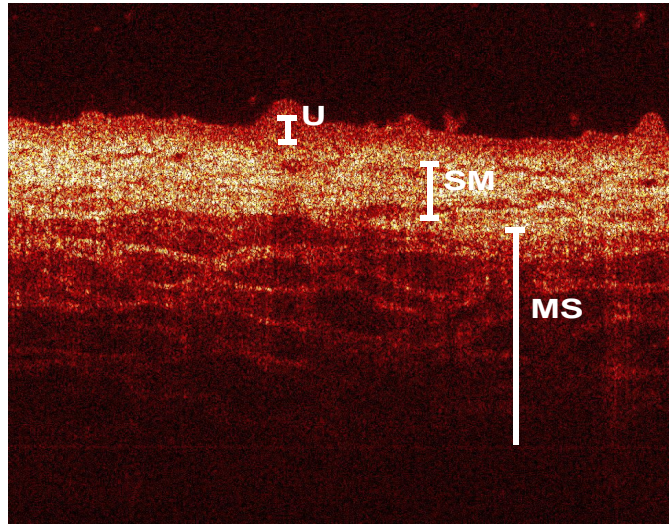


Figure 4-15: 2-D OCT of 2 stacked microscope glass slides with thickness of 225  $\mu\text{m}$  and 1 mm, respectively. Image size: 500 $\times$ 1000 pixels.





*Figure 4-16: In vivo 2-D endoscopic OCT of porcine bladder through cystotomy. U: urothelium, SM: submucosa, MS: muscularis layer. Image size:  $500 \times 1000$  pixels covering an area of  $2.9 \times 2.8 \text{ mm}^2$ .*

by our non-endoscopic OCT system [36] possibly because of higher coupling loss ( $>3$  dB) in the OCT scope, micro morphological details of the bladder wall, e.g., the urothelium (U) or epithelium, submucosa (SM) and the upper muscularis layer are readily delineated. Because most transitional cell carcinomas originate in the urothelium, the results demonstrate the potential of MEMS-based endoscopic OCT for early detection and staging of bladder cancers. Also, as a wide variety of inner organs (e.g., cervix, colon, joints) can be accessed and imaged by front-view endoscopic OCT, the results suggest the potential applications of this technique for noninvasive or minimally invasive imaging diagnosis in these tissues.

In summary, a novel front-view OCT endoscope based on a thermal CMOS-MEMS mirror for endoscopic light steering to achieve biomedical imaging at transverse and axial resolutions of roughly  $20 \mu\text{m}$  and  $10 \mu\text{m}$ , respectively, has been demonstrated. Cross-sec-

tional images of  $500 \times 1000$  pixels covering an area of  $2.9 \times 2.8 \text{ mm}^2$  can be acquired at  $\sim 5$  frames/s and with close to 100 dB dynamic range. It should be noted that a large ( $\phi 5 \text{ mm}$ ) OCT scope was chosen to fully use the internal clearance of a 22 Fr endoscope. Smaller OCT scopes can be developed to accommodate various types of endoscopes. Further technical improvement includes enhancing system signal to noise performance by increasing coupling efficiency in the endoscopic alignment and minimizing the dark-current noise induced by residual light of the resonant E-O modulator (broadband E-O modulation preferred). Also, the large-actuation electrostatic MEMS mirrors will reduce the thermal drift and improve light steering linearity.

#### 4.4 Other Fabricated Micro-optical Components

A  $6 \times 6$  array of thermal micromirrors is fabricated, as shown in Fig. 4-17. Each mirror is  $60 \text{ mm}$  by  $60 \text{ mm}$ . There is a  $40 \text{ mm}$ -thick silicon layer underneath the mirrors. The actuation is provided by the thin-film suspension that has a polysilicon heater embedded.

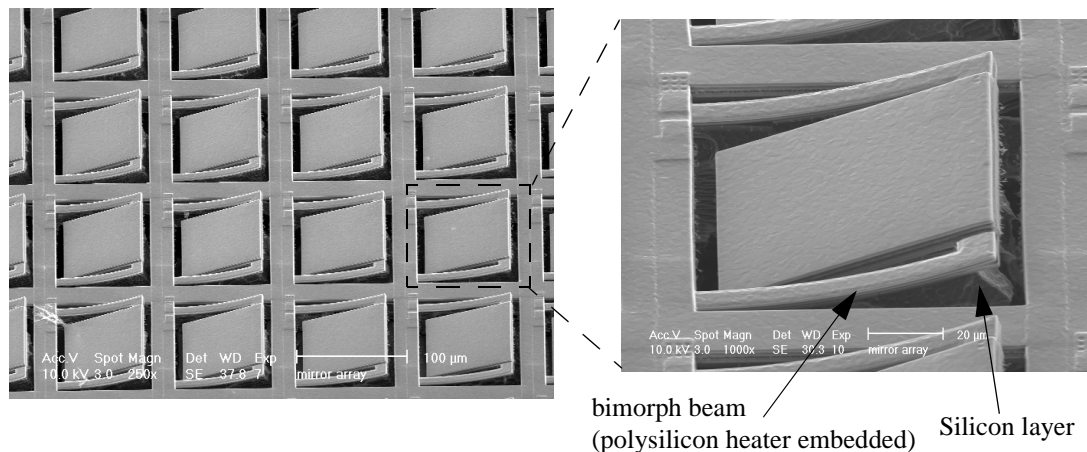
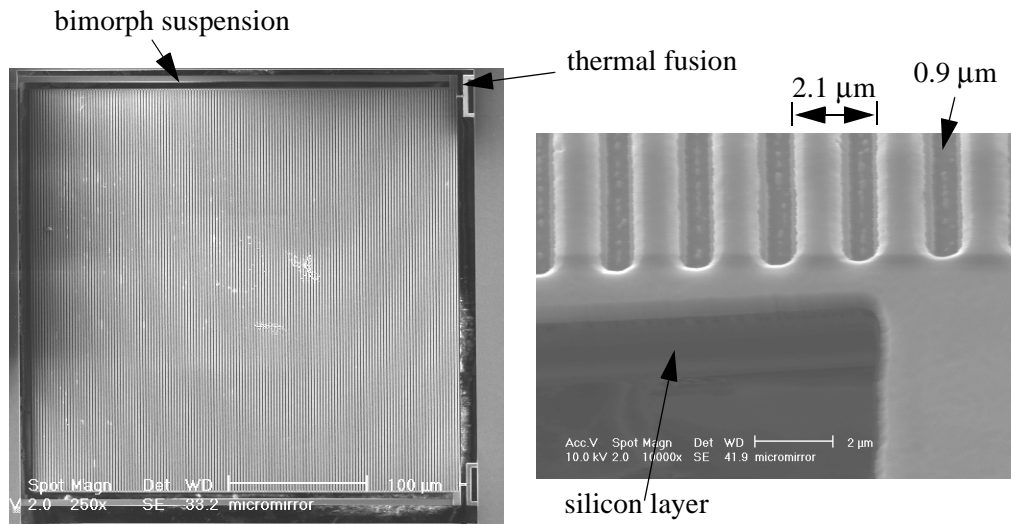


Figure 4-17: Micromirror array. Mirror size:  $60 \text{ μm} \times 60 \text{ μm}$ .



*Figure 4-18: A micro-grating made of metal-1 and metal-2 layers.*

A micro-grating is also fabricated, as shown in Fig. 4-18. The pitch of the grating is  $2.1\ \mu\text{m}$ . The grating is suspended by two Al/oxide beams with polysilicon heaters integrated. The grating has a  $40\ \mu\text{m}$ -thick silicon underneath. A thermal fuse [78] is used to hold the grating during the release process. After the release, the fuse can be burned to free the grating by applying a current to the integrated polysilicon heater. Then the grating can be tuned by applying a current to the integrated heater inside the Al/oxide suspension.

## **4.5 A New Electrostatic Micromirror Design**

### **4.5.1 The Concept**

From Section 4.2, we know that the curled comb drive is capable of generating large out-of-plane displacement ( $62\ \mu\text{m}$  for the designed micromirror). However, the rotation angle is inversely proportional to the arm length. As a mirror for biomedical imaging should be large, the large displacement generated by curled comb drives does not result in large rotation angle if the curled comb drives are placed at the edges of the mirror.

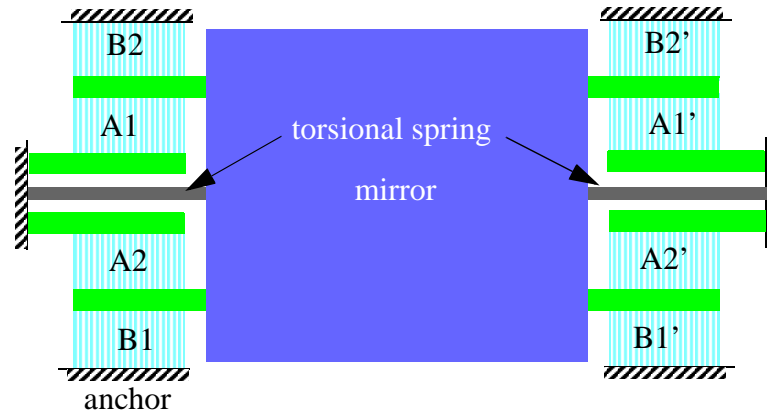


Figure 4-19: Topology of a new electrostatic micromirror with a large rotation range.

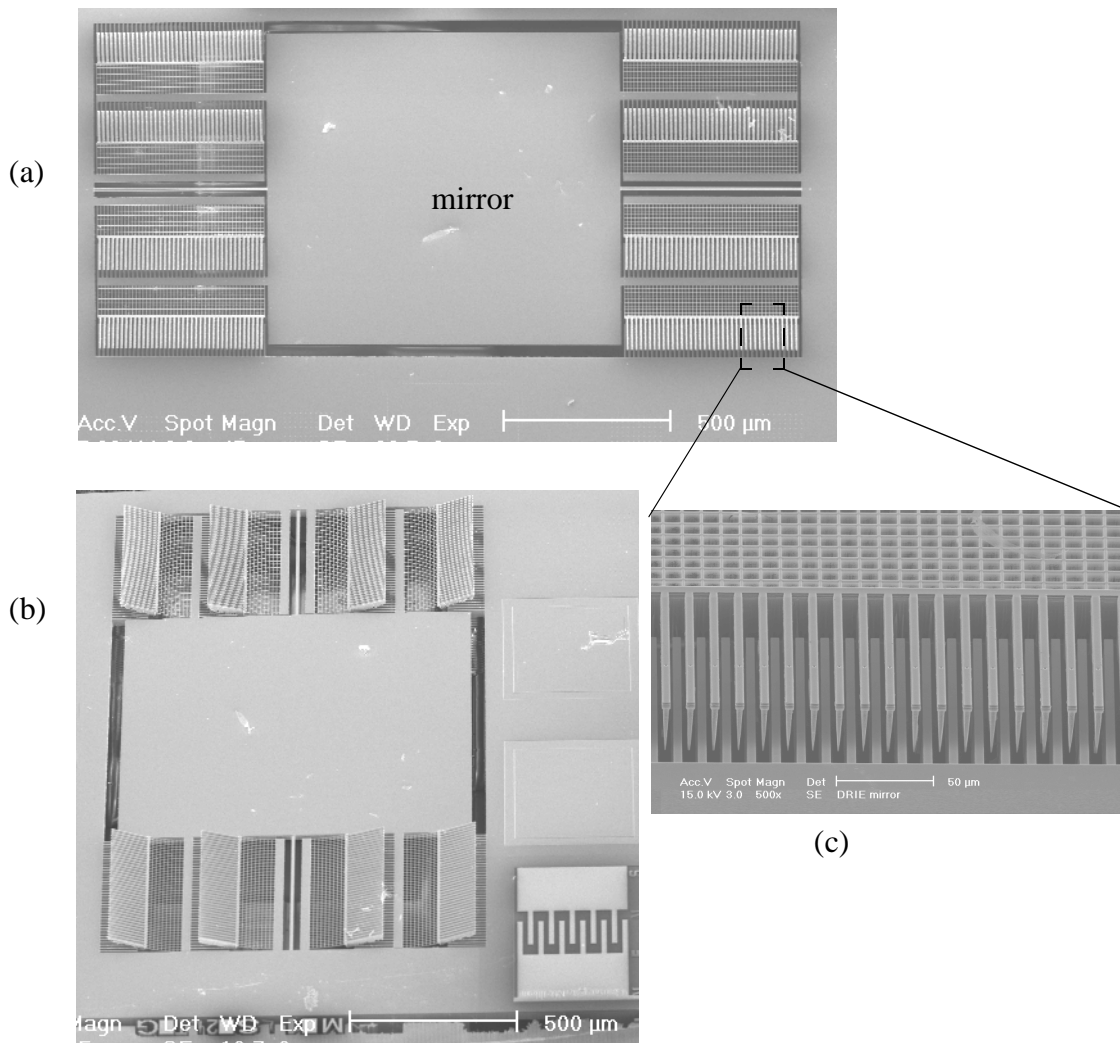
The solution is to shorten the arm length by moving the comb drives closer to the rotational axis, so that the rotation angle is increased without the need to increase the actuation displacement. The concept is illustrated in Fig. 4-19, in which a torsional beam is used. The comb drives are placed on both sides of the torsional beam instead of on the mirror sides as in Fig. 4-3. Using the same definitions as in Fig. 4-3, a comb drive **A** is anchored on the curled side and pulls the mirror up, while a comb drive **B** is anchored on the flat side and pulls the mirror down. Since they are closer to the torsional beam, the **A** comb drives generate most of the torque. The **B** comb drives generate smaller torque and are primarily used to balance the z-axis force.

For a rough estimation, the arm lengths of the comb drive forces in Fig. 4-3 and Fig. 4-19 are 0.7 mm and 0.25 mm, respectively. Therefore, by keeping the same displacement, the new design will have almost two times rotation angle increase.

### 4.5.2 Fabrication and Discussion

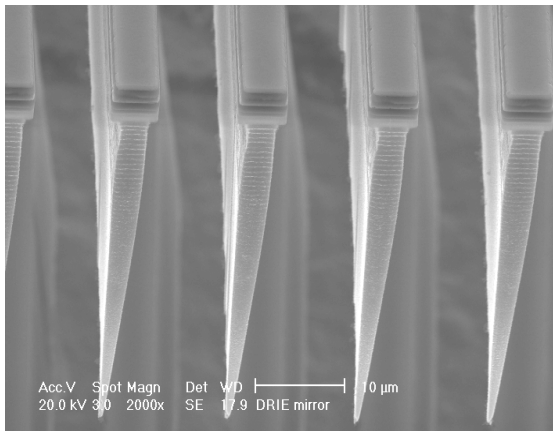
A fabricated micromirror is shown in Fig. 4-20. The active mirror area is 1 mm by 1 mm. The mirror rotates only  $0.7^\circ$  when 20 V d.c. is applied, which is surprisingly much smaller than the previous design.

Fig. 4-21 shows the SEMs of a curled comb drive. An interesting observation is that the end view of the curled comb fingers looks like cones (see Fig. 4-21(a)), while the flat

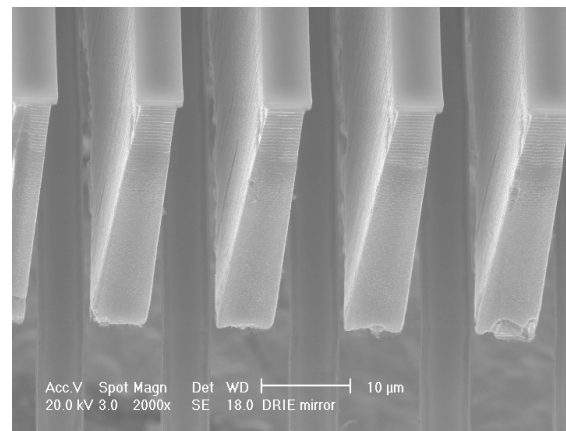


*Figure 4-20: SEMs of the new electrostatic mirror. (a) Top view. (b) Side view. (c) close-up of a comb drive.*

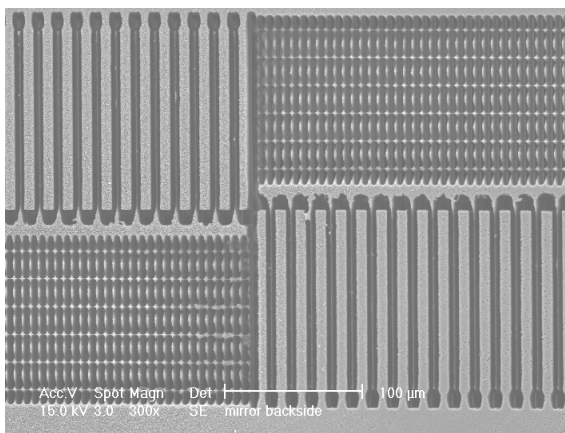
comb fingers become fat (see Fig. 4-21(b)). This is totally different from the previous design. In order to verify whether this phenomenon is caused by design or by process, a chip from the previous design was also processed under the same conditions. The backside view of the chip is shown in Fig. 4-21(c) and (d). Fig. 4-21(c) indicates that the comb fingers connected the thin-film mesh have a much narrower silicon layer than the anchored



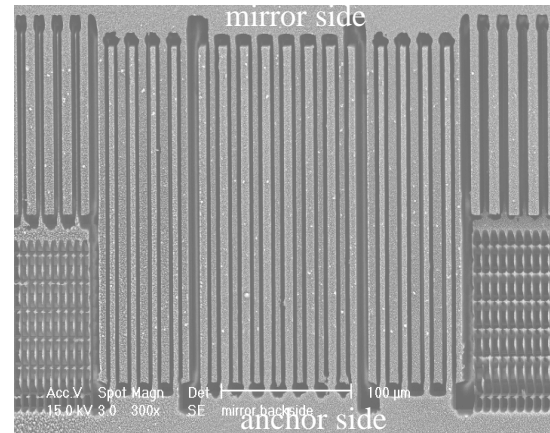
(a) Curled comb fingers



(b) Flat comb fingers



(c) Backside view of curled comb drives



(d) backside view of flat z-actuators

*Figure 4-21: SEMs of the curled comb fingers.*

---

## Summary

---

comb fingers. The z-actuators, which have flat comb fingers on both sides, have much less change in width, compared with layout (Fig. 4-21(d)).

It is clear that the unexpected observation is not caused by design. Surely it is a process issue. One hypothesis is that the thin-film mesh tends to curl up, which generates a stress to the comb fingers that are connected to the mesh. This stressed region may have a higher etching rate. Since the most stressed area is the intersection line of the etch front to the edges of the to-be-curved comb fingers, the to-be-curved comb fingers are then undercut more and more along the etch front and eventually become a cone shape. Further experiments are needed to verify this hypothesis.

### 4.6 Summary

Two types of SCS CMOS-MEMS mirrors have been demonstrated. These large, flat micromirrors have extensive applications in biomedical imaging areas. The thermally actuated micromirror has been successfully installed into an endoscopic OCT imaging system. Preliminary experiments show very promising resolution and scanning speed.

The buckling of the thermal micromirror causes problems for laser beam scanning. The bimorph mesh must be optimized to eliminate the buckling or at least to shift the buckling to a larger angle. On the other hand, the buckling may have a positive application, such as a binary optical switch.

The new electrostatic micromirror design should be fabricated in a “normal” processing condition. The observation about the “cone” shape cross-section needs more investigation.

## Chapter 5

# Gyroscope Theory, Modeling, Design and Simulation

### 5.1 Previous MEMS Gyroscope Work

Gyroscopes are devices which are used to measure rotation rate. There are three classes of gyroscopes with performance from low to high: rate grade, tactical grade and inertial grade [81]. Recently, markets in automotive and consumer electronic products are demanding low-cost gyroscopes with rate-grade performance for driving security and comfort, and motion stability control. The performance requirements for these applications include a full-scale range of at least 50 °/s and a resolution of 0.1 °/s in a bandwidth of 50 Hz [82]. System Planning Corporation (SPC)'s market study shows that the market for these gyroscope applications will be about 500 million US dollars by 2003 [83].

The first silicon micromachined gyroscope was proposed by Draper Lab in 1991 [24]. After that, various fabrication technologies, structural designs and drive/sense mechanisms have been investigated. In the following discussion, “resolution” refers to the minimum detectable signal in certain bandwidth of detection, and “noise floor” refers to the “resolution” per square root of bandwidth of detection. Sometimes the literature doesn't mention the detection bandwidth, and then only the resolution is listed without bandwidth information in this context.



During the early 1990s, bulk micromachining and metal electroforming were mostly used to form large masses. Draper Lab's single-crystal-silicon-on-glass tuning fork gyroscope demonstrated a resolution of  $1.5\text{ }^{\circ}/\text{s}$  in a 60 Hz bandwidth in 1993 [52]. U-Michigan's metal electroforming vibrating ring gyroscope achieved a resolution of  $0.5\text{ }^{\circ}/\text{s}$  in a 10 Hz bandwidth in 1994 [10]. In mid-90's, surface micromachined gyroscopes enabled the read-out circuits to be easily integrated on the same chip. Murata demonstrated a polysilicon surface micromachined vibratory gyroscope with a resolution of  $7\text{ }^{\circ}/\text{s}$  in 1995 [84]. Delco's electroformed vibrating metal ring gyroscope achieved  $0.5\text{ }^{\circ}/\text{s}$  resolution in 1997 [85]. UC-Berkeley's surface micromachined z-axis gyroscope achieved a noise floor of  $1\text{ }^{\circ}/\text{Hz}^{1/2}$  in 1996 [25] which was improved to  $0.2\text{ }^{\circ}/\text{Hz}^{1/2}$  in 1997 [86]. Samsung investigated a surface micromachining gyroscope made from  $7.5\text{ }\mu\text{m}$  thick polysilicon and achieved  $0.1\text{ }^{\circ}/\text{s}$  resolution in 1997 [87]. HSG-IMIT reported a surface micromachined gyroscope with a resolution of  $0.05\text{ }^{\circ}/\text{s}$  at a bandwidth of 50 Hz in 1999 [88]. Carnegie Mellon demonstrated both lateral-axis and z-axis gyroscopes [17][18] using the maskless post-CMOS micromachining process [13]. Analog Devices Inc. reported an integrated z-axis gyroscope with  $0.05\text{ }^{\circ}/\text{Hz}^{1/2}$  noise floor in 2002 [89].

Bulk micromachined gyroscopes also made noticeable progress after 1995. The micro-gyroscope with a clover-leaf shape and a metal post attached to the center, developed at JPL, provided an angle random walk of  $0.1\text{ }^{\circ}/\text{Hz}^{1/2}$  and a bias stability of  $70\text{ }^{\circ}/\text{hr}$  in 1997 [90]. Murata reported a deep RIE gyroscope with decoupling of the sense and drive modes and a resolution of  $0.07\text{ }^{\circ}/\text{s}$  at bandwidth of 10 Hz in 1999 [91].

Bulk and surface micromachining technologies have beneficial and detrimental attributes. Generally speaking, bulk micromachining gyroscopes have large mass but no on-chip read-out electronics and require Si-Si and/or Si-glass anodic bonding and two-side alignment. Surface micromachining gyroscopes have integrated read-out electronics but small mass, and they suffer from thin-film residual stress, squeeze-film damping and sacrificial layer release problems. The ideal case is to combine the advantages of the two micromachining processes. Bosch reported in 1997 a yaw rate gyro fabricated by using the combination of bulk and surface micromachining [26]. Samsung achieved 0.015 °/s at 25 Hz bandwidth by using a mixed technology [92]. However, the mixed technology still suffers from sacrificial layer release and squeeze-film damping problems and often requires expensive SOI wafers.

### **5.1.1 Modeling and Simulation of MEMS Gyroscopes**

Modeling the specific issues of gyroscopes at the microscale is important to understand theoretical operation and to optimize structural design or even steer the development of new fabrication technology. Since MEMS gyroscopes involve multiple physical domains (*e.g.*, electronics, mechanics, electrostatics, and thermodynamics), complete static and dynamic analysis is very difficult. A practical way to do this is to derive simplified models for mechanical components and then use commercially available circuit simulators. For examples, Bosch implemented a network-type model in MAST/SABER [103]. Carnegie Mellon developed a NODAS (*i.e.*, NOdal Design of Actuators and Sensors)

library which uses VerilogA to transform mechanical components into equivalent electrical models and then use Spectre/Cadence to perform the simulation [55].

NODAS is a library of parameterized mechanical component models equipped with electrical properties. The library is composed of beams, plate masses, anchors, electrostatic comb drives, and electrostatic gaps. A gyroscope can be formed by interconnecting these components. The schematic of the gyroscope can be then loaded into the Spectre nodal simulator to perform both electrical and mechanical simulations. Imperfection sources can be included in the component models to evaluate manufacturability. Therefore the multi-domain simulation of the whole gyroscope system can be used to achieve optimal design(s) and gain understanding of special issues existing in MEMS gyroscopes.

## **5.2 Design Issues For Vibratory Gyroscopes**

### **5.2.1 Operational Principle Of Vibratory Gyroscopes**

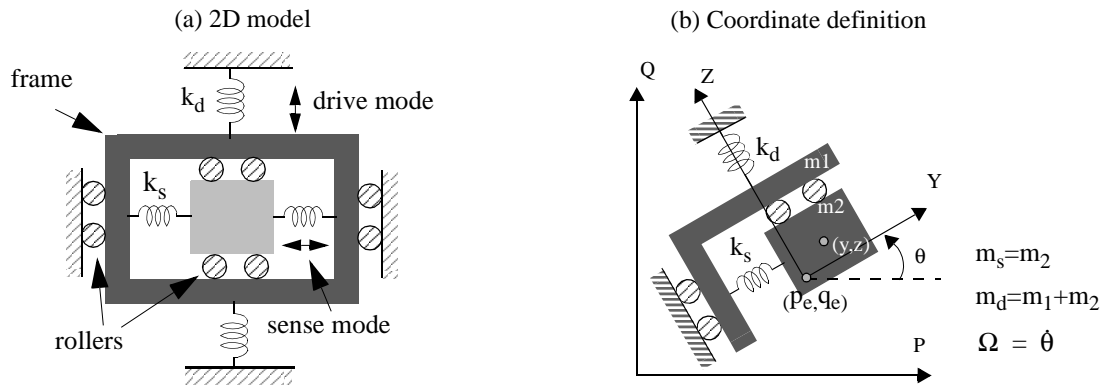
The operation of vibratory gyroscopes is based on Coriolis acceleration which is proportional to the velocity  $\vec{V}$  of the vibrating structure and the external rotation rate  $\vec{\Omega}$ , i.e.,

$$\vec{a}_{co} = 2 \cdot \vec{\Omega} \times \vec{V} \quad (5-1)$$

The primary vibrating motion is the drive mode and the secondary motion due to the Coriolis force is the sense mode. The vibrating structure may be in the form of a vibrating beam or gimbal. Gimballed structures have an advantage of decoupling the drive and sense modes. Notice that vibration can be either translational or torsional. A translationally vibrating gimballed gyroscope will be used as an example to describe the operational prin-

ciple. Fig. 5-1(a) shows the simplified 2D model. It consists of a frame, a proof mass and a network of suspensions. The suspensions provide appropriate elastic stiffness and constraints such that the proof mass may only move in the x-direction against the frame while the frame may only move in the y-direction. The structure is a two-fold, orthogonal spring-mass system where the outer mass is driven by an actuator (drive mode) while the inner mass displacement from Coriolis force is sensed by an accelerometer (sense mode). Suppose the proof mass (along with the frame) is driven to vibration in the y-direction. Then according to Eq. (5-1) there will be a Coriolis force acting on the proof mass along the x-direction in the presence of an external rotation around the z-axis. The displacement amplitude of the proof mass is the measure of the rotation rate.

In order to analyze the dynamics of the gyroscope, Lagrange's equation is used to derive the equation of motion [111]. The coordinate and parameter definitions are shown in Fig. 5-1(b). (P,Q) and (Y,Z) are the fixed and rotating coordinates, respectively.  $(p_e, q_e)$  is the equilibrium point of the double spring-mass system, and  $(y, z)$  are the rotating coordinates of the center of mass of the proof mass. By using Lagrange's equation and through



proper coordinate transformation, the equations of motion (EOM) for the gyro are obtained as the following,

$$\ddot{y} + \left(\frac{B_s}{m_s}\right)\dot{y} + \left(\frac{k_s}{m_s}\right)y - \Omega^2 y - 2\Omega\dot{z} - \dot{\Omega}z + \ddot{p}_e \sin\theta + \ddot{q}_e \cos\theta = 0 \quad (5-2)$$

$$\ddot{z} + \left(\frac{B_d}{m_d}\right)\dot{z} + \left(\frac{k_d}{m_d}\right)z - \Omega^2 z + \frac{2m_s}{m_d}\Omega\dot{y} + \frac{m_s}{m_d}\dot{\Omega}y + \ddot{p}_e \cos\theta - \ddot{q}_e \sin\theta = \frac{F_z}{m_d} \quad (5-3)$$

where  $B_s$  and  $B_d$  are damping coefficients,  $k_s$  and  $k_d$  are spring constants,  $m_s$  and  $m_d$  are masses, and  $\Omega$  is rotation rate. The subscripts 's' and 'd' stand for the sense mode and drive mode, respectively. The damping and spring force terms are the second and third terms in Eq. (5-2) and Eq. (5-3). The rest of the terms are all related to rotation.  $\Omega^2 y$  and  $\Omega^2 z$  are centrifugal acceleration,  $\Omega\dot{z}$  and  $\Omega\dot{y}$  are Coriolis acceleration,  $\dot{\Omega}y$  and  $\dot{\Omega}z$  are angular acceleration, and  $\ddot{p}_e$  and  $\ddot{q}_e$  are linear acceleration terms. The z-motion is coupled into the y-motion through both Coriolis force and centrifugal force. For instance, Eq. (5-2) includes  $\Omega^2 y$  and  $\Omega\dot{z}$  terms. A comparison of the amplitudes of these two terms is made by temporarily assuming  $y=z=A\cos\omega t$ . The typical upper range of  $\Omega$  is about 10 rad/s and  $\omega$  is about  $10^4$  rad/s. Then  $(\Omega^2 y)/(\Omega\dot{z}) = \Omega/\omega \ll 1$ , i.e., the centrifugal term is negligible. The ratio of the angular acceleration to the Coriolis acceleration  $(\dot{\Omega}y)/(\Omega\dot{z}) = (\dot{\Omega}/\Omega)(y/\dot{z}) = (\dot{\Omega}/\Omega)/\omega \ll 1$ , so the angular acceleration is also negligible. The linear acceleration may be large. However, the Coriolis acceleration signal is modulated by the vibration signal which typically has much higher frequency than that of

the linear acceleration. Thus the linear acceleration can be filtered out. Therefore, Eq. (5-2) and Eq. (5-3) can be simplified as

$$\ddot{y} + \left(\frac{B_s}{m_s}\right)\dot{y} + \left(\frac{k_s}{m_s}\right)y = 2\Omega\dot{z} \quad (5-4)$$

$$\ddot{z} + \left(\frac{B_d}{m_d}\right)\dot{z} + \left(\frac{k_d}{m_d}\right)z = \frac{F_z}{m_d} \quad (5-5)$$

In this simplest form, the drive mode has no influence from the sense mode and can be well controlled. It is known that

$$Q_i = \frac{m_i\omega_i}{B_i}; \quad \omega_i = \sqrt{\frac{k_i}{m_i}} \quad i=s, d \quad (5-6)$$

where  $Q_i$  and  $\omega_i$  are mechanical quality factors and resonance frequencies, respectively.

Assume  $F_z(t) = F_0 \sin(\omega t)$ . Then  $z(t)$  and  $y(t)$  can be easily solved, *i.e.*,

$$z(t) = \frac{F_0}{k_d} \frac{1}{\sqrt{\left(1 - \left(\frac{\omega}{\omega_d}\right)\right)^2 + \left(\frac{\omega}{Q_d \omega_d}\right)^2}} \sin(\omega t - \phi_d) = Z \sin(\omega t - \phi_d) \quad (5-7)$$

$$\begin{aligned} y(t) &= \frac{2\Omega m_s \omega F_0}{k_s k_d} \frac{1}{\sqrt{\left(1 - \left(\frac{\omega}{\omega_d}\right)\right)^2 + \left(\frac{\omega}{Q_d \omega_d}\right)^2}} \frac{\sin(\omega t - \phi_s)}{\sqrt{\left(1 - \left(\frac{\omega}{\omega_s}\right)\right)^2 + \left(\frac{\omega}{Q_s \omega_s}\right)^2}} \\ &= Y \sin(\omega t - \phi_s) \end{aligned} \quad (5-8)$$

where  $Y$  and  $Z$  are the amplitudes of  $y(t)$  and  $z(t)$ , respectively, and  $\phi_d$  and  $\phi_s$  are the phases of  $y(t)$  and  $z(t)$ , respectively. The  $Y$ -to- $Z$  ratio is equal to

$$\frac{Y}{Z} = \frac{2\Omega m_s \omega}{k_s} \frac{1}{\sqrt{\left(1 - \left(\frac{\omega}{\omega_s}\right)^2\right)^2 + \left(\frac{\omega}{Q_s \omega_s}\right)^2}} = \frac{2K(\omega)\omega\Omega}{\omega_s^2} \quad (5-9)$$

where

$$K(\omega) = \frac{1}{\sqrt{\left(1 - \left(\frac{\omega}{\omega_s}\right)^2\right)^2 + \left(\frac{\omega}{Q_s \omega_s}\right)^2}} \quad (5-10)$$

The phase difference between  $y(t)$  and  $z(t)$  is given by

$$\phi = \phi_d - \phi_s = \text{atan}\left(\frac{\omega_d/\omega_s}{Q_s(1 - (\omega_d/\omega_s)^2)}\right) - 90^\circ \quad (5-11)$$

Assume  $Q_s = 10$ ,  $\omega_s = 10$  kHz. Then for a  $1^\circ/\text{s}$  rotation,  $Y/Z = 6 \times 10^{-6}$  or 6 ppm! So, in most cases, vacuum packaging is needed to obtain high quality factors. On the other hand, since the sensor works at resonance, the bandwidth is given by

$$BW = \frac{\omega_s}{Q_s} \quad (5-12)$$

If  $Q_s$  is high (*e.g.*,  $10^4$ ), then  $BW = 1$  Hz. This value of  $BW$  may be too small for many applications, thus limiting the maximum value of  $Q_s$ .

Moreover, the mechanical sensitivity can be derived from Eq. (5-9), *i.e.*,

$$\frac{Y}{\Omega} = \frac{2K(\omega)m_s\omega Z}{k_s} = \frac{2K(\omega)\omega Z}{\omega_s^2} \quad (5-13)$$

The thermomechanical noise, or Brownian noise, is given by

$$\frac{\Omega_{min}}{\sqrt{BW}} = \sqrt{\frac{k_B T \omega_s}{m_s Q_s \omega_s^2 Z^2}} = \sqrt{\frac{k_B T}{m_s Q_s \omega_s Z^2}} \text{ if } \omega = \omega_s. \quad (5-14)$$

Eq. (5-13) and Eq. (5-14) show that the sensitivity and noise have opposite demands to the resonant frequency  $\omega_s$  but both are improved with increasing  $Q_s$ .

### 5.2.2 Design Issues for Vibratory Gyroscopes

A gyroscope design procedure includes architecture design, mechanical component design, electrical design and system design and overall performance assessment. The architecture of a gyroscope mainly depends on the available fabrication technology. The detailed design issues are listed in the following:

#### *(1) Architecture*

At least four questions should be answered: Will a vibrating beam design or vibrating gimbal design be used? Is the drive mode translational or torsional vibration? Is the drive placed on outside or inside of the gimbal if used? Is a single proof mass or dual-antiphase vibrating proof mass used?

#### *(2) Performance requirement*

The given specifications (resolution, bandwidth, sensitivity) roughly determine the chip size and some key parameters such as spring constant, resonance frequency, and mechanical quality factor. The most simplified model as described in Eqs. (5-5-4) and (5-



5) and its derivative equations Eqs. (5-5-9) to (5-14) can be used to optimize the parameters. The performance of a gyroscope is a function of its housing pressure.

*(3) Linear acceleration*

Although, as shown in the 2D model described by Eqs. 5-2 and 5-3, the linear acceleration has different frequency components from the Coriolis acceleration, its amplitude may be much larger than that of the Coriolis acceleration. The operating point of the Coriolis acceleration sense mode is a function of the linear acceleration and may easily move out of the linear operating region. Therefore, designs should incorporate either a mechanism to reject the linear acceleration or extra accelerometers to compensate the linear acceleration. A gyroscope with two shuttles oscillating at  $180^\circ$  phase difference can cancel out external acceleration. However, it requires vibration matching of the two shuttles. Since the main focus of my work is on the gyroscope effects, only single-shuttle gyroscopes are considered to simplify the gyroscope design.

*(4) Mode coupling*

From the rough estimation of Eq. (5-9), the sense motion is very small and is less than 10 ppm compared to the drive motion. Thus even a small amount of mechanical or drive force asymmetry will make the coupled drive motion overwhelm the sense signal. This is called quadrature error [25]. Since both signals have the same or very close frequencies, they cannot be easily separated unless a special phase lock technique is employed [90]. In most cases, force balancing is needed to compensate the mode coupling and thus null the quadrature error.

*(5) Frequency tuning*

The larger the velocity of the vibrating structure, the higher the resolution. The velocity can be increased by a factor of  $Q_d$  if the structure is driven to resonance of the drive mode. Meanwhile, if the structure oscillates at the resonance of the sense mode, both  $Y/Z$  ratio and resolution will be multiplied by  $Q_s$ . Therefore, the two resonances are often tuned to be within -3dB bandwidth. So as  $Q_s$  and/or  $Q_d$  increases, gyro bandwidth decreases and tuning control becomes more critical. The commonly used frequency tuning method is the electrical spring softening [25]. It was also reported to tune resonant frequencies by modifying sidewalls of spring beams through ion milling [84].

In this work, a new frequency tuning method which uses an integrated polysilicon heater to thermally change the curvature of the spring beams is introduced in Section 6-1. The spring constant changes with the curvature.

*(6) Process variations and material defects*

Vibratory gyroscopes have an extremely strict requirement to symmetry to minimize the mode coupling. Unfortunately, any fabrication process can only create symmetrical designs to certain precision. There are always process variations, randomly distributed defects or contaminations in the structural materials, and non-uniformity in the structural layers. These effects may cause large mode coupling, high cross-sensitivity, low linear acceleration rejection, and need for greater frequency tuning range. One of the major design tasks is to identify the sensitivity of the device performance to these imperfections with the goal of optimizing manufacturability.

*(7) Multi-axis integration and utility of gyroscope/accelerometer array*

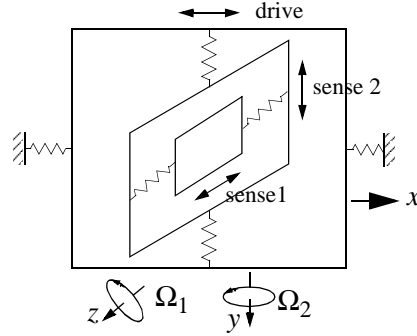
Most IMUs are still made from assembling individual inertial sensors together. Not only is the size increased, but also the cost and effort for alignment and wiring is high. To develop monolithic IMUs with six degree-of-freedom (DOFs) and on-chip signal processing circuits is an ultimate goal of inertial MEMS research. 6-DOF IMUs require three-dimensional actuation and sensing capability. The vertical actuation/sensing method demonstrated in this thesis complements the commonly used lateral actuation/sensing, which enables fabrication of monolithic IMUs using an array of accelerometers and gyroscopes to improve the overall performance. For instance, the information obtained from accelerometers can be used to extract the angular rate from the mixed signal or null out the linear acceleration for gyroscopes by feedback force balancing.

### **5.3 Designs of CMOS-MEMS Gyroscopes**

#### **5.3.1 Basic Structures of Gimbaled Gyroscopes**

A gimbal in this text refers to a rigid frame with a proof mass suspended inside. The frame and the proof mass are constrained to move or rotate only in two mutually orthogonal axes. Instead of bearings as used in traditional gimbal rings, elastic spring beams are used to provide the mechanical support and movement freedom. A gimbaled structure may consist of two or more gimbals in series and may have one or more gimbals nested. Considering the necessities and structure complexity, only a gimbaled structure with two single-gimbals in series, or dual-gimbal, is practically feasible. Fig. 5-2 shows the schematics of two single-gimbaled structures. Notice that the vibration modes may be either

Figure 5-3: Two-fold gimbaled structure ( $z$  is orthogonal to  $x$ - $y$  plane).



translational or rotational. Not listed here are translational drive with rotational sense and rotational drive with translational sense. If another set consisting of a frame and spring is added to a single-gimbaled structure such that the additional vibration mode is orthogonal to the two existing modes, a two-fold gimbaled structure is formed as shown in Fig. 5-3. Note that this applies only to translational vibration. A two-fold gimbaled structure can sense two-axis rotation, but it is more complicated than the single-gimbaled structure.

The dual-gimbaled structures are shown in Fig. 5-4. The two gimbals are connected through a spring and therefore can be excited to their anti-phase vibration mode. The bal-

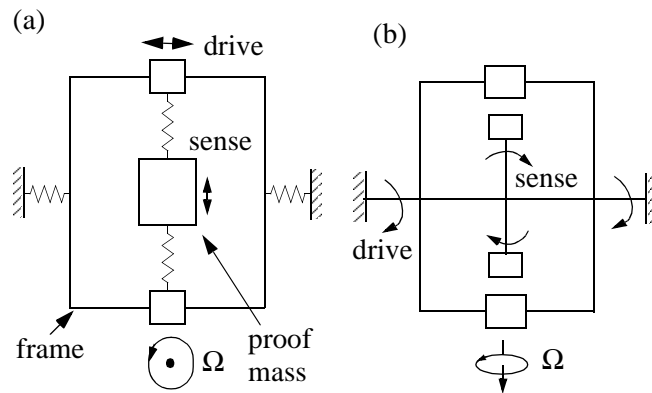
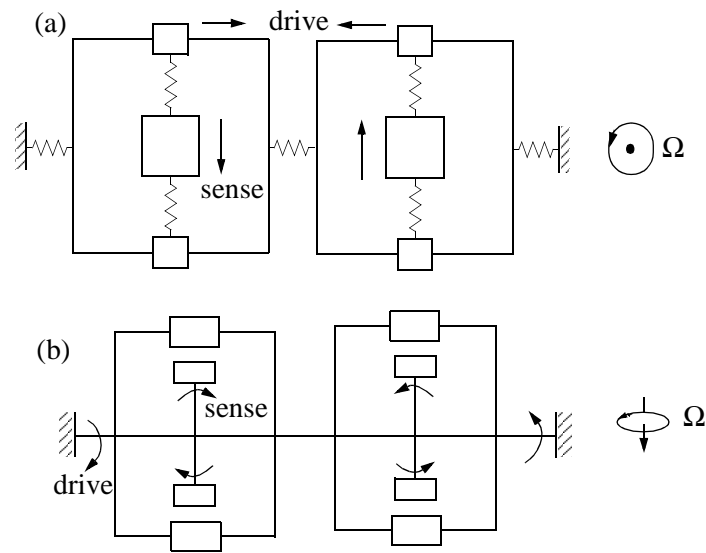


Figure 5-2: Single-gimbal structures: (a) translational drive; (b) torsional drive.



*Figure 5-4: Dual-gimbaled structures: (a) translational drive; (b) torsional drive.*

anced vibration mode has higher mechanical quality factor, and good linear acceleration rejection can be expected.

The drive can be placed on either outside or inside of a gimbal and may be another gyroscope performance issue. All the drives shown in Figs. 5-1 to 5-4 are placed on the outside frame of the gimbals, however the drive may be placed on the inside proof mass.

### 5.3.2 Design Considerations

The design can be roughly classified into four categories: architecture design, mechanical design, electrical design, and system design. Note that these design categories are not separated. Indeed, they have to interact with each other. At the architecture design stage, based on the available process, an appropriate topology should be designed to mini-

mize mode coupling and maximize linear acceleration rejection. Multi-axis integration, design complexity and operating environment should also taken into account. At the mechanical design stage, the task is to model mechanical components and optimize both designs of individual components and the whole structure. Sensitivity, resolution, bandwidth, resonance frequency matching and sensitivity to process variations are addressed at this stage. At the electrical design stage, capacitive sense interface, wiring configuration, parasitics and frequency tuning (electrostatic, thermal) are the main concerns. The system design issues include compensation for imperfections, automatic adjustment of the vibration excitation, force rebalancing, bandwidth control, and overall performance assessment.

#### **5.3.2.1 Spring Designs**

Mode coupling, sensitivity, and multi-axis integration depend on spring design. Ideally, each spring should have only one degree-of-freedom. However, springs are constructed from beams. The spring constants in any direction are finite values. This is one of the major sources of mode coupling.

In reality, the stiffness in the primary mode should be at least one order smaller than any other modes to separate the primary mode from other modes and reduce the off-axis motion. As introduced in Section 2.1, the thin-film CMOS-MEMS process provides beams with different thicknesses by choosing different interconnect metal layers as the etching mask. Typically, for the Agilent 0.5  $\mu\text{m}$  3-metal CMOS process, beams with metal-1, metal-2, metal-3 on the top are 1.9  $\mu\text{m}$ , 3.5  $\mu\text{m}$ , 5.0  $\mu\text{m}$  thick, respectively.

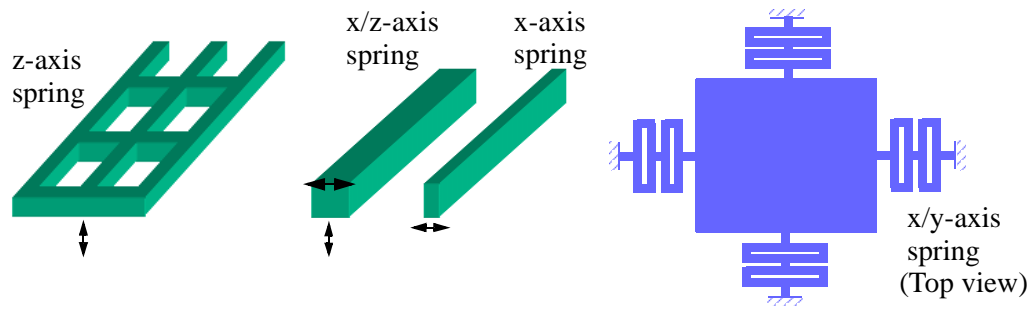


*Figure 5-5: Spring designs.*

Fig. 5-5 shows four spring designs for different axes. A z-axis compliant spring is realized by connecting multiple beams with short trusses and using beams with metal-2 on the top. Beams with metal-1 on the top are even more compliant in the z-direction, but they have large out-of-plane curling. An x/z-axis spring is obtained if the beam width is equal to the beam thickness. The lateral-compliant spring is realized by using narrow beams. Assuming the beam width is  $1.8\ \mu\text{m}$  and the beam thickness is  $5.0\ \mu\text{m}$ , the x-axis stiffness will be about one order smaller than the z-axis stiffness. The x/y-axis spring is obtained by symmetrically arranging four sub-springs. Each sub-spring consists of rectangularly closed beams in series which are flexible in both the x and y directions. The advantage of this x/y-axis spring is that the stiffnesses in the x and y directions are equal.

The same spring designs can apply to the DRIE CMOS-MEMS process. The only difference is that the DRIE process gives much higher vertical-to-lateral stiffness ratio because of the thick Si layer.

### **5.3.2.2 Phase Issue**

As discussed in Section 5.3.3, electrostatic force exists in all directions in a comb drive, which results in off-axis (i.e., the axes other than the primary axis) vibrations as well as the primary excitation vibration. These vibrations may have different phases and their phase relations are discussed in the following.

Since the mechanical structure can be considered as a second-order system along each axis, the phase delay between the acting force or acceleration and the resultant displacement is given by

$$\phi_X = \text{atan}\left(\frac{\omega/\omega_X}{Q_X(1 - (\omega/\omega_X)^2)}\right), \quad (5-15)$$

where  $X = x, y \text{ and } z$ ,  $\omega$  is the operating frequency,  $Q_X$  and  $\omega_X$  are the mechanical quality factor and resonant frequency in the  $X$  direction, respectively.

#### **(1) Excitation vibration versus voltage**

Normally, the device operates at the resonant frequency of the drive mode, i.e., the  $x$ -axis displacement has a  $90^\circ$  phase delay with respect to the actuation force. For electrostatic actuation, a differential voltage pair with a large d.c. offset voltage is often used to minimize the second harmonic term of the generated force which is then in-phase with the a.c. voltage. It often happens especially in open loop operation that the operating frequency is not exactly the resonance frequency of the drive mode. In this case, there will be a phase offset  $\alpha$  from  $90^\circ$  between the applied voltage and  $x$ -axis excitation vibration, as shown in Fig. 5-6.



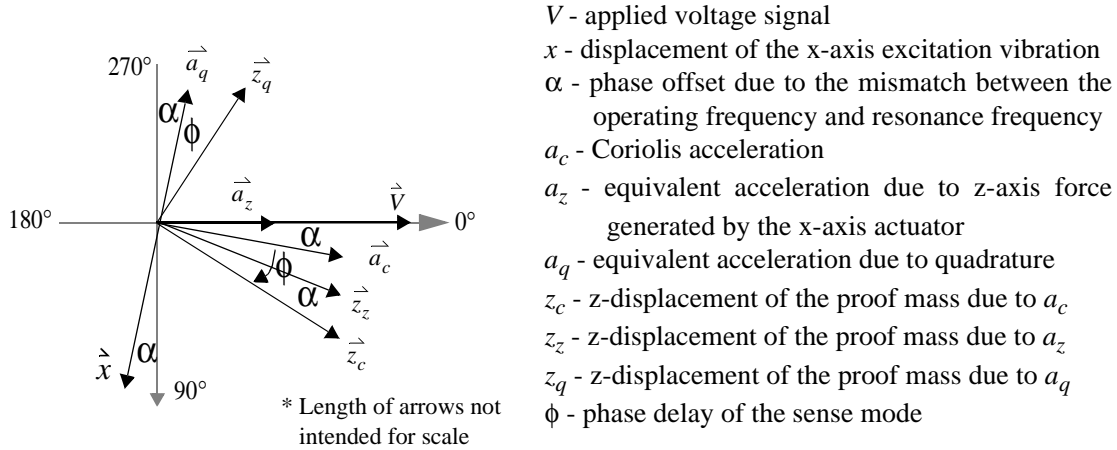


Figure 5-6: Phase relation of various signals in a gyroscope.

## (2) Coriolis versus quadrature

Due to defects and/or variations from fabrication processing, imperfections such as asymmetry and anisoelasticity in the structure are generated. Consequently, cross-coupled motions, i.e., quadrature motions, are produced. For example, the primary vibration is along the x-direction, but vibration may be also observed in the z-direction. This cross-coupled motion is commonly referred as "quadrature" motion. The quadrature motion is in-phase with the primary vibration. According to Eq. (5-1), the Coriolis acceleration has a 90° phase shift compared to the quadrature displacement (Fig. 5-6). This phase difference provides opportunities to suppress the quadrature signal by tuning the phase of demodulation and/or null this coupled excitation motion by properly applying anti-phase forces [25].

### **(3) Coriolis acceleration versus Coriolis displacement**

The Coriolis displacement has a phase delay,  $\phi$ , with respect to the Coriolis acceleration (Fig. 5-6).  $\phi$  depends on the resonant frequency ratio of the sense mode to the drive mode and is given by Eq. (5-15).

### **(4) Coriolis versus direct-coupled motions**

Both drive and sense springs are made of beams, and therefore the stiffness in any direction is a finite value. The finite stiffnesses of the drive mode in the off-axes result in vibrations that are mixed with the Coriolis motion. The stiffnesses along the x, y and z axes are denoted respectively as  $k_{d,x}$ ,  $k_{d,y}$  and  $k_{d,z}$  for the drive mode, and  $k_{s,x}$ ,  $k_{s,y}$  and  $k_{s,z}$  for the sense mode. Typically,  $k_{d,y}$  and  $k_{d,z}$  are much larger than  $k_{d,x}$ , i.e., the resonant frequencies in the y- and z- directions are much higher than that in the x-direction (which is normally the operating frequency). Therefore, the generated y- and z- axis displacements are in-phase with the applied voltage according to Eq. (5-15).

At zero rotation rate, the output signal reflects purely the coupled motions on the proof mass from the excitation vibration. At any non-zero rotation rate, the output signal is a mix of the coupled signals and the Coriolis signal. As mentioned above, the Coriolis signal has exactly  $90^\circ$  phase difference from the quadrature signal. A demodulator can phase out the quadrature signal and maximize the Coriolis signal at the same time. Alternatively, the quadrature motion can be compensated by applying a force on the frame along the Coriolis sense direction. The force can be provided by applying a voltage with a phase of  $(-90^\circ + \alpha)$  to an electrostatic comb drive.

As shown in Fig. 5-6, the phase difference between the Coriolis signal and z-axis direct-coupled signal is  $\alpha$ , which depends on the phase stability of the system and is close to zero. The phase technique used to suppress the quadrature signal does not apply to this direct-coupled signal. However, this direct-coupled motion can be nullified by applying a voltage with a phase of  $180^\circ$  to a z-axis comb drive on the frame.

### **(5) Coriolis versus combined motion couplings**

Both the quadrature and the z-axis direct-coupled motions act on the proof mass through a rigid frame, while the Coriolis force applies directly to the proof mass. Therefore, the quadrature and z-axis direct-coupled motions are actually mixed as a single motion with a compound amplitude and phase. This mixed motion or signal is defined as the combined coupling motion or coupling signal in the rest of this thesis. The Coriolis signal will have a phase delay of close to  $90^\circ$  with respect to the combined coupling signal if the quadrature motion dominates, or close to zero degree if the direct-coupled motion dominates.

#### **5.3.2.3 Noise Considerations**

The two main noise sources are the thermomechanical noise, *i.e.*, Brownian noise, and the electronics noise. The minimum detectable rotation due to Brownian noise is proportional to  $(m_s \omega_s)^{-1/2}$  as given in Eq. (5-14). Suppose the microstructure has a size of  $0.6 \text{ mm} \times 0.6 \text{ mm} \times 5.0 \text{ }\mu\text{m}$ . The density of the thin-film CMOS-MEMS structure is  $2700 \text{ kg/m}^3$ . If the curl matching frame and release holes are excluded, the central proof-mass is about 1 micro-gram. The mechanical Q-factor in the z-direction is about 5 at atmo-

spheric pressure due to the squeeze-film damping between the structure and substrate. According to Eq. (5-14), the noise floor due to Brownian noise is about  $0.1^\circ/\text{s}/\text{Hz}^{1/2}$ .

The DRIE process generates microstructures with a thick Si layer. This has two impacts. First, even if the same size as the thin-film structure is kept, the mass will still increase one order of magnitude. Secondly, since DRIE microstructures are flat, devices with large area (*e.g.*, 10x increase compared to thin-film devices) can be designed. Considering another one order of magnitude increase of the mechanical Q-factor in DRIE microstructures [31], the Brownian noise will be reduced to about  $0.005^\circ/\text{s}/\text{Hz}^{1/2}$  (still in “rate-grade”).

Assuming a x-axis gyroscope with a z-axis actuation and a y-axis sense, the output voltage is proportional to the y-axis displacement due to the Coriolis acceleration, i.e.,

$$V_{out} = \frac{Y}{g} \cdot V_m \quad (5-16)$$

where  $g$  is the comb-finger gap. Combining Eq. (5-16) with Eq. (5-13), the detectable rotation limited by the electronics noise is given by

$$\Omega_{min} = \frac{g \cdot \omega_s^2}{2K(\omega) \cdot \omega \cdot Z \cdot V_m} V_{sn} \quad (5-17)$$

where  $\omega_s$  is the resonant frequency of the sense mode,  $Z$  is the drive amplitude,  $V_m$  is the amplitude of the modulation signal, and  $V_{sn}$  is the noise floor of the on-chip pre-amplifier.

If the circuit noise floor is  $20 \text{ nV}/\text{Hz}^{1/2}$  at 200 kHz, the circuit-limited noise floor is  $0.004^\circ/\text{s}/\text{Hz}^{1/2}$ , assuming  $g = 1.5 \text{ }\mu\text{m}$ ,  $\omega_s = 5 \text{ kHz}$ ,  $K = 2$ ,  $Z = 3 \text{ }\mu\text{m}$ , and  $V_m = 1 \text{ V}$ .

### 5.3.3 Comb Drive 3D Motion Analysis

Fig. 5-7 shows the comb finger model with presumed lateral offset and vertical misalignment. In this first-order analysis, a parallel-plate approximation is used and fringing effects are ignored. The capacitance of the comb fingers can be expressed as

$$C(x, y, z) = \epsilon_0(h - z_0 + z)(x_0 + x) \left( \frac{1}{g + y_0 + y} + \frac{1}{g - y_0 - y} \right) \quad (5-18)$$

$$= \frac{2\epsilon_0(h - z_0 + z)(x_0 + x)}{g} \cdot \frac{1}{1 - \left( \frac{y + y_0}{g} \right)^2}$$

The geometric parameters in the above equation are defined in Fig. 5-7. The comb drive is used for generating x-axis motion. The y displacement is typically very small compared to the gap. The lateral offset,  $y_0$ , is also small, especially for DRIE structures. Thus  $[(y + y_0)/g]^2$  terms are neglected when deriving capacitance gradients, which are given by

$$\frac{dC}{dx} = \frac{2\epsilon_0(h - z_0 + z)}{g} \quad (5-19)$$

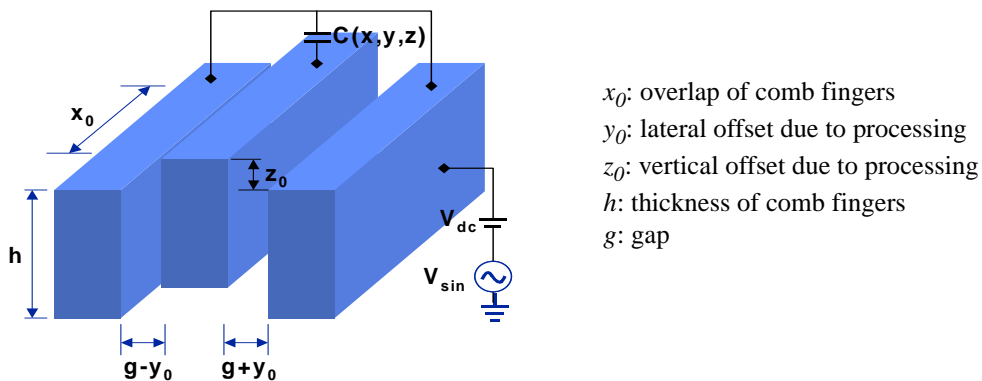


Figure 5-7: Comb finger model for 3D electrostatic force analysis.

$$\frac{dC}{dy} = \frac{4\epsilon_0(h - z_0 + z)(x_0 + x)(y + y_0)}{g^3} \quad (5-20)$$

$$\frac{dC}{dz} = \frac{2\epsilon_0(x_0 + x)}{g} \quad (5-21)$$

Electrostatic force per unit comb finger is then given by

$$F_X = \frac{1}{2} \cdot \frac{dC}{dX} \cdot V^2 \quad (5-22)$$

where  $X = x, y, \text{ or } z$ , and  $V$  is the applied voltage.

Then, the equations of motion can be written as

$$\ddot{X} = -\frac{\omega_X}{Q_X} \dot{X} - \omega_X^2 X + \frac{N \cdot F_X}{m} \quad (5-23)$$

where  $m$  is the mass of the movable structure. The above equations of motion are applied to the drive mode. For this actuation analysis, it is assumed that the sense mode is passive, i.e., the rotation rate is zero. Then there are only inertial forces acting on the central proof mass. Similar to the drive mode, the equations of motion of the sense mode can be expressed as

$$\ddot{X}_s = -\frac{\omega_{X_s}}{Q_{X_s}} \dot{X}_s - \omega_{X_s}^2 X_s + \omega_{X_s}^2 X \quad (5-24)$$

where  $X_s$  is the vector of  $x, y$ , and  $z$  displacements of the proof mass and  $X$  is the vector of displacements of the drive frame.

Eqs. (5-18) to (5-24) can be easily implemented in Matlab/Simulink. The Simulink model is hierarchical. Fig. 5-8(a) is the top cell with input voltage settings and output data savings. Fig. 5-8(b) is the sub-cell for the drive mode that includes another three subsequent lower levels of subcells. The sub-cell for sense mode is not shown in Fig. 5-8, but it



(b)

**Table 5-1: Device parameters**

108 Gyroscope and Micromirror Design Using Vertical-Axis CMOS-MEMS Sensing and Actuation

Transient analyses are conducted to understand the motion coupling and phase relation. Fig. 5-9 shows Simulink simulation results at different conditions. The primary excitation is along the x-axis. So both y-axis and z-axis displacements are off-axis motions.

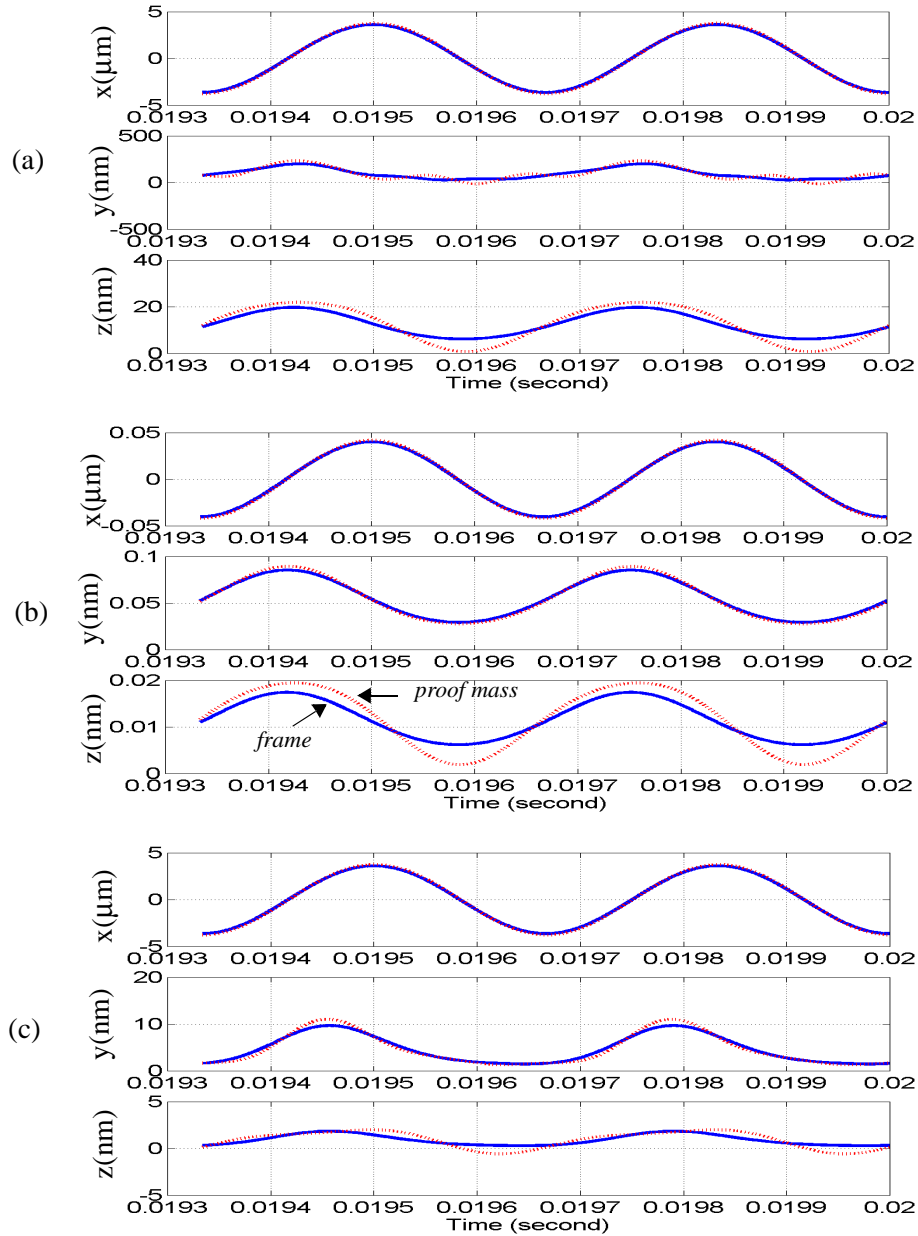


Figure 5-9: Simulink simulation results. (a)  $V_{ac} = 5$  V,  $V_{dc} = 18$  V. (b)  $V_{ac} = 0.5$  V,  $V_{dc} = 2$  V. (c)  $x_0$  is assumed to be 60 μm, instead 6 μm in the other conditions.



The y off-axis motion induces cross-axis sensitivity and the z off-axis motion directly mixes with the Coriolis signal. At the normal operating voltage ( $V_{ac} = 5$  V,  $V_{dc} = 18$  V), the y-axis and z-axis displacements are highly non-linear, *i.e.*, harmonics are present (Fig. 5-9(a)), and have only a  $45^\circ$  phase shift from the resonating x-axis motion. This makes the off-axis motion compensation difficult. If the voltage is small, *e.g.*,  $V_{ac} = 0.5$  V,  $V_{dc} = 2$  V, the y-axis and z-axis displacements are shifted by  $90^\circ$  from the x-axis motion, and the z-axis displacement in the sense mode is shifted by about  $5^\circ$  from the z-axis displacement in the drive mode, as shown in Fig. 5-9(b).

The non-linearity of the z-axis displacements is caused by the z-axis electrostatic force, which is proportional to the overlap of the comb fingers. If the x-axis displacement is much smaller than the overlap, the non-linearity of the z-axis displacement is small, as the case shown in Fig. 5-9(b). If the x-axis displacement is comparable to the overlap, high non-linearity of the z-axis force and displacement arises. The overlap may be increased to reduce the non-linearity of the z-axis displacements, as shown in Fig. 5-9(c), where  $x_0 = 60$   $\mu\text{m}$ . However, the y-axis displacements show a high non-linear behavior and both y-axis and z-axis displacements are large.

In summary, the directly coupled motion is highly non-linear and difficult to compensate. It may dominate the ZRO signal and is difficult to suppress by demodulation since it has the same phase as the Coriolis signal. Therefore, z-axis force cancellation techniques such as introduced in Section 6.2.8 should be included into a vibratory gyroscope design with comb-finger actuation for performance improvement.

### **5.3.4 Proposed CMOS-MEMS gyroscope designs**

These designs are divided into three categories according to the means of driving: lateral drive type; vertical drive type; and torsional drive type.

#### ***(1) Lateral drive type***

Lateral comb drives have been well studied and widely used. Since the drive mode is along one of the lateral axes, the rotation sense axis may be the other lateral axis and/or the vertical axis. Fig. 5-10 shows two single-axis gyroscopes with lateral drive. Although the topologies look complicated because of the drive and sense comb fingers, they are equivalent to the simplified model shown in Fig. 5-2(a). They can also be considered as an accelerometer attached inside a vibrating frame.

The drive mode is excited along the y-axis. Well controlled excitation vibration is crucial to a vibratory gyroscope since the vibration amplitude may vary and some undesired vibration modes may also be excited. Thus, besides the y-axis longitudinal comb drive for excitation, there is an x-axis transverse comb drive and a vertical comb drive for off-axis motion nulling. There are three other sets of comb fingers for x, y, and z position sensing.

The sense mode can be either in the x-axis or z-axis. As shown in Fig. 5-10(a), the z-axis gyro has an embedded x-axis accelerometer while in Fig. 5-10(b) the x-axis gyro has an embedded z-axis accelerometer. The embedded accelerometers determine the sensitivity and resolution of the gyroscopes. The operational principles and wiring configurations of the x-axis and z-axis accelerometers have been discussed in Section 2.3.2.

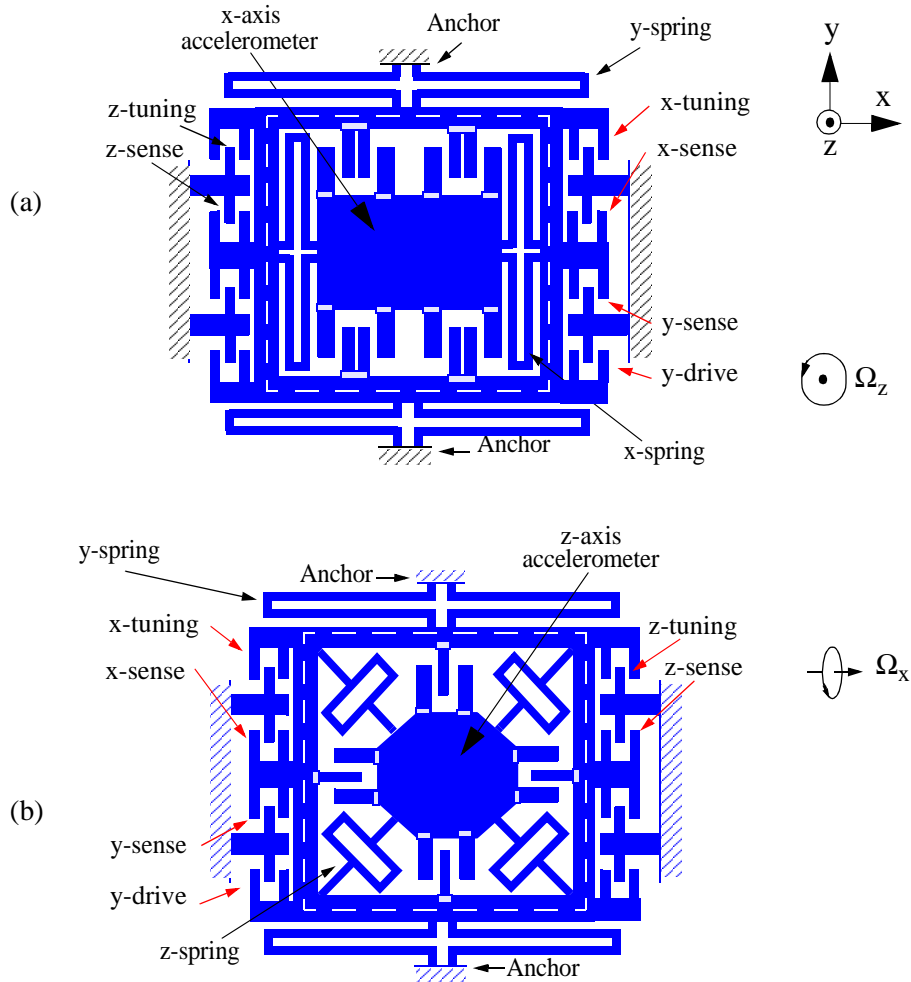


*Figure 5-10: Single-axis gyroscopes with lateral drive:  
(a) z-axis gyro; and (b) x-axis gyro.*

If the x-spring in the z-axis gyro (Fig. 5-10(a)) is replaced by an x/z dual-axis spring and a z-axis accelerometer is added, a x/z dual-axis gyro can be designed as shown in Fig. 5-11. Since the x/z-spring consists of multiple layers, the lithography misalignment and imperfect sidewalls make it difficult to design identical spring constants in both the x- and z- directions. Either thermal or electrostatic tuning of resonance frequency should be

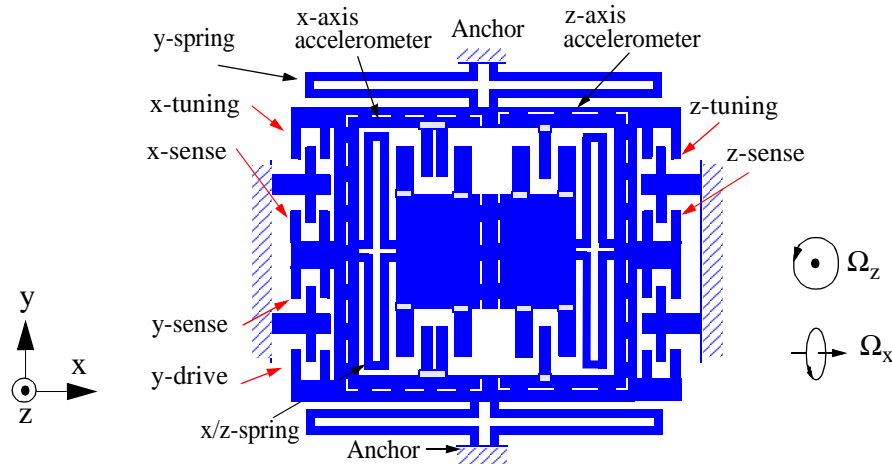


Figure 5-11: X/z dual-axis gyroscope with lateral drive.

used. Thermal tuning of resonant frequency can be implemented by integrating a polysilicon heater inside the spring. Electrostatic tuning of resonance frequency can be done by applying a DC bias to the sense comb fingers. Note that the x-axis spring has an electrical softening effect on the spring constant while the z-axis spring has an electrical “stiffening” effect (see Fig. 3-25).

Moreover, a dual-axis dual-gimbaled gyroscope can be achieved with lateral drive. The schematic is shown in Fig. 5-12. If the dual-axis accelerometers are replaced by z-axis or x-axis accelerometers, it becomes an x-axis or a z-axis gyroscope, respectively. The corresponding simplified model can be found in Fig. 5-4(a). The advantages of the dual-gimbal structure include the linear acceleration compensation and high mechanical Q-factor. Its disadvantages include larger size and increased structural complexity. Also the mode matching between the anti-phase vibrating shuttles is difficult to achieve.

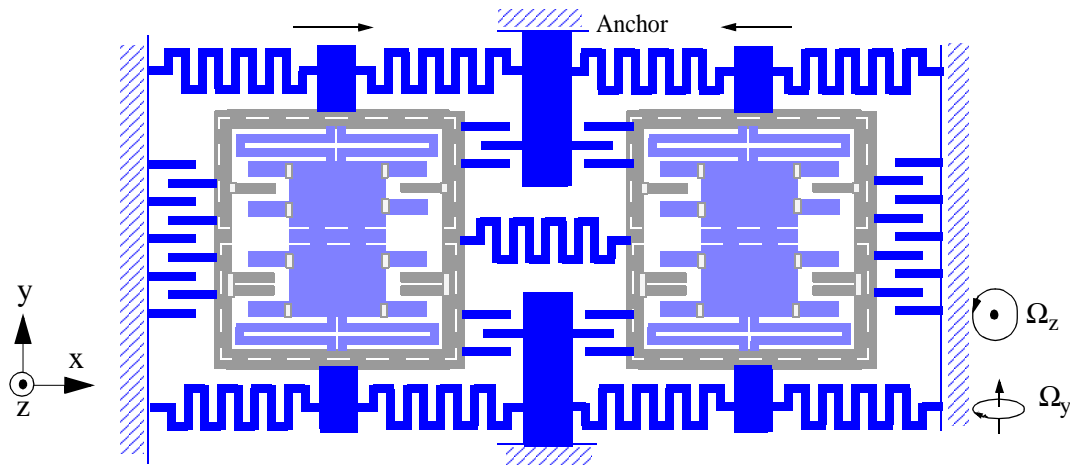


Figure 5-12: Y/z dual-axis dual-gimbaled gyroscope with lateral drive.

## (2) Vertical drive

A y-axis gyro with vertical drive is shown in Fig. 5-13. It has very similar topology as the x-axis gyro with lateral drive (Fig. 5-10(b)) except that the z-axis spring is switched to the drive gimbal while the x-spring is placed on the sense gimbal. The central accelerometer detects x-axis instead of z-axis motion.

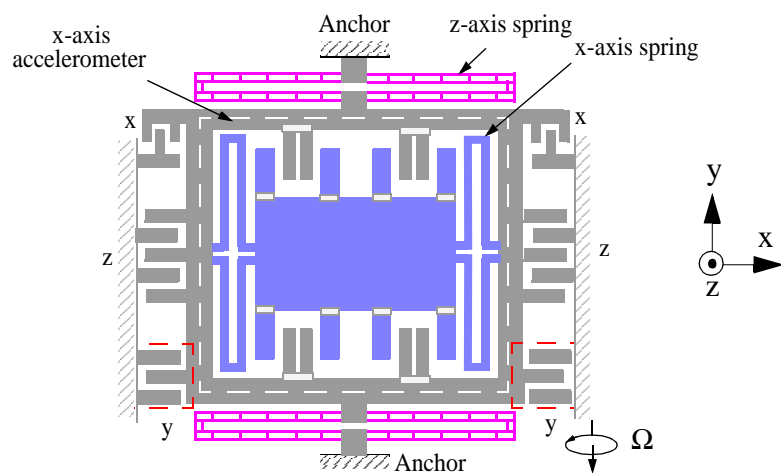


Figure 5-13: Y-axis gyroscope design with vertical drive.

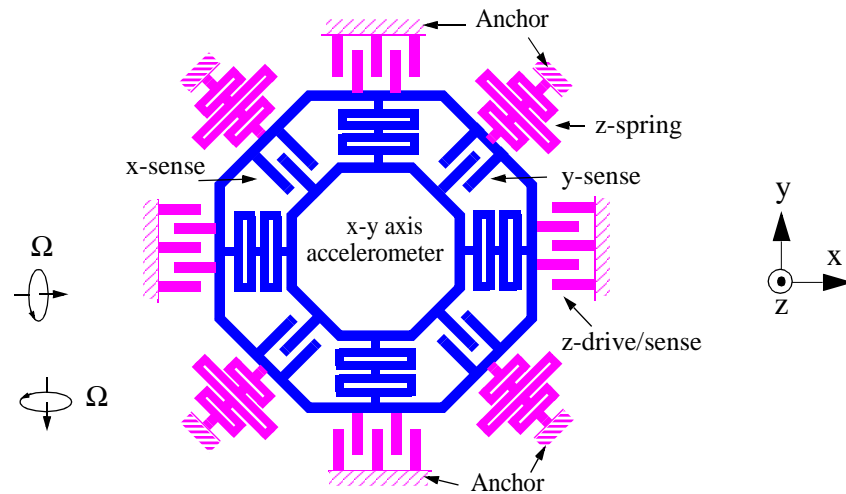


Figure 5-14: X/y dual-axis gyroscope design with vertical drive.

Dual-axis gyroscopes with vertical drive can be realized, too. As shown in Fig. 5-14, the topology of the x/y dual-axis gyroscope with vertical drive looks quite different from the x/z dual-axis gyro with lateral drive (see Fig. 5-11). The major difference is the embedded x-y dual-axis accelerometer. The x-y spring is introduced in Section 5.2.2. The sense comb fingers are divided into two groups. These two groups of comb fingers are orthogonal to each other. All the comb fingers are wired such that only the transverse lateral motion can be sensed. Therefore each group is responsible for sensing of only one axis.

### (3) *Torsional drive*

When a frame rotates along its central line, the two sides always move in the opposite directions. Most importantly, the torques on both sides generated by an external linear acceleration cancel each other assuming the frame is symmetric with respect to the rotation axis. Therefore, high linear acceleration rejection can be expected from gyroscopes

with torsional drive. Several vibratory gyroscope designs with torsional drive are sketched in Fig. 5-15 and Fig. 5-16. Fig. 5-15 shows three different topologies for y-axis single-gimbaled gyroscopes. Fig. 5-16 is a dual-gimbaled y-axis gyroscope.

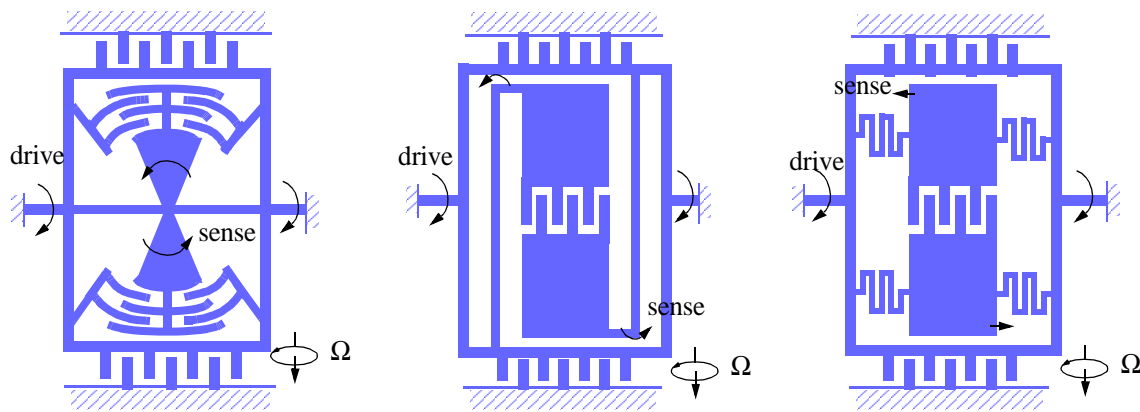


*Figure 5-15: Single-gimbaled gyroscopes with torsional drive.*

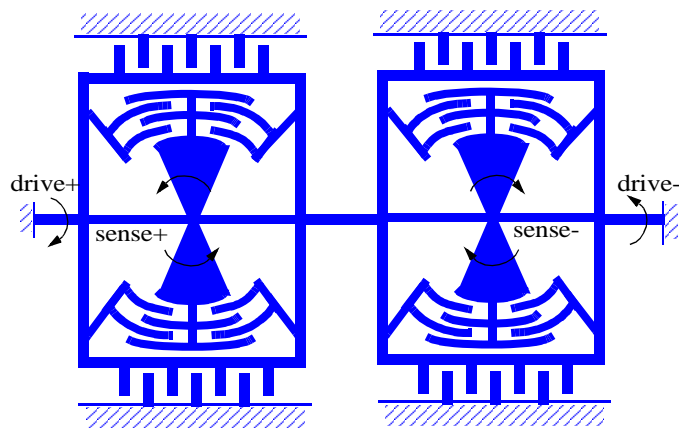


*Figure 5-16: Dual-gimbaled gyro with torsional drive.*

## **5.4 Gyroscope Simulation**

In order to compare the different designs and assess the expected performance of each design, a multi-level simulation strategy is employed. Lumped parameter simulation is performed at the early design stage for functionality evaluation, in which Matlab/Simulink can be used. Then a behavioral simulation is conducted by using the NODAS library [55] for quickly scanning and then choosing the geometric parameters.

Process variations are the major source to generate imperfection and structural asymmetry in gyroscopes. In this section, how various process variations affect the performance of a gyroscope will be investigated.

As the existing NODAS library is primarily designed for in-plane motion sensing/actuation for the thin-film CMOS-MEMS process, the beam and plate models are modified to fit microstructures fabricated by using the DRIE CMOS-MEMS process. Z-axis sensing and actuation models with lumped damping coefficients are also developed for lateral-axis gyroscopes.

In the following, high-level simulation of a gyroscope by Matlab/Simulink is described first. A x-axis gyroscope is modeled in Simulink as a nonlinear time-varying system. Then the NODAS model extension is introduced, followed by NODAS simulation of a DRIE z-axis gyroscope and its performance change with process variations. A DRIE z-axis gyroscope whose drive spring and sense spring both have silicon layer underneath is used as the example because silicon layer has the largest variations in DRIE microstruc-



It is evident that the z-axis actuation is nonlinear. In order to investigate the influence of this nonlinearity to the sensor output, the gyroscope is modeled as a nonlinear time-varying system dependent on the external rotation  $\Omega(t)$ . Considering the fact that  $\Omega(t)$  changes much slower (two orders of magnitude slower, at least) than the drive signal, we can simulate the system by sampling  $\Omega(t)$ . The system is then simplified as a LTI system during each sampling period. The block diagram is shown in Fig. 5-17(a). The z-axis actuation and the simplified LTI model can be easily represented using Simulink, as shown in Fig. 5-17(b). A simple Matlab program is used to update the system matrix and initial conditions and execute the simulation loop.



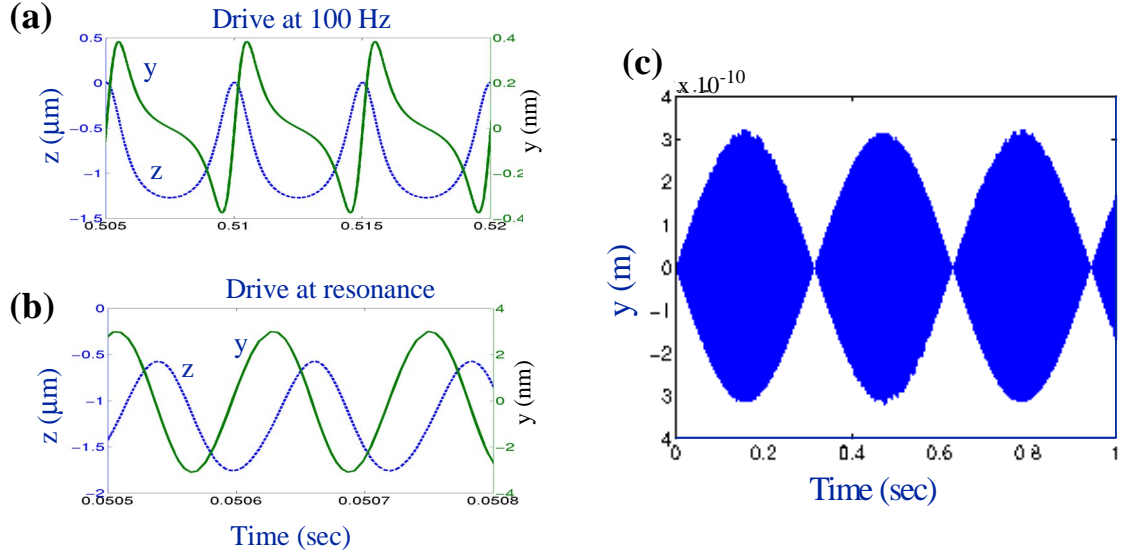


Figure 5-18: Matlab simulation result. Constant rotation in (a) and (b), and sinusoidal rotation in (c).

Fig. 5-18 shows a few simulation results. Among them, Fig. 5-18(a) and (b) are the  $y$ - and  $z$ -displacement waveforms with driving frequency at 100 Hz and resonance, respectively. The gyroscope vibrates in the  $z$ -direction and the induced Coriolis acceleration due to the external  $x$ -axis rotation is sensed in the  $y$ -direction. The rotation rate is constant for Fig. 5-18(a) and (b) and is set at 10 rad/s. Fig. 5-18(b) clearly shows that the second harmonic is suppressed when driven at resonance. The second harmonic is generated because the electrostatic force is proportional to the applied voltage squared. The nonlinear behavior of the  $z$ -axis comb drive does not affect the  $y$ - and  $z$ - waveforms. Fig. 5-18(c) is the  $y$ -displacement waveform when the whole structure resonates in the  $z$ -direction and  $\Omega = 1.0 \sin(10t)$  rad/s. The envelope of the waveform is proportional to  $\Omega(t)$ .

This analysis method is simple and can deal with arbitrary rotation input. Mode coupling and signal processing also can be easily incorporated. However, this method is based on a simplified lumped-parameter model without considering the actual topology or mechanical implementation of a gyroscope. On the other hand, the NODAS library [55] provides the capability to perform electromechanical analysis directly from topological construction. The next section describes how to use the NODAS library to do gyroscope design and simulation.

### **5.4.2 NODAS Simulation**

#### **5.4.2.1 Beam and plate NODAS models for DRIE beams**

As introduced in Section 2.2, the Si undercut existing in the DRIE process generates beams with a “T” shape cross-section as shown in Fig. 5-19(a). In order to calculate the moment of inertia of this irregular beam, first the centroid of the beam cross-section has to be computed. Then the moment of inertia with respect to the centroid is calculated [93]. Finally stiffnesses in different directions can be derived.

##### *(1) Centroid [94]*

The CMOS layer and Si layer have different effective Young’s moduli. To calculate the centroid of a structure with composite materials, one material is chosen as the reference, and then the other materials are scaled up or down according to their effective Young’s modulus ratio to the reference material. In Fig. 5-19(b), the CMOS layer is cho-

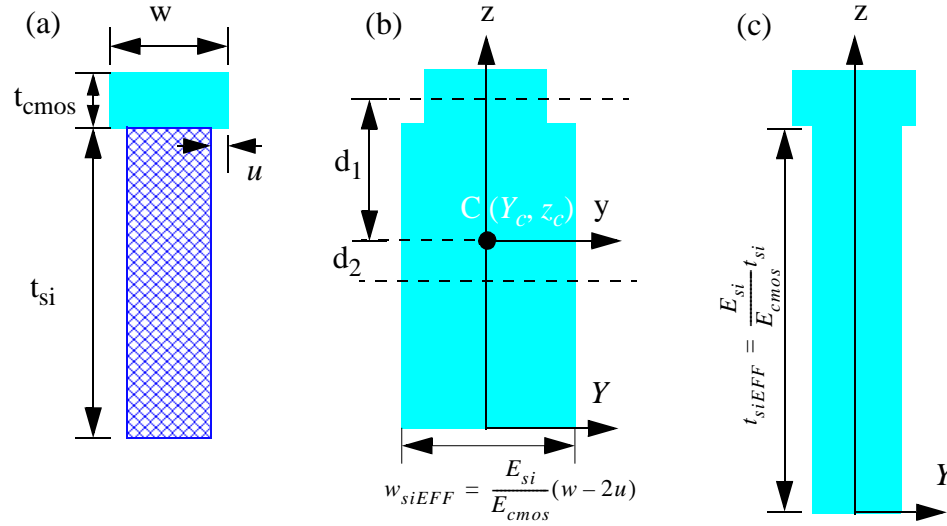


Figure 5-19: Calculation of moment of inertia for a "T" shape beam. (a) Beam cross-section; (b) Calculate  $I_y$  ( $Y$ -axis is used as a reference axis to compute the centroid  $C(Y_c, z_c)$ ); and (c) Calculate  $I_z$ .

sen as the reference, then the Si layer's width is scaled up to  $E_{si}/E_{cmos}$ , where  $E_{si}$  and  $E_{cmos}$  are the Young's modulus of the Si layer and CMOS layer, respectively. From the definition of the first moment of an area, the centroid  $(Y_c, z_c)$  in Fig. 5-19(b) can be expressed as,

$$Y_c = \frac{\sum_i A_i Y_i}{\sum_i A_i} = 0 \quad (5-25)$$

$$z_c = \frac{\sum_i A_i \bar{z}_i}{\sum_i A_i} = \frac{\left(t_{si} + \frac{t_{cmos}}{2}\right)t_{cmos}w + \frac{t_{si}}{2}t_{si}w_{siEFF}}{t_{cmos}w + t_{si}w_{siEFF}} \quad (5-26)$$

where  $A_i$ ,  $\bar{Y}_i$  and  $\bar{z}_i$  are area and coordinates of the centroids of each area, respectively, and  $i=1,2$ . As indicated in Fig. 5-19(a),  $t_{si}$  and  $t_{cmos}$  are the thicknesses of the Si layer and

CMOS layer, respectively,  $w$  is the beam width,  $u$  is the Si undercut on each side, and  $w_{siEFF}$  is the scaled-up effective width of the Si layer.

(2) *Moment of inertia*

By using the parallel-axis theorem [94], the moment of inertia with respect to the  $y$  axis can be expressed as

$$I_y = \sum_{i=1}^n (I_i + d_i^2 A_i) = \frac{1}{12} w \cdot t_{cmos}^3 + \left( t_{si} - z_c + \frac{1}{2} t_{cmos} \right)^2 w \cdot t_{cmos} \quad (5-27)$$
$$+ \frac{1}{12} w_{siEFF} \cdot t_{si}^3 + \left( z_c - \frac{1}{2} t_{si} \right)^2 w_{siEFF} \cdot t_{si}$$

Since the  $z$  axis is a centroidal axis, there is no need to calculate the centroid in Fig. 5-19(c) in order to compute the moment of inertia with respect to the  $z$  axis, *i.e.*,  $I_z$  which is given by the following equation,

$$I_z = I_{z-cmos} + I_{z-si} = \frac{1}{12} w^3 \cdot t_{cmos} + \frac{1}{12} (w - 2u)^3 \cdot t_{siEFF} \quad (5-28)$$

where  $t_{siEFF} = (E_{si}/E_{cmos})t_{si}$ .

(3) *Stiffness*

After the moment of inertia is obtained, the stiffnesses in various directions are readily given by [95]

$$k_x = \frac{\sum_{i=1}^n E_i A_i}{l} = \frac{E_{cmos} w t_{cmos} + E_{si} (w - 2u) t_{si}}{l} \quad (5-29)$$

$$k_y = \frac{12 \cdot E_{cmos} I_z}{l^3} \quad (5-30)$$

$$k_z = \frac{12 \cdot E_{cmos} I_y}{l^3} \quad (5-31)$$

$$k_{\phi x} = \frac{G_{eff} a^3 b}{3l} \left[ 1 - \frac{192a}{\pi^5 b} \sum_{n=1,3,\dots}^{\infty} \frac{1}{n^2} \tanh\left(\frac{n\pi b}{2a}\right) \right] \quad (5-32)$$

where  $l$  is the beam length,  $G_{eff}$  is the effective shear modulus of the beam,  $a = \min(t_{eff}, w_{eff})$ ,  $b = \max(t_{eff}, w_{eff})$ , and  $t_{eff}$  and  $w_{eff}$  are the effective thickness and width of the beam.

$$k_{\phi y} = \frac{6 \cdot E_{cmos} I_y}{l^2} \quad (5-33)$$

$$k_{\phi z} = \frac{6 \cdot E_{cmos} I_z}{l^2} \quad (5-34)$$

where  $k_x$ ,  $k_y$  and  $k_z$  are the stiffnesses of the beam in the x-, y- and z- directions, respectively, and  $k_{\phi x}$ ,  $k_{\phi y}$  and  $k_{\phi z}$  are the torsional stiffnesses of the beam with respect to the x, y and z axes, respectively.

#### (4) Extended NODAS models

After plugging in the above equations into the existing NODAS models [55], the DRIE-ready beam and plate models are obtained. The user design parameters include beam/plate width, beam/plate length, Si undercut, CMOS layer thickness and Si layer thickness. The mechanical properties for both materials are embedded in the models.

#### (5) Model verification

A fixed-fixed beam with a central mass is used to verify the extended NODAS models. The microstructure consists of a 5  $\mu\text{m}$ -thick CMOS layer and a 50  $\mu\text{m}$ -thick Si layer.

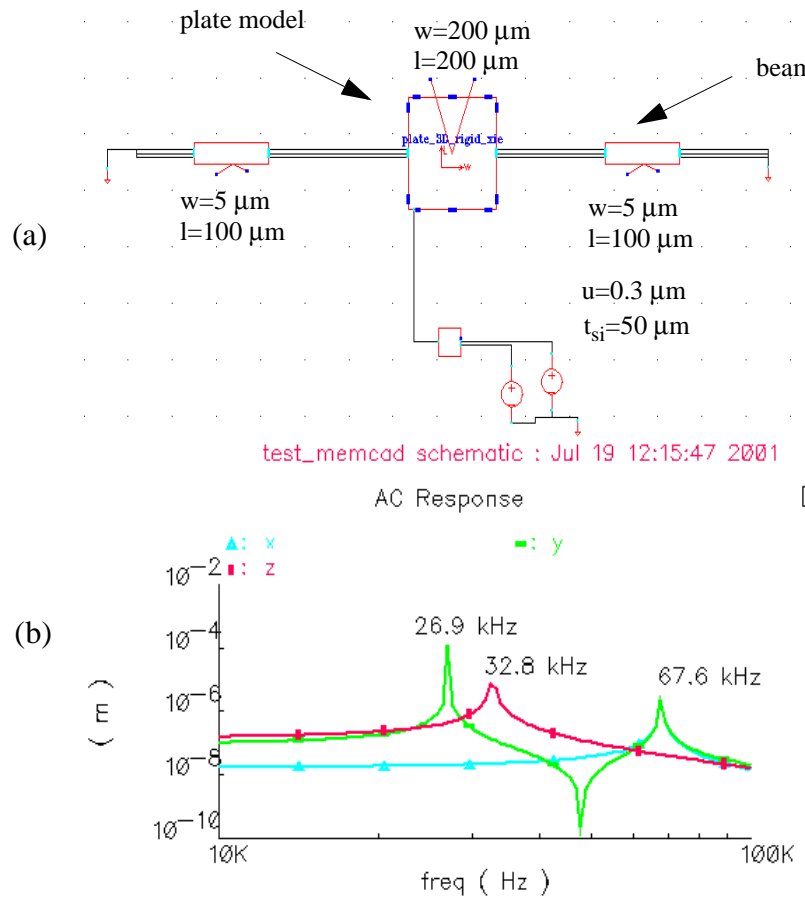


Figure 5-20: NODAS test model and frequency response simulation result.

Fig. 5-20 shows the NODAS model and its frequency response. Table 5-2 shows the NODAS simulation results compared to the ANSYS simulation. They match within 10%.

**Table 5-2: Comparison of NODAS simulation with ANSYS simulation**

	mode 1	mode 2	mode 3	Unit
NODAS	26.9	32.4	67.6	kHz
ANSYS	27.0	35.4	68.2	

### 5.4.2.2 NODAS Representation of a Gyroscope

The investigated gyroscope structure has no curved or polygonal shapes and thus can be constructed from the models in the NODAS library. From the simulation methodology point of view, there is no difference between lateral-axis and z-axis gyroscopes. However a DRIE z-axis gyroscope is chosen mainly because both its drive springs and sense springs have a Si layer. The process variations of the Si layer are the focus of the simulation study. Iyer has studied thin-film gyroscopes extensively [97]. Fig. 5-21 is a schematic drawing of a DRIE z-axis gyroscope, which is a simplified version of the gyroscope design shown in Fig. 5-10(a). It vibrates in the x-direction and senses the Coriolis acceleration in the y-direction. Fig. 5-22 shows the NODAS circuit schematic of the gyroscope. There are two types of comb drive models. One type is the longitudinal actuation comb drive; the other type is the transverse differential sense comb drive. The design parameter values are listed in Table 5-3. The Si undercut in the table refers to the undercut on each side of a beam.

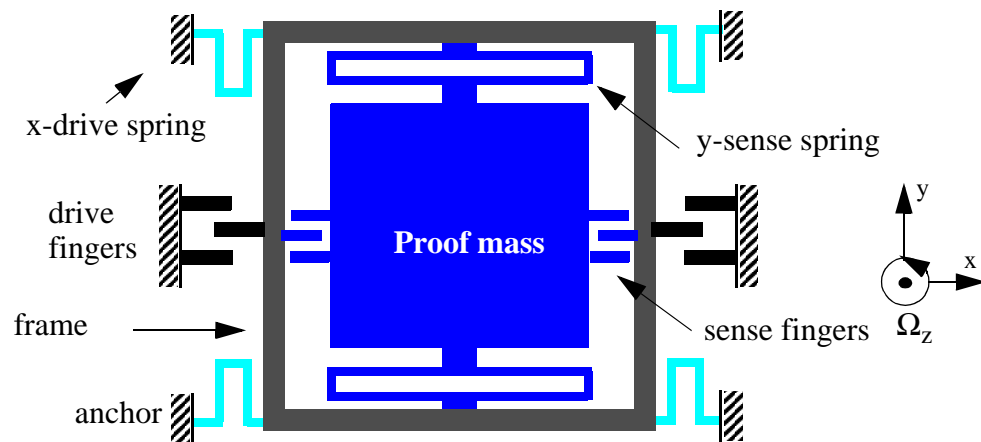


Figure 5-21: Topology of a z-axis gyroscope.



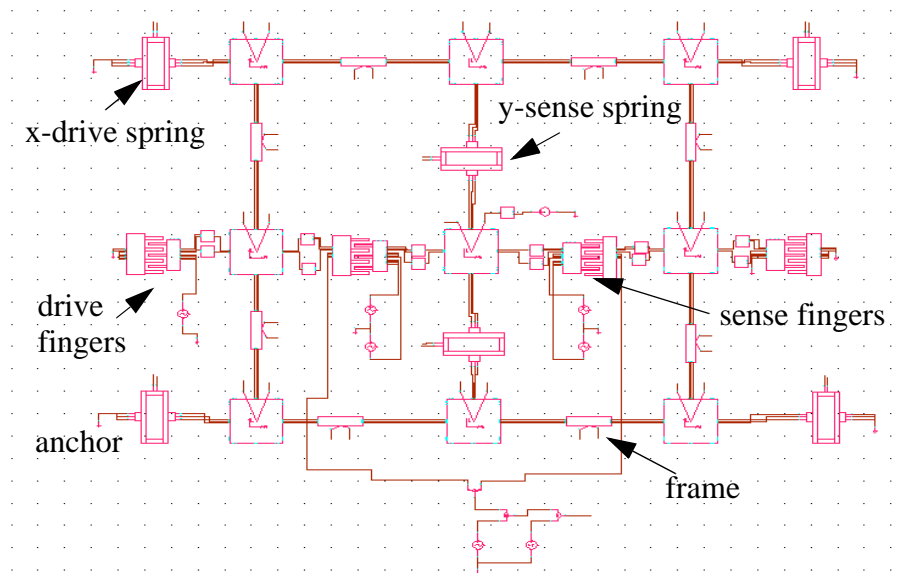


Figure 5-22: NODAS model of the z-axis gyroscope.

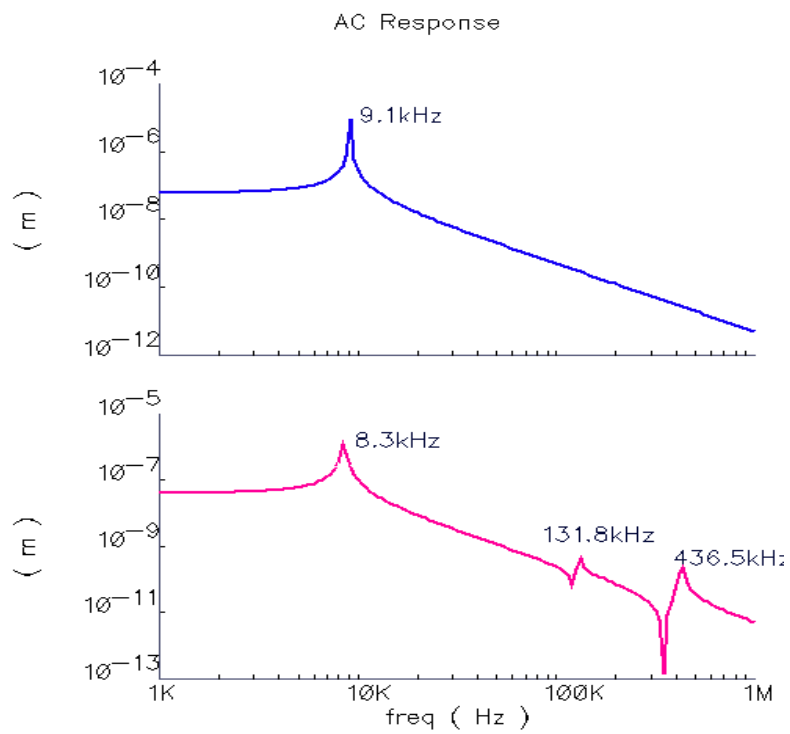
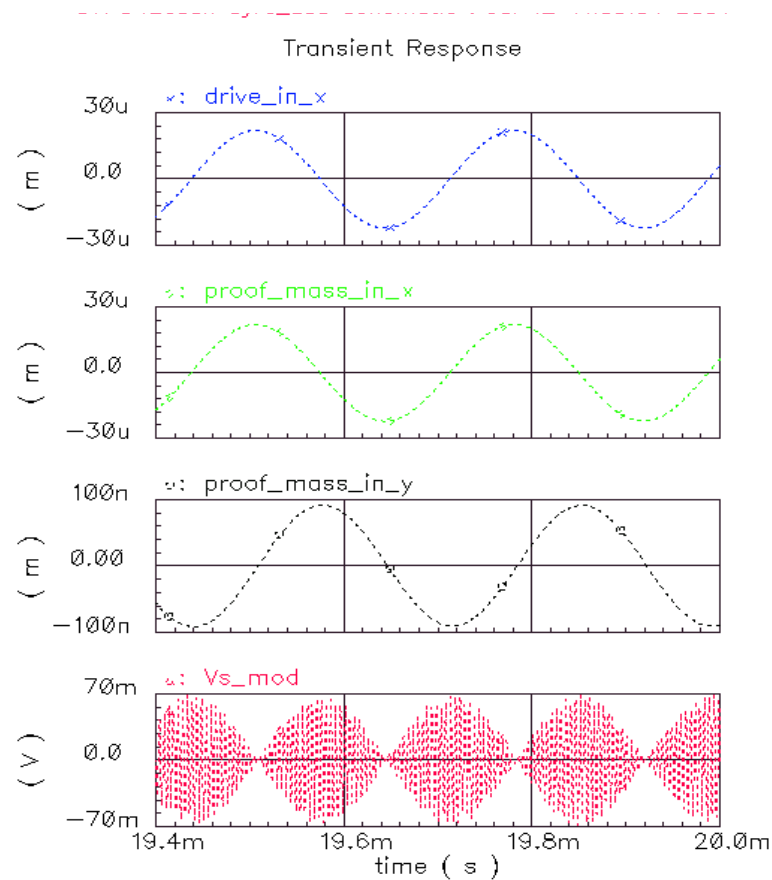


Figure 5-23: Frequency response of the z-axis gyroscope.

**Table 5-3: Design data sheet of the gyroscope for NODAS simulation**

	width	length		# of turns	width	length
frame	80 $\mu\text{m}$	800 $\mu\text{m}$	drive spring	1	6 $\mu\text{m}$	180 $\mu\text{m}$
proof mass	600 $\mu\text{m}$	660 $\mu\text{m}$	sense spring	1	6 $\mu\text{m}$	200 $\mu\text{m}$
Si thickness	50 $\mu\text{m}$		Si undercut	0.9 $\mu\text{m}$		

Fig. 5-23 shows the frequency response. The drive mode and sense mode are slightly separated. Spring softening or thermal heating can be used to tune the resonant frequency of the drive mode. Fig. 5-24 shows the transient response. From Eq. (5-1), the Coriolis

*Figure 5-24: Transient response of the z-axis gyroscope.*

acceleration is proportional to the vibration velocity, therefore, there is a  $90^\circ$  phase shift between the vibration displacement and the induced Coriolis force. If the sense mode has the same resonant frequency as that of the drive mode, the sense displacement will be  $90^\circ$  behind the Coriolis force. In this case, the drive displacement and sense displacement are either in-phase or  $180^\circ$  out-of-phase depending on the sign of the rotation rate. However, the phase shift indicated in Fig. 5-24 is about  $90^\circ$ . The reason for this is because the resonant frequency of the sense mode is designed to be slightly higher than that of the drive mode. This phase deviation from  $90^\circ$  depends on the difference between the two resonant frequencies and the damping.

### **5.4.3 Process Variation Simulation**

Process variations exist in every process step. Typical examples include lithography misalignment, curvature of CMP polished surface, overetch or underetch, and temperature fluctuation or gas flow disturbance during thin-film deposition, which result in variations in flatness, thickness, sidewall profile and sidewall cut-in. Shkel et al. explored the gyroscopic effects in the presence of imperfections associated with asymmetry and anisotropy of microstructures [96]. For CMOS-MEMS processes, microstructures may be affected by both CMOS processes and post-CMOS process steps. The misalignment of metal masks in CMOS processes, ion milling effects of top metal layer including variations of thickness, mass and curling, and sidewall slope variations due to oxide undercut and back scattering of energized ions are the major variations for thin-film CMOS-MEMS structures and have been studied in [97].

On the other hand, mechanical properties of DRIE CMOS-MEMS structures are dominated by Si layer. The variations of the CMOS layer have much smaller influence to a DRIE microstructure than that of the variations of the thickness and undercut of the Si layer. Also, the magnitudes of the variations in the Si layer are about one order larger than those in the CMOS layer. Therefore, only the thickness and undercut of the Si layer are chosen as the parameters to study process variations in this thesis.

The variations occur device to device and within a device. In order to understand how these variations affect the performance of a DRIE gyroscope, two simplified cases are considered: inter-die variation, which is defined as one that has the same impact everywhere on a whole wafer, and intra-die variation, which is modeled as a linear change in the variable across a structure [98].

For gyroscopes in terms of process variations, there is a variety of performance measures such as variations of resonant frequencies, vibration amplitude, sense amplitude, off-axis motion (or quadrature), zero-rate-output (ZRO), linear acceleration ( $g$ ) and  $g^2$  sensitivities. Among them,  $g$  sensitivity is related to the nonlinearity of the Coriolis acceleration sensing element and will be discussed in Section 6.2.6. ZRO and  $g^2$  sensitivity for a thin-film z-axis gyroscope were studied in [97].

The simulation can be carried out by using worse-case corner analysis, Monte Carlo analysis or parameter sweeping. The purpose of this study is to understand how the variation of each interested parameter affects the device performance. Therefore the parameter sweeping method is used in this thesis.

As discussed in the previous section, the gyroscope can be simulated in Cadence/SpectreS through a NODAS library. Both parameters (*i.e.*, thickness and undercut of the Si layer) will be swept in both the inter-die and intra-die cases. For every change of each parameter in either case, an AC analysis is needed to find the resonant frequencies of the drive mode and sense mode as the operating frequency must track the resonant frequency of the drive mode. Moreover, a rotation rate sweeping is also needed to check whether it has any influence to the resonant frequencies. As a result, there are hundreds of simulation runs. Each run takes 15 minutes to 1 hour depending on the complexity of the system. Therefore, the Open Command Environment for Analysis (OCEAN) in Cadence is used to automatically run the simulation and collect the resultant data.

#### **5.4.3.1 OCEAN**

OCEAN [99] is a text-based process run from a UNIX shell or from the Command Interpreter Window (CIW) of Cadence. OCEAN allows automation of setup, simulation and analysis of circuit data. OCEAN commands can be typed in an interactive session, or scripts containing OCEAN commands can be created and then loaded into OCEAN. There are three types of OCEAN commands, (1) Simulation Setup Commands to specify the analyses to be run, the nets and currents to save, the simulator option values and the circuit stimulus; (2) Simulator Run Commands to run the simulator; and (3) Data Access Commands to perform calculations on the results, print information and plot waveforms.

### 5.4.3.2 Simulation block diagram

All the simulation results, stored in the parameter storage format (PSF), are accessible through the OCEAN data access commands. Fig. 5-25 shows the block diagram of the

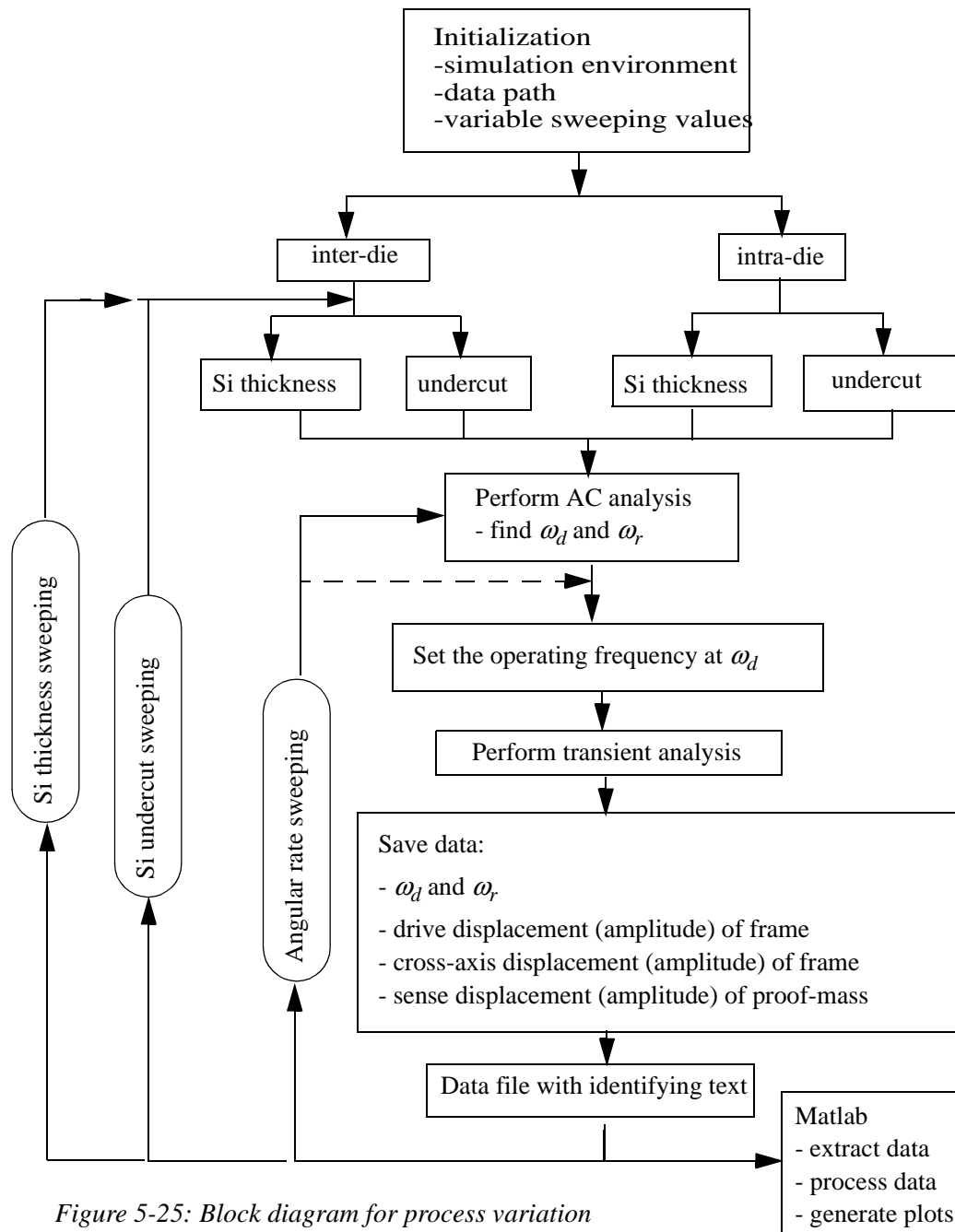


Figure 5-25: Block diagram for process variation simulation using OCEAN.

simulation procedure. First, simulation setup commands are used to set the simulation environment, generate values for variable sweeping and set other initialization conditions. The two cases, i.e., inter-die and intra-die variations, are simulated in sequence in a single OCEAN file. For each case, the two parameters, Si thickness and Si undercut, are independently considered. That is, one parameter stays at its nominal value when sweeping is performed to the other. Since the gyroscope is designed to always operate at  $\omega_d$ , the resonant frequency of the drive mode, an AC analysis is needed for each sweeping point to find  $\omega_d$ , which is then set as the operating frequency for the transient analysis. The transient analysis is used to extract the parameters of interest including the primary drive motion and coupled motion of the frame, and the sense motion of the proof mass. Alternatively, these motions can be extracted from another AC analysis. Note that this latter method provides only *rms* values. All the extracted data are saved in a file consecutively. The data can be accessed by the sequence or the identification text. Finally a Matlab program is used to process the data and plot graphs.

#### **5.4.3.3 Simulation Settings**

The same topology design as shown in Fig. 5-21 is used for this study. However, due to the convergence difficulty associated with the NODAS comb models<sup>\*</sup>, the comb fingers were removed to accelerate the simulation and their equivalent mass was added into the central proof-mass plate. The damping was provided by a lumped-parameter damper which simply consists of a damping factor. Force sources, instead of electrostatic comb

---

<sup>\*</sup>The problem was solved recently [100].

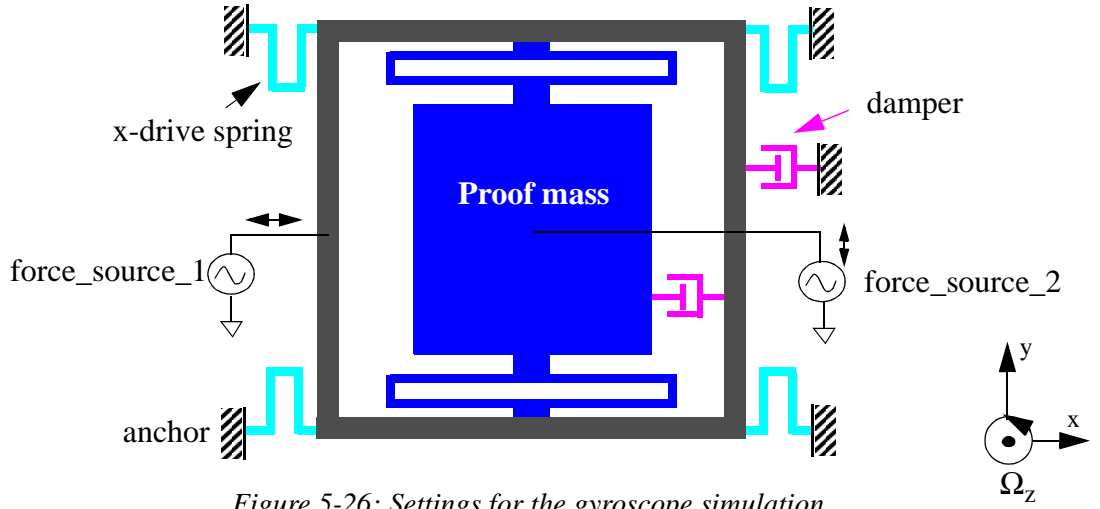


Figure 5-26: Settings for the gyroscope simulation.

drives, are used to actuate the device, as shown in Fig. 5-26. For the AC analysis in Fig. 5-25, both force sources are AC forces with an amplitude of  $1 \mu\text{N}$ . For the transient analysis, force\_source\_1 is a sinusoidal force source with an amplitude of  $1 \mu\text{N}$  and a frequency set at the resonant frequency of the drive mode obtained from the prior AC analysis.  $1 \mu\text{N}$  is chosen for the convenience to scale up the actual drive force needed to obtain the desired vibration amplitude.

The above settings apply to both inter-die and intra-die variations.

#### 5.4.3.4 Inter-die Variation

As discussed above, only two parameters vary with process variations in this study. They are Si thickness and Si undercut and their nominal value is  $50 \mu\text{m}$  and  $0.9 \mu\text{m}$ , respectively. The large undercut is required for obtaining electrical isolation of Si comb fingers (see Fig. 5-13). Fig. 5-27 shows the simulation results for these variables as a func-



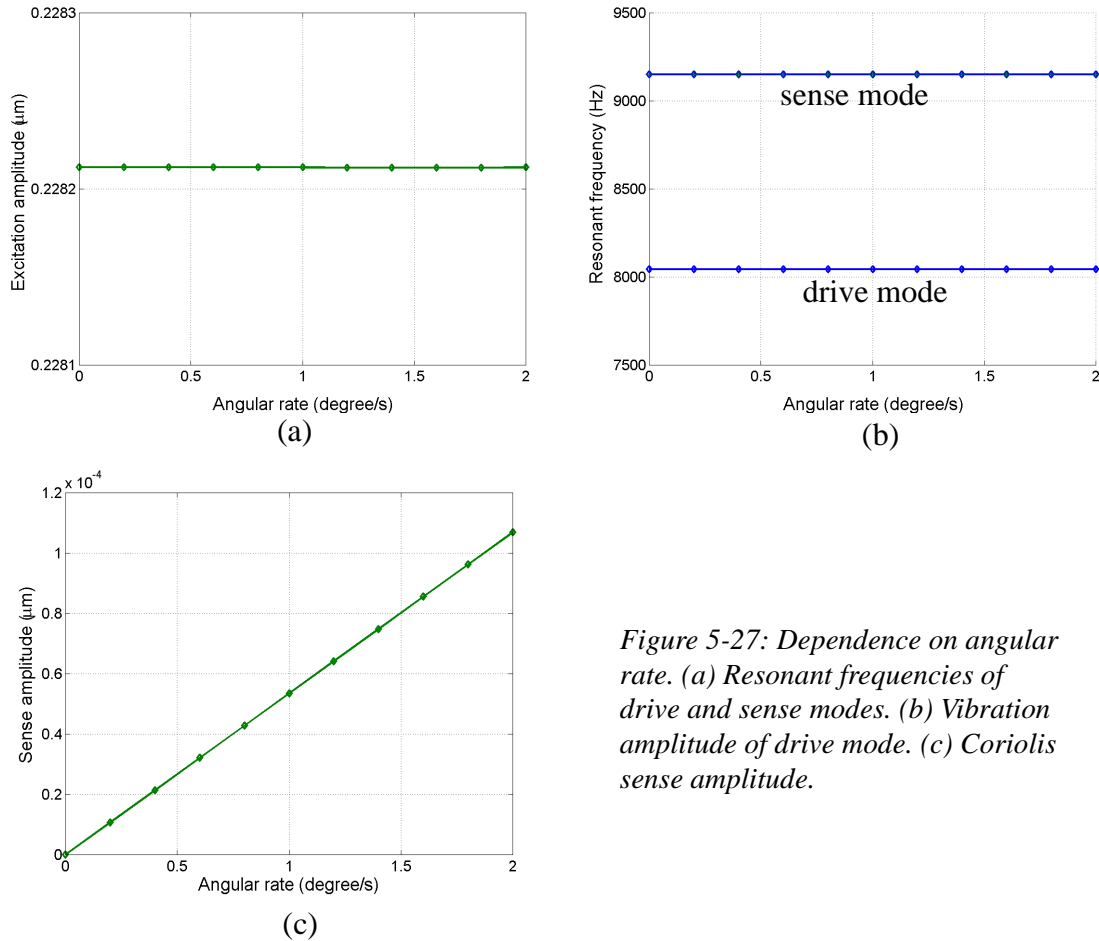


Figure 5-27: Dependence on angular rate. (a) Resonant frequencies of drive and sense modes. (b) Vibration amplitude of drive mode. (c) Coriolis sense amplitude.

tion of steady-state angular rate. Changing rotation rate does not change the resonant frequencies and excitation amplitude (Fig. 5-27(a)). As expected, the sense amplitude linearly depends on the rotation rate in the range of interest (Fig. 5-27(c)). The mechanical sensitivity with respect to the excitation amplitude is  $0.5 \text{ nm}/\mu\text{m}/\text{rad/s}$ , or  $0.01 \text{ nm}/\mu\text{m}/^\circ/\text{s}$ , or 10 ppm (part per million) per  $^\circ/\text{s}$ . Therefore if there is a gap of  $1.8 \mu\text{m}$ , the electrical sensitivity is  $11 \mu\text{V}/^\circ/\text{s}/\text{V}$  per  $1 \mu\text{m}$  excitation amplitude before any circuit amplification and ignoring attenuation from parasitic capacitance.

The two parameters affected by processing variations are the Si membrane thickness and the Si undercut. First, the thickness of the Si membrane varies from 10  $\mu\text{m}$  to 100  $\mu\text{m}$  while the Si undercut stays unchanged at its nominal value. For a structure composed of a homogeneous material, both in-plane spring constants and masses are linearly proportional to the out-of-plane thickness, and thus the resonant frequencies of the in-plane drive and sense modes will not change with the thickness of the structure in the out-of-plane direction. However, the simulation shows that both resonant frequencies increase with increasing Si thickness as shown in Fig. 5-28(a). This is due to the multi-layer structures provided by the DRIE CMOS-MEMS process. As shown in Fig. 2-6, a microstructure fabricated by the DRIE CMOS-MEMS process consists of a CMOS layer on the top and a Si layer underneath. The mechanical properties of such a beam are determined by both materials. The thickness variation of the CMOS layer is negligible compared to the Si layer thickness. When the Si layer becomes thinner, the mechanical properties of the beam will be more dominated by the CMOS layer. Since the effective Young's modulus of a CMOS layer is only one-third as much as that of silicon, the stiffness will decrease with decreasing Si thickness. Because both layers have almost the same mass density, the resonant frequencies decrease with decreasing Si thickness. Therefore, the Si layer should not be too thin. The resonant frequency gradients with respect to the Si thickness are plotted in Fig. 5-28(b). The plot shows that the resonant frequencies of the drive and sense modes change only 0.01%/ $\mu\text{m}$  and 0.02%/ $\mu\text{m}$  or less, respectively, for Si thickness greater than 40  $\mu\text{m}$ .

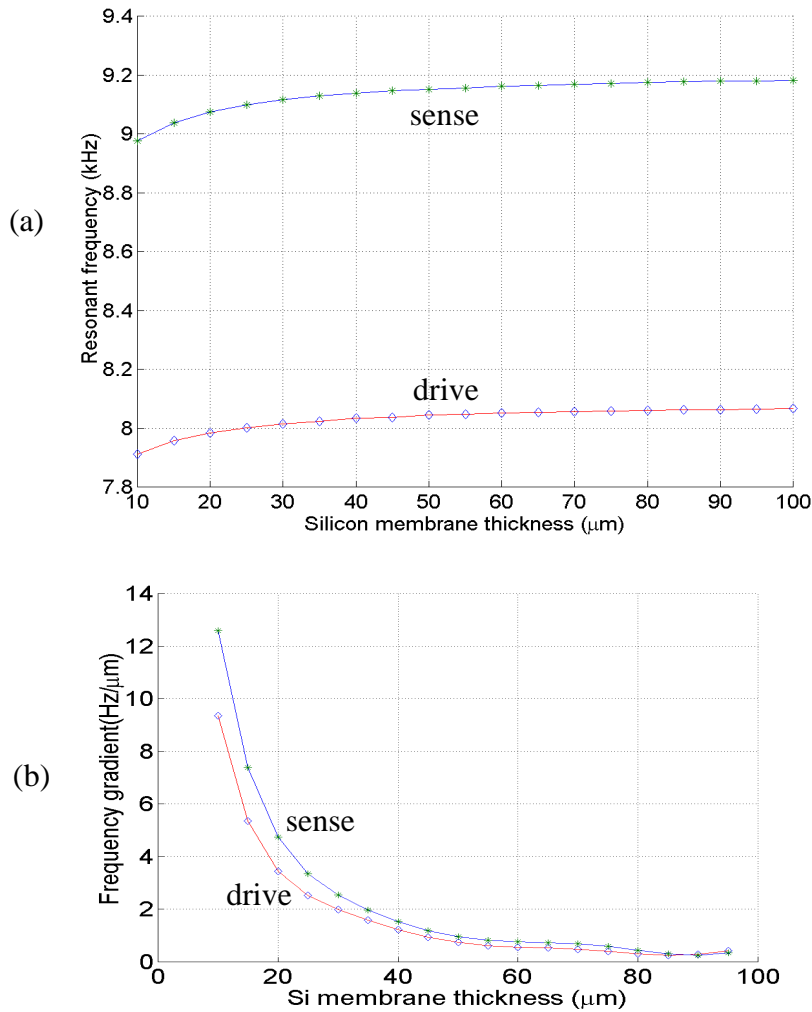


Figure 5-28: Inter-die variation: Si thickness dependence. (a) Resonant frequencies of drive and sense modes. (b) Frequency change rate with respect to Si thickness.

In these simulations, the amplitude of the force source is fixed. Thus, the amplitude of the excitation vibration decreases with increasing Si thickness as the stiffness has an approximate inverse dependence to Si thickness, as shown in Fig. 5-29(a). The displacement of the sense mode follows the same trend (see Fig. 5-29(b)).

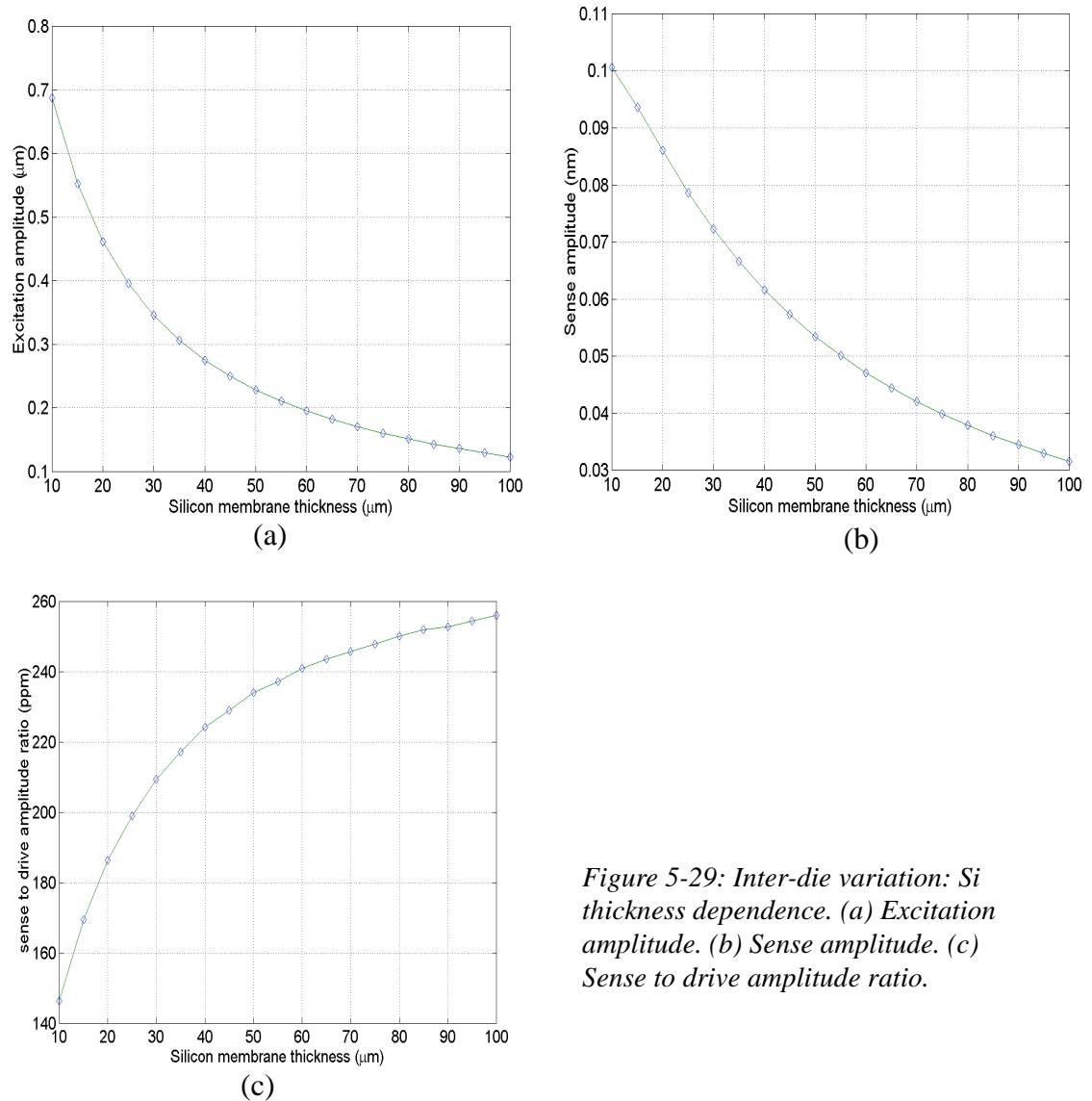


Figure 5-29: Inter-die variation: Si thickness dependence. (a) Excitation amplitude. (b) Sense amplitude. (c) Sense to drive amplitude ratio.

It is also interesting to see how the sense displacement changes with the drive displacement. It is one way to check the stability of the phase lag of the sense displacement with respect to the drive displacement or the stability of the mechanical sensitivity. Fig. 5-29(c) shows the dependency, in which the sense-to-drive amplitude ratio increases with increasing Si thickness. It means that the two modes are getting slightly closer when Si

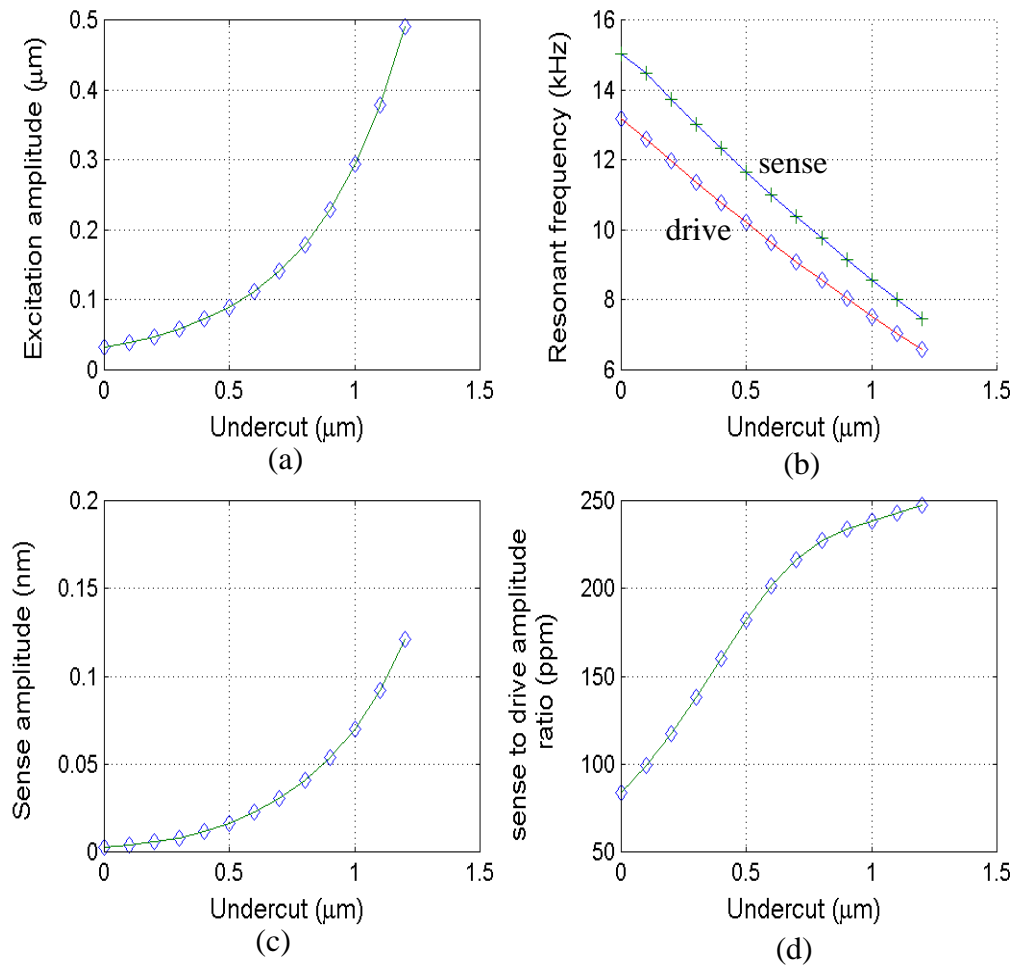


Figure 5-30: Inter-die variation: Undercut dependence. (a) Excitation amplitude. (b) Resonant frequencies of drive and sense modes. (c) Coriolis sense amplitude. (d) Sense to drive amplitude ratio.

thickness increases. After it reaches to 40  $\mu\text{m}$  or beyond, the dependency of the ratio to Si thickness is significantly reduced (see Fig. 5-29(c)).

Fig. 5-30 shows the influence of a inter-die undercut variation. The nominal value for undercut is 0.9  $\mu\text{m}$ . In this case, Si thickness stays unchanged at 50  $\mu\text{m}$ . The undercut decreases the width of Si layer of the spring beams, but the top CMOS interconnect layer

is always  $6.0\text{ }\mu\text{m}$  wide. The springs become less stiff with more undercut. Therefore, the resonant frequencies decrease and the amplitudes of the excitation and sense motion increase when the undercut increases. Also note that the undercut of the proof mass and drive frame will reduce the masses. However, since the frame and proof mass are about  $80\text{ }\mu\text{m}$  and  $600\text{ }\mu\text{m}$  wide, respectively, this effect has much less impact compared to the spring beam undercut.

Fig. 5-30(b) shows that the drive mode and sense mode change rapidly with the undercut, causing the phase lag or the mechanical sensitivity to change rapidly too but the trend slows down significantly after the undercut is  $0.8\text{ }\mu\text{m}$  or beyond (Fig. 5-30(d)).

From the above discussion, one can draw the following conclusions:

- 1). As long as the Si thickness is larger than about  $40\text{ }\mu\text{m}$ , the resonant frequencies of both drive and sense modes are insensitive to the Si thickness. The mechanical sensitivity also stabilizes after the Si thickness is larger than about  $40\text{ }\mu\text{m}$ .
- 2). The resonant frequencies decrease with increasing undercut. The mechanical sensitivity has small change with the undercut variation if the undercut is larger than  $0.8\text{ }\mu\text{m}$ .
- 3) The chosen nominal values for Si thickness and undercut is rational.

### 5.4.3.5 Intra-die Variations

Variations may not be uniform across a single die. Three cases for variations of both Si thickness and Si undercut of the spring beams are considered: 1) variation along the x axis; 2) variation along the y axis; and 3) variation along both the x- and y- axes. The thickness and width parameters of the drive and sense spring beams are defined in Fig. 5-31 and the detailed parameter settings are listed in Table 5-4. Note that variations of Si thickness and undercut are considered separately here. When the undercut is the variable, the Si thickness is fixed at  $t_0 = 50 \mu\text{m}$  which is the nominal value. When the Si thick-

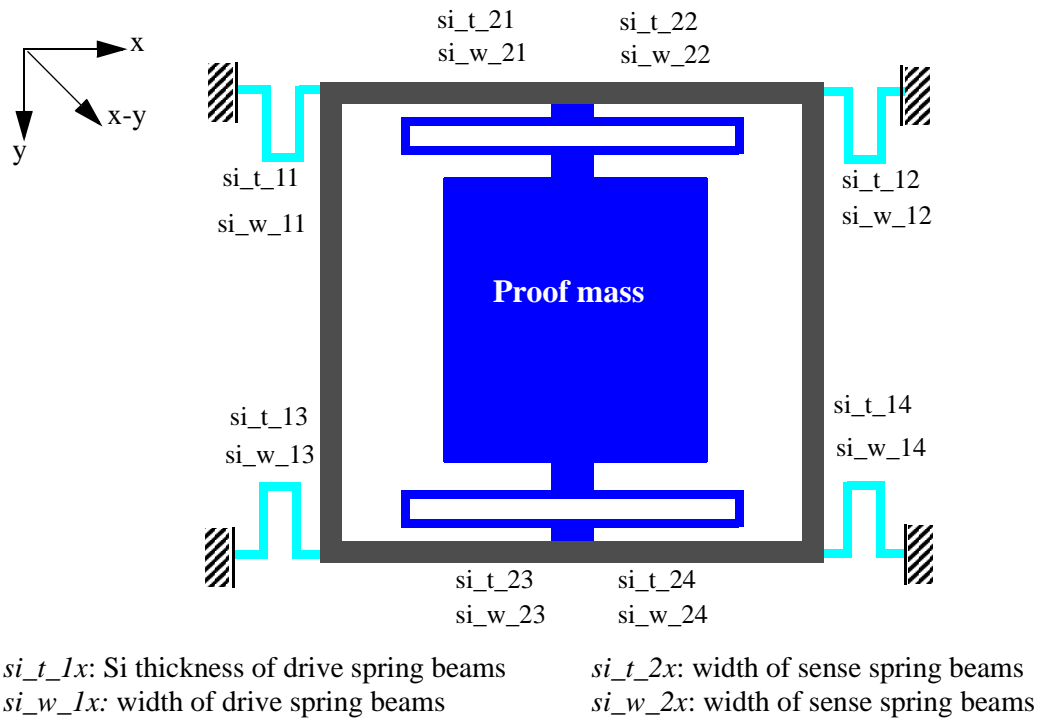


Figure 5-31: Parameter definition for distributed variation simulation.

ness is the variable, the undercut is fixed at its nominal value, i.e.,  $u_0 = 0.9 \mu\text{m}$ . So the nominal Si width of the spring beams  $W_0$  is equal to the width  $W_b$  of the top metal layer in the spring beams reduced by the undercuts on both sides, i.e.,  $W_0 = W_b - 2u_0$ .

**Table 5-4: Assignment of parameter values for distributed variation simulation**

Process variable			Undercut			Si thickness		
			x axis	x-y axis	y axis	x axis	x-y axis	y-axis
drive spring	Si layer width	si_w_11	$W_0 + \Delta u$	$W_0 + \Delta u$	$W_0 + \Delta u$	$W_0$ (fixed)		
		si_w_12	$W_0 - \Delta u$	0	$W_0 + \Delta u$			
		si_w_13	$W_0 + \Delta u$	0	$W_0 - \Delta u$			
		si_w_14	$W_0 - \Delta u$	$W_0 - \Delta u$	$W_0 - \Delta u$			
	Si layer thickness	si_t_11	$t_0$ (fixed)			$t_0 + \Delta t$	$t_0 + \Delta t$	$t_0 + \Delta t$
		si_t_12				$t_0 - \Delta t$	0	$t_0 + \Delta t$
		si_t_13				$t_0 + \Delta t$	0	$t_0 - \Delta t$
		si_t_14				$t_0 - \Delta t$	$t_0 - \Delta t$	$t_0 - \Delta t$
sense spring	Si layer width	si_w_21	$W_0 + \Delta u$	$W_0 + \Delta u/2$	$W_0 + \Delta u$	$W_0$ (fixed)		
		si_w_22	$W_0 - \Delta u$	0	$W_0 + \Delta u$			
		si_w_23	$W_0 + \Delta u$	0	$W_0 - \Delta u$			
		si_w_24	$W_0 - \Delta u$	$W_0 + \Delta u/2$	$W_0 - \Delta u$			
	Si layer thickness	si_t_21	$t_0$ (fixed)			$t_0 + \Delta t$	$t_0 + \Delta t/2$	$t_0 + \Delta t$
		si_t_22				$t_0 - \Delta t$	0	$t_0 + \Delta t$
		si_t_23				$t_0 + \Delta t$	0	$t_0 - \Delta t$
		si_t_24				$t_0 - \Delta t$	$t_0 - \Delta t/2$	$t_0 - \Delta t$



All the variations are assumed to be linearly graded. For example, in the case of undercut variation along the x axis, the undercut on one side of the device increases while the undercut on the other one side decreases.

The simulation results for the cases where the Si thickness is the variable are shown in Fig. 5-32. The resonant frequencies of both modes are almost unchanged within the considered Si thickness variation range (Fig. 5-32(a)). The lateral-stiffness of a spring beam is linearly dependent on the Si thickness. Therefore, the sum of spring stiffnesses cancels out the effects from the linearly graded variations. The excitation amplitudes have very small change ( $\sim 10$  ppm in  $5\text{ }\mu\text{m}$ ) with the Si thickness variation (Fig. 5-32(b)). This indicates that the resonant frequencies do change a small amount (less than 1 Hz which is the incremental frequency step for the simulation). However, the sense amplitude of the y-case changes significantly with the Si thickness variation (Fig. 5-32(c)). In principle, the sense amplitude is proportional to the operation frequency and the excitation amplitude. If these two quantities have very small changes, the sense amplitude should follow the same way. There must be other sources causing the unexpected change to the sense amplitude.

Fig. 5-32(d) plots the off-axis (i.e., the axis orthogonal to the primary drive axis) displacement. Again, the y-case has significant change with Si thickness variation. Comparing Fig. 5-32(c) and Fig. 5-32(d), it is clear that the off-axis motion directly couples into the Coriolis signal. It is understandable that the y-case has the largest off-axis motion, since the y-case has thicker springs on one side than those on the other side.

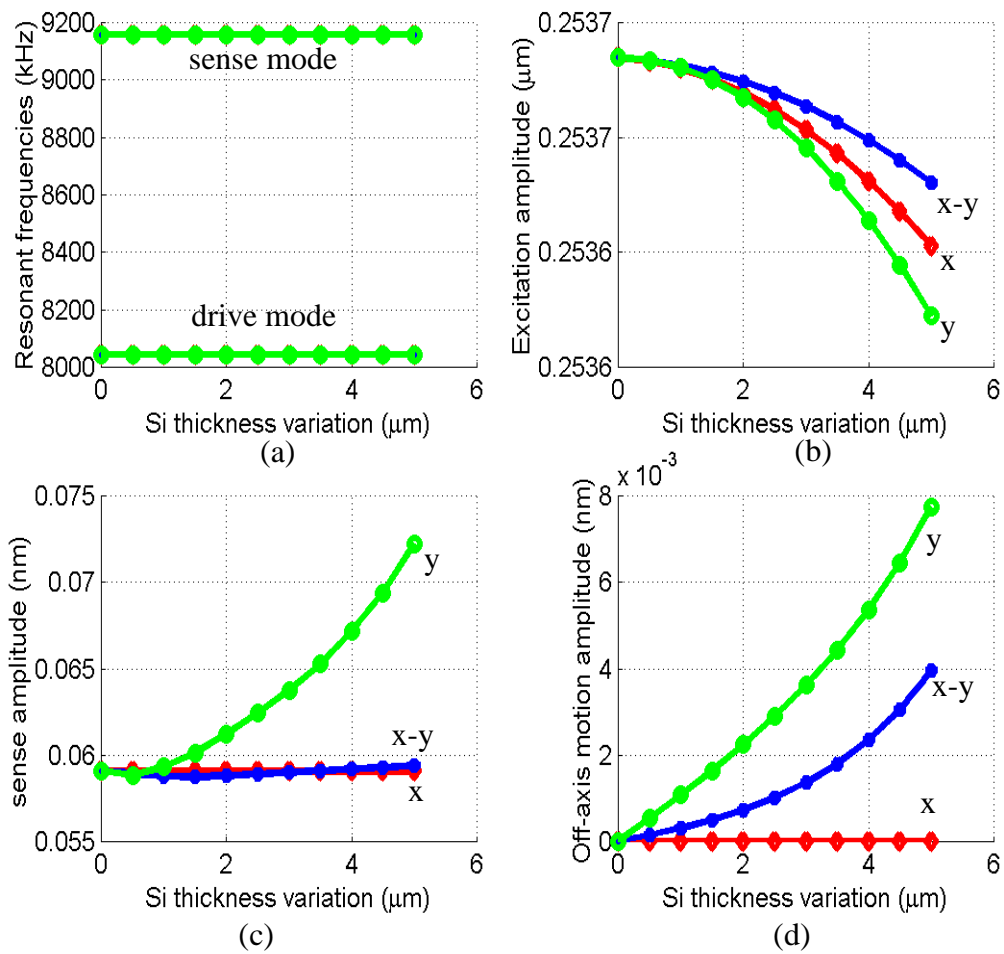


Figure 5-32: Intra-die variation: Si thickness dependence. (a) Resonant frequencies of drive and sense modes. (b) Vibration amplitude of drive mode. (c) Coriolis sense amplitude. (d) Off-axis motion on the drive frame.

Also note that the x-case, which has thickness variation along the drive direction, change little with the thickness variation in all the simulated aspects. Therefore, keeping the uniformity in the direction perpendicular to the drive direction is much more important than in the drive direction itself.

Similar to the Si thickness, the variations of the Si undercut are also considered in three cases as given in Table 5-4. The simulation results are shown in Fig. 5-33. Different from the Si thickness variation simulation results, the resonant frequencies of both sense and drive modes change with the variation of the undercut (Fig. 5-33(a)). This is due to the fact that the lateral-stiffness is proportional to the cube of the spring beam width. For the same reason, the excitation amplitudes slightly decrease with increasing undercut unbalance (Fig. 5-33(b)).

The sense amplitude in the x-case follows the excitation amplitude change as there is zero off-axis motion (Fig. 5-33(c)), while the sense amplitude of the x-y case is totally dominated by the coupled off-axis motion (Fig. 5-33(d)). However, the sense amplitude in the y case increases slightly even though the off-axis motion is large.

In summary, the same observation as the intra-die thickness variation case is obtained in the intra-die undercut case, i.e., variations along the perpendicular direction of the drive direction generate the largest off-axis motion.

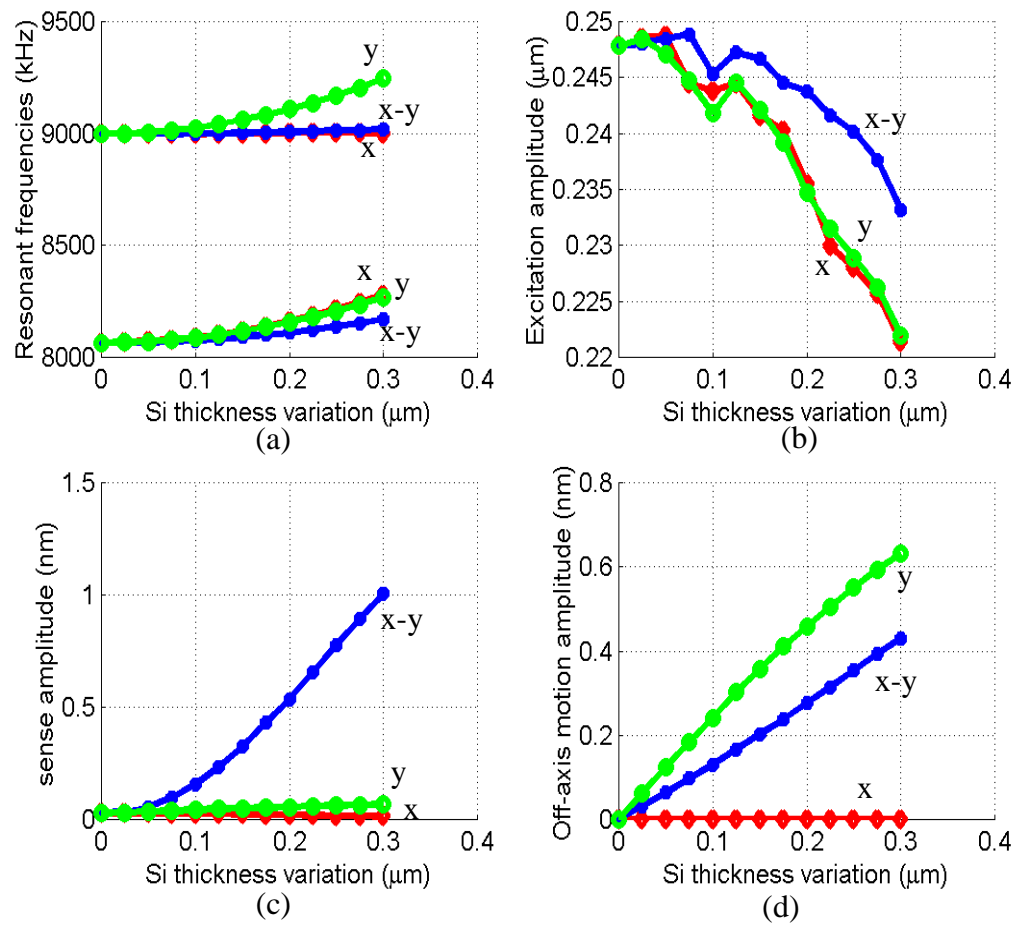


Figure 5-33: Intra-die variation: Undercut dependence. (a) Resonant frequencies of drive and sense modes. (b) Vibration amplitude of drive mode. (c) Coriolis sense amplitude. (d) Off-axis motion on the drive frame.

#### **5.4.3.6 Summary**

From the inter-die variation simulation, it is found that the thickness of the Si layer should be at least 40  $\mu\text{m}$  to make the resonant frequencies of both drive and sense modes insensitive to the Si thickness. Gyroscope performance always varies with the Si undercut variation. The best way to reduce the influence of the Si undercut may be to increase the beam width which of course adds more constraints to the design. Only simulation with fixed beam width is conducted in this thesis. More detailed simulations should be performed to make a rigorous conclusion.

The intra-die variation simulation also shows an interesting observation. Variations of either the Si thickness or undercut generate the largest off-axis motion when the changing direction of the variations are perpendicular to the excitation vibration direction.

## Chapter 6

# CMOS-MEMS Gyroscope Design, Fabrication & Characterization

The process variation simulation results in Chapter 5 show that a large coupled motion will be present and may dominate the Coriolis signal. Therefore, appropriate ways should be found to cancel the coupled motion. In this chapter, we introduce a DRIE CMOS-MEMS gyroscope which has extra sets of comb drives to compensate the off-axis motion. Before diving into the details of the DRIE gyroscope, characterization results of a thin-film CMOS-MEMS gyroscope are presented first.

### 6.1 Thin-Film CMOS-MEMS Gyroscope

#### 6.1.1 Structural Design

A lateral-axis microgyroscope needs either vertical actuation or vertical motion sensing. Considering the practical issues, such as the mismatch between rotor and stator fingers and the requirement of curl matching frames, vertical actuation as described in Chapter 3 is employed.

The topology of the lateral-axis gyroscope is shown in Fig. 6-1, which includes three key components: a z-axis comb drive, a y-axis accelerometer, and a z-axis position sensor

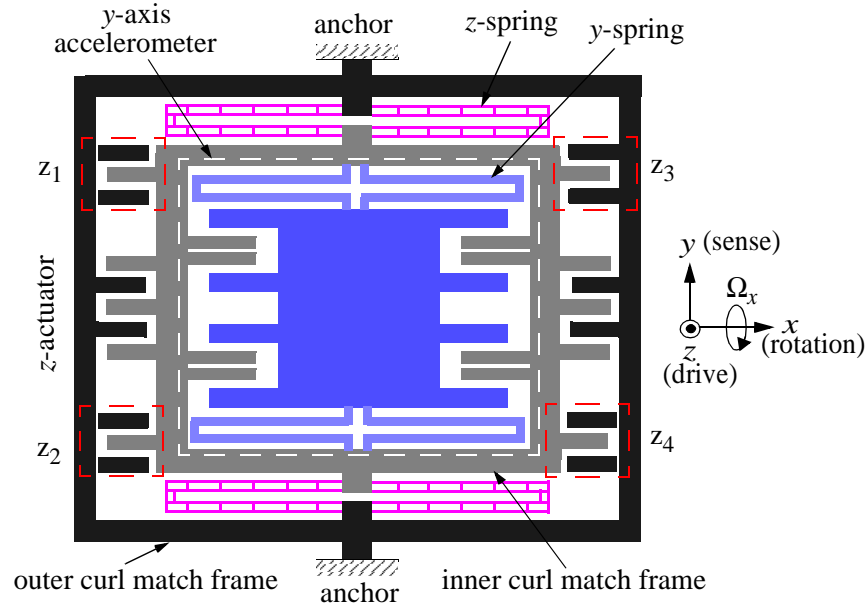


Figure 6-1: Topology of the lateral-axis gyroscope

used for feedback control of the z-axis actuation. The structure is a two-fold, orthogonal spring-mass system where the inner frame (together with the proof mass) is driven to vibrate in the z-direction by the comb drive while the induced Coriolis acceleration is sensed by the accelerometer. Thus, the rotation sense axis of this device is along the x-axis.

There are 180 comb fingers for z-axis actuation and 200 comb fingers for y-axis acceleration sensing. A y-axis actuator is also included inside the embedded y-axis accelerometer to compensate any off-axis motion coupled directly from the z-axis input excitation. Such coupling arises from manufacturing variations that cause imbalance in the proof mass and springs. Similar to the z-axis accelerometer in Fig. 3-9 in Section 3.2.3, all the motion sensors in the gyroscope have four groups of comb fingers forming a common-centroid configuration to reduce the influence of process variation on offset.

### 6.1.2 Fabrication and Characterization

The device was fabricated by using the thin-film CMOS-MEMS process as described in Section 2.2.1. Fig. 6-2 shows an SEM of a released gyroscope (CMOS circuitry is not shown). The gaps for both z-axis drive comb fingers and y-axis sense comb fingers are  $1.5\ \mu\text{m}$ . The microstructure is about  $0.8\ \text{mm}$  by  $0.6\ \text{mm}$ . Curl matching is achieved for both drive and sense comb fingers through the outer and inner frames, respectively.

The rotation sense axis of the gyroscope is along the x-direction. The y-axis spring suspending the inner accelerometer consists of tapered beams and exhibits minimal lateral curl, as shown in Fig. 6-3. However, the ends of the beams on the z-axis suspension curl up  $68\ \mu\text{m}$  (Fig. 6-4(a)). This curling can be compensated by injecting a current through a polysilicon resistor inside the spring beams. With the aid of an optical microvision

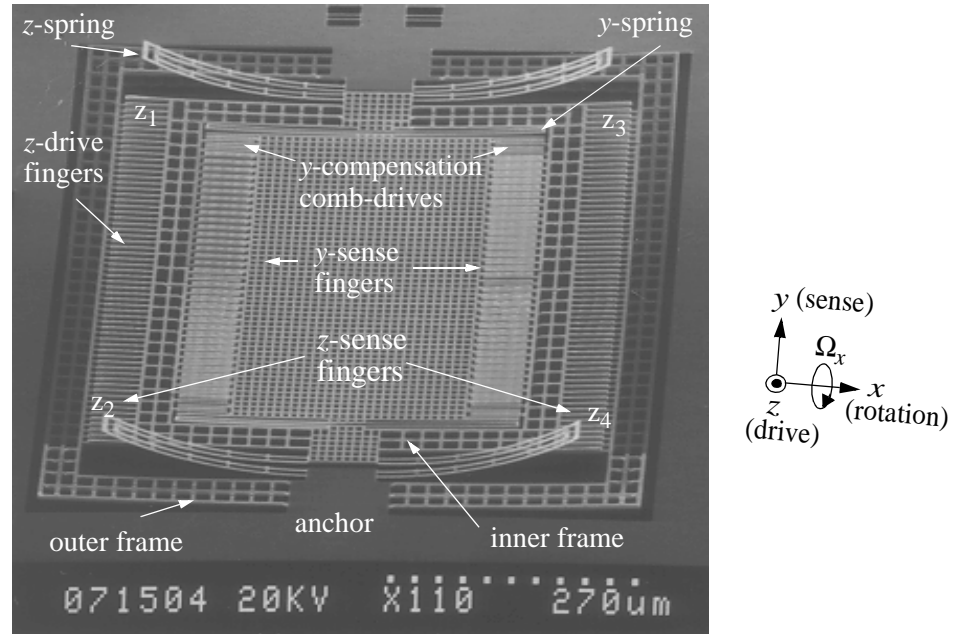


Figure 6-2: SEM of a released gyroscope.



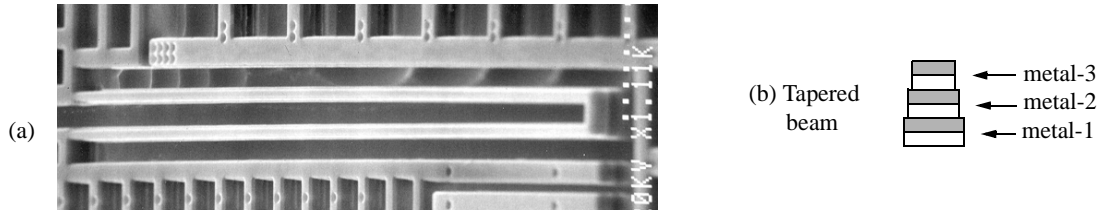


Figure 6-3: Lateral curling elimination. (a) a tapered y-spring demonstrating near perfect lateral alignment; (b) the cross-section of the tapered spring beam

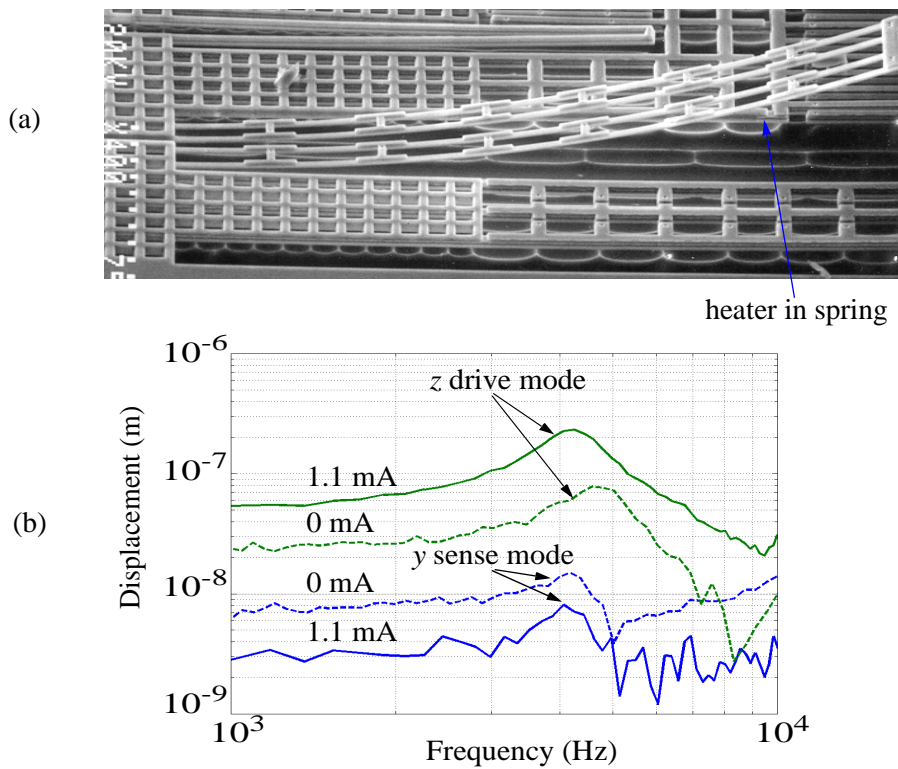


Figure 6-4: Resonant frequency matching and mode coupling suppression through heating. (a) SEM of a z-spring beam with an embedded polysilicon heater. (b) Frequency responses of the drive and sense modes with and without injecting current.

system [75], it was observed that flattening of the spring beams increases the suppression of the mode coupling and changes the resonant frequency of the drive mode (Fig. 6-4(b)). Meanwhile the resonance of the sense mode stays almost unchanged. Therefore, the inte-

grated heater provides an alternative method to match the resonant frequency between the sense and drive modes if necessary. The relationship between the heater current and the tip vertical deflection of the z-axis suspension beams is plotted in Fig. 6-5(a). Both the simulated and measured dependences of resonant frequency of the drive mode to the tip z-deflection are shown in Fig. 6-5(b). A rapid change occurs when the spring beams

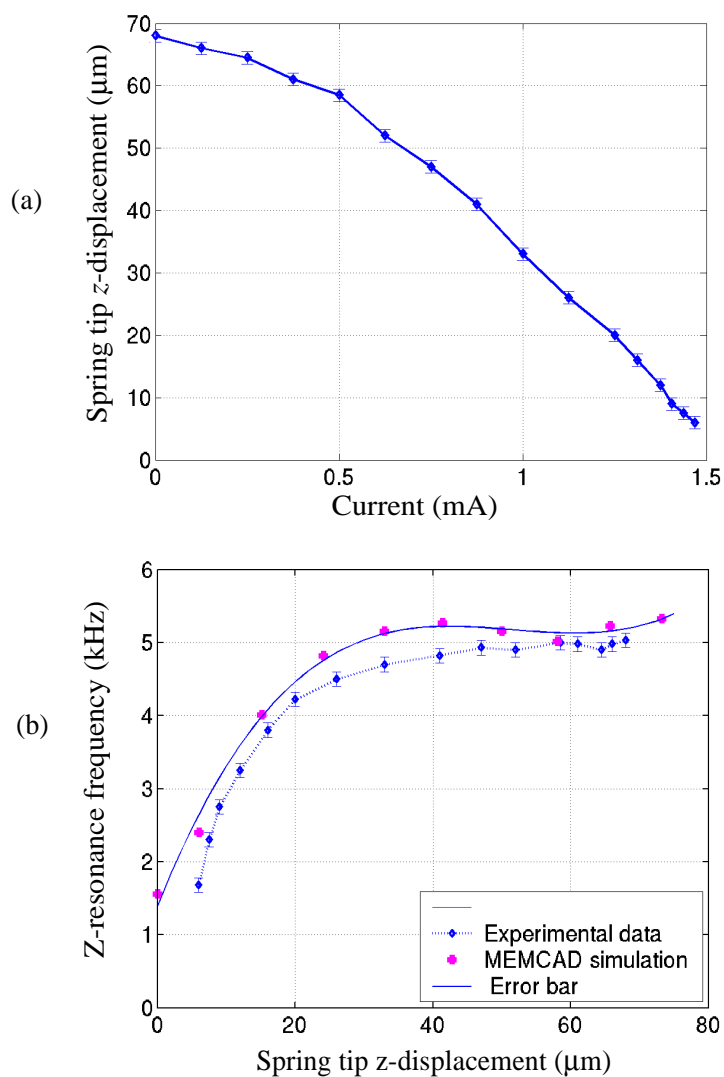


Figure 6-5: (a) Thermomechanical curling compensation as a function of applied current. (b) Resonant frequency tuning as a function of the z displacement at the cantilevered end of the spring

approach the curl matching state at a heater current of 1.1 mA. The experimental result is in agreement with the finite-element prediction by using the equivalent temperature approach developed by Lakdawala *et al* [57].

A fully-differential capacitive bridge is implemented, along with an on-chip differential preamplifier. A spectrum of the y-axis accelerometer response is plotted in Fig. 6-6 showing a resolution of  $100 \mu\text{G}/\text{Hz}^{1/2}$ . The rotation test result by using a turntable is shown in Fig. 6-7. The large DC offset is due to the remaining coupled motion. This test was performed in air with no current injected into the polysilicon heater to flatten the z-axis springs. Thus the coupled motion was large and drove the embedded y-axis accelerometer out of its linear range.

This large coupled motion was caused by the wobbling of the whole structure due to the lateral curling of the drive comb fingers. It is one of the main reasons to develop the

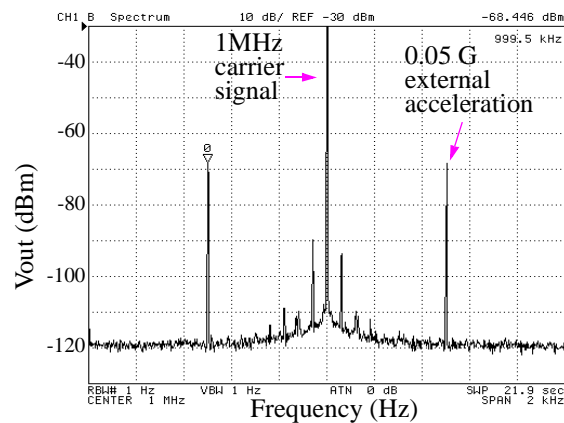
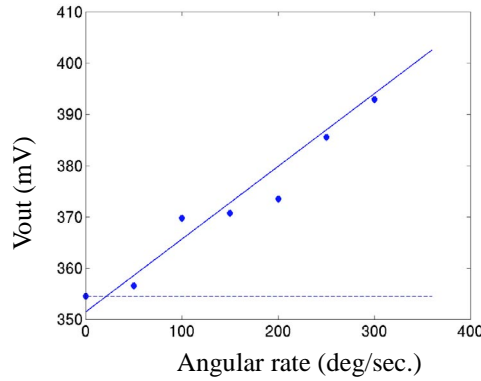


Figure 6-6: Spectrum of the y-accelerometer at a 500 Hz, 0.05 G external acceleration, showing a resolution of  $100 \mu\text{G}/\text{Hz}^{1/2}$ .



*Figure 6-7: Constant rotational rate measurement. A large DC offset was present because of the coupled motion from the drive mode.*

DRIE CMOS-MEMS process to make flat microstructures. In the following we will focus on the design, fabrication and characterization of a DRIE CMOS-MEMS gyroscope.

## **6.2 DRIE CMOS-MEMS Gyroscope**

### **6.2.1 Structural design**

As discussed in Section 5.2, eight possible topologies for DRIE gyroscopes are proposed. However, it is not realistic to validate all of them experimentally. Since the fabrication process has only been to a limited extent characterized, only relatively simple single-shuttle topologies were considered. Also, this thesis focuses on the unique vertical-axis actuation and sensing provided by the DRIE CMOS-MEMS process. Thus a topology with either vertical actuation or vertical sensing can be used. The vertical-axis compliance of a spring beam is achieved by using the thin-film layer. The thin-film lateral-axis CMOS-MEMS gyroscope introduced in the previous section shows that the vertical actuation by using z-compliant spring beams has a large mode coupling in the Coriolis acceler-

ation sense axis. The coupled motions result mostly from the lateral and vertical curling of the microstructures. Lateral-axis DRIE CMOS-MEMS gyroscopes have good overall flatness. From experience, the curling of the z-compliant thin-film spring beams affect the alignment of comb fingers very little. The misalignment can be less than  $0.1\text{ }\mu\text{m}$  through proper symmetric design. So lateral-axis DRIE gyroscopes are expected to have much better performance.

### **6.2.1.1 Vertical Actuation versus Vertical Sensing**

Lateral-axis gyroscopes with either vertical sensing or vertical actuation have very similar topologies as shown in Fig. 6-8. The major difference is the orientations of comb fingers. The orientation of lateral-axis sensing or actuation comb fingers is determined by the sensing or actuation axis. The orientation of vertical sensing or actuation comb fingers has no constraint. They may orient along the x-axis, y-axis, x-y axis or any arbitrary direction in the x-y plane. The actual orientation of vertical comb fingers depends on the orientation of the lateral comb fingers. For instance, the gyroscope shown in Fig. 6-8(a) has x-oriented comb fingers for x-axis actuation. A y-axis electrostatic force will be also generated since comb fingers always have some lateral offset even though very small in DRIE structures. This y-axis force produces a y-axis vibration acting on the central z-axis accelerometer. In order to minimize the sensitivity of the z-axis accelerometer to this undesired vibration, the z-axis comb fingers of the accelerometer orient along the y-axis. Also the z-axis comb fingers are divided into two groups with differential capacitance change with respect to the y-axis (see Fig. 6-8(a)). Then the sum of the differential capacitors is insen-

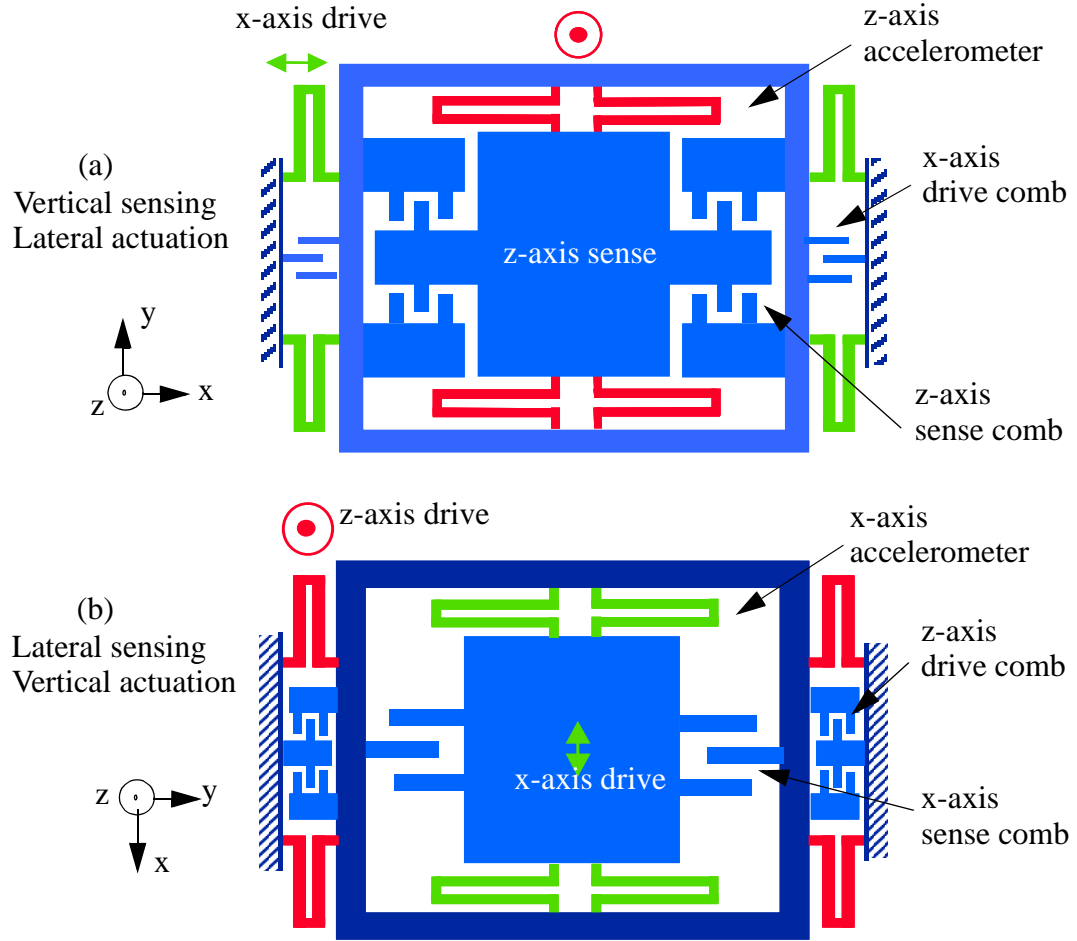


Figure 6-8: Comparison of vertical sensing and vertical actuation.

sitive to the  $y$ -axis vibration. Of course, globally, the  $z$ -axis comb fingers are divided into four groups to form a fully differential capacitive bridge for  $z$ -axis acceleration sensing. This will be discussed further in Section 6.2.4.

For the same consideration, the gyroscope with vertical actuation (see Fig. 6-8(b)) has  $x$ -axis oriented comb fingers for  $y$ -axis acceleration sense and  $y$ -axis oriented comb fingers for  $z$ -axis actuation.

Lateral spring beams have silicon underneath, and thus they are flat and have good comb-finger alignment and high stiffness ratio between the x, y and z axes. Therefore, the gyroscope shown in Fig. 6-8(a) that has a lateral-axis drive spring is expected to have a very stable excitation vibration. The gyroscope shown in Fig. 6-8(b) has a low sensitivity to vibrations in the directions orthogonal to the Coriolis acceleration direction.

In order to compare the performance of these two topologies, the electrostatic force analysis has to be studied first. Three-dimensional motion analysis for a comb drive is discussed in Section 5.3.3. The vibration coupled into the Coriolis force sense axis can be obtained from Eq. (5-22). In the vertical sensing case, the coupled motion refers to the motion coupled into the sense axis of the z-axis accelerometer, while in the vertical actuation case, the coupled motion is in the sense axis of the x-axis accelerometer. Notice the x-axis in Fig. 6-8(b) is along the orientation of the drive comb fingers. The amplitudes of the two coupled motions are respectively given by

$$z_c^{vs} = \frac{F_z^{vs}}{k_{z,drv}^{vs}} = \frac{1}{2} \cdot \frac{dC}{dz} \cdot \frac{V^2}{k_{z,drv}^{vs}} = \frac{\epsilon_0}{g} \cdot \frac{x_0 + x}{k_{z,drv}^{vs}} \cdot V^2 \quad (6-1)$$

$$x_c^{vd} = \frac{F_x^{vd}}{k_{x,drv}^{vd}} = \frac{1}{2} \cdot \frac{dC}{dx} \cdot \frac{V^2}{k_{x,drv}^{vd}} = \frac{\epsilon_0}{g} \cdot \frac{h - z_0 + z}{k_{x,drv}^{vd}} \cdot V^2 \quad (6-2)$$

where the subscripts “c”, and “drv” stand for coupling and drive mode, respectively, and the superscripts “vs” and “vd” for vertical sensing and vertical actuation, respectively.

The ratio of the two terms is readily given by

$$\frac{z_c^{vs}}{x_c^{vd}} = \frac{x_0 + x}{h - z_0 + z} \cdot \frac{k_{x,drv}^{vd}}{k_{z,drv}^{vs}} \quad (6-3)$$

Typically,  $x_0 = 3 \mu\text{m}$ ,  $h = 5 \mu\text{m}$  and  $z_0 = 1 \mu\text{m}$ . The spring constant ratio in the above equation may vary from 1 to 0.1 depending on the curling of the thin-film z-axis spring and the Si layer thickness of the x-axis spring. Thus, the vertical sensing topology has about an order of magnitude less coupled motion compared to the vertical actuation topology. The coupled motion in the vertical sensing case can be further reduced by using a z-axis force cancellation technique which will be discussed in Section 6.2.8.

Cross-sensitivity is another important performance measure of a gyroscope. Similar to the coupled motion, the cross-sensitivity studied here is also caused by an off-axis, undesired motion. This motion is along the rotation sense axis, i.e., y-axis in both topologies in Fig. 6-8. The amplitudes of the y-axis motions and their ratio can be expressed as

$$y^{vs} = \frac{F_y^{vs}}{k_{y,drv}^{vs}} = \frac{1}{2} \cdot \frac{dC}{dy} \cdot \frac{V^2}{k_{y,drv}^{vs}} = \frac{2\varepsilon_0(h - z_0 + z)(x_0^{vs} + x^{vs})(y^{vs} + y_0^{vs})}{g^3} \cdot \frac{V^2}{k_{y,drv}^{vs}} \quad (6-4)$$

$$y^{vd} = \frac{F_y^{vd}}{k_{y,drv}^{vd}} = \frac{1}{2} \cdot \frac{dC}{dy} \cdot \frac{V^2}{k_{y,drv}^{vd}} = \frac{2\varepsilon_0(h - z_0 + z)(x_0^{vd} + x^{vd})(y^{vd} + y_0^{vd})}{g^3} \cdot \frac{V^2}{k_{y,drv}^{vd}} \quad (6-5)$$

$$\frac{y^{vd}}{y^{vs}} = \frac{x_0^{vd} + x^{vd}}{x_0^{vs} + x^{vs}} \cdot \frac{y^{vd} + y_0^{vd}}{y^{vs} + y_0^{vs}} \cdot \frac{k_{y,drv}^{vs}}{k_{y,drv}^{vd}} \quad (6-6)$$

where  $x_0$  is about  $60 \mu\text{m}$  in the vertical actuation case but about  $5 \mu\text{m}$  in the vertical sensing case, and  $y_0$  in the vertical actuation case is about one order of magnitude greater than that in the vertical sensing case because of the thick, flat x-axis spring beams. The stiffness ratio in Eq. (6-6) may vary from 10 to 100. Therefore, the vertical actuation topology has about 60 to 80 dB greater cross-sensitivity than the vertical sensing.



### 6.2.1.2 The Gyroscope Topology

It is clear from the above discussion that the vertical sensing topology has better performance. Therefore a single-shuttle, single-axis, lateral-axis drive, vertical-axis sense topology has been chosen in this thesis, as illustrated in Fig. 6-9. This topology is similar to the one shown in Fig. 6-6(b). Since only its drive spring beams have silicon underneath, this topology is even more sensitive to process variations than the z-axis gyroscope discussed in Section 5.4.3 and thus an off-axis motion compensation mechanism should be included.

As shown in Fig. 6-9, the gyroscope primarily consists of a x-axis resonator and a z-axis accelerometer. A x-axis capacitive sensor, a y-axis actuator and a combined x/z-axis actuator also are integrated to control the excitation vibration and compensate the coupled motion.

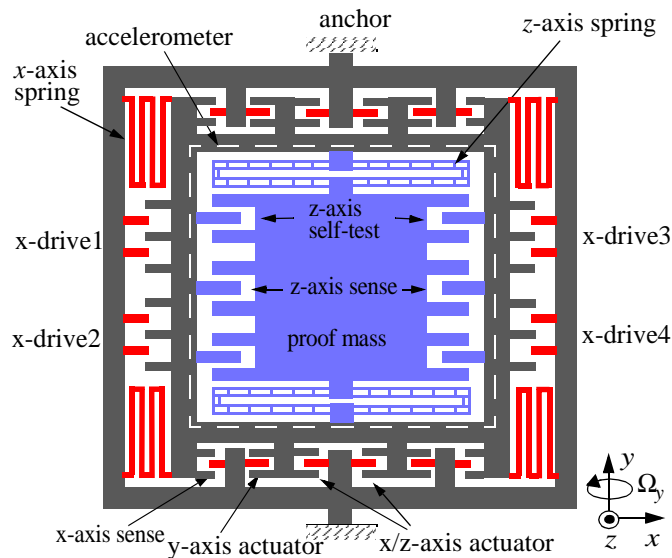


Figure 6-9: Topology of the lateral-axis DRIE gyroscope.

All the sensors and actuators are in the form of comb drives with the geometric parameters listed in Table 6-1. The z-axis accelerometer has thin-film spring beams for achieving z-axis compliance and is the same design as the DRIE accelerometer introduced in Section 3.3. The Si layer is used as a mechanical support.

**Table 6-1: Geometric parameters of comb drives of the gyroscope**

		finger width	finger length	# of fingers	overlap	gap	capacitance gradient or force
<b>Sense mode</b>	sense comb	4 $\mu\text{m}$	99 $\mu\text{m}$	41 $\times$ 8	95 $\mu\text{m}$	2.1 $\mu\text{m}$	83 aF/nm
	self-test comb	2 $\mu\text{m}$	15 $\mu\text{m}$	7 $\times$ 10	13.5 $\mu\text{m}$	2.1 $\mu\text{m}$	1.3 nN/V <sup>2</sup>
<b>Drive mode</b>	x-axis drive	3 $\mu\text{m}$	22 $\mu\text{m}$	67 $\times$ 4	6 $\mu\text{m}$	1.8 $\mu\text{m}$	16 nN/V <sup>2</sup>
	x-axis sense	3 $\mu\text{m}$	30 $\mu\text{m}$	23 $\times$ 4	10 $\mu\text{m}$	1.8 $\mu\text{m}$	0.13 fF/ $\mu\text{m}$
	y-axis drive	3 $\mu\text{m}$	70 $\mu\text{m}$	19 $\times$ 4	50 $\mu\text{m}$	2.1 $\mu\text{m}$	53 nN/V <sup>2</sup>
	x-axis/z-axis drive	3.6 $\mu\text{m}$	80 $\mu\text{m}$	19 $\times$ 4	60 $\mu\text{m}$	2.1 $\mu\text{m}$	4.1 nN/V <sup>2</sup> (x) 6.3 nN/V <sup>2</sup> (z)

The x-axis capacitive sensor, used to detect the drive motion, has separate groups of comb fingers located at each of the four corners to form a differential capacitive sensing bridge. A unity-gain buffer is required for the output bond pad. In the full system, the detected signal is amplified and fed back to the x-axis actuators to form an oscillator. However, in the experiments the gyroscope is run open loop. The y-axis actuator uses the parallel-plate electrostatic force existing in the comb fingers.

The combined x-axis/z-axis actuator is obtained by wiring the metal layers in the rotor fingers individually to bond pads and then configuring them off chip either as a x-axis actuator or a z-axis actuator. Section 3.3.1 includes the details of wiring.

In order to balance the excitation vibration in the x-y plane, the primary x-axis drive is divided into four groups. For instance, if the vibrating structure tends to rotate clockwise, the voltage(s) on the x-drive1 and/or x-drive4 can be increased to balance the rotation (see Fig. 6-9).

### **6.2.2 Device Design**

One of the advantages of the DRIE CMOS-MEMS process is that there is much less of a size constraint compared to the thin-film CMOS-MEMS process. The larger the device is, the better noise performance can be expected. However, there are a variety of factors that must be considered. First of all, the cost increases with the chip area. Secondly, the mechanical resonant modes change with the device size. There are trade-offs among the operating frequency, mechanical sensitivity and required driving voltage. Increasing the device size, i.e., increasing the proof mass, will either lower the operating frequency or require higher driving voltage for stiffer springs if the operating frequency remains unchanged. Thirdly, Brownian noise is just one of the noise sources. There is no use in decreasing the Brownian noise if it already reaches the electronics noise limit.

The Brownian noise given in Eq. (5-14) is the pure mechanical limit. In reality, the Coriolis signal is always modulated to a much higher frequency. Upon demodulation, the two side bands together with the accompanying noises are folded to give higher noise, i.e.,

$$\frac{\Omega_{min}}{\sqrt{BW}} = \sqrt{\frac{k_B T \omega_s}{m_s Q_s \omega_d^2 x_m^2}} \cdot \sqrt{2} \cdot \frac{180}{\pi} \quad (^\circ/\text{s}/\text{Hz}^{1/2}) \quad (6-7)$$

where  $\omega_s$  and  $m_s$  are the resonant frequency and mass of the sense mode, respectively,  $\omega_d$  is the excitation frequency and  $x_m$  is the amplitude of the excitation vibration. Since it is a lateral-drive, vertical-sense gyroscope,  $x_m$ , instead of  $Z$  as in Eq. (5-14), is used and is given by

$$x_m = Q_d \cdot \frac{F_d}{k_d} = Q_d \cdot \frac{F_d/m}{k_d/m} = \frac{Q_d}{\omega_d^2} \cdot \frac{F_d}{m} = \frac{\epsilon_0 Q_d}{2\omega_d^2} \cdot \frac{t}{g_d} \cdot \frac{N}{m} \cdot V^2 \quad (6-8)$$

where  $Q_d$ ,  $F_d$ ,  $k_d$  and  $m$  are the quality-factor, electrostatic drive force, stiffness and mass of the drive mode, respectively, and  $t$ ,  $N$  and  $g_d$  are the thickness, number and gap of drive fingers, respectively. If the applied voltage on one side of the comb drives has an  $180^\circ$  phase shift with respect to that on the other side, the d.c. and second harmonics are cancelled out. Assuming the applied voltage signal  $V = V_{dc} + V_{ac} \cos(\omega_d t + \theta)$ , where  $\theta$  is  $0^\circ$  on one side and  $180^\circ$  on the other side, Eq. (6-8) becomes

$$x_m = \frac{2\epsilon_0 Q_d}{\omega_d^2} \cdot \frac{t}{g_d} \cdot \frac{N}{m} \cdot V_{dc} V_{ac} \quad (6-9)$$

The design parameters are listed in Table 6-2. Substituting these values into the above equations and Eq. (5-9) to Eq. (5-17) gives the designed performance values listed in

Table 6-2. The electronics noise of the on-chip circuits is assumed to be  $10 \text{ nV/Hz}^{1/2}$  at 200 kHz, which is the frequency of the modulation signal.

**Table 6-2: Design data sheet of DRIE gyroscope**

$\omega_s$	5.0 kHz	$m_s$	50 $\mu\text{g}$	$k_s$	49 N/m	$g_s$	2.1 $\mu\text{m}$
$\omega_d$	4.0 kHz	$m_d$	80 $\mu\text{g}$	$k_d$	51 N/m	$g_d$	1.8 $\mu\text{m}$
$N$	134	$t$	50 $\mu\text{m}$	$V_m$	1 V	$V_{sn}$	10 nV/Hz <sup>1/2</sup>
$Q_s$	15	$Q_d$	40				
$x_m$	5.2 $\mu\text{m}$	$K$	2.8	$\phi$	-86.8°		
Brownian noise			0.01 °/s/Hz <sup>1/2</sup>	electronic noise limit			0.004 °/s/Hz <sup>1/2</sup>
Mechanical sensitivity			13 pm/°/s	sense/drive amplitude ratio			2.5 ppm/°/s

### 6.2.3 Compensation Scheme

There are two ways to reduce the influence of the coupled motion:

#### 1) Sense tracking

The z-axis accelerometer has an integrated self-test z-axis actuator. This z-axis actuator can be used to move the proof mass in the opposite direction of the coupled motion. From Table 6-1, the electrostatic force generated by the self-test z-axis actuator is  $1.3 \text{ nN/V}^2$ . The proof mass of the z-axis accelerometer is 50  $\mu\text{g}$  (Table 6-2), so that the z-axis actuator generates an equivalent acceleration of  $2.6 \times 10^{-3} \text{ G/V}^2$ . Therefore, the self-actuator is capable of tracking a 1 G maximum acceleration when 20 V is applied.

## 2) Drive cancellation

According to the analysis in Section 6.2.1.1, the excitation motion exists in all directions. The motions other than the primary vibration direction are defined as off-axis motions. These off-axis motions cause quadrature error, d.c. offset and cross-sensitivity.

In order to null the off-axis motions, the divided primary x-axis drives, y-axis actuator, and x/z-axis actuator may be used individually or in any combination.

The z-axis stiffness of the drive mode is about a hundred times larger than its x-axis stiffness, i.e., the x-axis resonant frequency is only about one tenth of the z-axis resonant frequency. Therefore, according to Eq. (5-11), the phase difference is very close to zero, that is, there is almost no phase lag for the z-axis actuation of the drive mode when the shuttle is operating at the x-axis resonant frequency. From Table 6-1, the x/z-axis actuator when used for z-axis actuation generates 6.3 nN/V<sup>2</sup> electrostatic force in the z-direction. The equivalent acceleration is given by

$$a_z = \ddot{z} = \frac{f_z}{k_{z,drv}} \cdot \omega_d^2 = \frac{6.3 \times 10^{-9}}{100 \times 51} \cdot \frac{(2 \cdot \pi \cdot 4 \times 10^3)^2}{9.81} = 8.0 \times 10^{-5} \text{ (G/V}^2\text{)} \quad (6-10)$$

An equivalent acceleration of 0.03 G can be generated when 20 V is applied. Therefore this method is not as effective as *sense tracking*. However, since there is no phase lag involved, it is easier to implement. In fact, well designed and fabricated DRIE gyroscopes are expected to have very small off-axis motions.

## 6.2.4 Simulation of the DRIE gyroscope

The structure shown in Fig. 6-9 looks complicated. Modal analysis and transient analysis are needed to understand the behavior and performance of the device. As discussed in

Chapter 5, the NODAS beam model and plate model suitable for DRIE microstructures have been developed. These NODAS models are used to find the mechanical modes and the sensitivity and study the compensation. Coventorware [60] are also used to verify the modal analysis.

#### 6.2.4.1 NODAS simulation

Fig. 6-10 is the NODAS representation of the gyroscope shown in Fig. 6-9. In the nominal case, the beam width of the x-drive spring beams is  $3.9\text{ }\mu\text{m}$  with a  $0.9\text{ }\mu\text{m}$  Si undercut on each side, and the thickness of the Si layer is  $50\text{ }\mu\text{m}$ . The simulated frequency response is shown in Fig. 6-11, where the resonant frequencies of the drive and sense modes are  $4.0\text{ kHz}$  and  $5.0\text{ kHz}$ , respectively. Transient analysis is also performed to find the phase relation between the drive signal and sense signal, as shown in Fig. 6-12. The Coriolis dis-

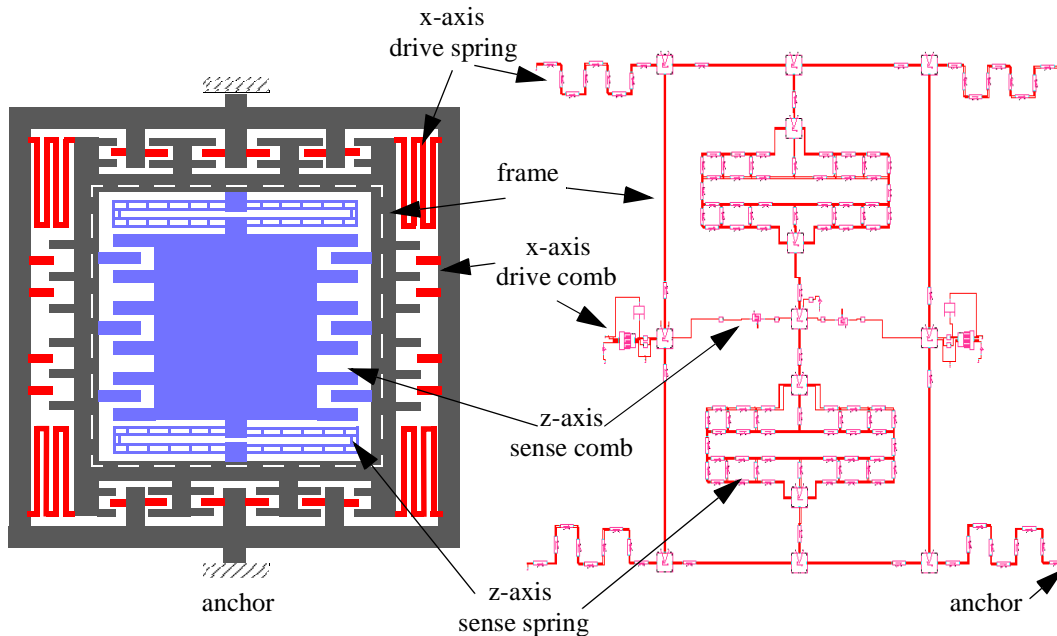


*Figure 6-10: NODAS schematic of the DRIE gyroscope.*

placement is  $87^\circ$ , instead of  $90^\circ$ , ahead of the excitation displacement, which is in agreement with the calculated value listed in Table 6-2.

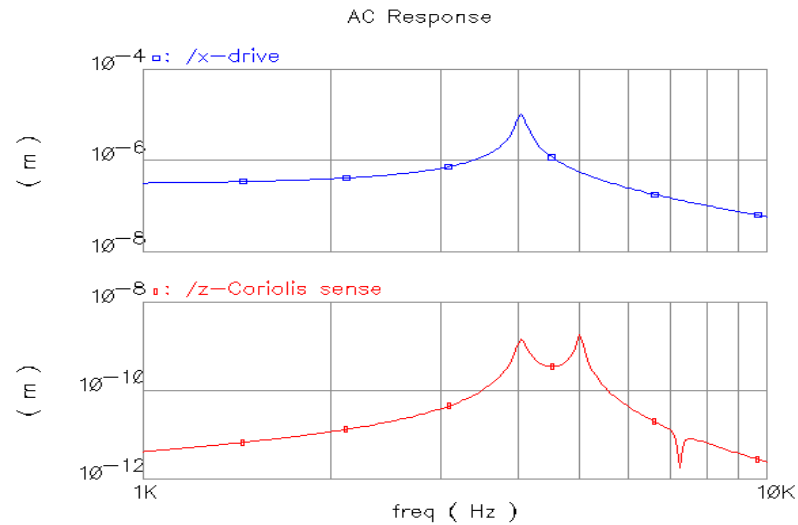


Figure 6-11: The simulated drive and sense modes for nominal case.

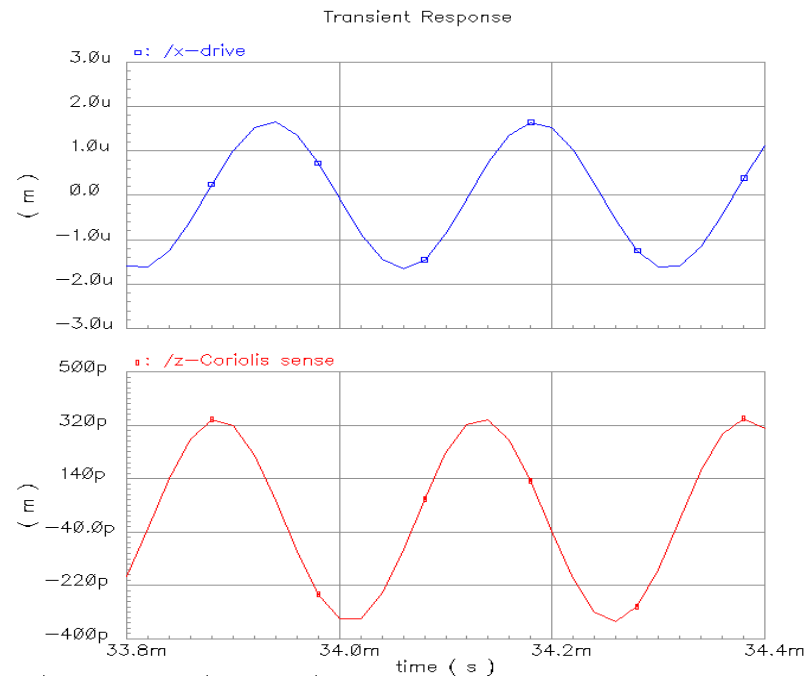


Figure 6-12: Transient analysis of the DRIE gyroscope



### 6.2.4.2 FEM analysis

Coventorware [60] is employed to verify the NODAS simulation. The layout of the gyroscope is shown in Fig. 6-13. It has exactly the same arrangement of the sensors and actuators as shown in Fig. 6-9. The structure consists of multiple layers and hundreds of comb fingers. It requires enormous computing power and time if a finite-element analysis is performed on the full structure. Since the low-order mechanical modes of the structure is of primary concern, the comb fingers simply contribute certain mass. Fig. 6-14 shows the 3D solid model generated by Coventorware, in which the comb fingers are taken away and modeled as solid plates. The thickness of the structure is 50  $\mu\text{m}$ . However, the z-spring beams are composed of only CMOS interconnect layers and are 4.9  $\mu\text{m}$  thick. The x-drive spring beams are 3.9  $\mu\text{m}$  wide with a 0.9  $\mu\text{m}$  Si undercut on each side.

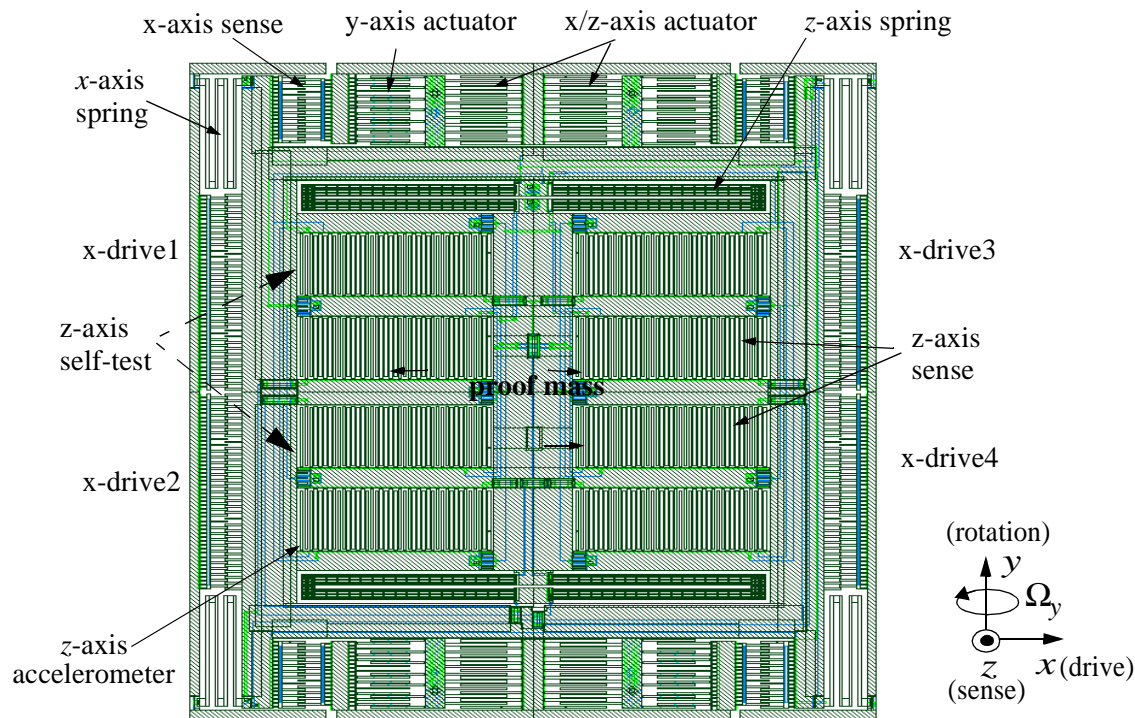
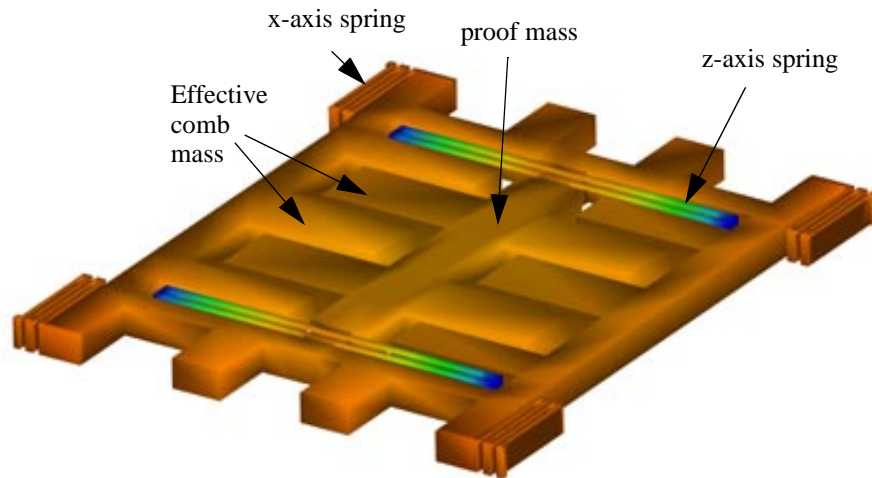


Figure 6-13: Layout of the DRIE x-axis gyroscope.



*Figure 6-14: 3D solid model of the gyroscope structure.*

The modes obtained from this FEM simulation are listed in Table 6-3. The primary drive and sense modes are 3.91 kHz and 4.84 kHz, respectively, which match the NODAS simulation results within 5%. The torsional mode  $\theta_y$  (sense) has resonance that is only 2% higher than the z-axis sense mode. The z-axis and  $\theta_y$  sense modes are designed to be 25% higher than the x-axis drive mode. The intent is that neither the z-sense mode nor the  $\theta_y$ -

**Table 6-3: First ten modes of the DRIE gyroscope**

Mode #	Frequency (kHz)	Description
1	3.91	x-axis drive
2	4.84	z-axis sense
3	4.94	$\theta_y$ sense
4	8.13	y-axis sense, y-axis drive, in phase
5	10.3	$\theta_x$ sense
6	13.2	$\theta_z$ drive
7	15.5	y-axis sense, y-axis drive, antiphase
8	17.4	z-axis sense, z-axis drive, antiphase
9	26.1	$\theta_x$ drive
10	26.4	$\theta_y$ drive

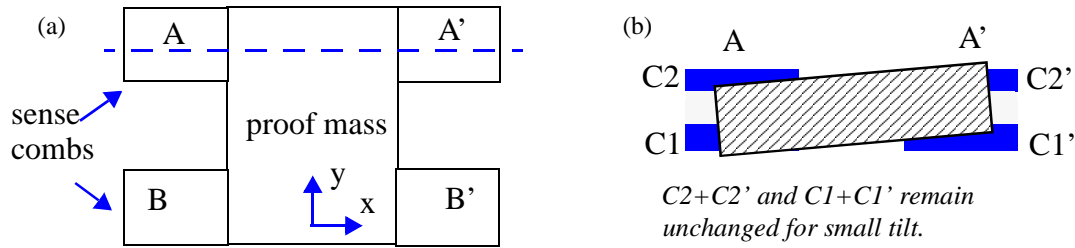


Figure 6-15: Compensation scheme for torsional vibration.  
(a) Top view. (b) Cross-sectional view.

sense mode will be excited when the device operates at the x-axis drive resonance. Further suppression of the torsional mode is provided by symmetrically distributing comb finger groups as shown in Fig. 6-15. The capacitors in Groups A and A' are summed up to reject the  $\theta_y$  vibration. Similarly, the capacitors in Groups A and B are summed up to reject the  $\theta_x$  vibration. The first four mode shapes are shown in Fig. 6-16.

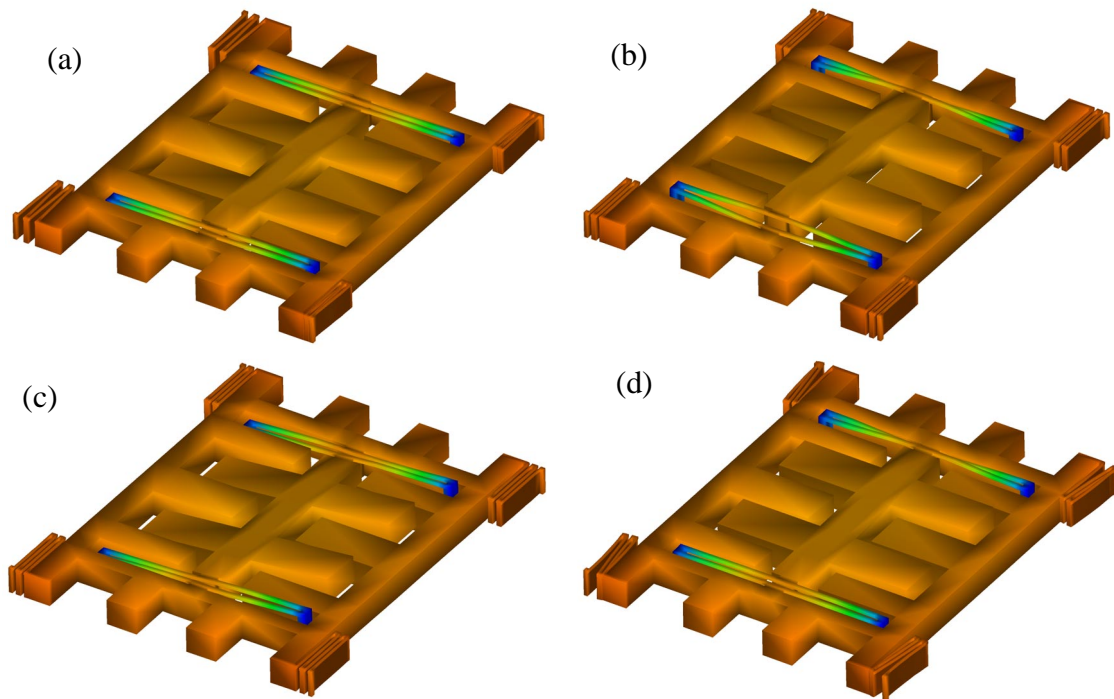


Figure 6-16: The first four modes in the gyroscope structure: (a) x-drive mode. (b) z-sense mode. (c) torsional y-sense mode. (d) y-sense and y-drive in-phase coupled mode.

## 6.2.5 DRIE Gyroscope Fabrication

The CMOS chips were fabricated through the Austria Micro Systems (AMS) 0.5  $\mu\text{m}$  3-metal CMOS process. The post-CMOS micromachining was done by using the DRIE CMOS-MEMS process introduced in Section 2.3.

A scanning electron micrograph (SEM) of the gyroscope is shown in Fig. 6-17. The drive fingers are located on the two sides of the device, and there are 78 comb fingers on each side. The x-drive springs are two-turn serpentine beams. The length and width of the folded beams are 156  $\mu\text{m}$  and 3.9  $\mu\text{m}$ , respectively. The total area of the microstructure is 0.85 mm by 1.0 mm.

The z-axis sense springs are single-turn and 250  $\mu\text{m}$  long. They consist of aluminum and oxide and have no silicon underneath, and therefore they are thin and compliant in the z-direction. Each spring branch is composed of many short beams, which increases the spring stiffness in the y-direction.

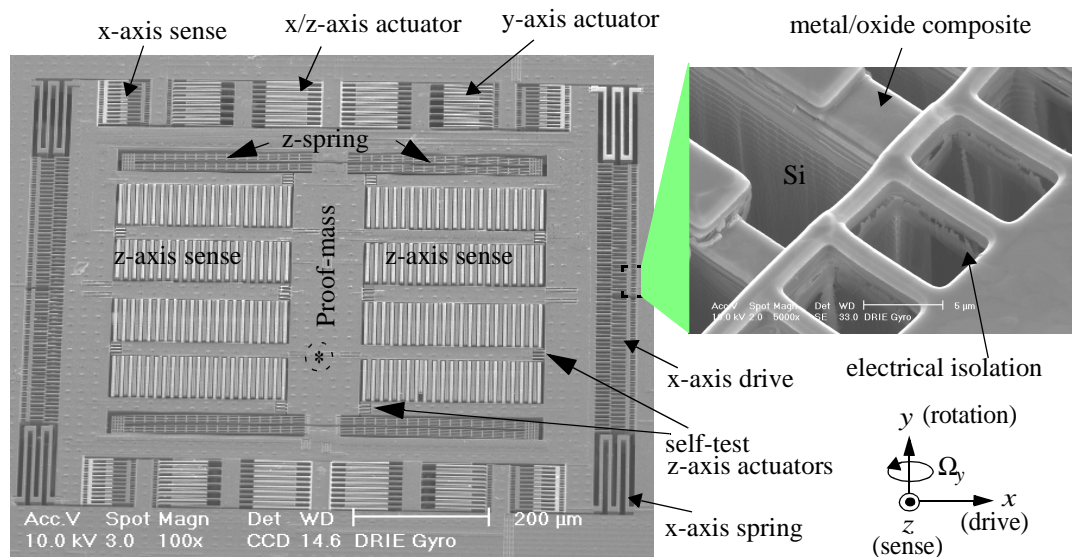


Figure 6-17: SEM of the x-axis DRIE gyroscope. The asterisk marks the spot for optical motion measurement

The z-axis sense comb fingers are divided into four groups to form a common-centroid configuration to reduce the cross-axis sensitivity and compensate the process variations. Each group has a pair of differential comb-finger sub-groups to minimize the y-axis sensitivity as discussed in Section 6.2.1.1. The total number of z-sense comb fingers is 320, and the finger overlap is 90  $\mu\text{m}$ . The operational principle of the z-displacement sensor is the same as the one described in Section 3.3.3.

#### **6.2.5.1 Process Issues**

##### *1). Backside etch*

The backside etch does not have critical requirement for alignment, but it does require well-controlled DRIE etching. The backside surface roughness of CMOS chips is directly transferred or even largely deteriorated to the backside of the resultant devices. So using double-polished wafers or polishing the backside after the CMOS processes is preferred. Moreover, a properly sized shadow mask will produce well-defined supporting frames and avoid any photolithography step(s).

##### *2). Undercut*

A relatively large undercut (e.g., 0.6  $\mu\text{m}$  on each side) is needed to obtain the z-compliant spring beams and the electrically isolated silicon (see Fig. 6-18(a)). Meanwhile, as small undercut as possible is desired to maximize the sensitivity or drive force from electrically isolated silicon comb fingers. One of the major problems during the post-CMOS processing is the incomplete undercut of silicon causing small shunt resistance to the silicon substrate (Fig. 6-18(b)).

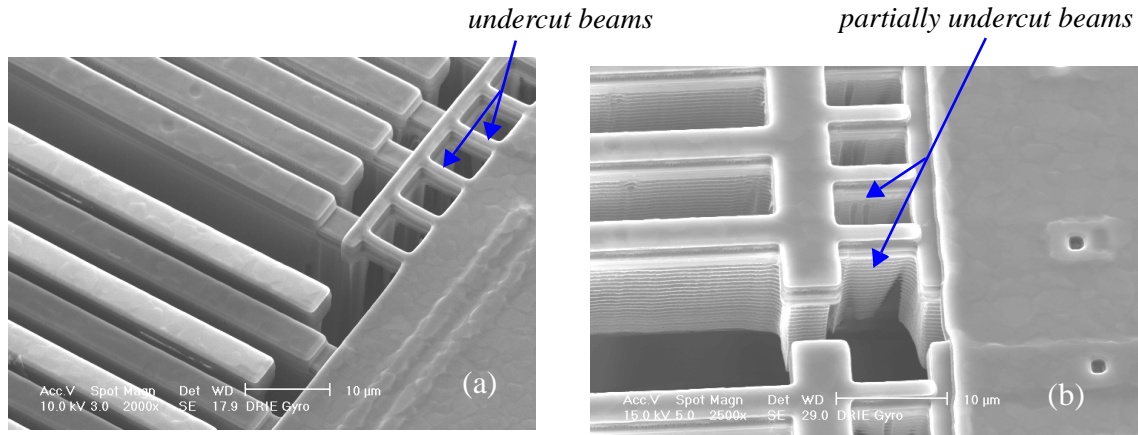


Figure 6-18: SEMs showing the electrical isolation of silicon. (a) Good electrical isolation. (b) Poor electrical isolation.

There are two ways to solve this problem. First, use no electrically isolated silicon in the design. In this case, the silicon layer functions solely as a mechanical support. Second, if electrically isolated silicon is required for the design, try to separately control the undercut for electrical isolation and for silicon comb finger gaps. An idea has been proposed by using the top metal interconnect layer as both etching mask and sacrificial layer. The detailed process flow will be discussed in Section 6.2.9.

### 3). Frontside release versus backside release

The standard release procedure is to perform the backside etch first and then release from the front side. This method is good for protecting microstructures. However, it suffers from difficulty in judging the end point of the deep Si etch step (see Fig. 2-5(c)).

Alternately, the frontside can be etched first and then the structure is released from a backside etch. This way, good control of the end point of the deep Si etch step is achievable. This is because the release of comb fingers and the Si undercut of thin-film beams can be visibly seen simply under an optical microscope without touching the die. How-



ever, there are two drawbacks. First, after the frontside etch, the top metal layer is exposed and is easily scratched. Second, it involves a wet photoresist removal step which requires extreme care and effort dealing with sticking problems.

### 6.2.6 Characterization

Experimental characterization of the DRIE gyroscope includes test of the embedded z-accelerometer, zero-rate output drift, responses to the rotation, noise floor, phase relation of the coupled signal and the Coriolis signal, rotation sweeping, temperature dependence and acceleration rejection.

#### 6.2.6.1 Z-accelerometer test

The embedded z-axis accelerometer has the same topology as the one introduced in Section 3.3.3. The frequency response of the z-axis accelerometer was measured by using the integrated self-test z-axis actuator and the result is shown in Fig. 6-19. The first three modes are clearly shown, which are the coupled x-drive mode (3.0 kHz), z-sense mode

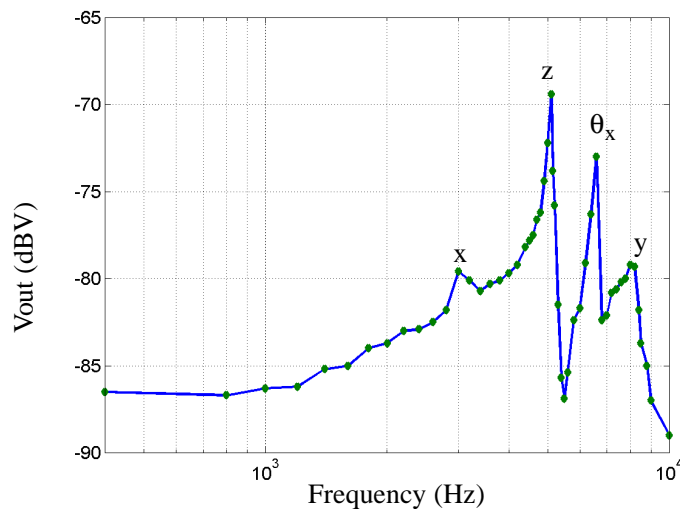


Figure 6-19: Frequency response of z-axis accelerometer.

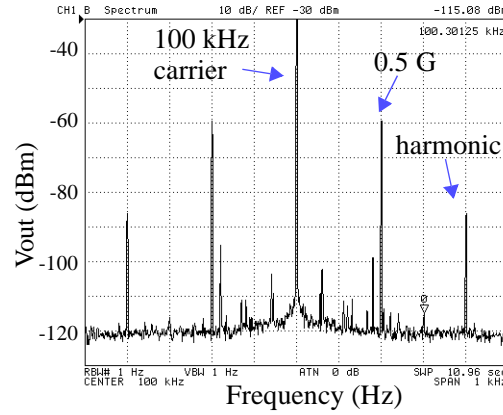


Figure 6-20: Spectrum of on-chip output signal when a 0.5 G 200 Hz external acceleration was applied.

(5.2 kHz) and  $\theta_x$  (8.2 kHz), respectively. Fig. 6-20 shows a spectrum when a 0.5 G 200 Hz acceleration generated by a shaker table is applied to the sensor. The second harmonic is present due to the nonlinearity of the sense capacitance. The measured noise floor of this z-accelerometer is  $0.5 \text{ mG/Hz}^{1/2}$ .

#### 6.2.6.2 Optical Measurement of Vibration

The performance of the gyroscope largely depends on the vibration stability, mode location and mode coupling. Vibration test results are measured by using an optical microvision system [75]. The measured frequency response is plotted in Fig. 6-21, where 18 V d.c. plus 5 V a.c. was applied. The measured spot was at the central proof mass. The x-axis drive mode has a resonant frequency of 3.0 kHz, and a mechanical Q-factor of 45. The measured orthogonal y-axis motion is a few nanometers, which is actually the resolution limit of the microvision system along the lateral axes. The coupled z-axis motion is large (about 3% of the drive amplitude at resonance), which implies that there is a mismatch



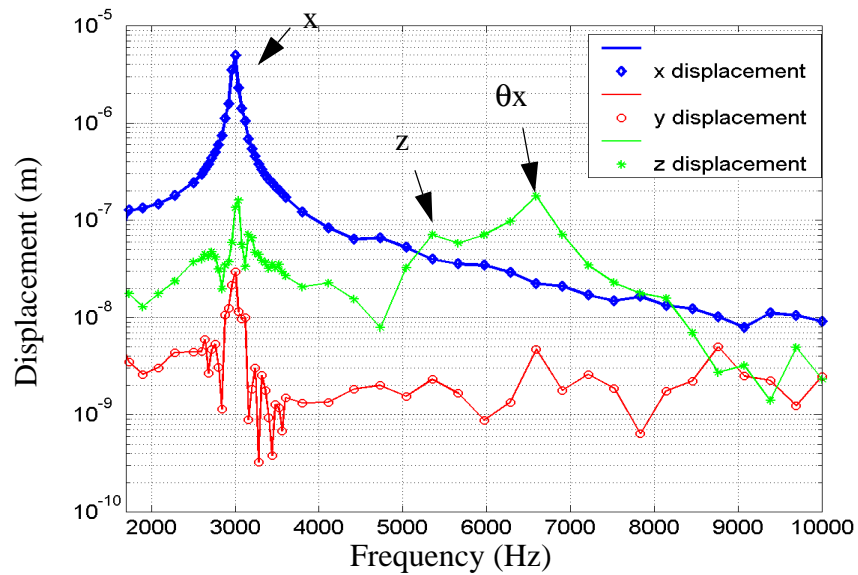


Figure 6-21: Frequency response of the DRIE gyroscope measured by using an optical microvision system when voltage applied to the x-drive comb fingers.

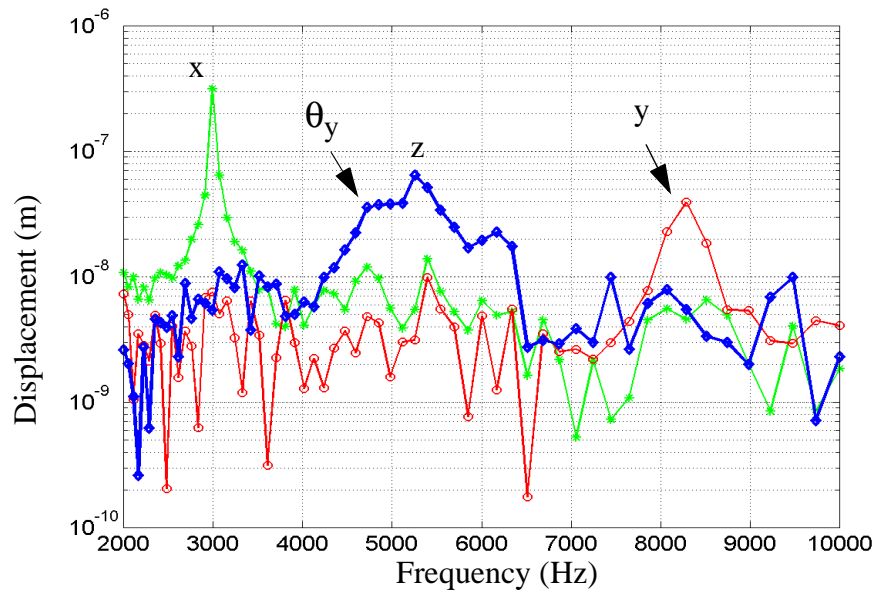


Figure 6-22: Frequency response of the DRIE gyroscope when voltage applied to the x/z-comb drives at the outer frame.

between the drive stator and rotor comb fingers. The first two sense modes, i.e., z-axis mode and  $\theta_x$ -mode, were also detected at 5.3 kHz and 6.6 kHz, respectively. Also note that 3 dB bandwidths of these two out-of-plane modes are much larger than the x-axis drive mode. The larger damping in the out-of-plane modes of the sense axis results from the large number of long, thick sense comb fingers. In contrast, the drive comb fingers have only 3  $\mu\text{m}$  overlap.

A microvision measurement was also conducted when 5 V a.c. plus 18 V d.c. was applied to the x-axis/z-axis comb drives (configured for z-axis actuation). The result is plotted in Fig. 6-22. Two more modes are present, i.e., the sense  $\theta_y$ - and y- modes, which are 4.7 kHz and 8.3 kHz, respectively.

The measurement result when the same voltage was applied to the self-test z-actuators is plotted in Fig. 6-23. The mechanical Q-factor of the sense z-mode is about 15. The large x-mode is coupled from the drive mode.

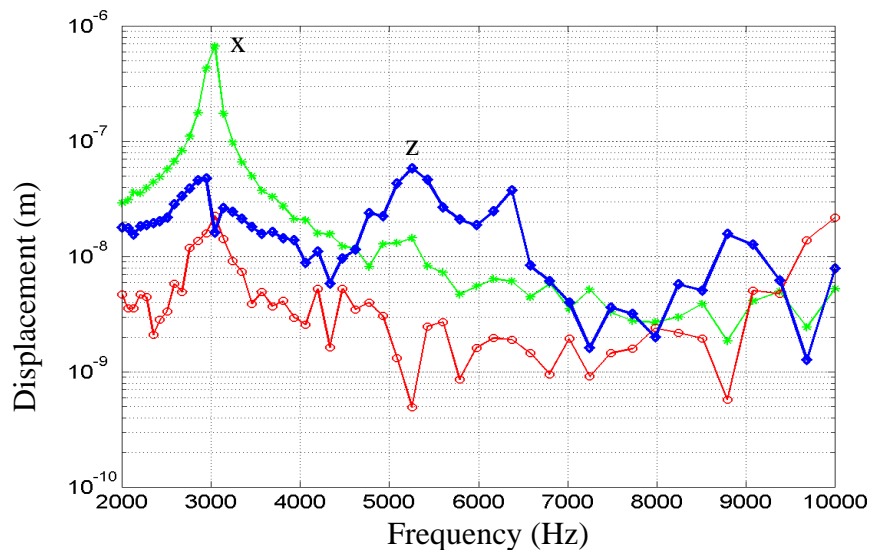


Figure 6-23: Frequency response of the DRIE gyroscope when voltage applied to the self-test z-actuators of the z-accelerometer.

## 6.2.6.3 Measurement Setup for Rotation Test

The test setup for gyroscope operation is shown in Fig. 6-24. A sinusoidal voltage signal plus a d.c. offset is applied to the drive comb fingers of the gyroscope. It was found by experiment that the resonant frequency of the drive mode is 3.0 kHz when 5 V (amplitude) a.c. plus 18 V d.c. is applied, and the vibration amplitude is about 5  $\mu\text{m}$  in that condition. The turntable (Ideal Aerosmith Inc.: Model 1270VS) provides a rotation rate up to 360  $^\circ/\text{s}$ . A LM1496 balanced modulator-demodulator is used to perform the first demodulation, i.e., to demodulate the signal from the carrier. A lock-in amplifier (Stanford Research, Model SR830 DSP) is used for the second demodulation, i.e., to pick up the rotation signal from the Coriolis signal. A spectrum analyzer (HP4395A) is also employed. To monitor the outputs of the demodulators, all instruments are connected via GPIB cables. Labview is running over these instruments to control timing, change parameters, acquire waveforms and collect data automatically.

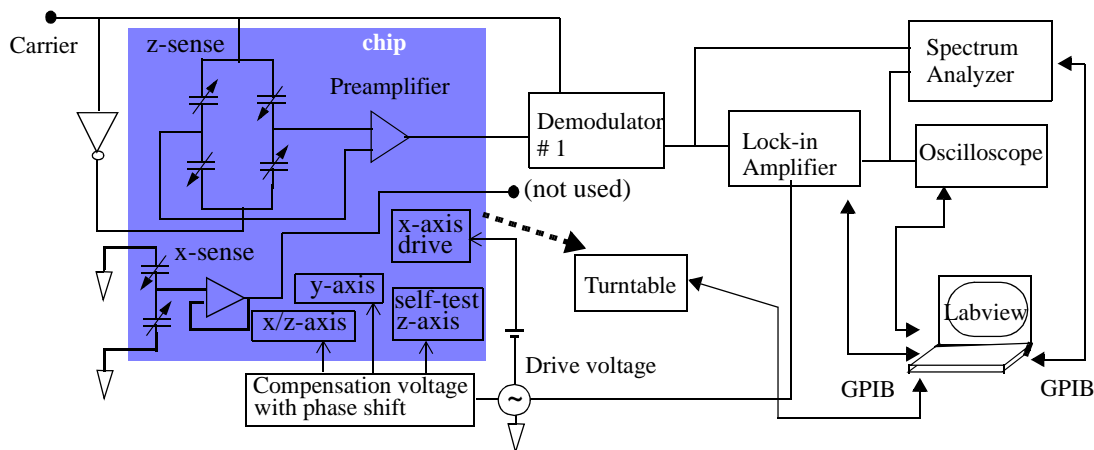


Figure 6-24: Test setup for characterizing the DRIE gyroscope.

#### **6.2.6.4 Zero-Rate Output (ZRO) Drift**

ZRO drift is one of major characteristics of a gyroscope. The drift may be caused by the aging or fatigue of structural materials or by the environmental changes such as temperature, humidity, vibration, electromagnetic radiation, etc.

For the ZRO drift measurement, the shuttle was excited to its resonance by applying 3 kHz 5 V a.c. plus 18 V d.c. voltage. The device was tested in the following three conditions:

- in a noisy open lab (without grounding floating electrodes)
- in a quiet Faraday cage (without grounding floating electrodes)
- in a quiet Faraday cage (with grounding floating electrodes)

The results are plotted in Fig. 6-25. The result tested in the noisy lab looks very bad (Fig. 6-25(a)), with drift of volts over hours. After moving the setup to the Faraday cage, the drift becomes much smaller because of the electromagnetic shielding and the quiet environment. As shown in Fig. 6-9, the DRIE gyroscope includes many comb fingers for driving, sensing or off-axis motion cancellation. Not all the comb drives are used at the same time, i.e., there are always some unused comb drives. If the electrodes of the unused comb drives are left unconnected, these electrodes will accumulate charge or pickup electromagnetic radiation to induce unwanted, unpredictable electrostatic force. By comparing Fig. 6-25(b) with Fig. 6-25(c), it is clear that grounding the unused electrodes significantly reduces the drift.

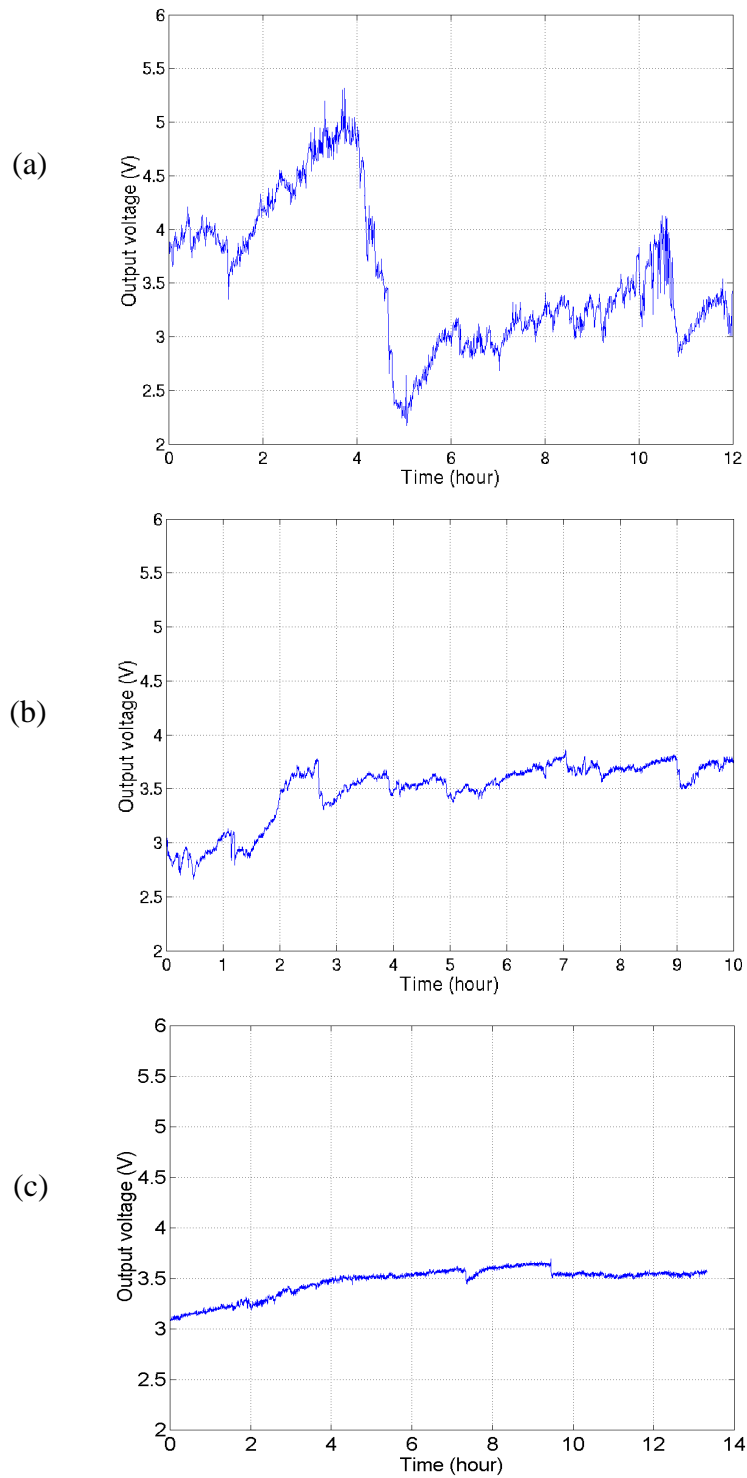


Figure 6-25: Zero-rate output of the DRIE gyroscope. (a) with floating electrodes in a noisy lab. (b) with floating electrodes in a Faraday cage. and (c) grounding floating electrodes in a Faraday cage.

### 6.2.6.5 Output Waveforms

Fig. 6-26(a) shows the response of the gyroscope to a hand-shaking rotation which was roughly one revolution per second. The turntable available for testing provides only a steady rotation rate. A Labview program was developed to generate different rotation waveforms on the turntable. Fig. 6-26(b) shows the gyroscope's response to a Labview-generated sine wave. However, the wave is not a perfect sine wave and the frequency can only reach up to a few Hz.

A DC motor (Dayton: Model 2L011) is employed to get a better sinusoidal rotation signal (Fig. 6-26(c)). The rotation amplitude can be calibrated by using the turn table. For monitoring the real-time rotation, a shaft decoder is required. The employed DC motor is capable of generating sinusoidal rotation signals with frequency up to a few tens hertz depending on the desired amplitude.

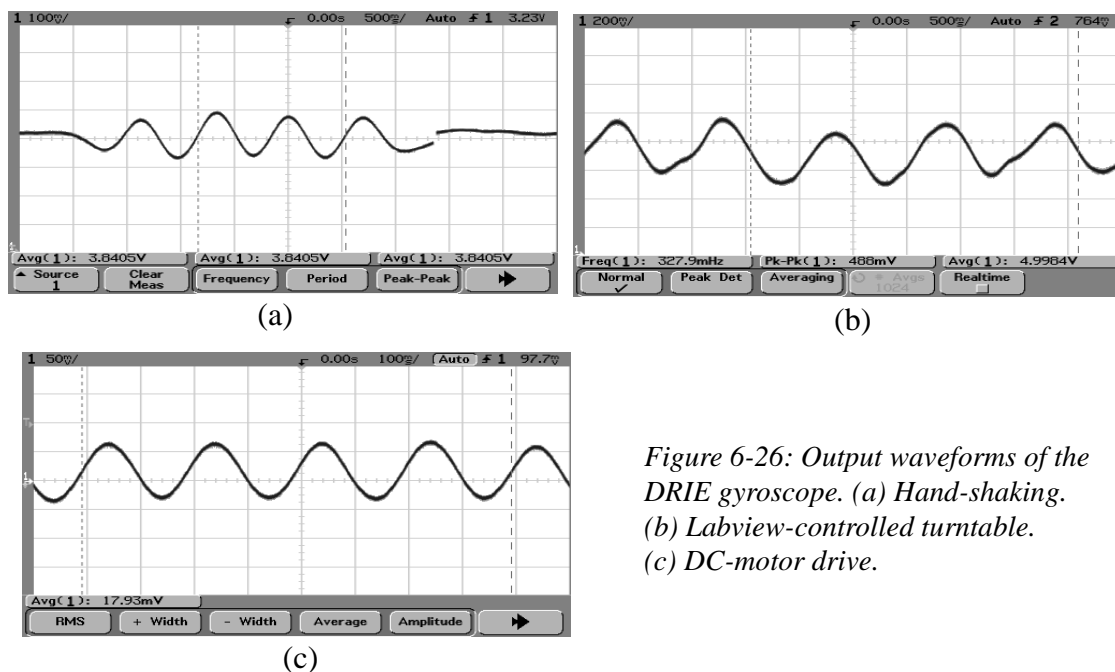
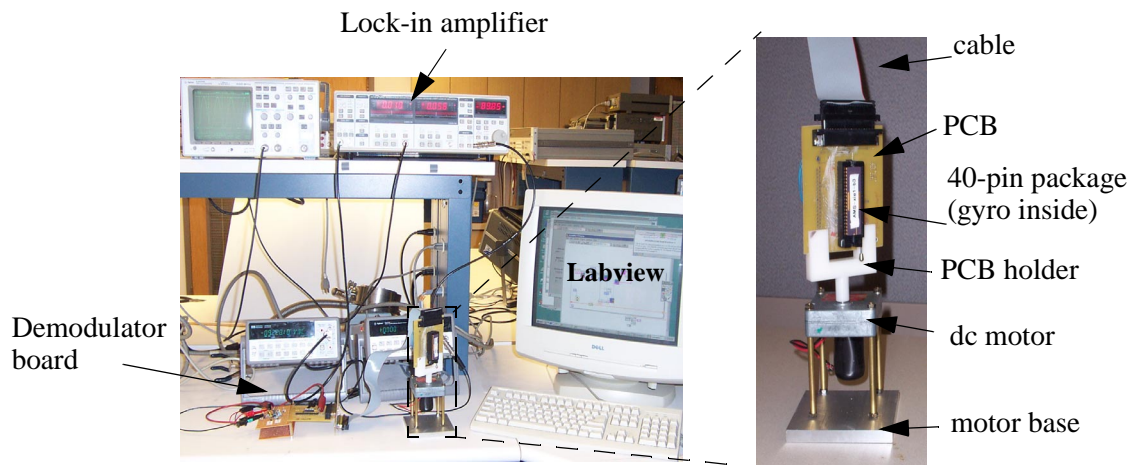


Figure 6-26: Output waveforms of the DRIE gyroscope. (a) Hand-shaking. (b) Labview-controlled turntable. (c) DC-motor drive.

### 6.2.6.6 Noise Floor

The PCB board holding the gyroscope package is vertically mounted on the DC motor, as shown in Fig. 6-27. The device operates at 3 kHz with a.c. amplitude of 5 V and d.c. offset of 18V. The modulation signal is a 1 V 200 kHz square wave. The lock-in amplifier is set to the maximum amplitude of the output signal in which the phase is  $-106^\circ$ . The spectrum of the output signal is shown in Fig. 6-28(a) where the DC motor rotates sinusoidally at 5 Hz with an amplitude of  $33^\circ/\text{s}$  (calibrated by the turn table). Several harmonics of 5 Hz are clearly shown. Other than the harmonics, there is a broad range of low frequency spectrum present due to the vibration of the PCB board. Fig. 6-28(b) shows the spectrum of the output signal at zero rotation.

Comparing Fig. 6-28(a) and Fig. 6-28(b), the  $33^\circ/\text{s}$  signal is  $(-24.58+89.15)=64.57$  dB above the noise floor at a bandwidth of 1 Hz. Therefore the equivalent minimum measurable rotation signal is  $0.02^\circ/\text{s}/\text{Hz}^{1/2}$ .



*Figure 6-27: Measurement setup (partial) with a DC motor to generate sinusoidal rotation rate.*

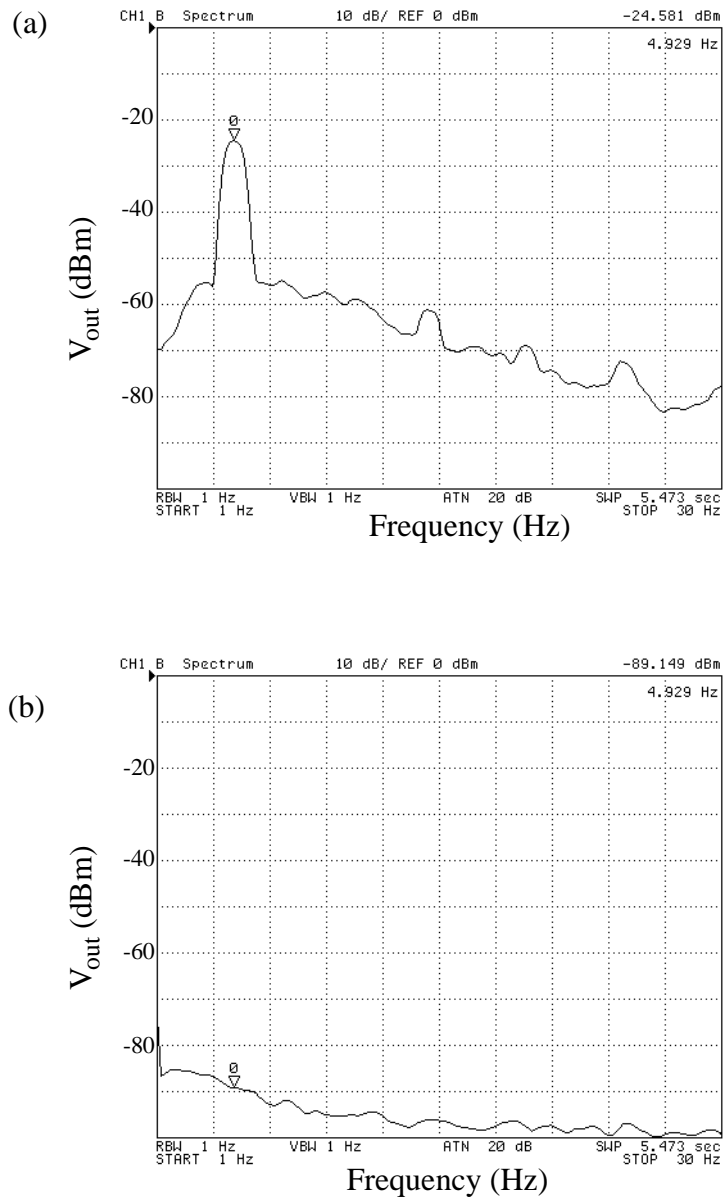


Figure 6-28: Spectrum of the output signal. (a) At 5 Hz  $33^\circ$ /s rotation. (b) At zero rotation.



### 6.2.6.7 Phase Relationship

Phase relations of the various motion signals in a vibratory gyroscope are analyzed in Section 5.3.2.2. The phase difference between the Coriolis signal and the combined coupling signal is experimentally explored in the following.

A Labview program was written to perform automatic phase sweeping. First the program sweeps the phase at zero rotation rate (Fig. 6-29(a)). Then the phase is swept at  $\Omega = 200^\circ/\text{s}$  (clock-wise) Fig. 6-29(b)). The difference between the two sweeps gives the sensitivity of the device at different phases (Fig. 6-29(c)). The ZRO signal from the lock-in

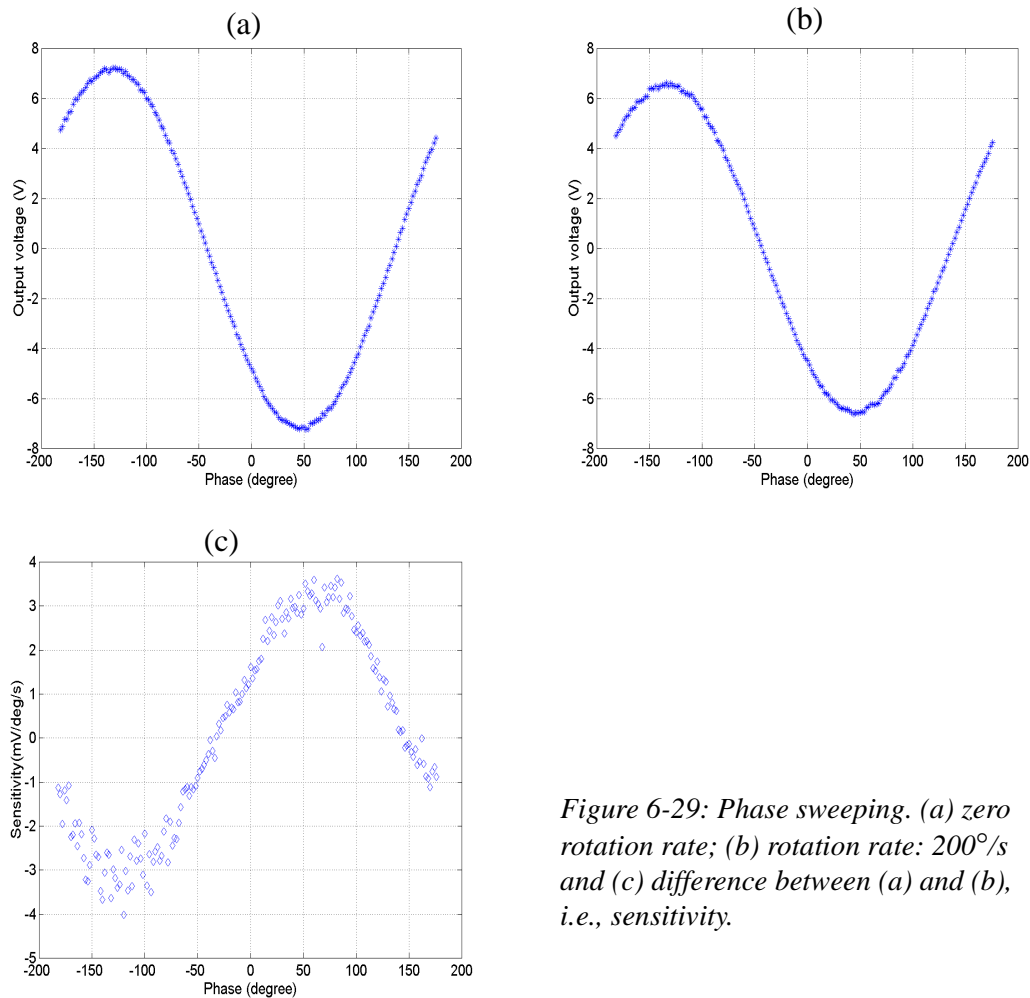


*Figure 6-29: Phase sweeping. (a) zero rotation rate; (b) rotation rate:  $200^\circ/\text{s}$  and (c) difference between (a) and (b), i.e., sensitivity.*

amplifier reaches its maximum at a phase of  $-130^\circ$ , while the Coriolis signal has the highest sensitivity at a phase of  $-108^\circ$ . So the Coriolis signal has a phase lag of  $12^\circ$  compared to the coupled signal in this specific case. Note that this phase lag depends on the resonant frequency separation of the drive and sense modes and on matching the operating frequency to the resonant frequency of the drive mode.

#### 6.2.6.8 Off-axis Motion Compensation

All the comb drives for off-axis motion compensation are electrically grounded for above experiments. Experiments were also performed by using these comb drives to reduce the coupled motion in the sense mode (along the y-axis). The results are listed in Table 6-4. The phase in the table refers to the phase delay of the compensation voltage with respect to the primary x-axis drive voltage. The compensation voltage was set to 5 V a.c. plus 15 V d.c.

**Table 6-4: Y-axis coupled motion reduction by compensation (All voltages at 5 V a.c. plus 15 V d.c.)**

	phase	coupled motion reduction
self-test z-axis actuator	$70 \pm 5^\circ$	10 dB
x/z-axis actuator (z)	0	4 dB
x/z-axis actuator (x)	0	8 dB

#### 6.2.6.9 Rotation Sweeping

In order to check the linearity of the device, a rotation sweep is performed. The rotation changes from  $-320^\circ/\text{s}$  to  $+320^\circ/\text{s}$ . The results are plotted in Fig. 6-30. The data in

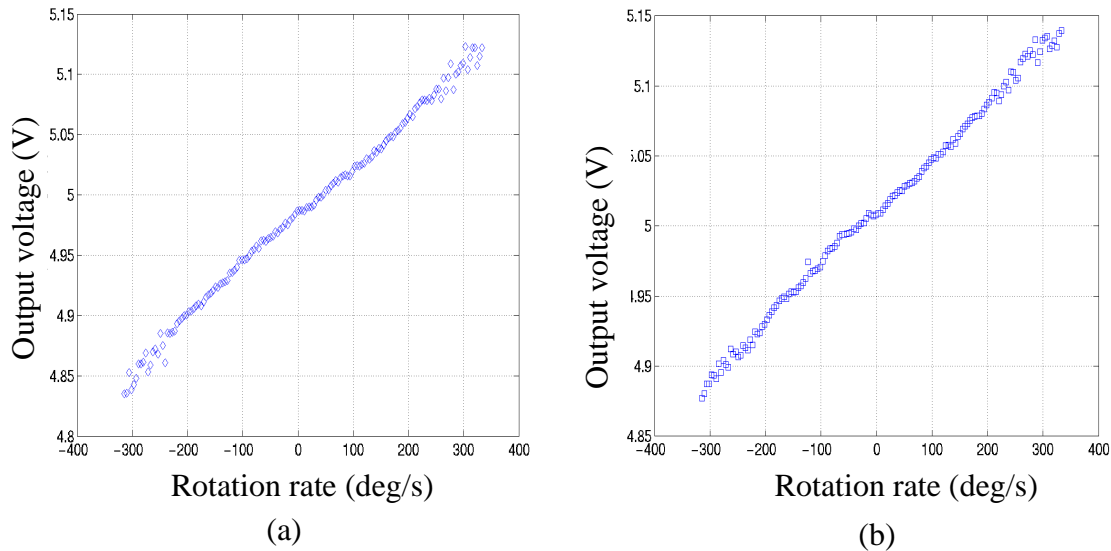


Figure 6-30: Rotation sweep. (a) taken in 12.5 minutes; and (b) taken in 25 minutes.

Fig. 6-30(a) was taken in a shorter time than the data in Fig. 6-30(b). Quicker measurement has better linearity. The drift is clearly present in Fig. 6-30(b).

#### 6.2.6.10 Thermal Stability

A thin-film heater was placed on the backside of the gyroscope DIP package. A 16 V (peak-to-peak) 1 mHz sinusoidal voltage plus 4 V d.c. was applied to the heater. The peak-to-peak temperature change is estimated to be about 50 K. Fig. 6-31 shows the output signal where the rotation rate was set to zero. The frequency of this zero-rate-output (ZRO) signal is 2 mHz, doubled the frequency of the input voltage signal. There is a phase delay between the heater voltage and thermal drift because the heater has to heat up the whole package. The plot also shows that increasing temperature decreases the ZRO amplitude. This is because the curling of the microstructure decreases with increasing temperature

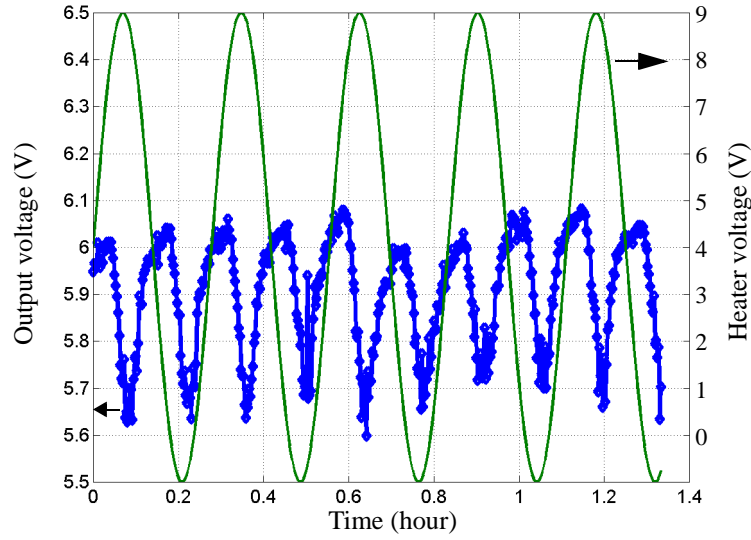


Figure 6-31: Thermal drift of the DRIE gyroscope.

and therefore decreases the d.c. offset at the sense node of the z-axis accelerometer. Note that a drift is also present in the ZRO signal.

The ZRO amplitude changes 380 mV due to the 50 K temperature variation. From Fig. 6-29(c), the sensitivity of the gyroscope at the testing point is 3 mV/°/s. Therefore the temperature dependence of the ZRO signal is 2.6 °/s/K. This large temperature coefficient is mainly contributed by the undesired thin-film comb fingers formed due to the over- undercut and also by electronics' temperature dependence.

Another factor is the resonant frequency stability. Since the drive mode has a silicon-dominated spring, its resonant frequency's temperature dependence is mainly determined by the temperature coefficients of linear expansion,  $\alpha_{Si}$ , and Young's modulus,  $\alpha_{E,Si}$ , of single-crystal silicon, *i.e.*,

$$\omega_{r'} = \sqrt{\frac{k(1 + \alpha_{Si} \cdot \Delta T)(1 + \alpha_{E,Si} \cdot \Delta T)}{m}} \approx \sqrt{\frac{k}{m}} \left( 1 + (\alpha_{Si} + \alpha_{E,Si}) \frac{\Delta T}{2} \right) \quad (6-11)$$

where  $\alpha_{Si}=2.6$  ppm/K and  $\alpha_{E, Si} = -90$  ppm/K [101]. Assuming a 50 K temperature change, the resonant frequency of the drive mode changes 0.2%. As the mechanical quality factor  $Q$  of the drive mode is 45, the bandwidth is 2.2% of the resonant frequency. Therefore, the resonant frequency change of the drive mode due to the temperature variation is small. The resonant frequency change due to packaging stress is not considered here, but it is an important issue [102].

The sense element is a z-axis accelerometer which has a z-compliant, multi-layer spring. The curling of the multi-layer spring beams changes with temperature due to the different coefficients of thermal expansion of the materials in the beams, and thus the spring constant changes, especially in the z-direction. In the thin-film lateral-axis gyroscope [21], the temperature dependence of this type of z-compliant spring was used to tune the resonant frequency of the sense mode to control the mode distribution. It was found that the resonant frequency for the thin-film spring changed about 15% over a 100 K temperature change. However, in the DRIE gyroscope, the z-spring has three metal layers, instead of one metal layer, which is the case in the thin-film gyroscope. This thicker spring has less temperature dependence than the one-metal layer counterpart. On the other hand, the resonant frequency of the sense mode in the DRIE gyroscope was designed to be 50% higher than that of the drive mode. This large mode separation guarantees the operating frequency is within the “low” frequency region (i.e., almost no gain and no phase delay) of the sense mode. Therefore when the temperature changes, only the change of the z-stiffness, which is predictable, affects the output.

### 6.2.6.11 Acceleration Rejection

The self-test z-actuator (see Fig. 6-17) was used to generate the acceleration. A 2 V 10 Hz sine wave plus a 5 V d.c. offset was applied to the z-actuator. The signal spectrum prior to any demodulation is shown in Fig. 6-32(a). The corresponding acceleration is about 0.5 g. The final output signal captured from an oscilloscope is shown in Fig. 6-32(b), in which peak-to-peak value is 60 mV. From Fig. 6-29(c), the sensitivity is 3 mV/°/s at this test point. Therefore the acceleration sensitivity of this gyroscope is 20 °/s/g. The cause of this large sensitivity is analyzed next.

In a vibratory gyroscope, the Coriolis signal has the same frequency as that of the excitation vibration and is modulated by the rotation. If the sensing element is a linear device in the whole interest range, any acceleration with frequencies other than the excitation frequency will be eliminated after the demodulation. However, the test result of the embedded z-axis accelerometer shows high nonlinearity (see Fig. 6-20 and Fig. 6-32(a)).

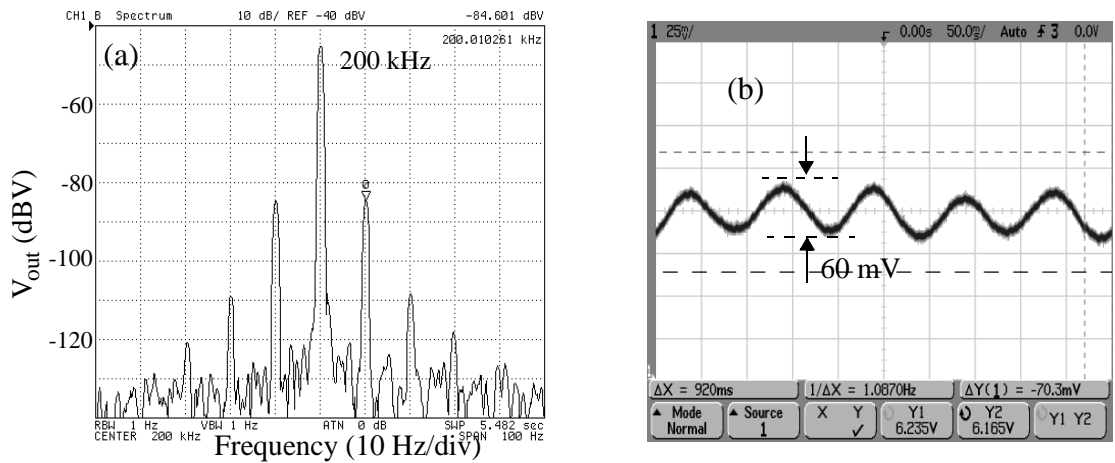


Figure 6-32: Acceleration sensitivity test. (a) The acceleration signal from the initial sense preamp output. Note the harmonics. (b) The output signal after demodulation.

The sense capacitance gradient in the z-direction can be expressed as

$$\frac{dC(z)}{dz} = b_0 + b_1 z + b_2 z^2 + b_3 z^3 + \dots \quad (6-12)$$

Normally, the third or higher harmonic terms are negligible. In this analysis, we consider only second harmonic term, i.e.,

$$\frac{dC(z)}{dz} = b_0 + b_1 z + b_2 z^2 \quad (6-13)$$

The shuttle experiences two external forces. One is,  $f_{cz}$ , the coupled force from the excitation vibration, and the other is,  $f_{ext}$ , the applied electrostatic force to generate the disturbance acceleration in the z-direction. Thus we have

$$\begin{aligned} z &= \frac{f_{cz} + f_{ext}}{k_z} = \frac{f_{cz0}(\cos \omega_d t) + f_{ext0}(\cos(\omega_a t + \phi_a))}{k_z} \\ &= z_c(\cos(\omega_d t)) + z_a(\cos(\omega_a t + \phi_a)) \end{aligned} \quad (6-14)$$

where  $z_c$  is the coupled motion amplitude,  $\omega_d$  is the operating frequency, and  $z_a$ ,  $\omega_a$  and  $\phi_a$  are the amplitude, frequency and phase of the external acceleration, respectively. The damping force is ignored since the resonant frequency of the z-sense mode is almost twice as much as the operating frequency. Substituting Eq. (6-14) into Eq. (6-13) gives  $dC/dz$ . The possible frequency components of the output signal of the first demodulator (see Fig. 6-24) are shown in Fig. 6-33. Since there are too many terms, instead of giving the full expression, the amplitude and phase of each frequency component is listed in Table 6-5. This table shows that if  $b_2$ , the coefficient of the second harmonic, is zero, i.e., the  $dC/dz$  is perfectly linear, the device will be completely insensitive to the external acceleration. This statement, of course, assumes that the frequency of the external acceleration is not

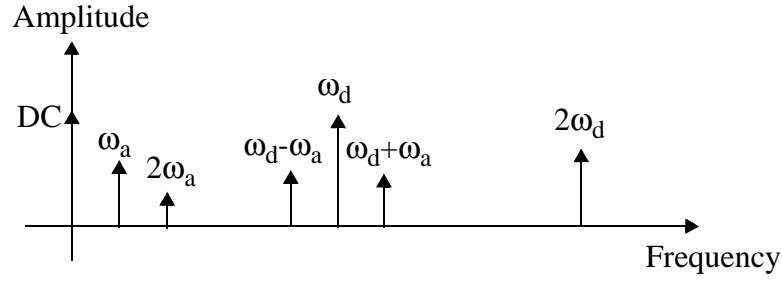


Figure 6-33: Frequency components of the output signal of the first demodulator.

the same as the drive frequency. If the two frequencies are equal, then they can only be distinguished by phase. In most cases, the phase of the disturbance signal may be unknown or even change with time. Therefore, a gyroscope must operate at a frequency above all expected environmental vibrations.

**Table 6-5: Amplitude/phase list of frequency components in the output of the first demodulator**

frequency	DC	$\omega_a$	$2\omega_a$	$\omega_d$
amplitude	$b_0 + b_2(z_c^2 + z_a^2)/2$	$b_1 z_a$	$-b_2 z_a^2/2$	$b_1 z_c$
phase	-	$\phi_a$	$2\phi_a$	$\phi_c$
frequency	$\omega_d - \omega_a$	$\omega_d + \omega_a$	$2\omega_d$	
amplitude	$b_2 z_c z_a$	$b_2 z_c z_a$	$-b_2 z_c^2/2$	
phase	$-\phi_a$	$\phi_a$	0	

In reality, it is hard to make  $b_2$  equal to zero. As shown in Fig. 6-20(a), the second harmonic is large. All the frequency components listed in Table 6-5 will appear in the input node of the second demodulator. The frequency of the carrier signal of the second demodulator is  $\omega_d$ , and its phase,  $\phi_{lkn}$ , is tunable and locked with the drive signal. The possible



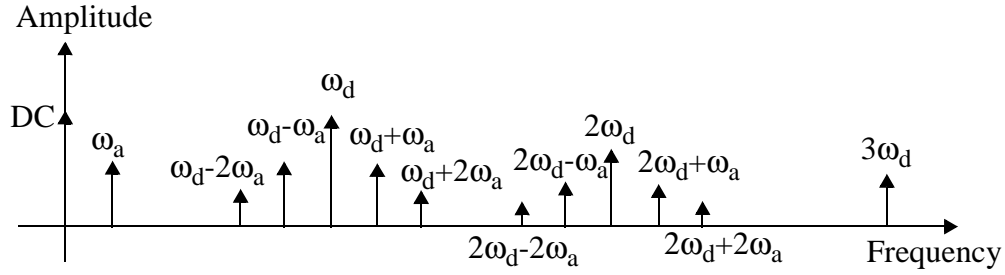


Figure 6-34: Frequency components of the output signal of the second demodulator.

frequency components after the second demodulation are shown in Fig. 6-34 and their amplitude and phase are listed in Table 6-6. The output stage of the demodulator is a low

**Table 6-6: Amplitude/phase of frequency components in the output of the second demodulator**

frequency	DC	$\omega_a$	$\omega_d$	$2\omega_d$
amplitude	$kb_1 z_c \cos(\phi_{lkn})$	$2kb_2 z_c z_a \cos(\phi_{lkn})$	$-kA$	$kb_1 z_c$
phase	-	$\phi_a$	$\phi_{2d}$	$\phi_{lkn}$
frequency	$\omega_d \pm \omega_a$	$\omega_d \pm 2\omega_a$	$2\omega_d \pm \omega_a$	$3\omega_d$
amplitude	$kb_1 z_a$	$-kb_2 z_a^2/2$	$kb_2 z_c z_a$	$-kb_2 z_c^2/2$
phase	$\phi_{lkn} \pm \phi_a$	$\phi_{lkn} \pm 2\phi_a$	$\phi_{lkn} \pm \phi_a$	$\phi_{lkn}$

pass filter. The cut-off frequency of the filter should be tunable according to the bandwidth of the rotation signal, which is typically 30 Hz. Note that the DC term is proportional to the amplitude of the coupled motion but has no relation to the acceleration signal. Thus, the gyroscope is insensitive to the disturbance vibrations with frequencies higher than the cut-off frequency of the demodulator. However, there are three differential fre-

quency components, i.e.,  $\omega_d - \omega_a$ ,  $\omega_d - 2\omega_a$ , and  $2\omega_d - \omega_a$ . Therefore, to make the above statement more strict, all the following conditions must be satisfied:

- 1)  $\omega_a > \omega_T$ ;
- 2)  $|\omega_d - \omega_a| > \omega_T$ ;
- 3)  $|\omega_d - 2\omega_a| > \omega_T$ ; and
- 4)  $|2\omega_d - \omega_a| > \omega_T$ .

where  $\omega_T$  is the cut-off frequency of the demodulator.

It is obvious from Table 6-5 that both the d.c. offset and the acceleration-generated output depend on the phase of the reference signal of the demodulator. There is also a phase lag between the two terms for reaching their own maxima.

From the above discussion, we know the bad acceleration rejection is caused by non-linearity of the capacitive sensing. However, from the simulation given in Chapter 3, the z-axis capacitive sensing interface should give a large linear range. So, what causes the difference?

After carefully checking the profile and structures of the device, it was found that the large non-linearity comes from the curling of the comb fingers. As shown in Fig. 6-35, one side of the comb fingers has silicon underneath and stays nearly flat while the other side of the comb fingers has silicon almost totally undercut and therefore curls up. This is even worse than the pure thin-film accelerometers in which the curling in both sides of the comb fingers can be matched through a matching frame [14].

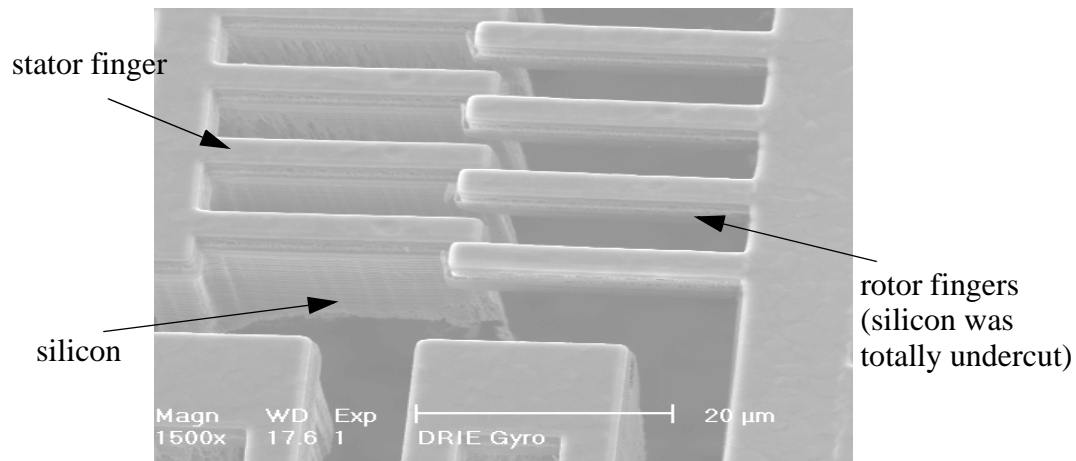


Figure 6-35: SEM of the drive comb fingers.

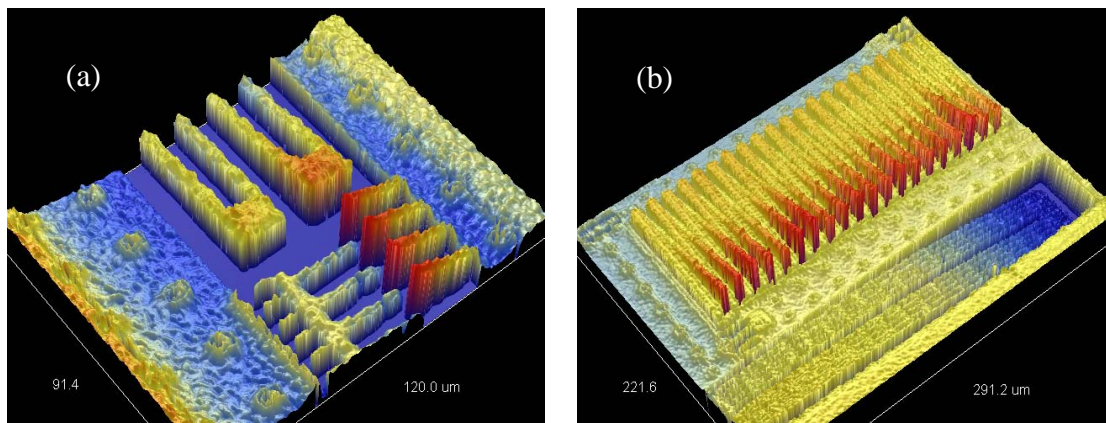


Figure 6-36: The curling of the springs and comb fingers. (a) X-drive spring and comb fingers; and (b) z-sense spring and comb fingers

The actual curling of the springs and comb fingers was characterized by using the Wyko white-light profilometer. The measurement results are shown in Fig. 6-36. The drive comb fingers on the shuttle side are about  $2.2 \mu\text{m}$  above the stator fingers and the rotor fingers in the sense comb are about  $6.5 \mu\text{m}$  above its stator fingers for this particular device.

### **6.2.7 Summary**

From the above discussion, the following statements can be made:

(1) The DRIE CMOS-MEMS process enables three different axis gyroscopes integrated on a single chip. Much better performance is expected for z-axis gyroscopes because, unlike lateral gyroscopes, z-axis gyroscopes do not have thin-film structures and thus have better thermal performance and higher linear acceleration rejection ratio.

(2) From the analysis in Section 5.3.3 and Section 6.2.6.7, the z-axis direct-coupled motion is even more problematic than the quadrature error. By using the same technique for achieving balanced capacitive bridges in the z-axis acceleration sensing (see Section 3.3.2), a method to cancel the vertical electrostatic force in lateral-axis comb-finger actuation is proposed in Section 6.2.8.

(3) A special process is needed to independently control the undercuts for electrical isolation and silicon comb fingers. A new process flow will be discussed in Section 6.2.9.

(3) The Si layer may be only used as a mechanical support. In this case, there will be much fewer process constraints. Comb fingers like the ones shown in Fig. 6-37 can be designed. The basic idea is to use the thick Si layer to keep the structure flat and undercut the Si beams at the same time to reduce parasitic capacitance of the active wiring/electrodes. Fig. 6-37(a) and (b) are wiring configurations for regular sense comb fingers and differential sense comb fingers, respectively. An initial Si undercut can be used to even further reduce parasitic capacitance as shown in Fig. 6-37(c) and (d).

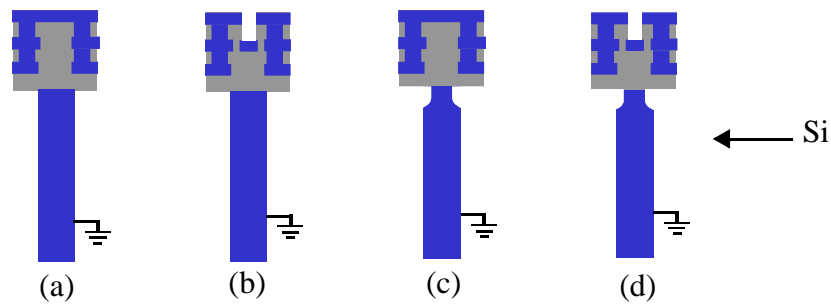


Figure 6-37: Comb finger designs with reduced parasitic capacitance. (a) Regular sense comb finger. (b) Differential sense comb finger. (c) Regular sense comb finger with an initial Si undercut. (d) Differential sense comb finger with an initial Si undercut.

(4) Since the DRIE CMOS-MEMS process provides flat structures, devices with larger size can be designed. Thus more drive comb fingers can be added to achieve higher vibration amplitude at moderate drive voltage.

A single-chip, six-degree-of-freedom, integrated IMU has been designed and fabricated jointly with Robert Bosch Corporation. A scanning electron micrograph (SEM) of the device is shown in Fig. 6-38. Further mechanical characterization and more reliable interface circuit design are undergoing.

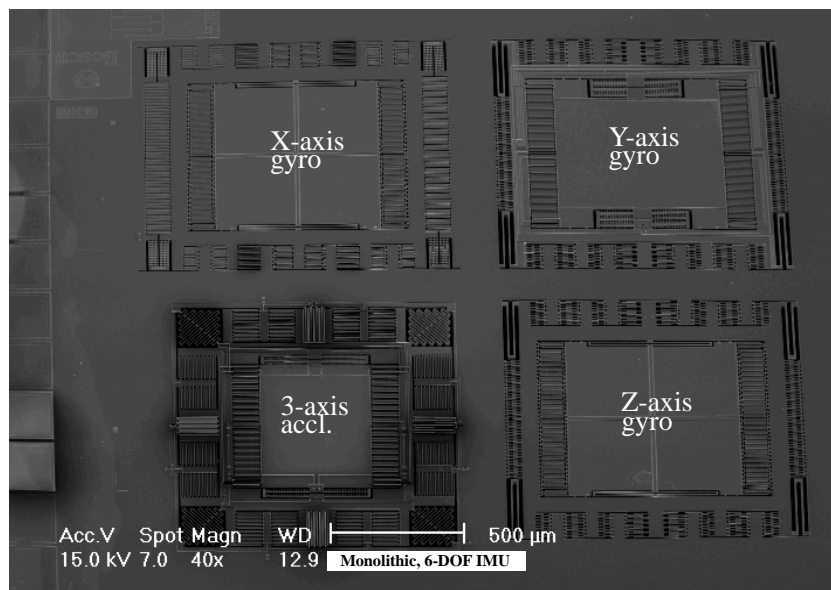


Figure 6-38: SEM of a released 6-DOF IMU.

### 6.2.8 Vertical-Axis Electrostatic Force Cancellation

Levitation force exists in polysilicon comb drives because of the ground plane under the comb fingers [121][28]. Similarly, as discussed in Section 3.3.1, comb fingers with a Si ground layer (see Fig. 3-20(c)) can generate vertical electrostatic force and have been used for vertical actuation. However, this vertical force is present even when only a lateral-axis actuation is needed. Fig. 6-39 shows a lateral-axis comb drive. The Si layer is grounded. When a voltage is applied as shown in Fig. 6-39(b), a z-axis force as well as a x-axis force is generated. The vertical force is not desired and causes coupling problems in a gyroscope as discussed in Section 6.2.1.1.

In contrast to the levitation force in comb drives with a ground plane, the vertical force in comb drives with Si layer underneath can be either positive or negative. As shown in Fig. 6-40, the direction of the vertical force is determined by the polarities of the stator and rotor fingers. When the stator is positive with the rotor grounded, the vertical force is up. When the rotor is positive with the stator grounded, the vertical force is down. In both

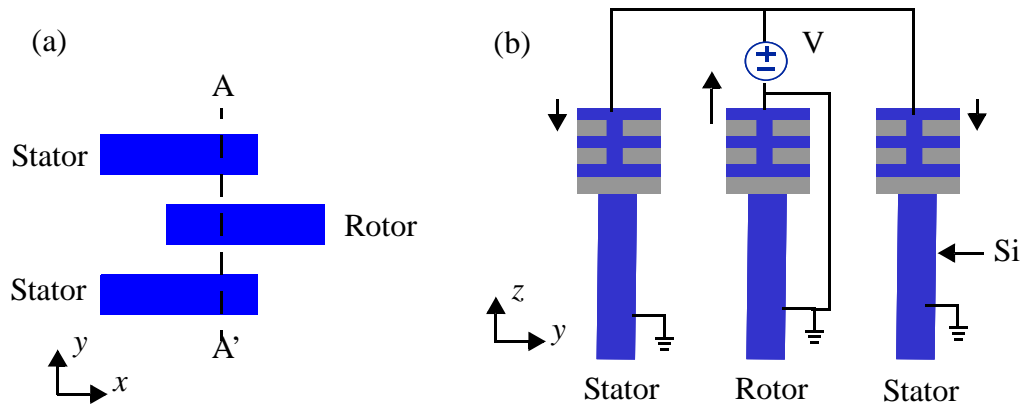


Figure 6-39: Lateral comb drive with vertical force.  
(a) Top view. (b) Cross-section view.

cases, the lateral force is in the same direction. Therefore, the vertical force can be cancelled out by proper wiring of the stator and rotor fingers.

## 6.2.9 A DRIE CMOS-MEMS Process With Controllable Si Undercut

### 6.2.9.1 Introduction

Single-crystal silicon (SCS) MEMS structures are often desired because of bulk silicon's excellent mechanical properties and IC-compatibility. For inertial sensors, bulk silicon also provides thick, flat structures and large mass which leads to high sensitivity and high resolution. Moreover, bulk silicon provides the feasibility to make large, flat scanning micromirrors for medical imaging applications.

In most cases, bulk silicon serves as electrodes for active sensing or actuation elements as well as the supporting material. Therefore, electrical isolation of bulk silicon is required. In our prior work, electrical isolation of bulk silicon has been realized by undercutting silicon underneath narrow metal/oxide beams. If the width of such a beam is equal to or smaller than twice of the undercut, the silicon underneath the beam will be totally

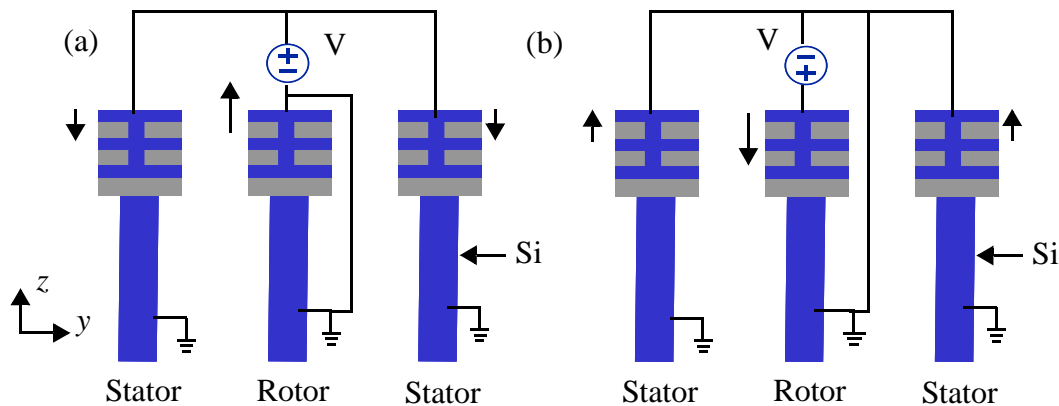


*Figure 6-40: Vertical force cancellation for lateral comb drive.  
(a) Positive z-axis force. (b) Negative z-axis force.*

undercut. Then the bulk silicon on both sides of the beam is electrically isolated but mechanically connected. The beams for isolation are very short though narrow to make the joint rigid.

However, all structures on the chip will be undercut. The amount of undercut depends on the trench width. There is a trade-off for setting the undercut value. The beams for isolation need large undercut for completely undercutting silicon, while the other structures such as comb fingers desire as small undercut as possible to provide maximum flatness.

#### **6.2.9.2 The concept**

A new process sequence is proposed to make SCS CMOS-MEMS devices with electrically isolated bare bulk silicon structures [122]. The process can be simplified if the interest is just to obtain either electrical isolation or bare silicon structures.

The problem arises from the conflict between the requirements to the undercut at different areas. One possible solution to this conflict is to selectively etch different areas. The same idea is described in Appendix A by using polysilicon as an extra etching mask. However, the currently employed etching recipe has low polysilicon-to-oxide etching rate ratio. With that low etch selectivity, using a thin polysilicon layer (0.25  $\mu\text{m}$ ) as the stop for the oxide etch is not practically feasible.

The new process flow is shown in Fig. 6-41. The top Al layer is chosen as the selective mask. We already know the etching selectivity between Al and oxide is high. The process is divided into four stages: (1) completely undercut the beams for isolation (Fig. 6-41(a)-(d)); (2) selectively etch top aluminum layer (Fig. 6-41(e)-(f)); (3) release the rest of the



structures (Fig. 6-41(g)-(h)); and (4) remove aluminum and oxide to attain bare SCS structures. The detailed process procedure is described below.

### **6.2.9.3 Process sequence**

#### *Stage I: Undercut isolation beams*

The process flow starts with a deep anisotropic backside etch, leaving a 10 to 200  $\mu\text{m}$  thick silicon membrane (Fig. 6-41(a)). There is no need for high backside to frontside alignment accuracy. Next an anisotropic dielectric etch is performed from the frontside (Fig. 6-41(b)). Then an anisotropic silicon etch is used to etch through the silicon membrane (Fig. 6-41(c)). The fourth step is to completely undercut isolation beams by using an isotropic silicon etch. In fact, this stage is exactly the process reported in [22].

#### *Stage II: Etch top aluminum layer*

The first step is to pattern photoresist or use a shadow mask to protect the on-chip circuits and bond pads (Fig. 6-41(e)). Then an ion milling of aluminum is performed to unveil structure patterns that are still covered by oxide (Fig. 6-41(f)).

#### *Stage III: Structure release*

First, an anisotropic oxide etch is performed (Fig. 6-41(g)). The interconnect metal layers act as the etching mask. Then a deep silicon etch is followed to release the whole structure (Fig. 6-41(h)). Compared to Stage I, no isotropic silicon etch is needed, so the deep silicon etch can be optimized to obtain minimum undercut to the sidewall straight.

#### *Stage IV: Bare SCS MEMS structures*

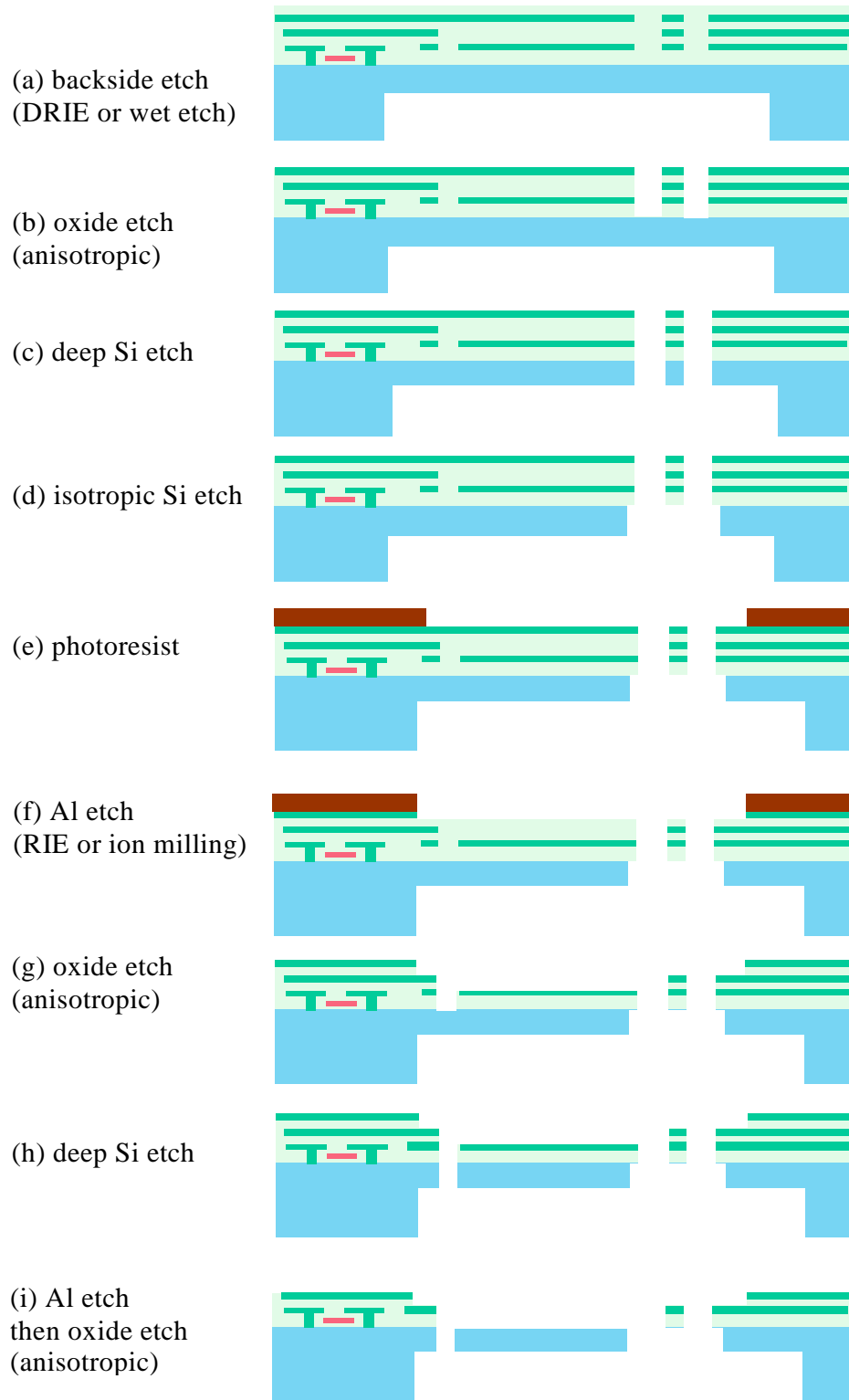


Figure 6-41: The cross-sectional view of the proposed CMOS-MEMS process flow.

This stage is just a repeat of Stage II. The on-chip circuits and bond pads are protected by the top metal layer (Fig. 6-41(i)) or by painting photoresist or using a shadow mask. Then an ion milling of aluminum is performed (Fig. 6-41(j)), followed by an anisotropic oxide etch to stop on the Si substrate (Fig. 6-41(k)).

#### **6.2.9.4 Process derivatives**

The process sequence described above can generate CMOS-MEMS structures with electrically isolated bare bulk silicon. However, sometimes only electrical isolation or only bare bulk silicon structures may be desired. In either of the two cases, the process can be simplified.

In the case where only electrical isolation is required, the metal and oxide on the top of bulk silicon do not need to be removed; therefore Stage IV is not necessary. The process sequence will include only Stage I, II and III. In the case where only bare bulk silicon structures are needed, no electrical isolation is required. Therefore, the process sequence will include only Stage III and IV plus a backside etch at the beginning.

## Chapter 7

# Conclusions and Future Work

In this thesis, techniques have been demonstrated for comb-finger-only three-dimensional capacitive sensing and electrostatic actuation, which allows single-chip integration of three-axis accelerometers and three-axis gyroscopes. Out-of-plane sensing and actuation have been explored extensively. In particular, a curled comb drive which is capable of generating 62  $\mu\text{m}$  out-of-plane displacement has been developed.

Lateral curling for thin-film beams with multiple metal layers has been alleviated by using a beam design with tapered cross-section. Thermomechanical tuning of the resonance frequency of a mechanical resonator has been obtained by using a thin-film flexure with an integrated polysilicon heater. This technique was used in the thin-film lateral-axis CMOS-MEMS gyroscope for resonance frequency matching between the sense and drive modes.

The thermally actuated micromirror rotates up to  $17^\circ$  and has been installed into an endoscopic optical coherence tomography (OCT) imaging system for *in vivo* imaging of biological tissue. The preliminary experiments show very promising resolution and scanning speed. This work opens the possibility to make compact, high-performance and low-cost OCT catheters and endoscopes for future clinical applications by using MEMS tech-

---

nology. The buckling problem of the bimorph actuation mesh of the thermal micromirror may be solved through either design or processing.

The electrostatic micromirror with the curled comb drive rotates up to  $\pm 5^\circ$ . It has low power consumption and potential high speed. The new electrostatic micromirror design with curled comb drives close to the rotational axis is expected to achieve  $\pm 10^\circ$ , though some process issues must be addressed. The single-axis scanning micromirrors have demonstrated a promising application in a biomedical imaging system. Dual-axis scanning micromirrors can be easily designed and will provide full 3-D image scanning in the optical coherence tomography application.

With the same chip size and same on-chip interface circuits, the DRIE accelerometers have one order of magnitude lower noise floor ( $0.5 \text{ mG/Hz}^{1/2}$ ) than the thin-film accelerometers, but still limited by electronics noise. Better interface circuits, preferably switch-capacitor circuits, should be used to improve the performance.

The DRIE lateral-axis gyroscope has a  $0.02^\circ/\text{s/Hz}^{1/2}$  noise floor, even though it has large d.c. offset and high ZRO fluctuation due to the Si undercut problem, no temperature compensation and open-loop operation. Measurements show that the Coriolis signal only had a  $12^\circ$  phase delay compared to the coupled signal in the DRIE CMOS-MEMS gyroscope. It was found from the 3-D motion analysis of a comb drive in Section 5.3.3 that the off-axis motions due to asymmetries in the structure are relatively large, highly nonlinear and in-phase with the Coriolis motion. The  $12^\circ$  phase delay indicates that the off-axis motion in the sense axis of the embedded accelerometer dominates the quadrature motion.

A vertical-axis electrostatic force cancellation technique has been proposed in Section 6.2.8 to eliminate the off-axis motion in the z-direction. However, the nonlinear behavior of the off-axis motion makes compensation difficult.

The fabricated DRIE gyroscope's performance was greatly degraded because the beams for electrical isolation of silicon required long undercut which eventually etched the silicon underneath the drive and sense comb fingers. The resultant curled comb fingers generate off-axis motion for actuation and non-linearity for sensing. A new process flow has been proposed to solve the undercut problems existing in the current DRIE CMOS-MEMS process. Gyroscopes fabricated by using the new process sequence are expected to have significant performance improvement. Performance and yield will be improved by using the current DRIE CMOS-MEMS process, with no electrical isolation of silicon and proper design to reduce parasitic capacitance. Next-generation, high-performance, robust gyroscopes must incorporate temperature compensation, linear acceleration cancellation by two anti-phase vibrating shuttles, automatic force balancing and closed-loop operation. Gyroscopes with a noise floor of  $0.001^\circ/\text{s}/\text{Hz}^{1/2}$  and a bias stability of  $5^\circ$  per hour are achievable.

The thesis is focused on development of sensing and actuation and demonstrates the feasibility to fabricate lateral-axis gyroscopes using the DRIE CMOS-MEMS process. However, the DRIE CMOS-MEMS process is most suitable for making z-axis gyroscopes where both the sense spring and drive spring can be made of single-crystal silicon. Better mechanical robustness and temperature performance can be immediately achieved

---

through z-axis gyroscope design, without increasing design complexity or modifying any process steps.

Even though it enables many applications such as accelerometers, gyroscopes and micromirrors, the DRIE CMOS-MEMS process is not yet mature. So far, only die-level processing has been performed. For commercial production, the feasibility of wafer-level processing must be studied. Controlling the thickness and backside uniformity of the Si layer is still a concern. Using silicon-on-insulator (SOI) wafers is a possible solution, but limits the CMOS compatibility.

## Appendix A

### DRIE CMOS-MEMS Process Flows Using Polysilicon as an Additional Etching Mask

#### A.1 SCS Comb Fingers and Springs

Beams with only SCS (single-crystal silicon) layers have much better mechanical properties and temperature performance than those with a CMOS layer on the top. The process flow shown in Fig. A-1 can be used to fabricate SCS microstructures.

The process flow starts with a regular backside DRIE silicon etch (Fig. A-1(a)). The second step is a frontside oxide etch. The polysilicon layer is used as an additional etching mask for the oxide etch (Fig. A-1(b)). This step must be finely controlled by timing. The

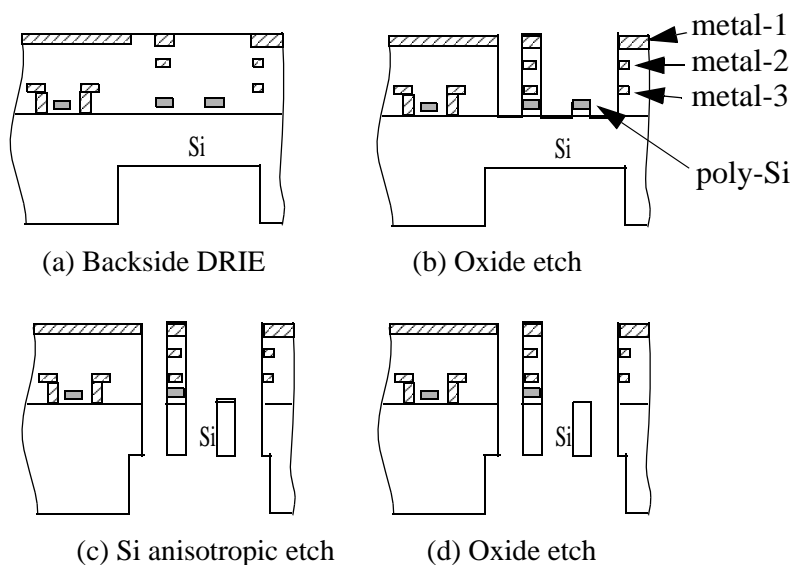


Figure A-1: Process flow for single-crystal silicon beams



oxide layer underneath the polysilicon layer is then used as the etching mask for the frontside DRIE silicon etch (Fig. A-1(c)). Finally the SCS microstructure is obtained by just adding a second short oxide etch.

## A.2 Process Sequence for Electrical Isolation of SCS Areas

The process flow stated in Section 2.2.1 has many advantages including electrical isolation of SCS areas. However, the electrical isolation relies on the undercut of silicon. This undercut increases the gap between comb fingers. In order to solve this problem, a new process flow is proposed as shown in Fig. A-2. Same as in Section A.1, the polysilicon

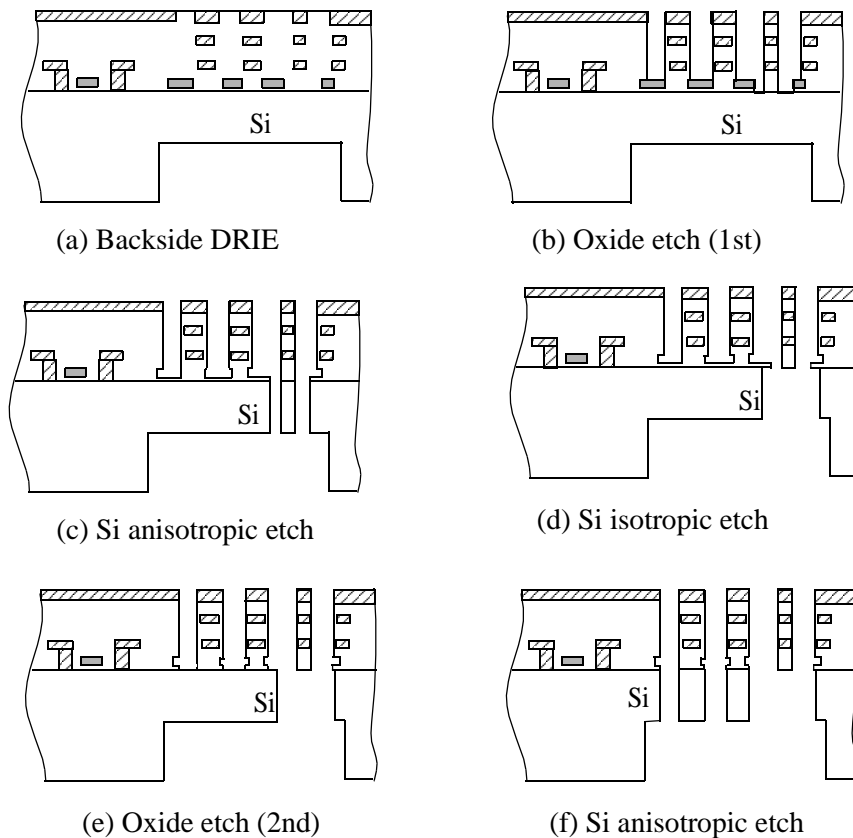


*Figure A-2: Process flow for electrical isolation of SCS areas*

layer is used as the etching mask for oxide etch. The gaps between comb fingers are covered by polysilicon while those areas around the isolation beams have no polysilicon (Fig. A-2(a)). Therefore, the first oxide etch only exposes silicon around the isolation beams (Fig. A-2(b)). The following silicon anisotropic etch and isotropic etch will undercut the isolation beams thoroughly (Fig. A-2(c) and (d)). At this point, the polysilicon between all comb fingers has been etched away. The second oxide etch exposes the silicon between comb fingers (Fig. A-2(e)), and the following silicon anisotropic etch releases the entire microstructure (Fig. A-2(f)).



## Appendix B

### OCEAN Script for Gyroscope Process Variation Simulation

The main program is “process\_var.ocn” which calls “parameter\_setting.ocn” and “nomi\_meas.ocn”. The output data will be saved in a file named “nomi.out”.

```
; ***** process_var.ocn *****
simulator( 'spectreS )
design(    "/tmp/xie/Sim/gyro_z_no_comb_1/spectreS/schematic/
          netlist/gyro_z_no_comb_1.c")
resultsDir( "/tmp/xie/Sim/gyro_z_no_comb_1/spectreS/
            schematic" )
option( 'compatible "spectre")
temp( 27 )

; the file to store simulation results
fp = outfile("./nomi.out" "w")
fprintf( fp "\nGyroscope Simulation: nominal case\n\n")
fprintf( fp "\n1. Undercut sweeping")
fprintf( fp "\n2. Thickness sweeping")

; Undercut sweep

;initialization

desVar( "t0" 50e-6 ) ; t0 is the Si layer thickness
desVar( "x0" 0.9u ) ; x0 is the Si undercut
desVar( "fvsin" 8000 ) ; fvsin is the drive frequency
desVar( "av0" 1.0 ) ; av0 is the rotation rate

n=0
x0 = list( 0 0.1u 0.2u 0.3u 0.4u 0.5u 0.6u 0.7u 0.8u 0.9u
          1.0u)
foreach( val x0
        desVar("x0" val)
        undercut = n*0.05e-6
        n = n + 1
        fprintf( fp "\n undercut is: %e\n", undercut)
        load( "parameter_setting.ocn" )
        load( "nomi_meas.ocn" )
        )
```

---

```

; Thickness sweep
; initialization

desVar( "t0" 50e-6 )
esVar( "x0" 0.9u )
desVar( "fvsin" 8000 )
desVar( "av0" 1.0 )

n=0
t0 = list( 0 10u 20u 30u 40u 50u 60u 70u 80u 90u 100u)
foreach( val t0
    desVar("t0" val)
    t_si = n*2.5e-6
    n = n + 1
    fprintf( fp "\n Silicon thickness is: %e\n", t_si)
    load( "parameter_setting.ocn" )
    load( "nomi_meas.ocn" )
)

close(fp)

; *** end ***

;***** parameter_setting.ocn *****

; Set the parameters to their default values

desVar( "fs11" "x0" )
desVar( "fs12" "x0" )
desVar( "fs21" "x0" )
desVar( "fs22" "x0" )
desVar( "fst11" "t0" )
desVar( "fst12" "t0" )
desVar( "fst21" "t0" )
desVar( "fst22" "t0" )
desVar( "is11" "x0" )
desVar( "is12" "x0" )
desVar( "is21" "x0" )
desVar( "is22" "x0" )
desVar( "ist11" "t0" )
desVar( "ist12" "t0" )
desVar( "ist21" "t0" )
desVar( "ist22" "t0" )
desVar( "thk_m" "t0" )
desVar( "thk_f" "t0" )
desVar( "angu_v" "av0" )

; *** end ***

```

---

```

; ***** nomi_meas.ocn *****
; first to do ac analysis to find resonant freq

desVar( "f_ac_s" 0.1u )
desVar( "f_ac_d" 25u )
ac(5000 20000 1000)

run()
relectResult('ac)

xd = mag( getData("/x_d") )
ys = mag( getData("/y_s") )

; find resonant frequency

f_drv = xmax( fxd )
f_drv2 = round( f_drv)
fprintf( fp "resonant frequency: %d\n",f_drv2)
f_sens = xmax( fys )
f_sens2 = round( f_sens)
fprintf( fp "resonant frequency: %d\n",f_sens2)

; second to extract parameters

; set parameters
desVar( "f_ac_d" 25u )
desVar( "f_ac_s" 0 )

ac(f_drv2-50 f_drv2+50 "Linear" 100)
run()
relectResult('ac)

y_s1 = value( getData( "/y_s") f_drv2)
x_d1 = value( getData( "/x_d") f_drv2)
y_d1 = value( getData( "/y_d") f_drv2)
x_s1 = value( getData( "/x_s") f_drv2)
y_s1_amp = mag(y_s1)
x_d1_amp = mag(x_d1)
y_d1_amp = mag(y_d1)
x_s1_amp = mag(x_s1)

fprintf( fp "frame_drive amplitude: %e\n",x_d1_amp)
fprintf( fp "frame_cross amplitude: %e\n",y_d1_amp)
fprintf( fp "mass_sense amplitude: %e\n",x_s1_amp)
fprintf( fp "mass_cross amplitude: %e\n",y_s1_amp)

; *** end ***

```



# Bibliography

- [1] H. Baltes, O. Brand, A. Hierlemann, D. Lange, C. Hagleitner, "CMOS MEMS - present and future," *MEMS 2002*, Las Vegas, Nev., USA, Jan. 20-24, 2002, pp.459 - 466.
- [2] J. H. Smith, S. Montague, J.J. Sniegowski, J. R. Murray, *et al.*, "Embedded micromechanical devices for the monolithic integration of MEMS with CMOS," in *Proc. Int. Electron Devices Meeting*, Washinton, DC, Dec. 10-13, 1995, pp.609-619.
- [3] T.A. Core, W.K. Tsang, S.J. Sherman, "Fabrication technology for an integrated surface-micromachined sensor," *Solid State Technology*, vol.36, no.10, pp.39-47.
- [4] W. Yun, R.T. Howe, P.R. Gray, "Surface micromachined, digitally force-balanced accelerometer with integrated CMOS detection circuitry," *Tech. Digest IEEE Solid-State Sensor & Actuator Workshop*, Hilton Head Island, SC, USA; 22-25 June 1992, pp.126-131.
- [5] M. Lemkin and B.E. Boser, "A three-axis micromachined accelerometer with a CMOS position-sense interface and digital offset-trim electronics," *IEEE Journal of Solid-State Circuits*, vol.34, no.4, pp.456 -468.
- [6] A.E. Franke, D. Bilic, D.T. Chang, P.T. Jones, T.-J. King, R.T. Howe, G.C. Johnson, "Post-CMOS integration of germanium microstructures", *MEMS'99*, Orlando, FL, USA; 17-21 Jan. 1999, pp.630-637.
- [7] D. Moser, O. Brand, H. Baltes, "A CMOS compatible thermally excited silicon oxide beam resonator with aluminum mirror," *Transducers'91*, 24-27 June 1991, San Francisco, CA, pp.547 - 550.
- [8] M. von Arx, O. Paul, H. Baltes, "Test structures to measure the heat capacity of CMOS layer sandwiches," *IEEE Transactions on Semiconductor Manufacturing*, vol.11 (1998), pp.217 - 224.
- [9] M. Schneider, T. Muller, A. Haberli, M. Hornung, H. Baltes, "Integrated micromachined decoupled CMOS chip on chip," *MEMS '97*, 26-30 Jan. 1997 Nagoya, Japan, pp.512 - 517.
- [10] O. Paul and H. Baltes, "Novel fully CMOS compatible vacuum sensor," *Sensors & Actuators A*, vol. 46/47 (1995), pp. 428-431.



- 
- [11] M. von Arx, O. Paul, H. Baltes, "Process-dependent thin-film thermal conductivities for thermal CMOS MEMS," *Journal of Microelectromechanical Systems*, vol.9 (2000), no.1, pp.136 -145.
- [12] H. Baltes, O. Paul and O. Brand, "Micromachined thermally based CMOS microsensors," *Proceedings of IEEE*, vol. 86, no. 8, pp.1660-1678.
- [13] G.K. Fedder, S. Santhanam, M.L. Reed, S.C. Eagle, D.F. Guillou, M.S.-C. Lu, L.R. Carley, "Laminated high-aspect-ratio microstructures in a conventional CMOS process", *Sensors and Actuators A*, vol.A57, pp.103-110.
- [14] G. Zhang, H. Xie, L. deRosset, G.K. Fedder, "A lateral capacitive CMOS accelerometer with structural curl compensation", *MEMS' 99*, Orlando, FL, USA; 17-21 Jan. 1999, pp.606-611.
- [15] H. Xie, G.K. Fedder, "A CMOS z-axis accelerometer with capacitive comb-finger sensing", *MEMS' 2000*, Miyazaki, Japan; 25-28 Jan. 2000, pp.496-501.
- [16] H. Luo, G. K. Fedder, and L. R. Carley, "A 1 mG lateral CMOS-MEMS accelerometer," *MEMS' 2000*, Miyazaki, Japan; 25-28 Jan. 2000, pp.
- [17] H. Xie, G. K. Fedder, A CMOS-MEMS Lateral-axis Gyroscope, in *The 14th IEEE International Conference on Micro Electro Mechanical Systems (MEMS 2001)*, Inter-laken, Switzerland, January 21-25, 2001, pp.162-165.
- [18] H. Luo, X. Zhu, H. Lakdawala, L.R. Carley and G.K. Fedder, "A copper CMOS-MEMS z-axis gyroscope," in *The 15th IEEE International Conference on Micro Electro Mechanical Systems (MEMS 2002)*, Las Vegas, Nevada, Jan. 21-25, 2002, pp.631-634.
- [19] H. Lakdawala and G. K. Fedder, "CMOS Micromachined Infrared Imager Pixel," in *Technical Digest of the 11th IEEE International Conference on Solid-State Sensors and Actuators (Transducers '01)*, June 10-14, 2001, Munich, Germany, pp.
- [20] H. Xie, L. Erdmann, Q. Jing, G.K. Fedder, "Simulation and characterization of a CMOS z-axis microactuator with electrostatic comb drives", *Proc. 2000 International Conference on Modeling and Simulation of Microsystems -- MSM'2000*, San Diego, CA; 27-29 Mar. 2000, pp.181-184.
- [21] H. Xie and G.K. Fedder, "Vertical Comb-finger Capacitive Actuation and Sensing for CMOS-MEMS," *Sensors & Actuators: A*, vol.95 (2002), pp.212-221.
- [22] H. Xie, L. Erdmann, X. Zhu, G.K. Fedder, "Post-CMOS processing for high-aspect-ratio integrated silicon microstructures", *Technical Digest. Solid-State Sensor and Actuator Workshop*, Hilton Head Island, SC, USA; June 4-8, 2000, pp.77-80.

- [23] Accelerometer Product Family, Analog Devices Inc., Norwood, MA 02062, <http://www.analog.com/imems>.
- [24] P. Greiff, B. Boxenhorn, T. King, L. Niles, "Silicon monolithic micromechanical gyroscope", *TRANSDUCERS '91*, San Francisco, CA, USA; 24-27 June 1991, pp.966-968.
- [25] W.A. Clark, R.T. Howe, R. Horowitz, "Surface micromachined Z-axis vibratory rate gyroscope", *Technical Digest. Solid-State Sensor and Actuator Workshop*, Hilton Head Island, SC, USA; 3-6 June 1996, pp.283-287.
- [26] M. Lutz, W. Golderer, J. Gerstenmeier, J. Marek, B. Maihofer, S. Mahler, H. Munzel and U. Bischof, "A precision Yaw Rate Sensor in Silicon Micromachining", *Transducers'97*, Chicago, June 16-19, 1997, pp.847-850.
- [27] Meng-Hsiung Kiang, O. Solgaard, K.Y. Lau and R.S. Muller, "Electrostatic comb drive-actuated micromirrors for laser-beam scanning and positioning," *Journal of Microelectromechanical Systems*, vol.7 (1998), pp.27-37.
- [28] A.P. Lee, C.F. McConaghy, P.A. Krulevitch, E.W. Campbell, G.E. Sommargren, and J.C. Trevino, "Electrostatic comb drive for vertical actuation," *SPIE*, vol.3224, pp.109-119.
- [29] A. Selvakumar and K. Najafi, "A high-sensitivity z-axis capacitive silicon microaccelerometer with a torsional suspension," *Journal of Microelectromechanical Systems*, vol.7 (1998), pp.192 -200.
- [30] R.A. Conant, J.T. Nee, K.Y. Lau and R.S. Muller, "A flat high-frequency scanning micromirror," *Technical Digest of the Solid-State Sensor & Actuator Workshop*, Hilton Head Island, SC, USA, June 4-8, 2000, pp.6-9.
- [31] H. Xie, L. Erdmann, X. Zhu, K. Gabriel and G.K. Fedder, J.MEMS3)H. Xie, L. Erdmann, X. Zhu, K. Gabriel and G. Fedder, "Post-CMOS Processing For High-aspect-ratio Integrated Silicon Microstructures", *Journal of Microelectromechanical Systems*, vol.11, no.2, 2002, pp.93-101.
- [32] D. Huang, E. A. Swanson, C. P. Lin, J. S. Schuman, W. G. Stinson, W. Chang, M. R. Hee, T. Flotte, K. Gregory, C. A. Puliafito, J. G. Fujimoto, "Optical coherence tomography," *Science*, vol.254 (1991), no.5035, pp.1178-1181.
- [33] 2.G. A. Tearney, M. E. Brenzinski, B. E. Bouma, S. A. Boppart, C. Pitris, J. F. Southern, and J. G. Fujimoto, "In vivo endoscopic optical biopsy with optical coherence tomography," *Science*, vol.276 (1997), no. 5321, pp.2037-2039.

- 
- 
- [34] Y. T. Pan, J. P. Lavelle, S. Bastacky, M. Zeidel, and D. Farkas, "Detection of tumorigenesis in rat bladders with optical coherence tomography," *Medical Physics*, vol.28 (2001), no.12, pp.2432-2440.
- [35] A. M. Sergeev, F. I. Feldchtein, et al., "In vivo endoscopic OCT imaging of precancer and cancer states of human mucosa," *Optics Express*, vol.1 (1997), no.13, pp.421-423.
- [36] Y. T. Pan, D. L. Farkas, "Noninvasive imaging of living human skin with dual-wavelength optical coherence tomography in two and three dimensions," *Journal of Biomedical Optics*, vol.3 (1998), no.4, pp.446-455.
- [37] A. M. Rollins, R. Ung, A. Chak, C. Wong, K. Kobayashi, M. V. Sivak, J. A. Izatt, "Real-time in vivo imaging of human gastrointestinal ultrastructure by use of endoscopic optical coherence tomography with a novel efficient interferometer design," *Optics Letters*, vol.24 (1999), no.19, pp.1358-1360.
- [38] W. Drexler, U. Morgner, F. X. Krtner, C. Pitris, S. A. Boppart, X. D. Li, E. P. Ippen, J. G. Fujimoto, "In vivo ultrahigh-resolution optical coherence tomography," *Optics Letters*, vol.24 (1999), no.17, pp.1221-1223.
- [39] U. Morgner, W. Drexler, F. Krtner, X. Li, C. Pitris, E. Ippen, J. Fujimoto, "Spectroscopic optical coherence tomography," *Optics Letters*, vol.25 (2000), no.2, pp.111-113.
- [40] C. Saxer, J. de Boer, B. Park, Y. Zhao, Z. Chen, J. Nelson, "High-speed fiber-based polarization-sensitive optical coherence tomography of in vivo human skin," *Optics Letters*, vol.25 (2000), no.18, pp.1355-1357.
- [41] S. Yazdanfar, A. M. Rollins, J. A. Izatt, "Imaging and velocimetry of the human retinal circulation with color Doppler optical coherence tomography," *Optics Letters*, vol.25 (2000), no.19, pp.1448-1450.
- [42] G. Tearney, B. Bouma, J. Fujimoto, "High-speed phase- and group-delay scanning with a grating-based phase control delay line," *Optics Letters*, vol.22 (1997), no.23, pp.1811-1813.
- [43] L.J. Hornbeck, "Current status of the digital micromirror device (DMD) for projection television applications," *Technical Digest. International Electron Devices Meeting*, Washington, DC, 1993, pp.381-384.
- [44] W.H. Juan and S.W. Pang, "High-aspect-ratio Si vertical micromirror arrays for optical switching," *Journal of Microelectromechanical Systems*, vol.7 (1998), pp.207-213.

- [45] G.D. Su, H. Toshiyoshi, and M.C. Wu, "Surface-micromachined 2-D optical scanners with high-performance single-crystalline silicon micromirrors," *IEEE Photonics Technology Letters*, vol.13 (2001), pp.606-608.
- [46] A. Tuantranont, V.M. Bright, L.A. Liew, W. Zhang and Y.C. Lee, "Smart phase-only micromirror array fabricated by standard CMOS process," *MEMS' 2000*, Miyazaki, Japan; 25-28 Jan. 2000, pp.455-460.
- [47] P.R. Patterson, H. Dooyoung, N. Hung, H. Toshiyoshi, R. Chao, M.C. Wu, "A scanning micromirror with angular comb drive actuation," *MEMS 2002*, pp.544 - 547.
- [48] R. Usui, E. Asami, M. Kadota, K. Okada, "Development of the small size 3-Axis Fiber Optic Gyroscope," *Proceedings of the SPIE*, vol.3746, pp.268-271.
- [49] K. Taguchi, K. Fukushima, A. Ishitani, M. Ikeda, "Experimental investigation of a semiconductor ring laser as an optical gyroscope," *IEEE Transactions on Instrumentation and Measurement*, vol.48, no.6, pp.1314-1318.
- [50] K. Maenaka, T. Fujita, Y. Konishi, M. Maeda, "Analysis of a highly sensitive silicon gyroscope with cantilever beam as vibrating mass," *Sensors and Actuators A (Physical)*, vol.A54, no.1-3, pp.568-573.
- [51] M.W. Putty, K. Najafi, "A micromachined vibrating ring gyroscope," *Technical Digest. Solid-State Sensor and Actuator Workshop*, Hilton Head Island, SC, USA; 13-16 June 1994, pp.213-220.
- [52] J. Bernstein, S. Cho, A.T. King, A. Kourepenis, P. Maciel, M. Weinberg, "A micro-machined comb-drive tuning fork rate gyroscope," *Proceedings. IEEE. Micro Electro Mechanical Systems*, Fort Lauderdale, FL, USA; 7-10 Feb. 1993, pp.143-148.
- [53] C. Shearwood, C.B. Williams, P.H. Mellor, R.B. Yates, M.R.J. Gibbs, A.D. Mattingley, "Levitation of a micromachined rotor for application in a rotating gyroscope," *Electronics Letters*, vol.31, no.21, pp.1845-1846.
- [54] M. Kurosawa, Y. Fukuda, M. Takasaki, T. Higuchi, "A surface-acoustic-wave gyro sensor," *Sensors and Actuators A (Physical)*, vol.A66, no.1-3, pp.33-39.
- [55] G.K. Fedder, Qi Jing, "A hierarchical circuit-level design methodology for microelectromechanical systems", *IEEE Transactions on Circuits and Systems II*, vol.46, no.10, pp.1309-1315.
- [56] M.S.-C. Lu, X. Zhu, G.K. Fedder, "Mechanical property measurement of 0.5-mm CMOS microstructures", *Symposium on Microelectromechanical Structures for Materials Research*, San Francisco, CA, USA; 15-16 April 1998, pp.27-32.

- 
- [57] H. Lakdawala and G.K. Fedder, "Analysis of temperature-dependent residual stress gradients in CMOS micromachined structures," *Technical Digest of the 1999 International Conference on Solid State Sensors and Actuators (Transducers '99)*, Sendai, Japan, June 7-10, 1999, pp.526-529.
- [58] X. Zhu, *Post-CMOS Micromachining of Surface and Bulk Structures*, Ph.D. Thesis, Carnegie Mellon University, 2002.
- [59] F. Laermer and A. Schilp of Robert Bosch GmbH, "Method of anisotropically etching silicon," US-Patent No. 5501893, March 26, 1996, filed August 5, 1994.
- [60] MEMCAD User's Manual, Coventor, Inc., Cary, NC 27513, <http://www.coventor.com>.
- [61] D.A. Koester, R. Mahadevan, A. Shishkoff and K.W. Markus, "MUMPs Design Handbook, Rev. 4," Cronos Integrated Microsystems, Research Triangle Park, NC 27709, 1999.
- [62] C.S.B Lee, S. Han and N.C. MacDonald, "Multiple depth, single crystal silicon microactuators for large displacement fabricated by deep reactive ion etching," in *Technical Digest of the Solid-State Sensor and Actuator Workshop*, Hilton Head Island, SC, USA, June 8-11, 1998, pp.45-50.
- [63] E.M. Chow, H. T Soh, A. Partridge, J. A. Harley, T. W. Kenny, C. F. Quate, S. Abdollahi-Alibeik, J. P. McVittie and A. McCarthy, "Fabrication of high-density cantilever arrays and through-wafer interconnects," in *Technical Digest of the Solid-State Sensor and Actuator Workshop*, Hilton Head Island, SC, USA, June 8-11, 1998, pp.220-224.
- [64] G.K. Fedder and X. Zhu, "Method of fabricating micromachined structure and devices formed therefrom," *U.S. Patent Pending*, application filed September 30, 1999.
- [65] MOSIS Integrated Circuit Fabrication Service, <http://www.mosis.com>.
- [66] X. Zhu, D. W. Greve, and G. K. Fedder, "Characterization of Silicon Isotropic Etch by Inductively Coupled Plasma Etch in Post-CMOS Processing," in *Proceedings of the 13th IEEE International Conference on Micro Electro Mechanical Systems (MEMS 2000)*, January 23-27, 2000, Miyazaki, Japan.
- [67] J. Jiao, M. Chabloz, T. Matsuura and K. Tsutsumi, "Mask layout related area effect on HARSE process in MEMS applications," in *Technical Digest of the 1999 International Conference on Solid State Sensors and Actuators - Transducers '99*, Sendai, Japan, June 7-10, 1999, pp.546-549.

---

**Bibliography**

---

- [68] J.C. Greenwood, "Silicon in mechanical sensors", *J. Phys. E, Sci. Instrum.*, vol.21, pp.1114-1128.
- [69] D.C. Ghiglia and M.D. Pritt, "Two-Dimensional Phase Unwrapping: Theory, Algorithms, and Software," John Wiley & Sons, Inc., New York, 1998.
- [70] H. Xie, Y. Pan and G. K. Fedder, "A CMOS-MEMS micromirror with large out-of-plane actuation," Proceedings of the 2001 ASME International Mechanical Engineering Congress and Exposition - IMECE'01, New York, NY, Nov. 11-16 2001.
- [71] Y. Pan, H. Xie and G.K. Fedder, "Endoscopic Optical Coherence Tomography Based on a CMOS-MEMS micromirror", *Optics Letters*, vol.26, no.24 (Dec. 15, 2001), pp.1966-1968.
- [72] H. Xie, Y. Pan and G.K. Fedder, "A SCS CMOS Micromirror for Optical Coherence Tomographic Imaging," *IEEE MEMS 2002*, Las Vegas, Nevada, USA, January 20-24, 2002, pp.495-499.
- [73] Maxwell 2D field simulation, Version 1.9.04, Copyright 1984-1997, Ansoft Corporation, Pittsburgh, PA.
- [74] L.Y. Lin, J.L. Shen, S.S. Lee and W.C. Wu, "Surface-micromachined micro-XYZ stages for free-space microoptical bench," *IEEE Photonics Technology Letters*, vol. 9 (1997), pp.345-347.
- [75] W. Hemmert, M.S. Mermelstein and D.M. Freeman, "Nanometer resolution of 3-D motions using video interference microscopy," in *Technical Digest of the 12th IEEE International Conference on Micro Electro Mechanical Systems - MEMS'99*, Orlando, FL, USA, January 17-21, 1999, pp.302-308.
- [76] Wyko NT2000 Optical Profiler, <http://www.veeco.com>.
- [77] J. Buhler, J. Funk, O. Paul, F.-P. Steiner, H. Baltes, "Thermally actuated CMOS micromirrors," *Sensors & Actuators A*, Vol. 46-47 (1995), p.572-575.
- [78] G.K. Fedder, J.C. Chang, and R.T. Howe, "Thermal assembly of polysilicon microactuators with narrow-gap electrostatic comb drive", Technical Digest. IEEE Solid-State Sensor and Actuator Workshop, Hilton Head Island, SC, 22-25 June 1992, pp.63-68.
- [79] K. Takahata, N. Shibaike, H. Guckel, "A novel micro electro-discharge machining method using electrodes fabricated by the LIGA process," *MEMS'99*, pp.238 -243.
- [80] X. Zhang, X.N. Jiang, C. Sun, "Micro-stereolithography of polymeric and ceramic microstructures," *Sensors and Actuators A (Physical)*, vol.A77, no.2 pp.149-156.

- 
- [81] A. Lawrence, *Modern Inertial Technology: Navigation, Guidance, and Control*, New York: Springer-Verlag, 1993.
- [82] N. Yazdi, F. Ayazi, K. Najafi, "Micromachined Inertial sensors", *Proceedings of IEEE*, vol.86, no.8, pp.1640-1659.
- [83] <http://memsmarket.sysplan.com/study.html>
- [84] K. Tanaka, Y. Mochida, S. Sugimoto, K. Moriya, T. Hasegawa, K. Atsuchi, K. Ohwada, "A micromachined vibrating gyroscope", *Proceedings. IEEE Micro Electro Mechanical Systems 1995*, Amsterdam, Netherlands; 29 Jan.-2 Feb. 1995, pp.278-281.
- [85] D. Sparks, D. Slaughter, R. Beni, L. Jordan, M. Chia, D. Rich, J. Johnson, T. Vas, "Chip-scale packaging of a gyroscope using wafer bonding", *Sensors and Materials*, vol.11, no.4, pp.197-207.
- [86] T. Juneau, A.P. Pisano, J.H. Smith, "Dual axis operation of a micromachined rate gyroscope", *Transducers' 97*, Chicago, IL, USA; 16-19 June 1997, pp.883-886.
- [87] K.Y. Park, C.W. Lee, Y.S. Oh, Y.H. Cho, "Laterally oscillated and force-balanced micro vibratory rate gyroscope supported by fish hook shape springs", in *Proceedings of The Tenth Annual International Workshop on Micro Electro Mechanical Systems - MEMS'97*, Nagoya, Japan; 26-30 Jan. 1997, pp.494-499.
- [88] W. Geiger, J. Merz, T. Fischer, B. Folkmer, H. Sandmaier, and W. Lang, "The silicon Angular Rate Sensor System MARS-RR", *Transducers'99*, Sendai, Japan, June 7-10, 1999, pp.1578-1581.
- [89] J.A. Geen, S.J. Sherman, J.F. Chang and S.R. Lewis, "Single-chip surface-micromachining integrated gyroscope with 50 deg/hour root Allan variance", Digest of 2002 IEEE International Solid-State Circuits Conference, San Francisco, CA, Feb. 3-7, 2002, pp.426-427.
- [90] T.K. Tang, R.C. Gutierrez, C.B. Stell, V. Vorperian, G.A. Arakaki, J.T. Rice, W.J. Li, I. Chakraborty, K. Shcheglov, J.Z. Wilcox, W.J. Kaiser, "A packaged silicon MEMS vibratory gyroscope for microspacecraft", *MEMS'97*, Nagoya, Japan; 26-30 Jan. 1997, pp.500-505.
- [91] Y. Mochida, M. Tamura, K. Ohwada, "A micromachined vibrating rate gyroscope with independent beams for the drive and detection modes", *MEMS'99*, Orlando, FL, USA; 17-21 Jan. 1999, pp.618-623.
- [92] K.Y. Park, H.S. Jeong, S. An, S.H. Shin, and C.W. Lee, "Lateral gyroscope suspended by two gimbals through high aspect ratio ICP etching", *Transducers'99*, Sendai, Japan, June 7-10, 1999, pp.972-975.

---

**Bibliography**

---

- [93] F.P. Beer and E.R. Johnston, Jr., *Mechanics of Materials*, McGraw-Hill Book Co., Singapore, 1987, pp.170-172.
- [94] F.P. Beer and E.R. Johnston, Jr., *Mechanics of Materials*, McGraw-Hill Book Co., Singapore, 1987, pp.574-583.
- [95] S.P. Timoshenko and J.N. Goodier, *Theory of Elasticity*, Chapter 10, pp.309-313. McGraw-Hill, New York, New York, 3<sup>rd</sup> ed., 1970.
- [96] A. Shkel, R.T. Howe, and R. Horowitz, "Modeling and simulation of micromachined gyroscopes in the presence of imperfections," *MSM'99*, 19-21 April 1999, San Juan, Puerto Rico, pp.605-608.
- [97] S. Iyer, "Modeling and Simulation of Manufacturing Effects in a Z-axis CMOS-MEMS Gyroscope," Ph.D. Thesis, Carnegie Mellon University, 2002.
- [98] W. Maly and A. Strowjos, "Statistical Simulation of the IC manufacturing process," *IEEE Trans. on computer-aided design*, vol.CAD-1 (1982), pp.120-131.
- [99] OCEAN Reference, Cadence Design Systems, Inc., San Jose, CA, <http://www.cadence.com>.
- [100] S. V. Iyer, Q. Jing, G. K. Fedder, and T. Mukherjee, "Convergence and Speed Issues in Analog HDL Model Formulation for MEMS, in *Technical Proceedings of the Fourth International Conference on Modeling and Simulation of Microsystems (MSM 2001)*, March 19-21, 2001, Hilton Head, SC, USA.
- [101] N. Maluf, *An Introduction to Microelectromechanical Systems Engineering*, pp.21, Artech House, Inc., Boston, 2000.
- [102] K. Gilleo, "MEMS packaging issues and materials," *SPIE Vol.4339* (2000), pp.598-604.
- [103] G. Lorenz, R. Neul, "Network-type modeling of micromachined sensor systems", *Proc. 1998 International Conference on Modeling and Simulation of Microsystems, Semiconductors, Sensors and Actuators*, Santa Clara, CA, USA; 6-8 April 1998, p.233-238.
- [104] G.T.A. Kovacs, N.I. Maluf and K.E. Petersen, "Bulk micromachining of silicon," *Proceedings of IEEE*, vol.86, no.8, pp.1536-1551.
- [105] J.M. Bustillo, R.T. Howe and R.S. Muller, "Surface micromachining for microelectromechanical systems," *Proceedings of IEEE*, vol. 86, no.8, pp.1552-1574.
- [106] M.A. Schmidt, "Wafer-to-wafer bonding for microstructure formation," *Proceedings of IEEE*, vol. 86, no.8, pp.1575-1585.



- 
- [107] H. Guckel, "High-aspect-ratio micromachining via deep X-ray lithography," *Proceedings of IEEE*, vol. 86, no.8, pp.1586-1593.
- [108] A. Singh, D.A. Horsley, M.B. Cohn, A.P. Pisano, R.T. Howe, "Batch transfer of microstructures using flip-chip solder bump bonding," *TRANSDUCERS '97*, Chicago, 16-19 June, 1997, pp.265 -268.
- [109] E.C. Harvey, P.T. Rumsby, M.C. Gower, S. Mihailov, D. Thomas, "Excimer lasers for micromachining," *IEE Colloquium on Microengineering and Optics*, 1994, pp.1-4.
- [110] J. Eichholz, J. Quenzer, O. Schwarzelbach, M. Weib and B. Wenk, "HDL-A-model of a micromachined tuning fork gyroscope", *Proc. 2000 International Conference on Modeling & Simulation of Microsystems - MSM'2000*, San Diego, CA; 27-29 Mar. 2000, pp.170-173.
- [111] L. Meirovitch, *Analytical Methods in Vibrations*, New York: Macmillan Publishing Co., 1967.
- [112] F. Paoletti, M.A. Gretillat, N.F. de Rooij, "A silicon micromachined vibrating gyroscope with piezoresistive detection and electromagnetic excitation", *MEMS' 96*, San Diego, CA, USA; 11-15 Feb. 1996, pp.162-167.
- [113] H. Baltes, O. Paul, O. Brand, "Micromachined thermally based CMOS microsensors," *Proceedings of the IEEE*, vol.86 (1998), no.8, pp.1660 -1678.
- [114] A.V. Chavan, K.D. Wise, "A monolithic fully-integrated vacuum-sealed CMOS pressure sensor," *The IEEE Thirteenth Annual International Conference on Micro Electro Mechanical Systems - MEMS 2000*, pp.341 -346.
- [115] H. Dudaicevs, Y. Manoli, W. Mokwa, M. Schmidt, E. Spiegel, "A Fully Integrated Surface Micromachined Pressure Sensor With Low Temperature Dependence," *The 8th International Conference on Solid-State Sensors and Actuators - Transducers '95*, Vol.1, pp.616 -619.
- [116] O. Paul, D. Westberg, M. Hornung, V. Ziebart, H. Baltes, "Sacrificial aluminum etching for CMOS microstructures," *Proc. The IEEE Tenth Annual International Conference on Micro Electro Mechanical Systems - MEMS '97*, pp.523 -528.
- [117] H. Takao, H. Fukumoto, and M. Ishida, "A CMOS Integrated Three-Axis Accelerometer Fabricated With Commercial Submicrometer CMOS Technology and Bulk-Micromachining," *IEEE Transactions On Electron Devices*, vol.48, no.9, pp.1961-1968.

- [118] David F. Guillou, Suresh Santhanam and L. R. Carley, "Laminated, sacrificial-poly MEMS technology in standard CMOS," *Sensors and Actuators A*, vol.A85, no.1-3 pp.346-355.
- [119] J. Buhler, "Deformable Micromirror Arrays by CMOS Technology," Ph.D. Thesis, ETH Zurich, 1997.
- [120] S. Iyer, and T. Mukherjee, "Simulation of Manufacturing Variations in a Z-axis CMOS-MEMS Gyroscope," *MSM 2002*, Puerto Rico, April 21-25, pp.186-189.
- [121] W.C. Tang, M.G. Lim, and R.T. Howe, "Electrostatic comb drive levitation and control method," *Journal of Microelectromechanical Systems*, vol.1, no.4, (1992), pp.170-178.
- [122] H. Xie, G.K. Fedder, Z. Pan, and W. Frey, "New CMOS-MEMS processes for high-aspect-ratio bulk silicon microstructures", Carnegie Mellon University invention disclosure, #02-027, Oct. 29, 2001.

